Nonlinear Dynamic Behaviour and Instability of Advanced Materials and Structures

Author:
Gao, Kang

Publication Date:
2018

DOI:
https://doi.org/10.26190/unsworks/20892

License:
https://creativecommons.org/licenses/by-nc-nd/3.0/au/
Link to license to see what you are allowed to do with this resource.

Downloaded from http://hdl.handle.net/1959.4/61178 in https://unsworks.unsw.edu.au on 2024-04-29

Nonlinear Dynamic Behaviour and Instability of Advanced Materials and Structures

Kang Gao

A thesis submitted in fulfilment of the requirements for the degree of

DOCTOR OF PHILOSOPHY

UNSW

School of Civil and Environmental Engineering
Faculty of Engineering

November 2018

PLEASE TYPE

THE UNIVERSITY OF NEW SOUTH WALES
Thesis/Dissertation Sheet

Surname or Family name: Gao

First name: Kang

Other name/s:

Abbreviation for degree as given in the University calendar: PhD

School: School of Civil and Environmental Engineering

Faculty: Engineering

Title: Nonlinear dynamic behaviour and instability of advanced materials and structures

Abstract 350 words maximum: (PLEASE TYPE)

Owing to the rapidly advanced production techniques and falling cost of material manufacture, advanced materials are increasingly applied in both academia and industry fields. Classical static structural stability analysis provides a reliable and efficient tool to evaluate critical buckling load-carrying capacity of thin-walled structures made of traditional homogeneous materials. However, as the application of advanced materials is becoming diverse and more complex, such as thermal effect, damping effect and resting on or embedding in elastic foundation/medium, the problems of dynamic characteristics and stability of structures made of new materials need to be further studied. Thus, it is vital and essential to investigate the dynamic behaviour and stability of slender engineering structures (i.e., beam, plate and shell) made of advanced materials under different extreme conditions and develop an appropriate strategy to ensure safety and serviceability of these structures.

This dissertation aims to provide a comprehensive analytical framework for dynamic behaviour assessment of beam, plate and cylindrical shell made of advanced materials, as well as a vivid modelling on the damping effects, thermal effect and elastic foundation for structures under dynamic loadings. For dynamic buckling of beams, both the Galerkin-Force method and energy method are utilized by considering different boundary conditions, damping and thermal effects; For dynamic buckling of plates, based on the classical plate theory and accounting for von-Kármán strain-displacement relation, the nonlinear compatibility equation is derived. Then the Galerkin method and Airy's stress function are applied, and the obtained the nonlinear differential equations are solved numerically by the fourth-order Runge-Kutta method; As for the dynamic buckling of cylindrical shells, employing Hamilton's principle, the equations of motions are derived.

Therefore, by comparing with finite element methods, the other analytical methods in the open literature, the validity, accuracy, applicability of the proposed analytical models and solutions were comprehensively examined. The dynamic buckling analysis and dynamic assessment of thin-walled structures made of advanced materials conducted in this dissertation can help the optimum design of such structures under dynamic loadings, as well as a useful benchmark for design and analysis of nano/micro-sized devices and systems.

Declaration relating to disposition of project thesis/dissertation

I hereby grant to the University of New South Wales or its agents the right to archive and to make available my thesis or dissertation in whole or in part in the University libraries in all forms of media, now or here after known, subject to the provisions of the Copyright Act 1968. I retain all property rights, such as patent rights. I also retain the right to use in future works (such as articles or books) all or part of this thesis or dissertation.

I also authorise University Microfilms to use the 350 word abstract of my thesis in Dissertation Abstracts International (this is applicable to doctoral theses only).

Signature | Witness Signature | Date

The University recognises that there may be exceptional circumstances requiring restrictions on copying or conditions on use. Requests for restriction for a period of up to 2 years must be made in writing. Requests for a longer period of restriction may be considered in exceptional circumstances and require the approval of the Dean of Graduate Research.

FOR OFFICE USE ONLY

Date of completion of requirements for Award:

COPYRIGHT STATEMENT

'I hereby grant the University of New South Wales or its agents the right to archive and to make available my thesis or dissertation in whole or part in the University libraries in all forms of media, now or here after known, subject to the provisions of the Copyright Act 1968. I retain all proprietary rights, such as patent rights. I also retain the right to use in future works (such as articles or books) all or part of this thesis or dissertation.

I also authorise University Microfilms to use the 350-word abstract of my thesis in Dissertation Abstract International (this is applicable to doctoral theses only).

I have either used no substantial portions of copyright material in my thesis or I have obtained permission to use copyright material; where permission has not been granted I have applied/will apply for a partial restriction of the digital copy of my thesis or dissertation.'

Signed……………………………………………........................

Date……………………………………………...........................
25/08/2018

AUTHENTICITY STATEMENT

'I certify that the Library deposit digital copy is a direct equivalent of the final officially approved version of my thesis. No emendation of content has occurred and if there are any minor variations in formatting, they are the result of the conversion to digital format.'

Signed …………………………………………………........................

25/08/2018

Date ……………………………………………………..........................

ORIGINALITY STATEMENT

‘I hereby declare that this submission is my own work and to the best of my knowledge it contains no materials previously published or written by another person, or substantial proportions of material which have been accepted for the award of any other degree or diploma at UNSW or any other educational institution, except where due acknowledgement is made in the thesis. Any contribution made to the research by others, with whom I have worked at UNSW or elsewhere, is explicitly acknowledged in the thesis. I also declare that the intellectual content of this thesis is the product of my own work, except to the extent that assistance from others in the project's design and conception or in style, presentation and linguistic expression is acknowledged.’

Signed ……………………………………………..........

Date …………………………………………….............. 25/08/2018

INCLUSION OF PUBLICATIONS STATEMENT

UNSW is supportive of candidates publishing their research results during their candidature as detailed in the UNSW Thesis Examination Procedure.

Publications can be used in their thesis in lieu of a Chapter if:

- The student contributed greater than 50% of the content in the publication and is the "primary author", ie. the student was responsible primarily for the planning, execution and preparation of the work for publication
- The student has approval to include the publication in their thesis in lieu of a Chapter from their supervisor and Postgraduate Coordinator.
- The publication is not subject to any obligations or contractual agreements with a third party that would constrain its inclusion in the thesis

Please indicate whether this thesis contains published material or not.

☐ *This thesis contains no publications, either published or submitted for publication (if this box is checked, you may delete all the material on page 2)*

☐ *Some of the work described in this thesis has been published and it has been documented in the relevant Chapters with acknowledgement (if this box is checked, you may delete all the material on page 2)*

☒ *This thesis has publications (either published or submitted for publication) incorporated into it in lieu of a chapter and the details are presented below*

CANDIDATE'S DECLARATION

I declare that:

- I have complied with the Thesis Examination Procedure
- where I have used a publication in lieu of a Chapter, the listed publication(s) below meet(s) the requirements to be included in the thesis.

Name	Signature	Date (dd/mm/yy)
Kang Gao		23/08/2018

Postgraduate Coordinator's Declaration (to be filled in where publications are used in lieu of Chapters)

I declare that:

- the information below is accurate
- where listed publication(s) have been used in lieu of Chapter(s), their use complies with the Thesis Examination Procedure
- the minimum requirements for the format of the thesis have been met.

PGC's Name	PGC's Signature	Date (dd/mm/yy)
Hamid Valipour		24/08/2018

For each publication incorporated into the thesis in lieu of a Chapter, provide all of the requested details and signatures required

<table>
<tr><td colspan="7">Details of publication #1:
Full title: Nonlinear dynamic stability analysis of Euler-Bernoulli beam-columns with damping effects under thermal environment
Authors: Gao K, Gao W, Wu D, Song C
Journal or book name: Nonlinear Dynamics
Volume/page numbers: 2017; 90:2423-2444
Date accepted/ published: Published</td></tr>
<tr><td>Status</td><td>Published</td><td>☒</td><td>Accepted and In press</td><td></td><td>In progress (submitted)</td><td></td></tr>
<tr><td colspan="7">The Candidate's Contribution to the Work

Kang Gao did more than 50% of the work, which includes proposing the conception and design of the work, performing analysis, collecting data and finally writing the manuscript.</td></tr>
<tr><td colspan="7">Location of the work in the thesis and/or how the work is incorporated in the thesis:
The corresponding work located in Chapter 3.</td></tr>
<tr><td colspan="7">Primary Supervisor's Declaration
I declare that:
• the information above is accurate
• this has been discussed with the PGC and it is agreed that this publication can be included in this thesis in lieu of a Chapter
• All of the co-authors of the publication have reviewed the above information and have agreed to its veracity by signing a 'Co-Author Authorisation' form.</td></tr>
</table>

Supervisor's name	*Supervisor's signature*	*Date (dd/mm/yy)*
Wei Gao		15/08/2018

Co-author's declaration

I authorise the inclusion of this publication in the student's thesis and certify that:

- the declaration made by the student on the declaration for a thesis with publication form correctly reflects the extents of the student's contribution to this work;
- the student contributed greater than 50% of the content of the publication and is the "primary author" ie. the student was responsible primarily for the planning, execution and preparation of the work for publication.

Co-author's name	*Co-author's signature*	*Date (dd/mm/yy)*
Wei Gao		15/08/2018
Di Wu		15/08/2018
Chongmin Song		15/08/2018

<table>
<tr><td colspan="6">Details of publication #2:
Full title: Nonlinear dynamic characteristics and stability of composite orthotropic plate on elastic foundation under thermal environment
Authors: Gao K, Gao W, Wu D, Song C
Journal or book name: Composite Structures
Volume/page numbers: 2017; 168:619-632.
Date accepted/ published: Published</td></tr>
<tr><td>Status</td><td>Published</td><td>☒</td><td>Accepted and In press</td><td></td><td>In progress (submitted)</td></tr>
<tr><td colspan="6">The Candidate's Contribution to the Work

Kang Gao did more than 50% of the work, which includes proposing the conception and design of the work, performing analysis, collecting data and finally writing the manuscript.</td></tr>
<tr><td colspan="6">Location of the work in the thesis and/or how the work is incorporated in the thesis:
The corresponding work located in Chapter 4.</td></tr>
<tr><td colspan="6">Primary Supervisor's Declaration
I declare that:
• the information above is accurate
• this has been discussed with the PGC and it is agreed that this publication can be included in this thesis in lieu of a Chapter
• All of the co-authors of the publication have reviewed the above information and have agreed to its veracity by signing a 'Co-Author Authorisation' form.</td></tr>
<tr><td colspan="2">Supervisor's name
Wei Gao</td><td colspan="2">Supervisor's signature</td><td colspan="2">Date (dd/mm/yy)
15/08/2018</td></tr>
<tr><td colspan="6">Co-author's declaration
I authorise the inclusion of this publication in the student's thesis and certify that:

• the declaration made by the student on the declaration for a thesis with publication form correctly reflects the extents of the student's contribution to this work;
• the student contributed greater than 50% of the content of the publication and is the "primary author" ie. the student was responsible primarily for the planning, execution and preparation of the work for publication.</td></tr>
<tr><td colspan="2">Co-author's name</td><td colspan="2">Co-author's signature</td><td colspan="2">Date (dd/mm/yy)</td></tr>
<tr><td colspan="2">Wei Gao</td><td colspan="2"></td><td colspan="2">15/08/2018</td></tr>
<tr><td colspan="2">Di Wu</td><td colspan="2"></td><td colspan="2">15/08/2018</td></tr>
<tr><td colspan="2">Chongmin Song</td><td colspan="2"></td><td colspan="2">15/08/2018</td></tr>
</table>

<table>
<tr><td colspan="6">Details of publication #3:
Full title: Nonlinear primary resonance of functionally graded porous cylindrical shells using the method of multiple scales
Authors: Gao K, Gao W, Wu B, Wu D, Song C.
Journal or book name: Thin-Walled Structures
Volume/page numbers: 2018; 125:281-293.
Date accepted/ published: Published</td></tr>
<tr><td>Status</td><td>Published</td><td>☒</td><td>Accepted and In press</td><td></td><td>In progress (submitted)</td></tr>
<tr><td colspan="6">The Candidate's Contribution to the Work

Kang Gao did more than 50% of the work, which includes proposing the conception and design of the work, performing analysis, collecting data and finally writing the manuscript.</td></tr>
<tr><td colspan="6">Location of the work in the thesis and/or how the work is incorporated in the thesis:
The corresponding work located in Chapter 5.</td></tr>
<tr><td colspan="6">Primary Supervisor's Declaration
I declare that:
• the information above is accurate
• this has been discussed with the PGC and it is agreed that this publication can be included in this thesis in lieu of a Chapter
• All of the co-authors of the publication have reviewed the above information and have agreed to its veracity by signing a 'Co-Author Authorisation' form.</td></tr>
</table>

Supervisor's name	*Supervisor's signature*	*Date (dd/mm/yy)*
Wei Gao		15/08/2018

Co-author's declaration

I authorise the inclusion of this publication in the student's thesis and certify that:

- the declaration made by the student on the declaration for a thesis with publication form correctly reflects the extents of the student's contribution to this work;
- the student contributed greater than 50% of the content of the publication and is the "primary author" ie. the student was responsible primarily for the planning, execution and preparation of the work for publication.

Co-author's name	*Co-author's signature*	*Date (dd/mm/yy)*
Wei Gao		15/08/2018
Di Wu		15/08/2018
Binhua Wu		16/08/2018
Chongmin Song		15/08/2018

Details of publication #4:
Full title: Nonlinear dynamic stability of the orthotropic functionally graded cylindrical shell surrounded by Winkler-Pasternak elastic foundation subjected to a linearly increasing load.
Authors: Gao K, Gao W, Wu D, Song C.
Journal or book name: Journal of Sound and Vibration
Volume/page numbers: 2018; 415:147-168.
Date accepted/ published: Published

Status	*Published*	☒	*Accepted and In press*		*In progress (submitted)*	

The Candidate's Contribution to the Work

Kang Gao did more than 50% of the work, which includes proposing the conception and design of the work, performing analysis, collecting data and finally writing the manuscript.

Location of the work in the thesis and/or how the work is incorporated in the thesis:
The corresponding work located in Chapter 6.

Primary Supervisor's Declaration
I declare that:
- the information above is accurate
- this has been discussed with the PGC and it is agreed that this publication can be included in this thesis in lieu of a Chapter
- All of the co-authors of the publication have reviewed the above information and have agreed to its veracity by signing a 'Co-Author Authorisation' form.

Supervisor's name	*Supervisor's signature*	*Date (dd/mm/yy)*
Wei Gao		15/08/2018

Co-author's declaration
I authorise the inclusion of this publication in the student's thesis and certify that:

- the declaration made by the student on the declaration for a thesis with publication form correctly reflects the extents of the student's contribution to this work;
- the student contributed greater than 50% of the content of the publication and is the "primary author" ie. the student was responsible primarily for the planning, execution and preparation of the work for publication.

Co-author's name	*Co-author's signature*	*Date (dd/mm/yy)*
Wei Gao		15/08/2018
Di Wu		15/08/2018
Chongmin Song		15/08/2018

Details of publication #5:
Full title: Nonlinear dynamic buckling of the imperfect orthotropic E-FGM circular cylindrical shells subjected to the longitudinal constant velocity.
Authors: Gao K, Gao W, Wu D, Song C.
Journal or book name: International Journal of Mechanical Sciences
Volume/page numbers: 2018; 138:199-209.
Date accepted/ published: Published

Status	*Published*	☒	*Accepted and In press*		*In progress (submitted)*	

The Candidate's Contribution to the Work

Kang Gao did more than 50% of the work, which includes proposing the conception and design of the work, performing analysis, collecting data and finally writing the manuscript.

Location of the work in the thesis and/or how the work is incorporated in the thesis:
The corresponding work located in Chapter 7.

Primary Supervisor's Declaration
I declare that:

- the information above is accurate
- this has been discussed with the PGC and it is agreed that this publication can be included in this thesis in lieu of a Chapter
- All of the co-authors of the publication have reviewed the above information and have agreed to its veracity by signing a 'Co-Author Authorisation' form.

Supervisor's name	*Supervisor's signature*	*Date (dd/mm/yy)*
Wei Gao		15/08/2018

Co-author's declaration
I authorise the inclusion of this publication in the student's thesis and certify that:

- the declaration made by the student on the declaration for a thesis with publication form correctly reflects the extents of the student's contribution to this work;
- the student contributed greater than 50% of the content of the publication and is the "primary author" ie. the student was responsible primarily for the planning, execution and preparation of the work for publication.

Co-author's name	*Co-author's signature*	*Date (dd/mm/yy)*
Wei Gao		15/08/2018
Di Wu		15/08/2018
Chongmin Song		15/08/2018

Abstract

Owing to the rapidly advanced production techniques and falling cost of material manufacture, advanced materials are increasingly applied in both academia and industry fields. Classical static structural stability analysis provides a reliable and efficient tool to evaluate critical buckling load-carrying capacity of thin-walled structures made of traditional homogeneous materials. However, as the application of advanced materials is becoming diverse and more complex, such as thermal effect, damping effect and resting on or embedding in elastic foundation/medium, the problems of dynamic characteristics and stability of structures made of new materials need to be further studied. Thus, it is vital and essential to investigate the dynamic behaviour and stability of slender engineering structures (i.e., beam, plate and shell) made of advanced materials under different extreme conditions and develop an appropriate strategy to ensure safety and serviceability of these structures.

This dissertation aims to provide a comprehensive analytical framework for dynamic behaviour assessment of beam, plate and cylindrical shell made of advanced materials, as well as a vivid modelling on the damping effect, thermal effect and elastic foundation for structures under dynamic loadings. For dynamic buckling of beams, both the Galerkin-Force method and energy method are utilized by considering different boundary conditions, damping and thermal effects; For dynamic buckling of plates, based on the classical plate theory and accounting for von-Kármán strain-displacement relation, the nonlinear compatibility equation is derived. Then the Galerkin method and Airy's stress function are applied, and the obtained the nonlinear differential equations are solved

numerically by the fourth-order Runge-Kutta method; As for the dynamic buckling of cylindrical shells, by employing Hamilton's principle, the equations of motions are derived.

Therefore, by comparing with finite element methods, the other analytical methods in the open literature, the validity, accuracy, applicability of the proposed analytical models and solutions were comprehensively examined. The dynamic buckling analysis and dynamic assessment of thin-walled structures made of advanced materials conducted in this dissertation can help achieve the optimum design of such structures under dynamic loadings, as well as a useful benchmark for design and analysis of nano/micro-sized devices and systems.

Acknowledgements

Many people have made invaluable contributions, both directly and indirectly to my research. My most profound gratitude goes first and foremost to Professor Wei Gao, my supervisor, for his invaluable academic advice, consistent encouragements and insightful suggestions throughout my PhD study. The ideas and attitudes that I learnt from him on research as well as career development are priceless. In addition, I would like to express my heartfelt gratitude to my co-supervisor Professor Chongmin Song for providing me with valuable advice and continuous support in the past three years. Without their tremendous help and illuminating instruction, the completion of this thesis would be impossible.

I am also deeply indebted to my colleagues and the staff in the School of Civil and Environmental Engineering of UNSW for their kind assistance during my PhD life. Thank all the members in our group and the friends in office 713 for working, eating and playing together. It is them that made my life more colourful and left me a memorable experience.

Last but not the least, I would like to thank my family: my father Yong Gao, my mother Xiuchuan Liu, my younger sister Yan Gao for their love and care throughout these years and my life in general. At the end, I would like express appreciation to my beloved girlfriend Xiaomeng Qu who always stood by and accompanied me for sharing my happiness and suffering these years.

Contents

Nomenclature

Greek letter

α_x, α_y	Coefficient of linear expansion along the x and y axes
ε	Small parameter in the order of the amplitude of the response
$\psi(z)$	Material's exponential function
$\varepsilon_x^0, \varepsilon_y^0$	Normal strains
γ_{xy}^0	Shear strain at the middle surface
$\kappa_x, \kappa_y, \kappa_{xy}$	Change of curvatures and twist
κ_i	Exponential factor
δU_s	Virtual variation of the strain energy
δU_e	The virtual variation of potential energy stored in the deformed elastic foundation
δV_e	The variation of work done by the external load
δV_d	The virtual variation of potential energy of non-conservative forces
δK	The virtual variation of the kinetic energy
ρ	Mass density
ρ_0	The density of the homogeneous orthotropic material
$\rho_{\min}$	Minimum values of Mass density

$\rho_{\max}$	Maximum values of Mass density
ϖ_0	The fundamental frequency of the structure
ζ	The damping ratio of the beam
r_g	The radius of gyration of the section
ξ	The slenderness ratio of the beam
τ	Dimensionless time
Δt	The temperature change

English letter

a	Length of the plate
b	Width of the plate
c_d	The damping coefficient of the structure
c_d^*	Dimensionless damping coefficient
h	Thickness of the plate
e_0	Initial imperfection
e^*	Dimensionless initial imperfection
cc	Complex conjugate of the preceding terms
k_w	Winkler foundation modulus
k_{px}, k_{py}	Shear layer stiffness of Pasternak model along x and y direction

p	Average axial stress of the applied external force
t	Time
u	The displacement along x axis
v	Velocity
v^*	Dimensionless velocity
v_{12}, v_{21}	Poisson ratio in x and y directions
w	The displacement along z axis
w^*	Dimensionless deformation
dx	A small element along x-axis
$f(x)$	Buckling mode shape of the beam-column
d_1-d_4, c_1-c_4	The values of constants for different boundary conditions
A	Cross-sectional area
$A(T_1)$	Unknown complex function
$A_{11}, A_{12}, A_{21}, A_{22}, A_{66}$	Coefficients
$A^*_{11}, A^*_{12}, A^*_{21}, A^*_{22}, A^*_{66}$	Coefficients
$B_{11}, B_{12}, B_{21}, B_{22}, B_{66}$	Coefficients
$B^*_{11}, B^*_{12}, B^*_{21}, B^*_{22}, B^*_{66}$	Coefficients
$C^*_{11}, C^*_{12}, C^*_{21}, C^*_{22}, C^*_{66}$	Coefficients

$D_{11}, D_{12}, D_{21}, D_{22}, D_{66}$	Coefficients
$D^*_{11}, D^*_{12}, D^*_{21}, D^*_{22}, D^*_{66}$	Coefficients
D	Power dissipation function
E	Young's modulus
E_1, E_2	Young's modulus in x and y directions
E_{01}, E_{02}	Young’s moduli of the homogeneous orthotropic material along x, y directions
E_{min}	Minimum values of Young’s modulus
E_{max}	Maximum values of Young’s modulus
G_{12}	Shear modulus
G_0	Shear modulus of the homogeneous orthotropic material
G_{min}	Minimum values of shear modulus
G_{max}	Maximum values of shear modulus
H_1	Coefficients
J_1, J_2	Coefficients
K_1	Coefficient
$\bar{K}_w, \bar{K}_p$	Dimensionless elastic constants of foundations
I	The second moment of area
L	Length

L_1, L_2, L_3	Coefficient
M	Bending moment
M_1	Coefficient
M_B	The bending moment with respect to point B
N_0	The coefficient porosity
N_1	Coefficient
N_m	Porosity coefficient of mass density
P	External force
Q	Shear force
$P(t)$	The time-dependent external force
P_{cr}	The critical buckling load
T	The kinetic energy
U_a	Axial displacement due to axial shortening
U_b	Axial displacement due to the bending shortening
V	Potential energy
$W_{mn}(t)$	Time-varying amplitude of *w*
W_0	The initial eccentricity value of the plate

List of Figures

List of Tables

Chapter 1 Introduction

1.1 Background

As the basic elements in engineering practices, the mechanics and mechanism of beam, plate and shell structure have been investigated extensively in the past. Classical static structural stability analysis provides a reliable and efficient tool to evaluate the critical buckling load-carrying capacity of thin-walled and slender engineering structures (i.e., bar structures, plates or shells structures, cylindrical columns) [1-3]. On the bases of the well-established theoretical foundations (force-equilibrium and energy method)[4-7], accompanied with the availability of high-speed digital computers[1, 8], the static structural stability analysis has been widely implemented in different engineering fields [1, 9-11]. However, the static buckling analysis framework hardly provides general guidelines for structural design against dynamic buckling due to its incompetence of estimating the structural behaviour subjected to dynamic loads (i.e., wind effect, earthquakes, and stochastic dynamic loads) [12-14]. The time-dependent forces are intrinsic among engineering applications, and more importantly, excessively simplifications on such type of loading conditions in both structural analysis and design could compromise the structural safety.

Due to the rapidly advanced production techniques and falling cost of material manufacture, advanced materials are increasingly used in flexible batteries, replacement bones, structural components, lightweight sensors and so on in both academia and industry. As the application of advanced materials is becoming diversification and more complex, so the problems of dynamic characteristics and stability of structures made of new materials need to be further studied. Compared with the traditional homogeneous materials, composite materials have widely used in the engineering fields, such as reinforced-concrete slabs, high-way bridge decks, flight wings, ship hull, and aerospace structures for many decades, due to its outstanding stiffness, good energy-efficient and high strength-weight ratio. Even though fibre-reinforced or laminate composite materials have distinguished stiffness and large strength-weight ratio, severe stress concentrations or singularities at the corners of structure boundaries or interfaces between layers made of different materials would undermine the structure strength and even lead to non-deterministic buckling. Fortunately, an amazingly creative invention named functionally graded materials (FGMs) was proposed by material scientists during the spacecraft project, as a means of ultrahigh temperature resisting materials, which can effectively avoid stress concentrations or singularities due to the smooth transition of the material interface between metal and ceramic. Since then, the studies about FGMs have been completely blooming in almost all associated fields.

In general engineering applications (i.e. aerospace and mechanical engineering), structures are not only subjected to dynamic loadings but also exposed to the physical environment, such as thermal effects, moisture effects, etc. Furthermore, these structures usually rest on or embed in elastic foundation/medium. Under such circumstance, dynamic characteristics and stability of structures may be different from traditional ones. Thus, to ensure safety and serviceability of the thin-walled and slender engineering structures (i.e., beam, plate and shell), investigations on the dynamic characteristics and stability of such structures made of advanced materials under different conditions are much needed.

1.2 Objectives and Scope

The practical relevance and significance come from the increasing application of composite materials, orthotropic materials, FG orthotropic materials and the latest FG porous materials in modern engineering areas and the unknown influence of material properties, damping effect, thermal effect, elastic foundation, etc., on structures' dynamic characteristics and stability behaviours. Therefore, the primary purpose of this thesis is to provide a comprehensive analytical analysis framework for dynamic behaviour assessment of beam, plate and cylindrical shell made of advanced materials, as well as a vivid modelling on the damping effect, thermal effect and elastic foundation for structures under dynamic loadings. More explicitly, the following objectives have been encompassed in this research:

1. A unified nonlinear dynamic buckling analysis for Euler-Bernoulli beam-columns subjected to constant loading rates is proposed with the incorporation of mercurial damping effects under thermal environment. Both the Galerkin-Force method (GFM) and energy method (EM) are capable of handling effectively different boundary conditions, damping and thermal effects.
2. Nonlinear dynamic characteristics and stability of composite orthotropic plate on Winkler-Pasternak elastic foundation subjected to different axial velocities was developed with damping and thermal effects for the first time.
3. The nonlinear primary resonance behaviour of cylindrical shells made of functionally graded (FG) porous materials subjected to a uniformly distributed harmonic load including the damping effect was investigated. Three types of FG

porous distributions, namely symmetric porosity distribution, non-symmetric porosity stiff or soft distribution and uniform porosity distribution were considered.

4. The dynamic stability analysis of an FG orthotropic circular cylindrical shell surrounded by a Winkler-Pasternak elastic foundation subjected to linearly increasing load with the consideration of damping effect has been presented.
5. An analytical approach on the nonlinear dynamic buckling of the orthotropic circular cylindrical shells made of an exponential law functionally graded material (E-FGM) subjected to the longitudinal constant velocity is investigated with the incorporation of mercurial damping effect.

The developed method presented herein provides a comprehensive analytical analysis framework for dynamic stability assessment of thin-walled structures made of advanced materials with consideration of damping effects, thermal effects and elastic foundations, and the obtained conclusions can help optimum design of such structures under dynamic loadings, as well as a useful help for design and analysis of nano/micro-sized devices and systems.

1.3 Methodology

Among various approaches for estimating critical dynamic buckling load of structures, three major categories can be classified. The first category is the total energy-phase plane approach [15, 16], which emphasises on establishing the sufficiency conditions for structural stability (lower bounds) or instability (upper bounds) due to the characteristics of the system phase plane. The second category can generally be recognised as the total potential approach which was proposed by Simitses in 1965 [17]. Within this framework of analysis, the energy balance equation was implemented so the relationship between the potential energy and load parameter can be robustly established. The third type is the equation of motion approach, which was proposed by Budiansky and Roth in 1962 [18]. The governing equation can be solved numerically according to the parameters of the concerned structures, and also such approach can be flexibly modelled by computational methods which have been widely implemented [8, 19, 20]. Therefore, Budiansky-Roth criterion is used to evaluate dynamic buckling responses in this study.

The dynamic buckling phenomena of thin-walled structures have been investigated analytically, numerically and experimentally for more than half of century in various areas. The increasing application of FGM, such as orthotropic FG, FG porous, etc., makes the research of dynamic buckling more complex. It is true that the traditional finite element method (FEM) can serve as a reference to verify the dynamic characteristics of simply structures. However, the advantages of analytical methods over FEMs are: Firstly, for linear problems, the traditional FEM approach (i.e. ANSYS that used in this study) is very fast. For nonlinear dynamic analysis, the FEM takes more time to achieve a better convergence. Moreover, one needs to spend much time on problems, like mesh refinement, modelling, applying various boundary conditions, etc. Secondly, although the traditional FEM can get reliable results for eigenvalue problem, the results of nonlinear dynamic buckling are affected by many uncertainty properties, such as analysis types, element types, boundary conditions and the damping effects. One needs to be proficient with the software and improper picking will lead to large errors and even incorrect results. Take the damping effects as an example, in ANSYS; there are five types of damping models. Each of them has the strict requirements for the analysis types, and not all of them can be used in different analysis types. Thirdly, the modelling of FGMs is still at early stage, which is more complicated and time-consuming than traditional materials. Finally, the developed method presented provides a comprehensive analytical analysis framework for dynamic stability assessment of thin-walled structures, as well as a vivid modelling on the damping effects under different environment (thermal effect or rest on or embed in elastic foundation/medium) for structures under dynamic loadings. The nonlinear dynamic buckling analysis can help the optimum design of structures under dynamic loadings faster and efficiently.

The research of the nonlinearities due to nonlinear material properties and nonlinear boundary supports as well as nonlinear structural joints is out of the scope of present thesis. Because for dynamic buckling analysis, the structures will be failure in a few seconds while the material properties still remain in elastic range at this moment. Therefore, the material nonlinearities are often ignored in the dynamic buckling analysis. The influence of nonlinear boundary supports will be studied in the future, and the author mainly focus on traditional boundary conditions in this thesis.

The accuracy of theoretical models of structures can only be validated by experimental results. However, due to the lack of experimental equipment, the uncertain material properties, the inadequacy of budgetary funds, experimental investigations will not be included in this study. It is true that the nonlinear phenomena can be predicted accurately according to the experimental method. The author tried to find any test results related to the topics and used them as the validation in the present thesis, while relevant experimental researches about dynamic buckling of structures made of advanced materials has received limited attention. Most of them focused on material properties and static behaviours. Therefore, in the present thesis, the author verified the numerical results with FEM or other numerical methods in the open literature and tried to use some of experimental results that can be used as a validation. Moreover, as we all known, FEMs are widely implemented in different engineering fields to examine the experimental or theoretical methods. Therefore, the results of FEMs are credible.

For dynamic buckling of beam structures, both the Galerkin-Force method (GFM) and energy method (EM) are used by considering different boundary conditions, damping and thermal effects. By integrating Hamilton's principles into Lagrange's equations, the governing equation of the energy method is derived in the form of partial differential equations (PDEs) for dynamic buckling of beams. The obtained the nonlinear differential equations are solved numerically by the fourth-order Runge-Kutta method. The proposed Galerkin-Force method is to introduce the buckled shape function as a trial function into force equilibrium equation in dynamic buckling. The performance of the proposed two approaches is confirmed by finite element method (FEM); For dynamic buckling of plates, based on the classical plate theory and accounting for von-Kármán strain-displacement relation, the nonlinear compatibility equation is derived. Then the Galerkin method and Airy's stress function are applied, and the obtained the nonlinear differential equations are solved numerically by the fourth-order Runge-Kutta method. As for the dynamic buckling of cylindrical shells, utilizing Hamilton's principle, the equations of motions are derived. And the nonlinear compatibility equation is considered by means of modified Donnell shell theory including large deflection. Based on a hybrid analytical-numerical method (Galerkin method and fourth-order Runge-Kutta method), the dynamic governing equation can be solved. Finally, the proposed method was validated with other publications.

Therefore, by comparing with finite element method, the other methods in open literature, the validity, accuracy, applicability of the proposed analytical models and solutions were verified. The dynamic buckling analysis and dynamic assessment of thin-walled structures made of advanced materials conducted in this dissertation can help optimum design of such structures under dynamic loadings, as well as a useful benchmark for design and analysis of nano/micro-sized devices and systems.

1.4 Thesis online

The main purpose of this dissertation is to provide a comprehensive analytical analysis framework for dynamic behaviour assessment of beam, plate and cylindrical shell made of advanced materials, as well as an accurate modelling on the damping effects, thermal effect and elastic foundation for structures under dynamic loadings. The dissertation consists of seven chapters, and a brief overview of each chapter include in the dissertation is presented as follows:

Chapter 1 presents the background of dynamic buckling of beam, plate and cylindrical shell made of advanced materials and objectives, the scope of this research, followed by the methodology that used in this study. The structure of the dissertation and some associated publications are also listed in detail.

Chapter 2 surveys the previous work related to the dynamic characteristic and stability analysis of beam, plate and cylindrical shell made of advanced materials. The review covers the development of FG materials, the classification of dynamic buckling criterions and loading types. Then various methods on dynamic behaviours and stability analysis of beam, plate and cylindrical shell made of advanced materials are subsequently discussed. The influence of thermal effect, damping effect and elastic foundation is also presented.

Finally, based on the present review, a summary of knowledge gap is proposed for a better understanding of the present problems and the research objectives are further explicated.

Chapter 3 proposes two analytical-numerical methods (EM and GFM) for dynamic stability assessment of Euler-Bernoulli beam. The proposed analytical-numerical methods can incorporate multiple types of parameters of the dynamic response of structures within a unified nonlinear ordinary differential equation, such as beam geometry, material properties, loading rate, and different boundary conditions, especially damping and thermal effects. Consequently, the structural stability assessment against dynamic loading can be examined. The research found that the presence of the damping effects can strengthen structure ability against buckling by increasing the dynamic buckling load. However, the buckling time of structure will be delayed for a damped system. Moreover, the critical buckling is deceased for the temperature change from temperature fall to temperature rise. Temperature rise would defer the time of buckling while temperature fall would accelerate the time of buckling.

Chapter 4 develops an analytical solution about the nonlinear dynamic characteristics and stability of an eccentrically composite orthotropic plate on Winkler-Pasternak elastic foundation subjected to different axial velocities. Both damping effects and thermal effects are considered. The characteristics of natural frequency, linear and nonlinear vibration, frequency-amplitude curve and nonlinear dynamic responses were investigated; then various effects of constant velocity, damping ratio, temperature change, buckling mode, initial imperfection, elastic foundation parameter on nonlinear dynamic buckling of the plate were also discussed. The accuracy of the obtained results of frequency parameters is verified against the published paper by other methods and shows that the proposed method has good accuracy. Moreover, the proposed method can be applied to micro- and nanostructures.

Chapter 5 studies the nonlinear primary resonance analysis of cylindrical shells made of functionally graded (FG) porous materials subjected to a uniformly distributed harmonic load including the damping effect. Three types of FG porosity distributions (symmetric, non-symmetric stiff or soft and uniform) are investigated. The Galerkin method in conjunction with the method of multiple scales was utilised to obtain the Duffing-type equation. The detailed parametric studies on porosity distribution, porosity coefficient, damping ratio, amplitude and frequency of the external harmonic excitation, aspect ratio and thickness ratio, shown that the distribution type of FG porous cylindrical shells significantly affects primary resonance behavior and the response presents a hardening-type nonlinearity, which provides a useful help for the design and optimize of FG porous shell-type devices working under external harmonic excitation.

Chapter 6 conducts nonlinear dynamic buckling of functionally graded orthotropic cylindrical shell surrounded by Winkler-Pasternak foundation subjected to a linearly increasing loading with damping effect. The material properties vary gradually in the thickness direction based on an exponential distribution function. Hamilton's principle and modified Donnell shell theory were used to obtain the nonlinear differential governing equations. Effects of inhomogeneous parameters, loading speeds, damping ratios, aspect ratios and thickness ratios on dynamic buckling were also discussed.

Chapter 7 implements dynamic buckling of the imperfect orthotropic E-FGM cylindrical shell subjected to a longitudinal constant velocity. Both FG stiff and FG soft cylindrical shells are considered. The dynamic longitudinal loading on the shell is accomplished by applying a constant displacement rate at one end with respect to the other. According to the improved Donnell shell theory, the nonlinear compatibility equation and the equation of motion were derived with the consideration of initial imperfection and damping effects. The governing equation was solved by fourth-order Runge-Kutta method and the nonlinear dynamic stability of the orthotropic FG cylindrical shell is assessed based on Budiansky-Roth criterion. The Effect of various velocities, initial imperfections, damping ratios, inhomogeneous parameters κ_1 and κ_2 on nonlinear dynamic buckling of the orthotropic FG cylindrical shells were studied.

Chapter 8 concludes a summary of the work done in this dissertation, followed by the further recommendations of present work in the future study.

1.5 List of publications

During the three years of my PhD life, the following journal and conference papers have been published. They are direct outputs of my research towards the writing of this thesis and corresponding to the Chapter 3 - Chapter 7, respectively. The details of the papers are:

Journal papers

Gao K, Gao W, Chen D, Yang J. Nonlinear free vibration of functionally graded graphene platelets reinforced porous nanocomposite plates resting on elastic foundation, *Composite Structures*. 2018; 204: 831-846.

Gao K, Gao W, Wu D, Song C. Nonlinear dynamic stability of the orthotropic functionally graded cylindrical shell surrounded by Winkler-Pasternak elastic foundation subjected to a linearly increasing load. *Journal of Sound and Vibration*. 2018; 415:147-168.

Gao K, Gao W, Wu B, Wu D, Song C. Nonlinear primary resonance of functionally graded porous cylindrical shells using the method of multiple scales. *Thin-Walled Structures*. 2018; 125:281-293.

Gao K, Gao W, Wu D, Song C. Nonlinear dynamic buckling of the imperfect orthotropic E-FGM circular cylindrical shells subjected to the longitudinal constant velocity. *International Journal of Mechanical Sciences*. 2018; 138:199-209.

Gao K, Gao W, Wu D, Song C. Nonlinear dynamic characteristics and stability of composite orthotropic plate on elastic foundation under thermal environment. *Composite Structures*. 2017; 168:619-632.

Gao K, Gao W, Wu D, Song C. Nonlinear dynamic stability analysis of Euler-Bernoulli beam-columns with damping effects under thermal environment. *Nonlinear Dynamics*. 2017; 90:2423-2444.

Conference papers

Gao K, Gao W, Wu D, Song C. Dynamic stability of the eccentrically composite rectangular orthotropic plates subjected to different loading rates; *The Twenty-Fifth Annual International Conference on COMPOSITES/NANO ENGINEERING (ICCE-25); Rome, Italy; July 16-22, 2017*

Gao K, Gao W, Wu D, Song C. Dynamic buckling analysis of beams including damping effect. *The 24th Australasian Conference on the Mechanics of Structures and Materials; Perth, Australia, 6-9 December 2016*.

Chapter 2 Literature Review

This chapter reviews the existing studies about the dynamic behaviours and stability of beams, plates and cylindrical shells made of advanced materials. The similarities and differences are summarised based on various methodologies (analytical, numerical, hybrid or experimental aspects), loading conditions, external environments (thermal effect, damping effect or elastic foundation) and boundary conditions in Section 2.1. Section 2.2 reviews the dynamic behaviours and stability of beams. After that, the dynamic behaviours and stability of orthotropic plates are reviewed in Section 2.3. Section 2.4 summarised the past and current study on dynamic buckling of isotropic cylindrical shells, followed by dynamic analysis of orthotropic cylindrical shells and FG porous structures, respectively. The influence of thermal effect, damping effect and elastic foundation is shown in Section 2.7. Finally, Section 2.8 gives a summary of research objectives in this dissertation.

2.1 Introduction

An amazingly creative invention named functionally graded materials (FGMs) was proposed by material scientists during the spacecraft project in 1984, as a means of ultrahigh temperature resisting materials. Since then, the studies about FGM have been completely blooming in almost all associated fields. Generally, FGMs are made from a mixture of metallic and ceramic ingredients. As one of the most promising materials in lightweight structures, the mechanics and mechanism of FGMs have been investigated extensively in the past.

Nearly all of the studies regarding FGMs can be classified into three models based on the material graded along the focused direction: power-law FGM (P-FGM), sigmoid law FGM (S-FGM) and exponential law FGM (E-FGM). Tornabene [21] thoroughly investigated the free vibration of power-law FG conical, cylindrical shell and annular plate according to the shear deformation theory. Pradhan [22] presented dynamic behaviour of FGM cylindrical shells for various boundary conditions based on power law model. The influence of constituent volume fractions on the frequency features of an FG cylindrical shell was presented by Loy et al. [23] based on the power-law model. In 2001, A Sigmoid-FGM made of two power-law functions to define volume fraction was first reported by Chung and Chi [24]. In the second year, they concluded that the stress singularity of a cracked body would reduce apparently when using sigmoid FGM[25]. Hamed et al. [26] investigated free vibration of sigmoid FGM beams. Jung et al. [27] analysed the forced-vibration of a sigmoid FG plate according to the four-variable refined plate theory. Duc et al. [28] proposed the dynamic response of the imperfect symmetric thin sigmoid FGM plate resting on elastic foundation. Ravichandran [29]investigated the thermal residual stresses of the E-FGMs. Atmane [30] studied the free vibration behaviour of E-FGM beams with a variable cross-section with different boundary conditions. Chakraborty et al. [31] used finite element method to study the thermoelastic behaviour of FGM beam structures.

According to design standards and codes, thin-walled and slender engineering structures not only need to satisfy the load-carrying capacity but also sustain the stability condition. Therefore, the buckling behaviours of such structures under different effects (axially-loaded[32], pressure-loaded[33], torsional-loaded[34], thermal effect[35], combined axial-radial mechanical load[36], combined thermo-mechanical effect[37] and so on) has been extensively and systematically investigated based on experimental analysis and theoretical method more than half a century. In engineering practice, however, dynamic loads (i.e., wind effect, earthquakes, and stochastic dynamic loads) are commonly and intrinsically applied on the structures, excessively simplifications on such type of loading conditions in both structural analysis and design could compromise the structural safety.

Among various approaches for estimating critical dynamic buckling load of structures, three major categories can be classified. The first category is the total energy-phase plane approach [15, 16], which emphasises on establishing the sufficiency conditions for structural stability (lower bounds) or instability (upper bounds) due to the characteristics of the system phase plane. The second category can generally be recognized as the total potential approach which was proposed by Simitses in 1965 [17]. Within this framework of analysis, the energy balance equation was implemented so the relationship between the potential energy and load parameter can be robustly established. The third type is the equation of motion approach, which was proposed by Budiansky and Roth in 1962 [18]. The governing equation can be solved numerically according to the parameters of the concerned structures, and also such approach can be flexibly modelled by computational methods which have been widely implemented [8, 19, 20].

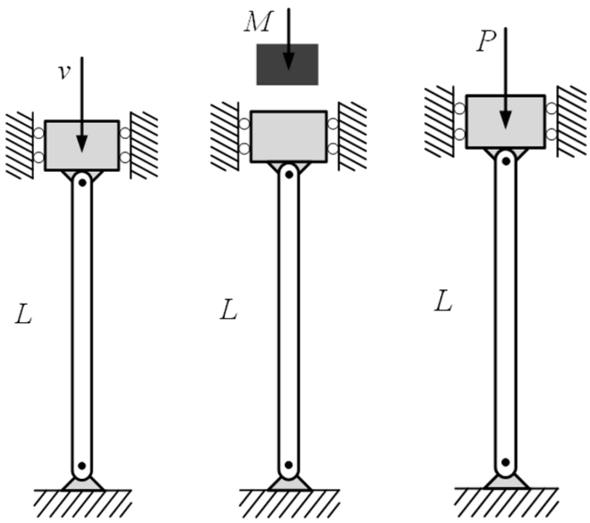

Figure 2.1 Different types of loading schemes

Additionally, nearly all of the researchers regarding dynamic buckling can be classified into three categories according to the following loading schemes [38], as shown in Figure 2.1.

1. Constant velocity or displacement loading scheme [4, 14, 39-44];

2. Constant mass impulse loading scheme [38, 45-49];

3. Force-time impulse loading scheme [7, 50-52].

2.2 Dynamic behaviours and stability of beams

In 1951, Hoff [53], as one of the earliest researchers on dynamic buckling, who studied that a perfectly straight pinned-pinned column subjected to a uniform velocity in a perfectly rigid testing machine. Motamarri et al.[43] studied the dynamic elastic buckling of beam-columns of various boundary conditions under a constant speed compression. This type of load differs from the other two loading schemes in that the time required to reach the structure critical load is larger than the time required for the elastic wave to travel from one end to the other. So normally the inertial effects can be ignored. In practice, the transition from dynamic to quasi-statics is nearly impossible[44], so normally the static loading-bearing capacity is measured by hydraulic testing machines, which means the structure is loaded by a constant displacement rate of the one end with respect to the other. Therefore, the threshold velocity values between static and dynamic are the key concerns in experiments and theoretical analysis. Based on this idea, Gao et al. [54] proposed two analytical-numerical methods, Galerkin-Force method (GFM) and energy method (EM), to investigate the dynamic behaviours of Euler-Bernoulli beam-columns under loading rates. In their analytical model, both the influence of the different boundary conditions, damping and thermal effects on dynamic response are obtained. The increasing application of the lightweight material in engineering practices, such as buildings, bridges and multi-span large frame structures makes the research of dynamic behaviours of such structures more important. The structures exposed in the strong earthquake and large wind effect may experience rapid shortenings or elongations. Under such circumstance, the time-dependent term in the analysis should not be ignored during analysis. Azad et al. [55] applied Hoff's method in analysing concentrically braced frames to stimulate the periodic vibration of earthquakes. Through dynamic experiments and FE analyses, they concluded that it is essential to consider the inertia effect when studying the seismic behaviour of concentrically braced frames.

Recently, the studies of dynamic buckling analysis of beams made of FGMs become popular due to higher stiffness and thermal resistance of these materials. Ghiasian et al.[56] studied the dynamic buckling response of FGM beams subjected to sudden thermal change with/without elastic foundation. Ren et al.[57] presented the mechanical buckling of a graphite column in non-equilibrium molecular dynamics (NEMD) simulations under different loading velocities. The dynamic instability of FG multilayer graphene nanocomposite beams under a periodic axial force with the consideration of thermal effect was examined by Wu et al. [58] and found that more graphene nanoplatelets additive near the top and bottom layers can strengthen the natural frequency and reduce the unstable region. Smyczynski and Magnucka [59] analysed the dynamic stability of a five-layer sandwich beam which consists of two metal layers, porous metal layer and two binding layers between them. Lim et al. [60, 61] investigated the dynamic response of metallic corrugated sandwich columns under high compressive rates. Additionally, structures' behaviours and stability of velocity impulse also occur in high speed travelling plates in the printing industry, aeronautics and flat-type fuel assemblies in research nuclear reactors[62].

Dynamic buckling phenomenon not only exists in the macroscopic scale but also witnessed by some scholars in laboratory among nanodevices, nanosensors and nanostructures. Xiong and Jiang [63]investigated dynamic buckling response of single-walled carbon nanotubes (SWCNTs) subjected to a sudden step load by modelling the SWCNTs as a thin cylinder shell. Compared with molecular dynamic models, the FE methods in ABAQUS were verified. Based on continuum mechanics, the dynamic torsional buckling of a double-walled carbon nanotube (DWCNT) surrounded by the elastic medium was presented by Sun and Liu[64]. After that, they also studied the dynamic shell buckling characteristics of multi-walled carbon nanotubes (MWCNTs) surrounded by the elastic medium subjected to a step axial load[65]. Hu et al. [66]proposed the axial dynamic buckling analysis of the SWCNT resting on the elastic foundation by complicated structure-preserving method. According to these studies, though traditional methodologies can be applied in dynamic buckling analysis of carbon nanotubes, nanostructures embrace some specific mechanical or dynamical properties, such as size effect or nonlocal effect, van der Waals interactions, etc. Therefore, experimental methods need to be considered when designing nanodevices under dynamic loads.

2.3 Dynamic behaviours and stability of orthotropic plates

Composites orthotropic plate has widely used in the engineering fields, such as reinforced-concrete slabs, high-way bridge decks, flight wings, ship hull, and aerospace structures for many decades, due to its outstanding stiffness, good energy-efficient and high strength-weight ratio. Nowadays, the application of such structure is becoming diversification and more complex, so the problems of dynamic characteristics and stability of orthotropic plate have been further studied.

From 1978 to 1997, Ari-Gur [49, 67-70] thoroughly investigated the dynamic buckling of columns subjected to a longitudinal moving mass based on experimental analysis and theoretical methods. At the same time, he [71]studied a rectangular plate impacted by a moving mass. After that, in 1997, he [72] also presented a rectangular fibre reinforced laminated plate subjected to half-sine compressive pulse load. Papazoglou et al.[73] studied the dynamic response of composite laminated plates under suddenly applied constant load, linearly increasing load and step loading with considering of damping effects. Ekstrom [74] investigated a simply-supported rectangular orthotropic plate subjected to a constant rate of loading (linearly increasing load). Recently years, Azarboni et al.[75]presented dynamic buckling of an imperfect rectangular plate with different boundary conditions under various force-time functions. Mojahedin et al. [76] presented the buckling behaviour of FG circular plates made of the porous material on higher-order shear deformation theory. The buckling of FG circular plate made of porous due to thermal effect also studied by Jabbari et al. [77].

For dynamic analysis of orthotropic plates, many researchers paid attention to natural frequency, linear and nonlinear vibration responses, and frequency-amplitude curves. Eslami et al.[78] studied a rectangular orthotropic plate subjected to a uniformly distributed harmonic transverse loading considering damping effects and in-plane loads. Yeh et al.[79] investigated the large deflections and nonlinear flexural vibrations of orthotropic rectangular plates using the generalised double Fourier series. Eshmatov [80] presented the nonlinear vibrations of viscoelastic orthotropic plates based on Kirchhoff-Love hypothesis and Reissner-Mindlin generalised theory. By using Eringen’s nonlocal elasticity theory, Sari and Al-Kouz [81] investigated the free vibration of non-uniform orthotropic Kirchhoff plates. The free vibration of moderately thick orthotropic rectangular plates was presented by Wang et al.[82]. A more general boundary condition can be considered in their model by using Raleigh-Ritz method. Moreover, Buckling and postbuckling behaviour of orthotropic plate were reported by some researchers based on various methods. Ferreira and Virtuoso [83] introduced the semi-analytical models into postbuckling analysis of orthotropic plate and found that the proposed method can obtain more accurate results than other analytical ones. The buckling responses of the orthotropic nanoplates resting on the elastic foundation subjected to the nonuniform biaxial load was presented by Golmakani and Rezatalab[84]. Unlike other scholars, nonlocal elasticity theory was used to explore the buckling behaviour of graphene sheets in nanoscale.

Dynamic buckling analysis of orthotropic plates has received considerable attention due to the existence of dynamic loading environments. Patel et al. [85] studied the dynamic instability of layer orthotropic composite plates embedded in the elastic medium. The periodic loading scheme was considered in this model. The refined plate model, which considers transverse shear and rotary inertia effects, was developed to investigate the dynamic buckling behaviour of composite laminate plates by Chattopadhyay and Radu[86]. Kubiak [87] presented the dynamic buckling of orthotropic plates subjected to an in-plane pulse load while the plates occupy a varying widthwise material property. The results obtained from analytical-numerical method validated with the finite element method. Gao et al. [88] proposed an analytical computational method for dynamic stability of composite orthotropic plate subjected to different axial velocities. This type of load differs from the other two loading schemes in that the time required to reach the structural critical load is larger than the time required for the elastic wave to spread from one end to the other. Therefore, the inertial effects can be ignored commonly.

2.4 Dynamic behaviours and buckling of isotropic cylindrical shells

The thin-walled cylindrical shell structure has been widely used in aerospace engineering and other engineering disciplines for many decades, such as propellant tank of space shuttle, the skin of ballistic missile, air receiver tanks, distillation columns, heat exchangers/condensers, due to its outstanding stiffness, large space cover, lower cost and high strength-weight ratio.

Most of those works about FG cylindrical shells focus on free vibration, forced vibration, nonlinear vibration and thermal responses. With the expanding application of FG structures, buckling or stability behaviour of FG structures keep attracting researchers' attention. Shen, as one of the highly cited researchers on buckling behaviour of functionally graded structures, thoroughly studied pressure-load post-buckling [33, 89], axially-loaded postbuckling[90], thermal buckling and post-buckling[91, 92], post-buckling subjected to combined axial and radial mechanical load[36, 93, 94], torsional buckling and post-buckling [95-97] of FG structures. Following his work, a large number of theoretical and numerical techniques are developed to study the stability behaviour of FG structures. Wattanasakulpong et al. [98] studied the free vibration of layered FG bars and verified with the experimental results.

Although the static buckling and post-buckling of FG structures is well understood, a clear understanding of the dynamic stability of such structures' behaviour has not gained much attention. However, the time-dependent forces are intrinsic among engineering applications, and more importantly, excessively simplifications on such type of loading conditions in both structural analysis and design could compromise the structural safety. Sofiyev [99] derived the dynamic buckling equation of FG cylindrical shell subjected to non-periodic impulsive loading. Then this work is applying in the case of FG truncated conical shell[100, 101]. Huang et al. [102]studied the dynamic buckling of the functionally graded cylindrical shells subjected to linearly increasing load. This type of loading model also appeared in Dung's [103] and Bich's [104] recent work. Nevertheless, there is another type of loading should be noticed, the constant velocity, which was first proposed by Hoff[53]. Then based on his work, Motamarri et al. [43] studied the dynamic elastic buckling of beam-columns of various boundary conditions under a constant speed compression.

Topics on dynamic stability of cylindrical shell keep attracting researchers' attention these years. Shaw et al. [105] studied the dynamic instability of the composite cylindrical shells subjected to axial and/or torsional impulse load. Liao and Cheng [106] investigated dynamic buckling characteristics of a laminated composite stiffened or non-stiffened shells subjected to periodic in-plane forces. Based on the energy criterion, Gu et al. [107] presented the plastic buckling of cylindrical shells under external impulsive velocity and asymmetric external loadings, respectively. With respect to dynamic buckling of the FG cylindrical shell structures, Ng et al. [108] and Darabi et al. [109] derived the dynamic buckling equations of FG cylindrical shells subjected to periodic axial loading based on small deflection theory and large deflection theory, respectively. While the non-periodic impulsive loading scheme of dynamic buckling for FG cylindrical shell was studied by Sofiyev [99]. Then, after that, in 2004, he also investigated the buckling behaviour of an FG cylindrical shell subjected to linearly increasing torsional loading. Huang and Han [102] then analysed the dynamic stability of FG cylindrical shell subjected to the linearly increasing load with the consideration of large deflection and thermal effects. Shariyat [110] studied the dynamic buckling of preloaded, imperfect FGM cylindrical shell subjected to combined axial load and external pressure under thermal environment. Then, he [111] also analysed dynamic buckling of the abruptly loaded hybrid FG cylindrical shell subjected to thermo-electro-mechanical loads including the temperature-dependent property. Static and dynamic buckling of an imperfect stiffened FG cylindrical shell under axial load was presented by Bich et al. [112]. Based on the *kp*-Ritz method, Lei et al. [113] investigated the dynamic buckling of carbon nanotube-reinforced functionally graded cylindrical panels under periodic loadings. However, up to date, the investigation on dynamic buckling of orthotropic FG cylindrical shells subjected to such type of loading has received limited attention.

2.5 Dynamic behaviours and stability of orthotropic cylindrical shells

In the last subsection, the dynamic buckling analysis of FG cylindrical shells' studies was done by considering in homogenous, isotropic graded materials. However, in engineering practices, the material-oriented or orthotropic materials are commonly used in all kinds of fields to maximise the material property and optimise the structures, which is even more critical for the FG structures. Additionally, due to the nature of fabrication techniques and physical composition, the FGMs are easier to loss of isotropy and become anisotropic with principal directions parallel or/and perpendicular to each layer[114, 115]. For example, Kaysser and IIschner [116] found that a graded Cu-Ni-Sn specimen exhibited a lamellar or duplex structure after the plasma spray processing. A similar phenomenon also reported by Sampath et al. [117] that equiaxed grain microstructures are observed by Transmission electron micrographs (TEMs). Thus, it is not unnatural to consider the orthotropic FGMs when studying the dynamic buckling behaviours of cylindrical shells. Based on such idea, Sofiyev [99-101, 118] thoroughly investigated the dynamic responses of the anisotropic FG cylindrical shells these years based on theoretical and computational methods. Vel [119] presented the free and forced vibration of anisotropic FG cylindrical shells with simply supported boundary condition by using an exact elasticity solution. Pelletier and Vel [120] investigated the steady-state response of FG cylindrical shell subjected to mechanical load under thermal environment. Based on the pseudo-Stroh formalism and transfer matrix method, Wang and Sudak [121] analysed an anisotropic FG, thermoelastic, multi-layered cylindrical panel. The free vibration of a simply-supported, fluid-filled orthotropic FG cylindrical shell was studied by Chen et al.[122].

Nevertheless, investigations involving the orthotropic FGMs cylindrical shells for the dynamic buckling analysis are limited in number. Some works about orthotropic FG cylindrical shells is focused on static buckling, free vibration, force vibration, nonlinear vibration and thermal responses. Sofiyev, as one of the main researchers on orthotropic FG cylindrical shells, has thoroughly investigated such structures under various conditions. For instance, Sofiyev and Kuruoglu [123] presented buckling and vibration characteristics of FG anisotropic cylindrical shell subjected to external pressure was studied by considering shear deformation and rotary inertia. Then, Najafov, Sofiyev and Kuruoglu [124] also investigated the torsional stability and vibration of FG orthotropic cylindrical shell on elastic foundation. The buckling of FG orthotropic cylindrical shells with the consideration of shear deformable subjected to lateral pressure also discussed by Sofiyev et al. [125]. Recently, both the nonlinear free vibration including shear deformable theory and large amplitude vibration on nonlinear Winkler elastic foundation of FG orthotropic cylindrical shells were reported by Sofiyev[126, 127]. While other scholars mainly focused on crack analysis and failure behaviours of orthotropic FGMs [128-133]. Rao and Rahman [128] studied the cracks behaviours of orthotropic cylindrical shells by finite element method (FEM). Xu et al. [129] presented the semi-infinite cracks of FG orthotropic materials. By using an equivalent domain integral approach, Dag [133] analysed the thermal stresses in FG orthotropic cylindrical shells. Then, Dag et al. [131] also discussed the mechanical and thermal effects on fracture failure of orthotropic cylindrical shells.

2.6 Dynamic behaviours and stability of FG porous structures

Most recently, a novel functionally graded (FG) pure metallic porous material was proposed in recent years by changing the cell geometry, density and/or material composition from point to point within the porous foams or metallic foams in the process of fabrication [134-137]. Such materials can be widely used in various industries such as energy absorbing systems, porous electrodes, sound absorbers, heat exchangers, construction materials, electromagnetic shielding, etc., due to excellent impact energy absorption, high specific strength, and low thermal conductivity and other distinctive characteristics [138-141]. Nearly all of the early researchers regarding FG porous structures were focused on problems of elastic buckling or dynamic buckling analysis. Magnucki and his co-workers firstly and thoroughly investigated the static and dynamic stability of FG porous structures (such as porous beams[142] or porous sandwich beam[143], porous plates[144, 145] or porous sandwich plates[146] and porous circular cylindrical shells[147-150]) based on theoretical and finite element methods. For example, Magnucki and Stasiewicz[142] studied the buckling behaviour of asymmetric porosity distributed bar based on the principle of stationarity of the total potential energy including the effect of shear strain. The buckling and strength of a sandwich beam with a metal foam core were presented by Magnucka-Blandzi and Magnucki[143]. Magnucka-Blandzi [144, 146] also investigated the dynamic buckling of a porous circular plate and static buckling of a rectangular sandwich plate with the porous core. Furthermore, Belica and Magnucki [147-150] employed a nonlinear hypothesis of deformation of a plane cross-section and Hamilton's principle to carry on analytical and numerical studies on dynamic buckling of porous cylindrical shells subjected to external pressure and axial compression. Porous structures are not only subjected to different loading conditions but also saturated with liquid and gas. Under such circumstances, the dynamic properties or mechanical mechanism would be different. Therefore, Jabbari et al. [76, 151-154] studied the stability of saturated FG porous circular plate with or without piezoelectric layers subjected to a radially loading, thermal buckling and combined thermal and mechanical loads on the ground of linear poroelasticity theory of Biot[155]. Following their work, the post-buckling behaviour of saturated FG porous circular plates subjected to a uniformly radially loading with simply-supported and clamped boundary conditions was presented by Feyzi and Khorshidvand[156].

Natural frequencies and other nonlinear dynamic properties play an essential role in the design [157-159] and analysis of FG porous structures in the large amplitude deflections. More and more researches paid attention to the dynamic behaviour of FG porous structures in the engineering practices. Chen et al. [160] applied the Timoshenko beam theory and Lagrange equation to investigate the free and forced vibration characteristics of shear deformable FG porous beams with symmetric and asymmetric porosity distributions. Furthermore, by using the same method, the nonlinear free vibration of shear deformable sandwich beams with an FG porous core was studied[161]. In this study, they also considered a non-symmetric porosity distribution and a uniform porosity distribution when compared with Magnucki[143] and the results showed that with the consideration of two layers at the top and bottom sides, the vibration behaviour of the structure is improved. The rapid development of manufacturing technique makes it possible to introduce nanofillers such as carbon nanotubes (CNTs) and graphene platelets (GPLs) into porous materials. The novel porous nanocomposites occupy both advantages of CNTs or GPLs and porous materials. Kitipornchai et al.[162] presented the influence of both porosity and GPLs dispersion pattern on the free vibration of FG porous nanocomposite beams. Following this idea, Chen et al. [163] studied the nonlinear vibration and postbuckling behaviour of GPLs reinforced FG porous beams. Based on the Reddy's third-order shear deformation theory, the dynamic characteristics of a porous rectangular plate resting on a Pasternak foundation was solved by differential quadrature method[164]. Ebrahimi and Habibi [165] employed the third order shear deformation plate theory and finite element method to predict the deflection and vibration characteristics of a saturated FG porous rectangular plate. There are also some studies dealing with the random distribution of porosity during the multi-step sequential infiltration technique. Wattanasakulpong and Ungbhakorn [166] conducted an investigation of random porosity volume fraction on the linear and nonlinear vibration of FG porous beams with elastically restrained ends. Using the semi-analytical differential transform method, the free vibration of rotating FG porous beam was studied by Ebrahimi and Mokhtari [167] based on the Timoshenko beam theory. They [168] also presented the free vibration of a rotating double-tapered functionally graded (FG) porous beam based on Euler–Bernoulli beam theory and then the governing equation is solved by the differential transform method.

As can be seen, most of those works about FG porous structures focus on beam and plate structures, and investigations involving the application of FG porous cylindrical shells are still limited in number. However, in engineering practices, the cylindrical shell/sheet structures are widely used in all kinds of fields in order to match the desired functionality and optimize the structures [169-171], such as the propellant tank of the space shuttle, the skin of the ballistic missile, oil refineries, petrochemical plants, power plants, pressure vessel and so on. Ghadiri and SafarPour [172] applied the first-order shear model and modified couple stress theory to analyse the free vibration characteristics of

FG porous microshell in the thermal environment. Wang and Wu [173] calculated the natural frequencies of an FG porous cylindrical shell with different boundary conditions using sinusoidal shear deformation theory and Rayleigh-Ritz method. Additionally, the understanding of free vibration and nonlinear vibration analysis is crucial to FG porous cylindrical shells. However, no previous work has been done for FG porous cylindrical shells with external harmonic excitation, especially for the resonant characteristics with different internal porosity distributions. Thus, it is of great importance to analyse the forced vibration behaviour of FG porous cylindrical shell due to the time-dependent external forces and the proper understanding and development of primary resonance of FG porous cylindrical shell can help engineers avoid the peak resonances of the structural system in the design process.

2.7 The influence of thermal effect, damping effect and elastic foundation on dynamic characteristics and stability of structures

Despite of diversely proposed computational schemes (i.e. Galerkin method, finite element method, finite difference method, etc.) for dynamic buckling [7, 20, 174, 175], from the authors' knowledge, early dynamic buckling studies on structures subjected to axial loads have been investigated in the way such that damping effects are ignored [11, 19, 20, 43, 176-178]. However, damping property (i.e., a non-conservative energy contribution) is one of the most important aspects of engineering dynamics, which intrinsically exists in all physical systems[179, 180]. Kounadis and Raftoyiannis [181] investigated the nonlinear dynamic stability criteria for one degree of freedom system under step loading and concluded that the structure would buckle when the phase-point velocity vanished regardless of the length of loading duration and damping effects. After one year, Kounadis [182] subsequently studied two nonlinear two-degree-of-freedom systems under step loading with and without damping effects. It was shown that when viscous damping was incorporated, the lower bound of critical load for dynamic buckling could be estimated. Mallon et al. [183] presented numerical approaches for analysing a series of thin shallow arches subjected to a pulse load and also found that the increase of damping coefficient would lead to an increasingly dynamic buckling critical load. Moreover, Lee [184] investigated a rod with intermediate spring support with a follower force at one end, also suggested that damping effects cannot always be neglected especially for some particular engineering systems.

In engineering practices (i.e. aerospace and mechanical engineering), structures are not only subjected to dynamic loadings but also exposed to the physical environment, such as thermal effects, moisture effects, etc. Thermal effects due to temperature changes, in turn, have an influence on structure dynamic characters and the stress state [185, 186]. The combined effect of moisture and temperature (hygro-thermal environment) on dynamic response was investigated by Ebrahimi and Barati[187]. Shariyat [110] studied the dynamic thermal buckling of FGM imperfect cylindrical shell and the results shown that thermal stresses would change the buckling behaviour. Ansari et al. [185] investigated the post-buckling behaviour of nanofilms under the action of thermal loads. Wu [188] found that region of instability is sensitivity to temperature change for a beam under transverse magnetic fields and thermal loads. The nonlinear dynamic buckling analysis of FGM beam due to the sudden uniform temperature rise was proposed by Ghiasian et al.[189]. The hybrid iterative Newton-Raphson-Newmark method was utilised to solve the governing equation in this study. The influence of the three-parameter elastic foundation was also included in the analytical method, which will be discussed later. These studies have shown that temperature changes have a significant influence on dynamic behaviour and further affect the performance and stability of structures.

Furthermore, these structures normally rest on or embed in elastic foundation/medium. Under such circumstance, dynamic characteristics and stability of structures may be different from traditional ones. Li et al. [190] studied the nonlinear vibration and thermal buckling of an orthotropic annular plate with a central rigid mass. Barati et al.[191] presented the thermo-mechanical buckling analysis of embedded nanosize FG plates. Taczala et al. [192] studied the nonlinear stability of stiffened functionally graded materials plates in the thermal environment using finite element method. Based on second-order shear deformation plate theory, the free vibration analysis of the functionally graded nanoplates embedded in an elastic medium was discussed by Panyatong et al.[193]. Yang and Shen [194] investigated the dynamic response of initially stressed functionally graded rectangular thin plates resting on an elastic foundation. Uğurlu et al.[195] presented the effects of elastic foundation and fluid on the dynamic response characteristics of rectangular Kirchhoff plates. The dynamic behaviour of a beam on a nonlinear elastic foundation under a sudden step loading was investigated by Jabareen and Sheinman[177]. Both Budiansky-Roth and Hoff-Simiteses dynamic buckling criteria were applied in their research. These studies have shown that elastic foundation has a significant influence on dynamic behaviour and further affect the performance and stability of structures.

2.8 Summary

The literature review on dynamic characteristics and stability of beam, plate and cylindrical shell were presented above. The research hotspots and methodologies were also demonstrated, as well as the shortcomings and limitations of the past literature. Due to the enormous growth of FGMs' application in lightweight structures and the complex physical environment that these structures may expose to, a large number of new problems has emerged. Thus, to ensure safety and serviceability of the Thin-walled and slender engineering structures (i.e., beam, plate and shell), investigations on the dynamic characteristics and stability of such structures made of advanced materials under different conditions are much needed.

It is noticeable from the above review that very few studies have addressed the dynamic characteristics and stability of structures made of advanced materials under different environment. Therefore, based on the open literature, a comprehensive knowledge gap is proposed for a better understanding of the present problems, the following aspects are mentioned:

1. The influence of different boundary conditions, damping and thermal effects on the dynamic buckling of beam is not thoroughly studied. A more comprehensive mathematical model is needed.
2. From the previously reported literature, Winkler-Pasternak elastic foundation has a significant influence on dynamic behaviour and further affect the performance and stability of structures. While the dynamic behaviours and stability of composite orthotropic plate subjected to different axial velocities resting on elastic foundation are unclear.
3. It is noted that no study has been reported yet on the nonlinear primary resonance behaviour of cylindrical shells made of functionally graded (FG) porous materials

subjected to a uniformly distributed harmonic load including the damping effect, let alone the influence of different porosity distributions.

4. The review confirmed that most of the studies about orthotropic FG cylindrical shells focused on static buckling, free vibration, force vibration, nonlinear vibration and thermal responses, the dynamic stability analysis of FG orthotropic circular cylindrical shell has not touched yet.

Chapter 3 Nonlinear dynamic stability analysis of Euler-Bernoulli beam-columns with damping effects under thermal environment

3.1 Introduction

This chapter proposed two hybrid analytical-numerical methods for nonlinear dynamic buckling analysis of Euler-Bernoulli beam-columns under constant loading rates. Both the Galerkin-Force method (GFM) and energy method (EM) are capable of handling effectively different boundary conditions, damping and thermal effects. By integrating Hamilton's principles into Lagrange's equations, the governing equation of the energy method is derived in the form of partial differential equations (PDEs) for dynamic buckling of beams. Unlike traditional approaches for dynamic buckling analysis [43, 44], the proposed governing equation is able to incorporate damping and thermal effects simultaneously. The proposed Galerkin-Force method is to introduce the buckled shape function as a trial function into force equilibrium equation in dynamic buckling. Damping effects under thermal environment are also formulated in the ordinary differential equations (ODEs). The exhilarating performance of the proposed two approaches is confirmed by finite element method (FEM), and the damping, thermal effects on structural dynamic buckling behaviour are comprehensively investigated.

3.2 Nonlinear dynamic buckling analysis with damping and thermal effects

3.2.1 *The Galerkin-Force method (GFM)*

The governing equation for the dynamic buckling of Euler-Bernoulli beam can be derived from the free body diagram and the moment-curvature relation for the beam. The schematic illustration is presented in Figure 3.1.

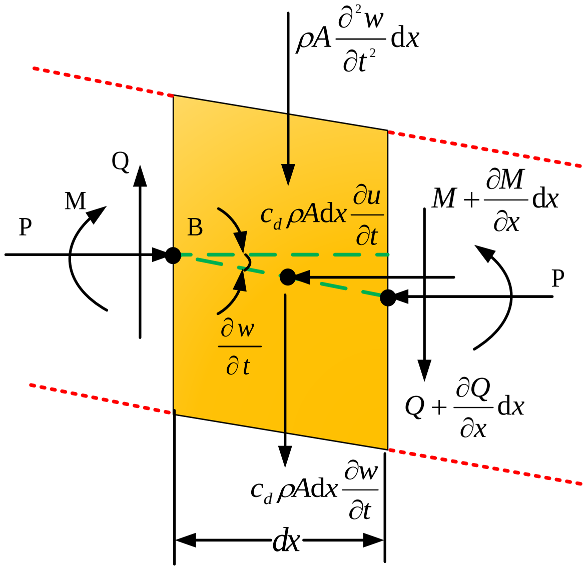

Figure 3.1 The free body diagram of a small element *dx*

It is assumed that counter-clockwise is positive. By neglecting the rotational inertia of the infinitesimal body, the sum of moments about Point B can be calculated as:

$$\begin{aligned}&\sum M_B=0\\&-M-\rho A\frac{\partial^2 w}{\partial t^2}dx\bullet\frac{dx}{2}-(Q+\frac{\partial Q}{\partial x}dx)dx+(M+\frac{\partial M}{\partial x}dx)-P\frac{\partial w}{\partial x}dx\\&-c_d\rho A\frac{\partial w}{\partial t}\bullet\frac{dx}{2}-c_d\rho Adx\frac{\partial u}{\partial t}\bullet\left(\frac{\partial w}{\partial x}\bullet\frac{dx}{2}\right)=0\end{aligned}\tag{3.1}$$

Eq. (3.1) can be simplified by ignoring the second order infinitesimal term

$$Q = \frac{\mathrm{d}M}{\mathrm{d}x} - P\frac{\partial w}{\partial x} \tag{3.2}$$

The resultant force of the y-axis gives

$$\begin{gathered}\sum F_y = 0 \\ Q = Q + dQ + \rho A\frac{\partial^2 w}{\partial t^2}dx + c_d\rho A\frac{\partial w}{\partial t}dx\end{gathered} \tag{3.3}$$

Therefore

$$\frac{dQ}{dx} = -\rho A\frac{\partial^2 w}{\partial t^2} - c_d\rho A\frac{\partial w}{\partial t} \tag{3.4}$$

According to the relation of moment and curvature, one obtains

$$M = EI\frac{\partial^2 (w-e)}{\partial x^2} \tag{3.5}$$

Differentiating Eq.(3.5) with respect to x and substituting it into Eq.(3.2), then differentiating Eq. (3.2) with respect to x and substituting it into Eq. (3.4), one can obtain the governing equation for dynamic buckling

$$EI_{yy}\frac{\partial^4 (w-e)}{\partial x^4} - P\frac{\partial^2 w}{\partial x^2} + \rho A\frac{\partial^2 w}{\partial t^2} + c_d\rho A\frac{\partial w}{\partial t} = 0 \tag{3.6}$$

Eq.(3.6) is the partial differential equation for the continuous beam including damping effects.

$$w(x,t) = w_0(t)f(x) \tag{3.7}$$

$$e(x,t) = e_0 f(x) \tag{3.8}$$

where $w(x, t)$, $e(x, t)$ denote the structural deflection of the beam and the initial imperfection respectively.

Hoff (1951) [39] assumed the first mode shape as the buckling mode shape of the beam-column under constant speed compression for various boundary conditions, so the corresponding deflection functions $f(x)$ can be approximated as below. It is also assumed that the effects of rotational inertia and transverse shear are negligible.

For a simply-supported beam (the same as free-free, hinged-free), the first mode shape function can be defined as:

$$f(x) = \sin\frac{\pi x}{L} \tag{3.9}$$

Therefore, for different boundary conditions and geometries, different first mode shape functions should be selected [43, 196, 197]. Moreover, the absolute value of maximum or minimum deflection for different boundary conditions is normalized to 1.

Clamped-clamped:

$$f(x) = \frac{1}{2}(1-\cos\frac{2\pi x}{L}) \tag{3.10}$$

Clamped-pinned [198]:

$$f(x) = 0.1591[\sin\frac{4.494x}{L} - \frac{4.494x}{L} + 4.494(1-\cos\frac{4.494x}{L})] \tag{3.11}$$

Clamped-free (cantilever):

$$f(x) = 1 - \cos\frac{\pi x}{2L} \tag{3.12}$$

Pinned-free:

$$f(x) = \sin\frac{\pi x}{2L} \tag{3.13}$$

By substituting Eqs.(3.7) and (3.8)into Eq.(3.6), one obtains:

$$[EIw(t) - e_0]\frac{\mathrm{d}^4 f}{\mathrm{d}x^4} - Pw(t)\frac{\mathrm{d}^2 f}{\mathrm{d}x^2} + \rho A f(x)\frac{\partial^2 w}{\partial t^2} + c_d \rho A f(x)\frac{\partial w}{\partial t} = 0 \tag{3.14}$$

By multiplying $f(x)$ in both side of Eq.(3.14) and applying Galerkin method, Eq.(3.14) can be further reformulated as:

$$\begin{aligned} &EIw(t)\int_0^L f(x)\frac{\mathrm{d}^4 f}{\mathrm{d}x^4}\mathrm{d}x - EIe_0\int_0^L f(x)\frac{\mathrm{d}^4 f}{\mathrm{d}x^4}\mathrm{d}x - Pw(t)\int_0^L f(x)\frac{\mathrm{d}^2 f}{\mathrm{d}x^2}\mathrm{d}x \\ &+ \rho A\frac{\partial^2 w}{\partial t^2}\int_0^L (f(x))^2 \mathrm{d}x + c_d \rho A\frac{\partial w}{\partial t}\int_0^L (f(x))^2 \mathrm{d}x = 0 \end{aligned} \tag{3.15}$$

Let

$$\begin{aligned} d_1 &= \int_0^L \frac{1}{L}(f(x))^2 \mathrm{d}x \\ d_2 &= \int_0^L L f(x)\frac{\mathrm{d}^2 f}{\mathrm{d}x^2}\mathrm{d}x \\ d_3 &= \int_0^L L\left(\frac{\mathrm{d}f}{\mathrm{d}x}\right)^2 \mathrm{d}x \\ d_4 &= \int_0^L L^3 f(x)\frac{\mathrm{d}^4 f}{\mathrm{d}x^4}\mathrm{d}x \end{aligned} \tag{3.16}$$

The values of constants d_1-d_4 for different boundary conditions are shown in Table 3.1.

Table 3.1 Value of Constants for d_1-d_4

Boundary condition	d_1	d_2	d_3	d_4
Pinned-Pinned	0.5	-4.9348	4.9348	48.7045
Clamped-Clamped	0.375	-4.9348	4.9348	194.818
Clamped-Pinned	0.425453	-5.15721	5.16187	104.174
Clamped-Free	0.22676	0.337096	1.2337	-0.83175
Pinned-Free	0.5	-1.2337	1.2337	3.04403

Eq. (3.15) can be further transformed into:

$$EIw(t)d_4 - EIe_0 d_4 - Pw(t)d_2 L^2 + \rho A \frac{\partial^2 w}{\partial t^2} d_1 L^4 + c_d \rho A \frac{\partial w}{\partial t} d_1 L^4 = 0 \tag{3.17}$$

In order to maintain the readability of the thesis by efficiently expressing all formulations, the following dimensionless quantities are necessarily introduced:

$$w^* = \frac{w}{L}, e^* = \frac{e_0}{L}, r_g^2 = \frac{I}{A}, \xi = \frac{L}{r_g}, \tau = \frac{t}{L^2\sqrt{\frac{\rho A}{EI}}}, v^* = L\sqrt{\frac{\rho A}{EI}} \cdot v \tag{3.18}$$

where r_g represents the radius of gyration of the section and ξ denotes the slenderness ratio of the beam.

Hence, Eq. (3.17) can be further reformulated as:

$$EI(w^* - e_0^*)d_4 L - Pw^* d_2 L^3 + \rho A \frac{L}{L^4 \frac{\rho A}{EI}} \cdot \frac{\partial^2 w^*}{\partial \tau^2} d_1 L^4 + c_d \rho A \frac{L}{L^2\sqrt{\frac{\rho A}{EI}}} \frac{\partial w^*}{\partial \tau} d_1 L^4 = 0$$

(3.19)

And then simplified as

$$d_4 LEI(w^* - e_0^*) - d_2 L^3 P w^* + d_1 EIL \cdot \frac{\partial^2 w^*}{\partial \tau^2} + d_1 L^3 c_d \rho A \sqrt{\frac{EI}{\rho A}} \frac{\partial w^*}{\partial \tau} = 0 \tag{3.20}$$

By considering the viscous damping as internal damping effects, one can obtain that:

$$\begin{aligned} c_d &= 2\varpi_0 \zeta \\ c_d^* &= c_d L^2 \sqrt{\frac{\rho A}{EI}} \end{aligned} \tag{3.21}$$

where c_d denotes the damping coefficient of the structure; ϖ_0 denotes the fundamental frequency of the structure; and ζ denotes the damping ratio of the beam.

Dividing by $d_1 EIL$ at both side of Eq.(3.20), one obtains:

$$\frac{\partial^2 w^*}{\partial \tau^2} + \frac{d_1 L^3 c_d \rho A}{d_1 EIL} \sqrt{\frac{EI}{\rho A}} \frac{\partial w^*}{\partial \tau} - \frac{d_2 L^3 P}{d_1 EIL} w^* + \frac{d_4 LEI}{d_1 EIL} (w^* - e_0^*) = 0 \tag{3.22}$$

By substituting Eq. (3.21) into Eq.(3.22), Eq. (3.22) can be further reformulated as:

$$\frac{\partial^2 w^*}{\partial \tau^2} + c_d^* \cdot \frac{\partial w^*}{\partial \tau} - \frac{d_2 P L^2}{d_1 EI} \cdot w^* + \frac{d_4}{d_1} (w^* - e_0^*) = 0 \tag{3.23}$$

Also, the reaction force for the beam can be calculated as:

$$P = -P(t) \tag{3.24}$$

For the axial displacement of the beam at the roller support, it can be divided into two parts, U_a, the axial displacement due to axial shortening and U_b (t), the axial displacement due to the bending shortening. That is:

$$\begin{aligned} &U(t) = v \cdot t \\ &U_a = U(t) - U_b(t) \\ &U_b(t) = \int_0^L \frac{1}{2}\left[\left(\frac{\partial w}{\partial x}\right)^2 - \left(\frac{\mathrm{d}e}{\mathrm{d}x}\right)^2\right]\mathrm{d}x \end{aligned} \tag{3.25}$$

Thus, U_a can be alternatively expressed as

$$U_a = v \cdot t - d_3 \frac{w_0^2(t) - e_0^2}{2L} \tag{3.26}$$

It is assumed that the thermal effect is a uniform temperature load, while the change of the material property due to the thermal load is ignored [110, 185]. Therefore, the reaction force generated by the beam-column can be formulated as:

$$P(t) = \frac{EA}{L}\left[U_a(t) - \alpha_x \Delta t L\right] \tag{3.27}$$

where α_x means coefficient of linear expansion and Δt represents the temperature change. The coefficient of thermal expansion in steel beam is positive (α_x=12×10^{-6} K^{-1}) for the rise of temperature and is negative (α_x=-12×10^{-6} K^{-1}) for the fall of temperature based on the room temperature (20^{o}C).

Then, by substituting Eq. (3.26) into Eq. (3.27), Eq. (3.27) can be reformulated as:

$$P(t) = \frac{EA}{L}\left[v \cdot t - d_3 \frac{w_0^2(t) - e_0^2}{2L} - \alpha_x \Delta t L\right] \tag{3.28}$$

According to the dimensionless quantities of Eq.(3.18), the buckling load and the normalised buckling load can be represented as:

$$P(t) = EA\left[v^* \cdot \tau - \frac{1}{2}\left(w^{*2} - e^{*2}\right)d_3 - \alpha_x \Delta t\right] \tag{3.29}$$

$$P^*(t) = \frac{P(t)}{EA} = v^* \cdot \tau - \frac{1}{2}\left(w^{*2} - e^{*2}\right)d_3 - \alpha_x \Delta t \tag{3.30}$$

Therefore, by substituting Eqs.(3.29) and (3.24) into Eq.(3.23), Eq.(3.23) can be reformulated as:

$$\frac{\partial^2 w^*}{\partial \tau^2} + c_d^* \cdot \frac{\partial w^*}{\partial \tau} + \xi^2 (\frac{d_2}{d_1}) w^* \left[v^* \cdot \tau - \frac{1}{2}\left(w^{*2} - e^{*2}\right)d_3 - \alpha_x \Delta t\right] + \frac{d_4}{d_1}(w^* - e_0^*) = 0$$

(3.31)

Consequently, Eq.(3.31) is the unified governing nonlinear ordinary differential equation for dynamic buckling analysis of Euler-Bernoulli beams with various boundary conditions considering damping effects under thermal environment from Galerkin-Force method.

3.2.2 *The Energy method (EM)*

For this particular study, a simply-supported Euler-Bernoulli beam with arbitrary cross-section is investigated. The general structural layout is illustrated in Figure 3.2, $e(x)$, $w(x)$ denote the initial imperfection and the structural deflection of the beam respectively. Also, the considered beam is subjected to a constant compression rate.

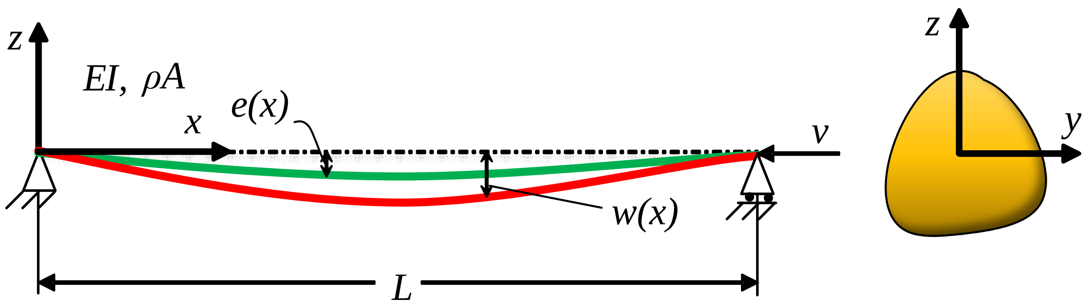

Figure 3.2 A simply-supported Euler-Bernoulli beam

For this particular structural system, the kinetic energy can be formulated as:

$$T = \frac{\rho A}{2}\int_0^L \left(\frac{\partial w}{\partial t}\right)^2 \mathrm{d}x \tag{3.32}$$

The potential energy:

$$V = \frac{EI_{yy}}{2}\int_0^L \left(\frac{\partial^2 (w-e)}{\partial x^2}\right)^2 dx - \left(-\frac{P}{2}\int_0^L \left[\left(\frac{\partial w}{\partial x}\right)^2 - \left(\frac{de}{dx}\right)^2\right] dx\right) \tag{3.33}$$

where the first term of Eq.(3.33) is strain energy and the second term of Eq.(3.33) is the potential energy due to the external forces.

The power dissipation function:

$$D = -\int_0^L \frac{c_d \rho A}{2}\left(\frac{\partial w}{\partial t}\right)^2 \mathrm{d}x \tag{3.34}$$

where c_d denotes the coefficient of damping.

Consequently, the Lagrange's equation of the structural system can be formulated as:

$$L \equiv T - V \tag{3.35}$$

The same as the Galerkin-Force method, by substituting Eqs.(3.32) and (3.33) into Eq. (3.35) and according to Eqs. (3.7) and (3.8), Eq.(3.35) can be formulated as:

$$
\begin{aligned}
L = & \frac{\rho A}{2}\left(\frac{\partial w_0}{\partial t}\right)^2 \int_0^L f^2(x)dx - \frac{EI_{yy}}{2}\left(w_0 - e_0\right)^2 \int_0^L \left(\frac{d^2 f}{dx^2}\right)^2 dx \\
& -\frac{P}{2}\left(w_0^2 - e_0^2\right)\int_0^L \left(\frac{df}{dx}\right)^2 dx
\end{aligned}
\tag{3.36}
$$

Let

$$
\begin{aligned}
c_1 &= \int_0^L \frac{1}{L} f^2(x)\mathrm{d}x \\
c_2 &= \int_0^L \frac{L^3}{\pi^4}\left(\frac{\mathrm{d}^2 f}{\mathrm{d}x^2}\right)^2 \mathrm{d}x \\
c_3 &= \int_0^L \frac{L}{\pi^2}\left(\frac{\mathrm{d}f}{\mathrm{d}x}\right)^2 \mathrm{d}x
\end{aligned}
\tag{3.37}
$$

The values of constants c_1-c_3 for different boundary conditions are shown in Table 3.2.

Table 3.2 Value of Constants for c_1-c_3

Boundary condition	c_1	c_2	c_3
Pinned-Pinned	1	1	1
Clamped-Clamped	0.75	4	1
Clamped-Pinned	0.85224	2.14149	1.047
Clamped-Free	0.453521	0.0625	0.25
Pinned-Free	1	0.0625	0.25

The same values of Table 3.2 are also verified by reference [43].

Eq. (3.36) can be further transformed into:

$$L=\frac{1}{2}c_1\rho AL\left(\frac{\partial w_0}{\partial t}\right)^2-\frac{1}{2}c_2\frac{EI_{yy}}{L^3}\left(w_0-e_0\right)^2-\frac{1}{2}c_3\frac{P\pi^2}{L}\left(w_0^2-e_0^2\right) \tag{3.38}$$

For Lagrange's Equations [199]:

$$\frac{\partial L}{\partial w_0}-\frac{\mathrm{d}}{\mathrm{d}t}\left(\frac{\partial L}{\partial \dot{w}_0}\right)+\frac{\partial D}{\partial \dot{w}_0}=0 \tag{3.39}$$

By substituting Eqs.(3.38) and (3.34) into Eq. (3.39), one obtains:

$$c_1\rho AL\left(\frac{\partial^2 w_0}{\partial t^2}+c_d\frac{\partial w}{\partial t}\right)+c_2\frac{EI_{yy}\pi^4}{L^3}\left(w_0-e_0\right)+c_3\frac{P\pi^2}{L}w_0=0 \tag{3.40}$$

According to Eq.(3.25), U_a can be alternatively expressed as

$$U_a=v\cdot t-c_3\frac{w_0^2(t)-e_0^2}{2L} \tag{3.41}$$

In order to maintain the readability of the chapter by efficiently expressing all formulations, the following dimensionless quantities are necessarily introduced:

$$c=\sqrt{\left(E/\rho\right)},r_g^2=\frac{Iyy}{A},\xi=\frac{L}{r_g},\tau=\frac{t}{T} \tag{3.42}$$

where c is the velocity of the axial stress wave and $T=\frac{L\xi}{c\pi^2}\sqrt{\frac{c_1}{c_2}}$.

$$w_0^*=\frac{w_0}{\kappa r_g},e_0^*=\frac{e_0}{\kappa r_g}\text{ where }\kappa=2\sqrt{\frac{c_2}{c_3}} \tag{3.43}$$

By considering the viscous damping as internal damping effects, one can obtain that:

$$\begin{aligned} C &= 2\rho A \varpi_0 \zeta \\ c_d &= \frac{C}{\rho A} = 2\varpi_0 \zeta \\ c_d^* &= c_d \cdot T \end{aligned} \tag{3.44}$$

where C denotes the total damping coefficient of the structure; ω_0 denotes the fundamental frequency of the structure, and ζ denotes the damping ratio of the beam.

Then, the reaction force generated by the beam-column can be formulated as:

$$P(t) = \frac{EA}{L}\left[U_a(t) - \alpha_x \Delta t L\right] = \frac{c_2 EI\pi^2}{c_3 L^2} v^* \tau - \frac{c_2 EI\pi^2}{L^2}\left(w^{*2} - e^{*2}\right) - EA\alpha_x \Delta t \tag{3.45}$$

Hence, according to Eqs. (3.43) and (3.45), Eq. (3.40) can be further reformulated as:

$$\frac{\partial w_0^{*2}}{\partial \tau^2} + c_d^* \frac{\partial w_0^*}{\partial \tau} - \left[v^*\tau - c_3\left(w_0^{*2} - e_0^{*2}\right) - \frac{c_3 \xi^2 \alpha_x \Delta t}{c_2 \pi^2}\right] w_0^* + \left(w_0^* - e_0^*\right) = 0 \tag{3.46}$$

where $v^* = \dfrac{c_3 \sqrt{c_1}\xi^3}{c_2\sqrt{c_2} c\pi^4} v$.

Eq.(3.46) is the unified governing nonlinear ordinary differential equation for dynamic buckling analysis of Euler-Bernoulli beams with various boundary conditions with the consideration of damping effects under thermal environment.

Therefore, the normalised dynamic load is

$$P^*(\tau) = \frac{P(\tau)}{P_{cr}} = v^*\tau - c_3\left(w_0^{*2} - e_0^{*2}\right) - \frac{c_3 \xi^2 \alpha_x \Delta t}{c_2 \pi^2} \tag{3.47}$$

where P_{cr} denotes the static buckling load for a given boundary condition, that is,

$$P_{cr} = \frac{c_2 \pi^2 EA}{c_3 \xi^2} = \frac{\pi^2 EA}{\left(\frac{2}{\kappa}\xi\right)^2} \tag{3.48}$$

3.3 Numerical results and discussion

In order to demonstrate the applicability and effectiveness of the proposed methods, four types of models on the dynamic buckling analysis of three types of boundary conditions are investigated with/without thermal effects and with/without damping effects. Throughout this study, the solutions of the unified nonlinear ordinary differential equations (Eq. (3.31) and Eq.(3.46)) are solved numerically by the Runge-Kutta method.

3.3.1 *Verification of structural critical load*

In order to assess the accuracy of the proposed method, an alternative approach, known as the finite element method (FEM), is also adopted so the computational results obtained from both approaches can be compared.

Regarding the adopted FE model, the viscous damping effect is introduced via the *Rayleigh damping*, which can be formulated as:

$$[\mathbf{C}] = \alpha[\mathbf{K}] + \beta[\mathbf{M}] \tag{3.49}$$

where **[K]**, **[M]** are the stiffness matrix and mass matrix of the structure, respectively; α and β can be calculated from the chosen first two natural frequencies for different cases [200].

Even though the damping model used in FEM is different from the one being implemented in the proposed method, a comparable level of damping values can be still achieved by the following equation:

$$\zeta = \frac{\beta}{2\varpi} + \frac{\alpha\varpi}{2} \tag{3.50}$$

where ζ is the damping ratio implemented in the proposed method.

In this subsection, a rectangular steel beam-column with a length of 1m, depth of 0.02m and width of 0.06 is investigated. The information of the geometrical and material properties is shown in Table 3.3. For this particular analysis, the yield strength is 340 MPa, which implies that buckling happens before yielding for all investigated examples.

Table 3.3 Parameter values

Property	Value	Unit
b	0.06	(m)
h	0.02	(m)
L	1.0	(m)
E	210	(GPa)
ρ	7850	(kg/m^3)
e_0	5×10^{-4}	(m)
ζ	0.02	N/A
α_x	1.2×10^{-5}	(1/ºC)
ΔT	+1	(ºC)
v	0.03	(mm/ms)

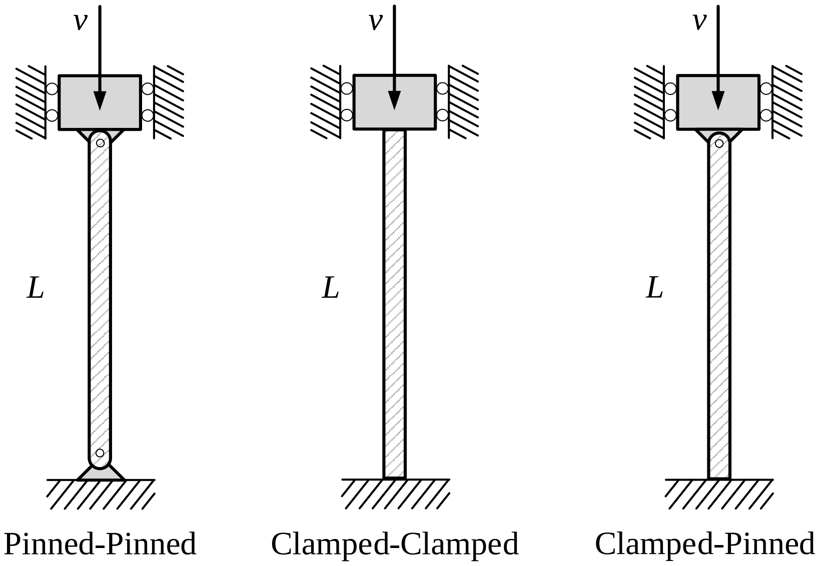

Figure 3.3 Beam-columns with three different boundary conditions subjected to constant compressive rate

In order to comprehensively appreciate the damping and thermal effects on the dynamic buckling analysis of the structure, three Euler-Bernoulli beam-columns have been investigated with distinctive boundary conditions as illustrated in Figure 3.3. For each concerned beam-column, four investigations have been explicitly conducted which are including:

a) Conventional dynamic buckling analysis without damping and thermal effects;

b) Dynamic buckling analysis with damping effect only;

c) Dynamic buckling analysis with thermal effect only;

d) Dynamic buckling analysis with both damping and thermal effects.

Figure 3.4, Figure 3.5 and Figure 3.6 show the relationship between axial load and end-shortening of the beam of 12 scenarios for different methods under the same axial loading speed, *v*. The numerical results of the Galerkin-Force Method (GFM) and Energy

Method (EM) are compared with those of Finite Element Method (FEM) to demonstrate the performance of the proposed methods in the presence of damping effects under thermal environment. Despite different scenarios, the comparisons show that the results of the proposed methods agreed very well with the results obtained from the FEM.

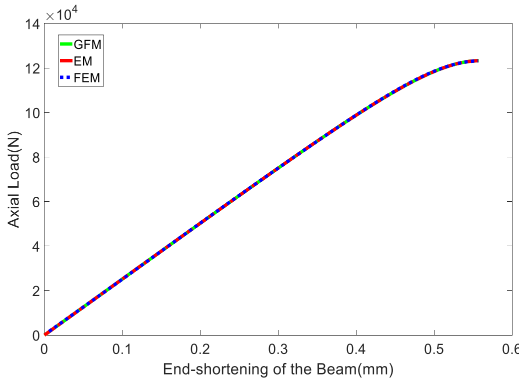

(1) Simplified Model

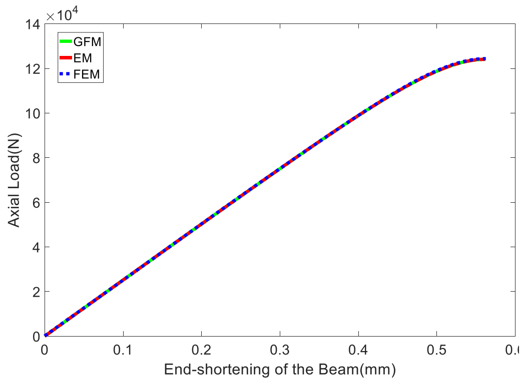

(2) Considering Damping Effect

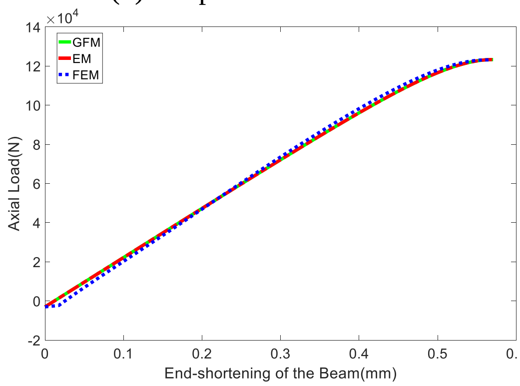

(3) Considering Thermal Effect

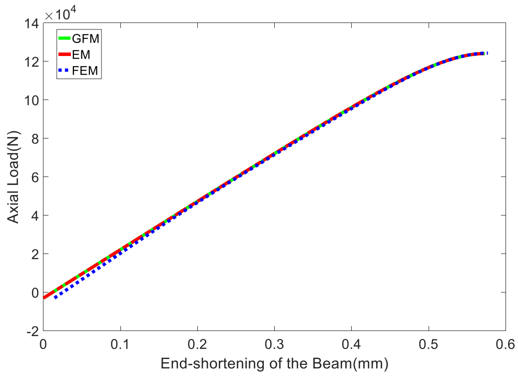

(4) Considering both Damping and Thermal Effect

Figure 3.4 The relationship between axial load and end-shortening of the pinned-pinned type beam for different models

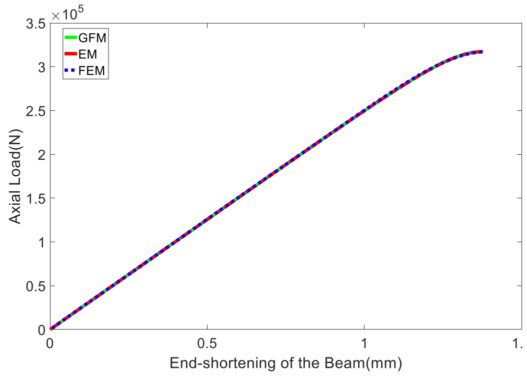

(1) Simplified Model

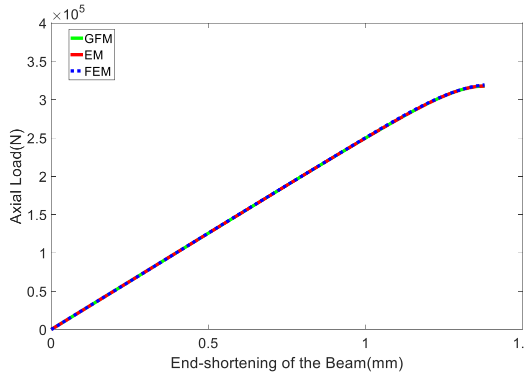

(2) Considering Damping Effect

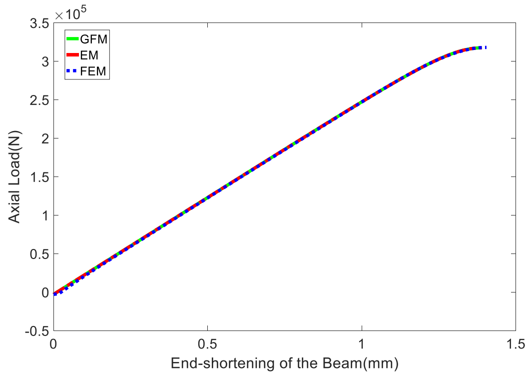

(3) Considering Thermal Effect

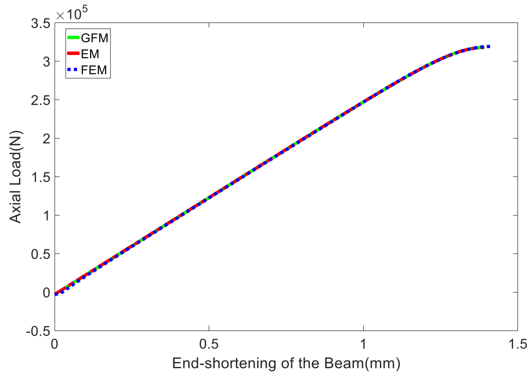

(4) Considering both Damping and Thermal Effect

Figure 3.5 The relationship between axial load and end-shortening of the clamped-clamped type beam for different models

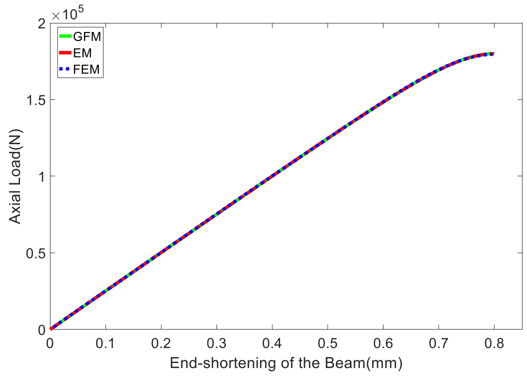

(1) Simplified Model

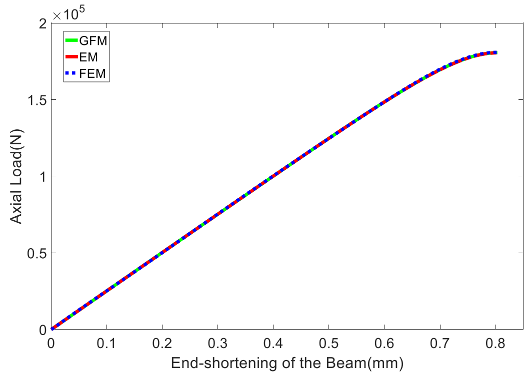

(2) Considering Damping Effect

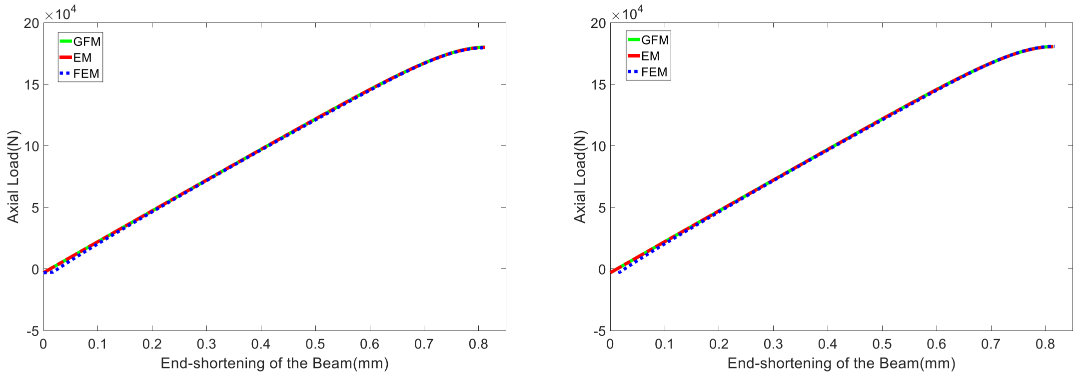

(3) Considering Thermal Effect

(4) Considering both Damping and Thermal Effect

Figure 3.6 The relationship between axial load and end-shortening of the clamped-pinned type beam for different models

In order to explore the differences of GFM, EM and FEM further, the critical values of Figure 3.4, Figure 3.5 and Figure 3.6 are also reported in Table 3.4,Table 3.5,Table 3.6 and Table 3.7. Table 3.4 shows the critical values of the simplified model. The results of GFM and EM are sharing a high degree of similarity. The maximum end-shortenings of the beams obtained by the GFM and EM are slightly larger than the FEM ones for different boundary conditions, except the case of the clamped-clamped condition. Likewise, the critical buckling loads obtained by the GFM and EM are larger than FEM ones whose relative differences are 0.07%, 0.04% and around 0.2% for P-P, C-C and C-P, respectively.

In the presence of damping effects, the critical values would increase for all three methods, which are shown in Table 3.5. It is evident that the results of FEM increased faster than other two methods. For the undamped system, the errors between Analytical-Numerical Methods (or ANMs, which includes both GFM and EM) and FEM is almost positive in Table 3.4. However, the errors turned out to be negative for almost all cases for a damped system. By carefully examining Table 3.5, it can be noticed that the damping effect has a significant influence on the beam-column with clamped-clamped boundary condition.

Table 3.4 Simplified Model of different boundary conditions for different methods

Simplified Model		GFM(1)	EM(2)	FEM(3)	((1)-(3))/(3)	((2)-(3))/(3)
P-P	Disp(mm)	0.5572	0.5572	0.5565	0.12%	0.12%
	Load(N)	123289.4295	123289.5076	123202.8433	0.07%	0.07%
C-C	Disp(mm)	1.3764	1.3764	1.3845	-0.59%	-0.59%
	Load(N)	317297.0083	317297.3954	317155.7688	0.04%	0.04%
C-P	Disp(mm)	0.7997	0.7989	0.7965	0.40%	0.30%
	Load(N)	180056.2270	179933.1369	179563.2074	0.27%	0.21%

Table 3.5 Damping effects of different boundary conditions for different methods

Damping effects		GFM(1)	EM(2)	FEM(3)	((1)-(3))/(3)	((2)-(3))/(3)
P-P	Disp(mm)	0.5619	0.5618	0.5625	-0.10%	-0.13%
	Load(N)	124069.3688	124069.7696	124377.8760	-0.25%	-0.25%
C-C	Disp(mm)	1.3790	1.3785	1.3965	-1.25%	-1.29%
	Load(N)	317773.7130	317773.7426	318625.0000	-0.27%	-0.27%
C-P	Disp(mm)	0.8032	0.8014	0.8025	0.09%	-0.13%
	Load(N)	180622.4431	180499.4169	180853.7828	-0.13%	-0.20%

Table 3.6 Thermal effects of different boundary conditions for different methods

Thermal effects		GFM(1)	EM(2)	FEM(3)	((1)-(3))/(3)	((2)-(3))/(3)
P-P	Disp(mm)	0.5707	0.5692	0.5650	1.00%	0.75%
	Load(N)	123291.7983	123292.8598	123131.7714	0.13%	0.13%

C-C	Disp(mm)	1.3896	1.3896	1.3930	-0.25%	-0.24%
	Load(N)	317301.5589	317301.8508	317417.0000	-0.04%	-0.04%
C-P	Disp(mm)	0.8118	0.8113	0.8110	0.09%	0.04%
	Load(N)	180068.8077	179946.1041	179679.0532	0.22%	0.15%

Table 3.7 Damping effects and thermal effects of different boundary conditions for different methods

Damping effects and Thermal effects		GFM(1)	EM(2)	FEM(3)	((1)-(3))/(3)	((2)-(3))/(3)
P-P	Disp(mm)	0.5766	0.5727	0.5770	-0.07%	-0.74%
	Load(N)	124857.0824	124073.0732	124319.9615	0.43%	-0.20%
C-C	Disp(mm)	1.3918	1.3913	1.4110	-1.36%	-1.40%
	Load(N)	317777.5873	317778.3685	319065.9036	-0.40%	-0.40%
C-P	Disp(mm)	0.8139	0.8142	0.8170	-0.37%	-0.34%
	Load(N)	180634.1171	180511.6822	180809.3937	-0.10%	-0.16%

For thermal effects, the rise of temperature is considered in this part of the investigation, which is also shown in Table 3.6. Compared with the simplified model, the critical values would increase under thermal environment. An interesting finding is that the thermal effect has a more significant influence on the system than the damping effect does.

Furthermore, when the thermal and damping effects are simultaneously considered (Table 3.7), the critical values are largest among all investigated cases of analysis. However, the results of FEM are larger than the results calculated by the other two methods.

3.3.2 *Verification of buckled structural configuration*

Strictly, in classical static structural stability analysis, the buckled shape (also called Eigen-function) is solved by a second order/fourth order homogeneous ordinary differential equation according to equilibrium equation. However, it is difficult to introduce such an idea to dynamic buckling analysis because of two reasons. The first reason is that normally the governing equations involved in the dynamic structural stability analysis are high order inhomogeneous partial differential equations, which has escalated the difficulty for solving such problem when compared with the static analysis; the second reason is that obtaining explicit solution becomes very intricate due to the insufficiency of the boundary conditions. Consequently, various numerical methods (e.g., Galerkin method, finite different method, etc.,) have been adopted to tackle such challenges.

In this chapter, the first mode shape of the beam-column has been adopted as the buckling shape of the structure under constant speed compression for various boundary conditions. Therefore, it is necessary to examine effectiveness and validity of the proposed methods in terms of the buckling shape modelling.

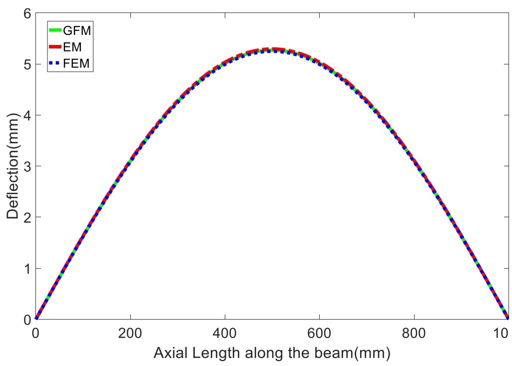

(1) Simplified Model

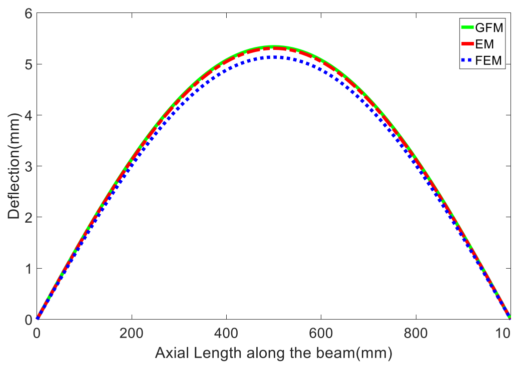

(2) Considering Damping Effect

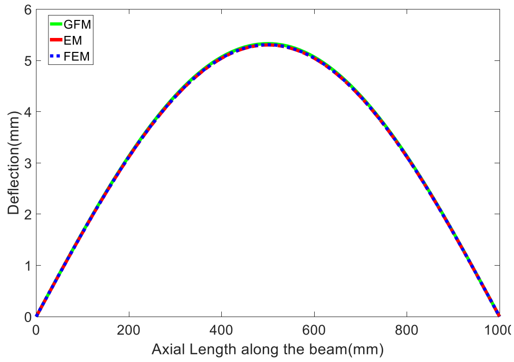

(3) Considering Thermal Effect

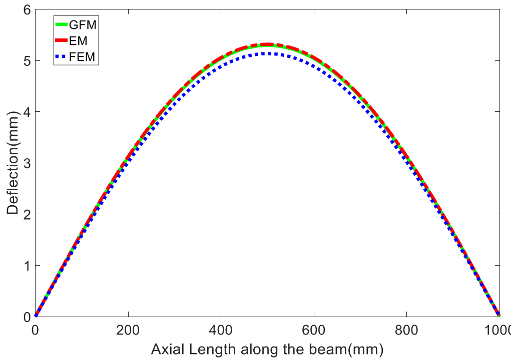

(4) Considering both Damping and Thermal Effect

Figure 3.7 The buckled shape of P-P beams for different models

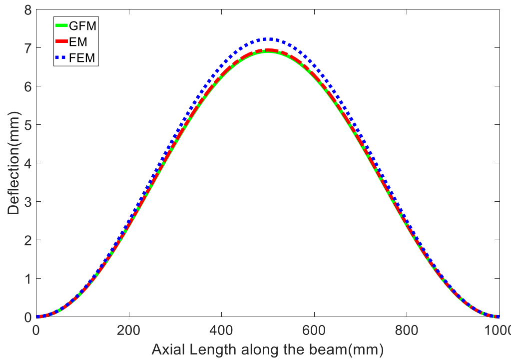

(1) Simplified Model

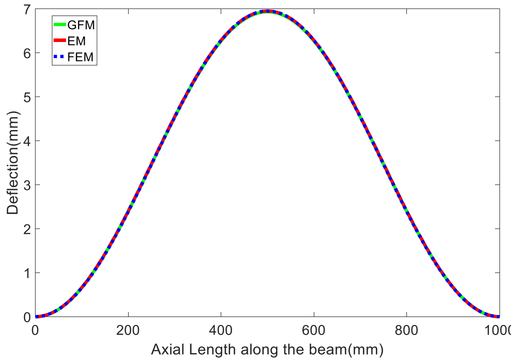

(2) Considering Damping Effect

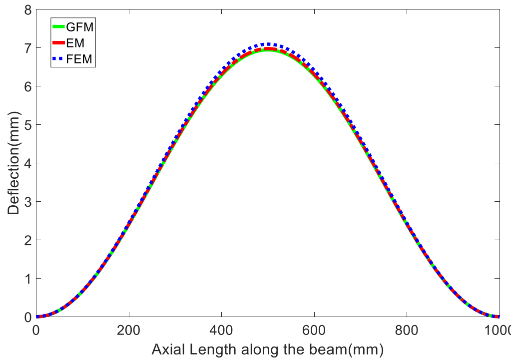

(3) Considering Thermal Effect

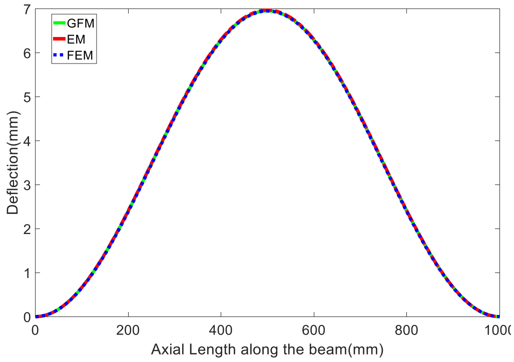

(4) Considering both Damping and Thermal Effect

Figure 3.8 The buckled shape of C-C beams for different models

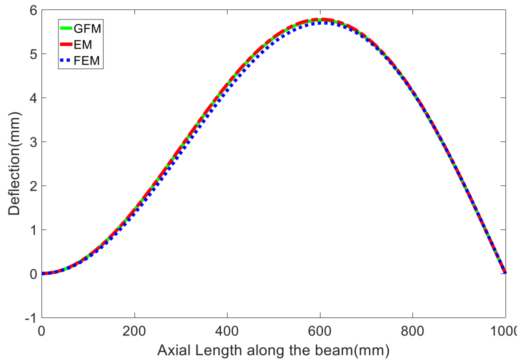

(1) Simplified Model

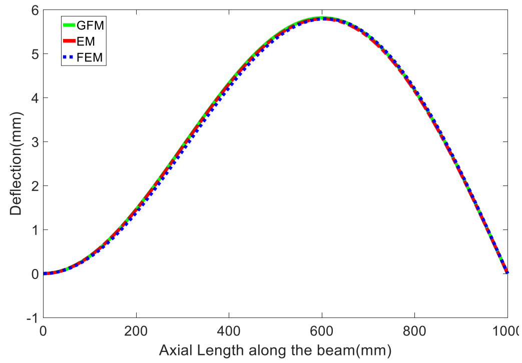

(2) Considering Damping Effect

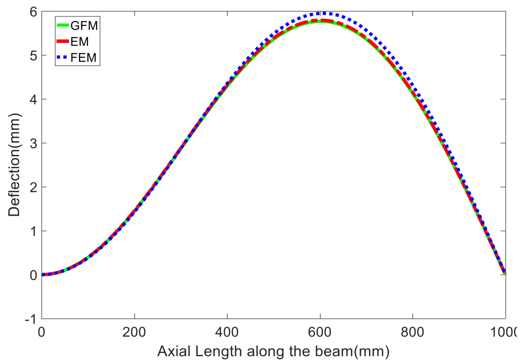

(3) Considering Thermal Effect

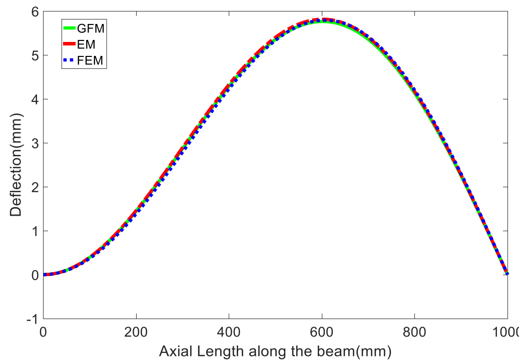

(4) Considering both Damping and Thermal Effect

Figure 3.9 The buckled shape of C-P beams for different models

Similar to Section 3.2, the 12 investigated scenarios are once again considered in this subsection. By implementing the proposed approaches and the FEM, the buckled structural configurations for all 12 concerned scenarios are demonstrated in Figure 3.7, Figure 3.8 and Figure 3.9. As clearly indicated by these figures, the structural deformations predicted by the proposed methods are in a good agreement with the FEM modellings. One remark regarding the structural deformation presented in these figures is that the Clamped-Clamped beam-column has the maximum transverse deflection whereas the Pinned-Pinned case has the least.

To comprehensively survey the differences between the proposed methods (i.e., GFM and EM) and reference method (i.e., FEM), the maximum transverse deflection reported in these figures is also formally presented in Table 3.8,Table 3.9,Table 3.10 and Table 3.11. Table 3.8 shows the maximum transverse deflection of the simplified model. It is clear that the results of GFM and EM are larger than the ones obtained from FEM, expect the case with the C-C boundary condition. If damping effect is considered, as shown in Table 3.9, the errors between ANM (GFM and EM) and FEM are decreased for C-C and C-P boundary conditions.

Table 3.10 shows the influence of thermal effect on the maximum transverse deflection. It is clearly indicated that the thermal effect would result in an increase in the structural displacement, especially for the FEM. For the results shown in Table 3.11, the structure is subjected to both damping and thermal effects simultaneously. The results calculated by the GFM and EM have a well-preserved agreement. However, an interesting remark is that the increase of maximum deflection is almost the same when only considering either damping or thermal effects.

Table 3.8 The maximum transverse displacement of simplified model under different boundary conditions

Simplified Model	GFM(1)	EM(2)	FEM(3)	((1)-(3))/(3)	((2)-(3))/(3)
P-P	5.2701	5.2941	5.2489	0.40%	0.86%
C-C	6.9112	6.9596	7.2293	-4.40%	-3.73%
C-P	5.7660	5.8143	5.6966	1.22%	2.07%

Table 3.9 The maximum transverse displacement of beam of damping effects under different boundary conditions

Damping effects	GFM(1)	EM(2)	FEM(3)	((1)-(3))/(3)	((2)-(3))/(3)
P-P	5.3362	5.3532	5.1331	3.96%	4.29%

C-C	6.9346	6.9513	6.9516	-0.24%	0.00%
C-P	5.8168	5.7927	5.7940	0.39%	-0.02%

Table 3.10 The maximum transverse displacement of beam of thermal effects under different boundary conditions

Thermal effects	GFM(1)	EM(2)	FEM(3)	((1)-(3))/(3)	((2)-(3))/(3)
P-P	5.3276	5.2966	5.3072	0.38%	-0.20%
C-C	6.9459	6.9789	7.0946	-2.10%	-1.63%
C-P	5.7676	5.7947	5.9506	-3.08%	-2.62%

Table 3.11 The maximum transverse displacement of beam of damping effects and thermal effects under different boundary conditions

Damping effects and Thermal effects	GFM(1)	EM(2)	FEM(3)	((1)-(3))/(3)	((2)-(3))/(3)
P-P	5.3162	5.3121	5.1331	3.57%	3.49%
C-C	6.9554	6.9724	6.9516	0.05%	0.30%
C-P	5.7655	5.8168	5.7940	-0.49%	0.39%

3.3.3 *Verification of different velocities for different boundary conditions*

In 1951, Hoff [39] proposed the constant velocity loading scheme of dynamic buckling and shown that the critical force strongly depends on compression rate and initial imperfection of a beam-column. Moreover, velocity is one of the critical parameters in the governing equation formulated as Eqs. (30)-(31) for GFM and Eqs. (46)-(47) for EM. Therefore, it is essential to study the impact of different velocities acting on the structures with various boundary conditions.

In Section 3.3, the results of ANM are determined by implementing the proposed GFM only, which are also compared with results obtained by the FEM. The material properties and other parameters of the investigated structures are given in Table 3. Both damping and thermal effects are simultaneously considered in all models. In order to study the dynamic buckling under different compression rates, three typical velocities are selected for each boundary condition with the same initial deflection e_0 of 0.5mm. For the P-P type, the structure is subjected to velocity of 0.01mm/ms, 0.03mm/ms, 0.05mm/ms; for the C-C type, it is subjected to velocity of 0.03mm/ms, 0.04mm/ms, 0.05mm/ms; and for the C-P type, it is subjected to velocity of 0.02mm/ms, 0.04mm/ms, 0.05mm/ms.

Figure 3.10 shows the load-longitudinal displacement curves for the P-P, C-C, and C-P type boundary conditions for different velocities. All solid lines are representing the results determined by the ANM, whereas all circles are representing the results of the FEM. In Figure 3.10, it can be clearly seen that the results obtained from ANM match very well with the results obtained from FEM for different velocities for all three considered boundary conditions. It is obvious that with the increase of compression rates, the axial force becomes larger until it reaches the peak load, which indicates the occurrence of buckling.

Figure 3.11 shows the buckled shape of different boundary conditions under different loading rates. The surface areas are plotted by the results from ANM and the circle, square and point lines are plotted by the results obtained from FEM, which is corresponding to different velocities. The results of ANM and FEM match well in lower velocities. However, with the increase of axial loading rate, the error by ANM is less than 1 percent, except the P-P type boundary condition, which is still in a good agreement with FEM. The reason for this phenomenon is that with the increase of velocities, higher-order vibrations are involved in the model, which is also shown in the following part.

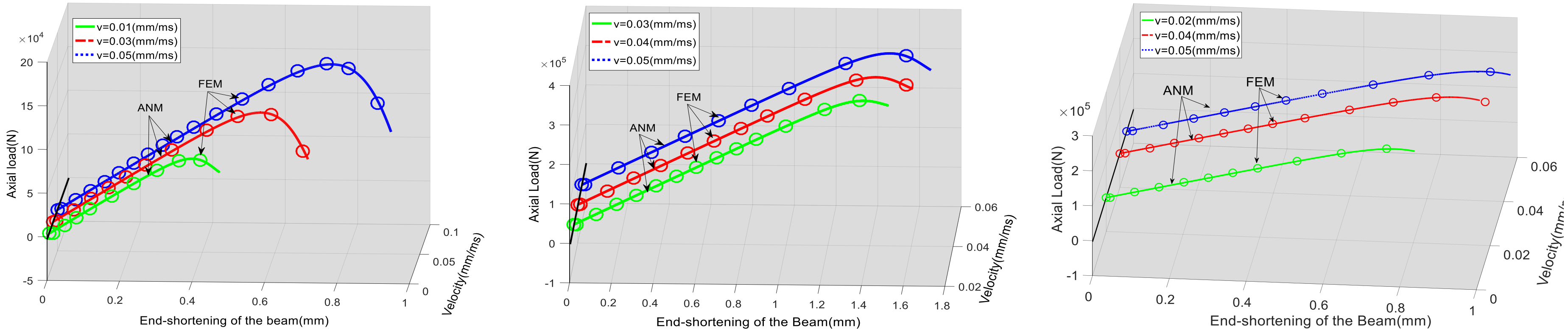

(a) P-P type (b) C-C type (c) C-P type

Figure 3.10 The relationship axial load and axial displacement for different velocities of different boundary conditions

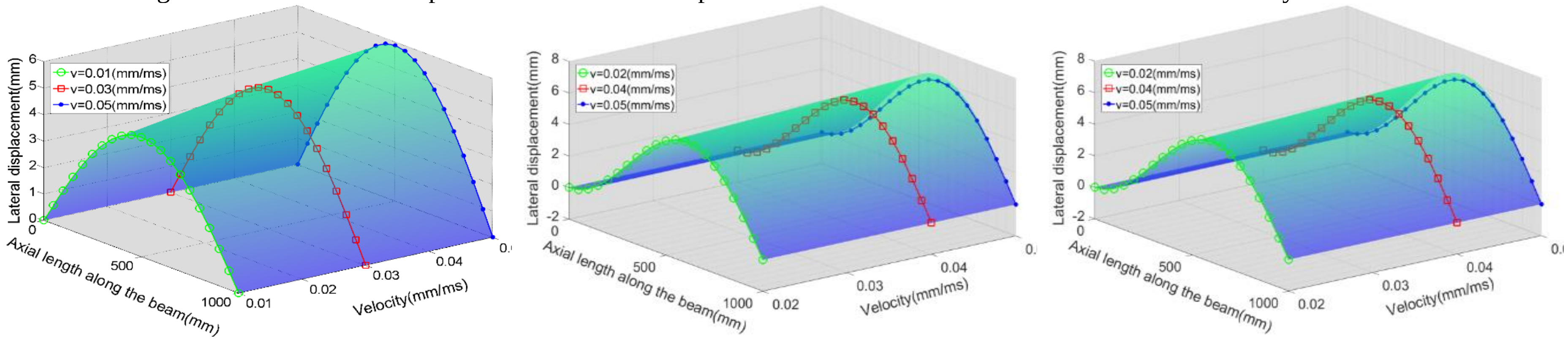

(a) P-P type (b) C-C type (c) C-P type

Figure 3.11 The relationship lateral displacement and axial length along the beam for different velocities of different boundary conditions

3.4 Parametric analysis

In section 3.3, the accuracy of the proposed GFM and EM used in dynamic buckling analysis has been examined by comparing with the results obtained by FEM for various boundary conditions under different compression rates. The ANM (both GEM and EM) shows a good agreement with FEM, so the proposed method will introduce to parametric analysis in this section. The influence of damping effects, thermal effects, velocity, initial eccentricity, the boundary condition is explored here by utilising the GFM approach. The corresponding material properties are shown in Table 3.3.

3.4.1 *The influence of damping effects*

In section 3.2 and 3.3, the results showed that the critical dynamic buckling load of the damped system is larger than the undamped system. In order to further explore the relationship between damping ratio and critical load, five damping ratios ζ from 0 (undamped system) to 0.08 are explicitly investigated as shown in Figure 3.12. It is obvious that the increase of the damping ratios result in an increase of dynamic dimensionless buckling load. When zoom in the key points, which is shown in the small rectangular box, the time instants of buckling are also delayed with the increasing of the damping ratio as shown in Table 3.12.

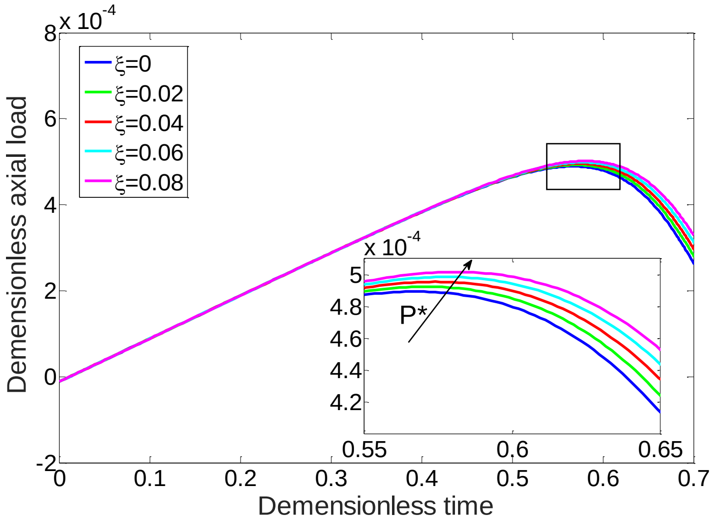

Figure 3.12 The time-load curve for different damping ratios

Table 3.12 The time-load curve for different damping ratios

Dimensionless time t^*	Dimensionless critical load $P_{cr}{}^*$
0.5680	4.89E-04
0.5701	4.92E-04
0.5739	4.95E-04
0.5783	4.99E-04
0.5810	5.02E-04

3.4.2 *The influence of thermal effects*

In this subsection, the influence of the variation of the thermal environment is investigated. The coefficient of thermal expansion in steel beam is positive (α_x=12×10^{-6} K^{-1}) for the rise of temperature and is negative (α_x=-12×10^{-6} K^{-1}) for the fall of temperature based on the room temperature (20^{o}C). It is assumed that thermal environment is a uniform temperature, which means that thermal load is a prestressing load in the beam, while the temperature-dependent material properties are ignored. The thermal stresses induced by a uniform temperature rise of fall are also shown in Eqs. (3.27) and (3.45).

Five temperature changes ΔT from -20^{o}C to +20 ^{o}C are explicitly studied, and 0 ^{o}C is defined as the reference temperature to represent the stress-free state case. The time-load curves under different temperature changes are plotted in Figure 3.13. It can be observed that for the structure has a negative force at the beginning of loading for temperature rise while a positive force for temperature fall. One can obtain two conclusions from this figure. The first one is that the critical buckling is decreased for temperature change ΔT from -20^{o}C to +20 ^{o}C. Since the temperature-dependent material properties are ignored in this analysis, the thermal effects are presented as a prestressing loading as shown in Eq.(3.30) and Eq.(3.47). The values of critical buckling load of each ΔT are shown in Table 3.13.

Moreover, with the ΔT change from -20^{o}C to +20 ^{o}C, the dimensionless time t^* is delayed, which means temperature rise would defer the time of buckling while temperature fall would cause the structure to buckle in shorter duration. The critical buckling load and the corresponding buckling time are the two critical impacts in dynamic buckling.

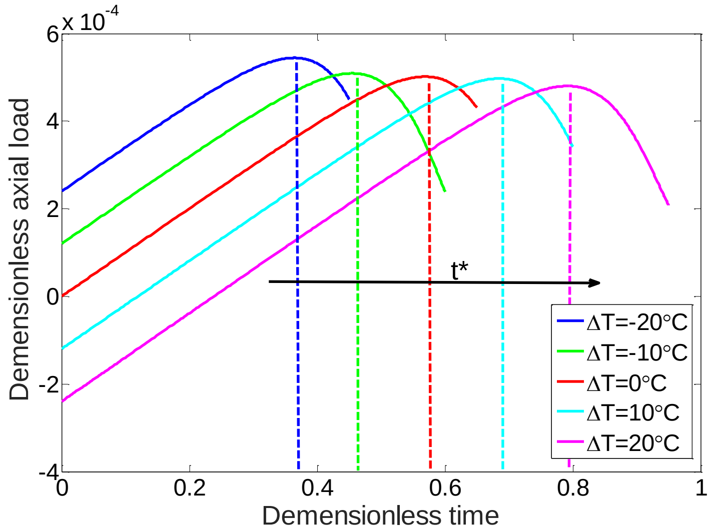

Figure 3.13 The time-load curve for different temperature change

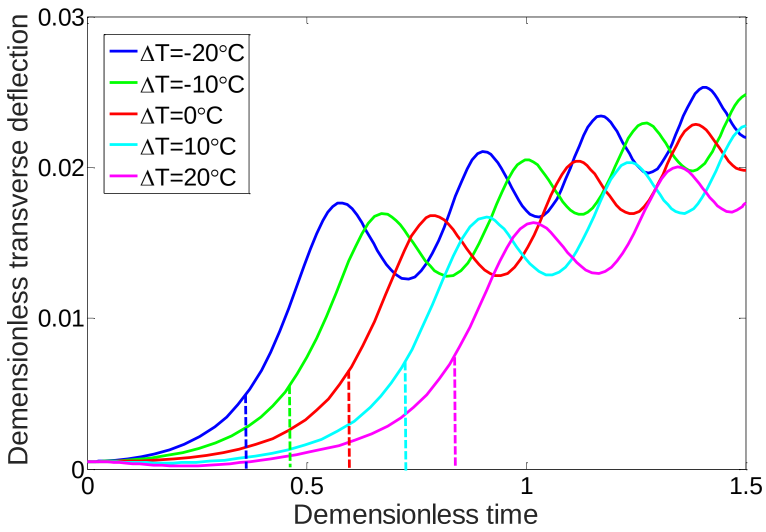

Figure 3.14 The time-deflection curve for different temperature change

In addition to the maximum deflection, the time-deflection curves are also plotted in Figure 3.14. Combined with Figure 3.14 and Table 3.13, another finding is that with ΔT changes from -20°C to +20 °C, the dimensionless transverse deflection is increasing with the increase of dimensionless buckling time.

Table 3.13 The critical values of beam column for temperature change

Temperature change/°C	t^*	t/s	P_{cr}^*	P_{cr} (N)	w^*	w (mm)
-20	0.3640	0.0122	5.4455E-04	137227.4479	5.0032E-03	5.0032
-10	0.4549	0.0152	5.0916E-04	128308.0928	5.2695E-03	5.2695
0	0.5691	0.0191	5.0158E-04	126399.1497	5.3555E-03	5.3555
10	0.6840	0.0229	4.9733E-04	125326.0961	5.4430E-03	5.4430
20	0.7920	0.0265	4.8020E-04	121009.7834	5.5532E-03	5.5532

3.4.3 *The influence of compression rates*

In section 3.3, the verification of different velocities for different boundary conditions has been discussed. In this part, more dynamic characteristic of dynamic buckling under different compression rates are studied.

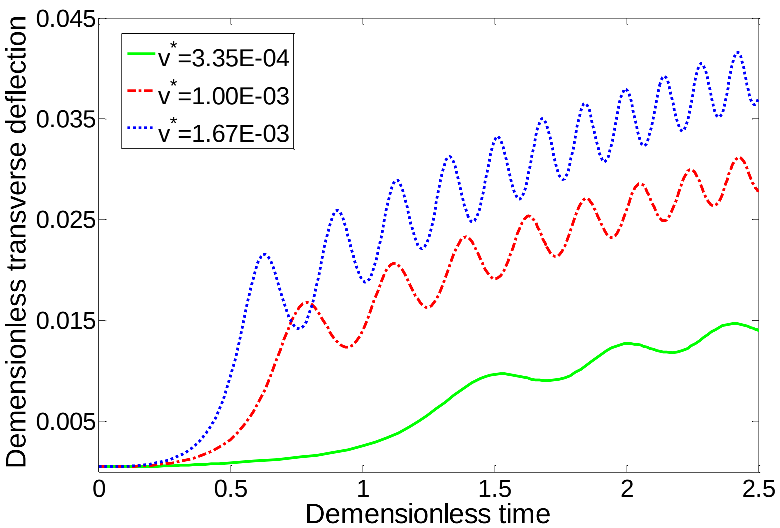

Figure 3.15 The time-deflection curve for different velocities

Figure 3.15 shows the time-deflection curves for a simply-supported beam-column for different dimensionless velocity, v^*. In this figure, the dynamic buckling responses give a charter of oscillation and an increasing of velocity would aggravate the vibration. This phenomenon can be observed when the structure is the onset of the buckle. Some researchers hold the opinion that the first inflexion on the response curve representing the critical condition [201]. However, the peak load already reached before the first inflexion if one observed Figure 3.13 and Figure 3.14 carefully.

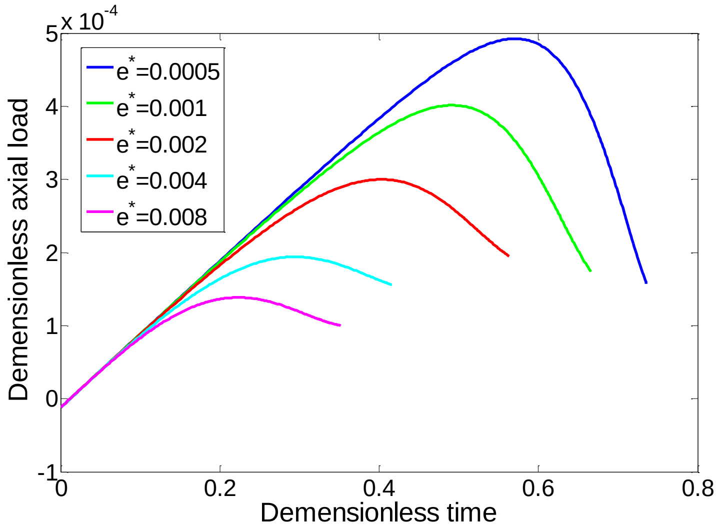

Figure 3.16 The time-load curve for different initial eccentricities

3.4.4 *The influence of initial eccentricity*

Initial eccentricity is one of the most important parameters in dynamic buckling analysis. In this section, five different dimensionless initial eccentricities e^* are discussed. In Figure 3.16, it is clearly demonstrated that a slight change of initial deflection would result in an apparent change in critical buckling load. For example, if initial deflection e^*increase from 5×10^{-4} to 1×10^{-3}, the dynamic critical load would decrease by 1.25 times. Therefore, initial eccentricity is much more important than other parameters.

3.4.5 *The influence of boundary condition*

This subsection is dedicated to understanding the effects of different boundary conditions on the buckling behaviour of a beam-column. In Section 3.3, different boundary conditions are shown in different terms of the first mode buckled shape function. Furthermore, the validity of the first mode buckled shape function for dynamic buckling analysis is examined by comparing the results from ANM and with the FEM results in Section 3.3.1.

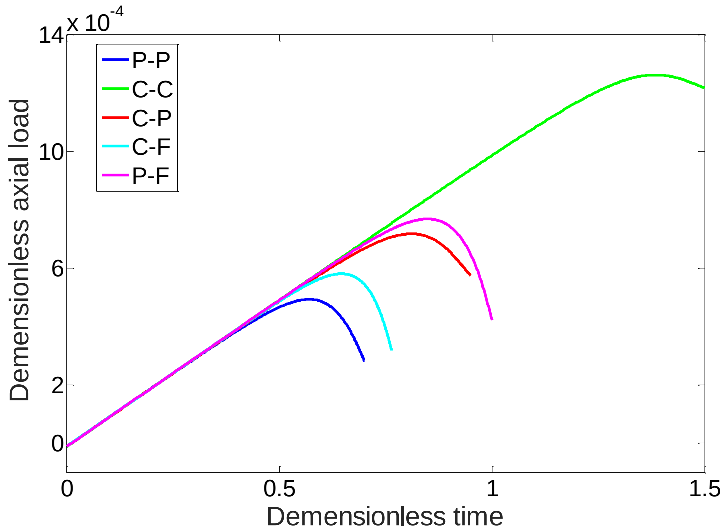

Figure 3.17 The time-load curve for different boundary conditions

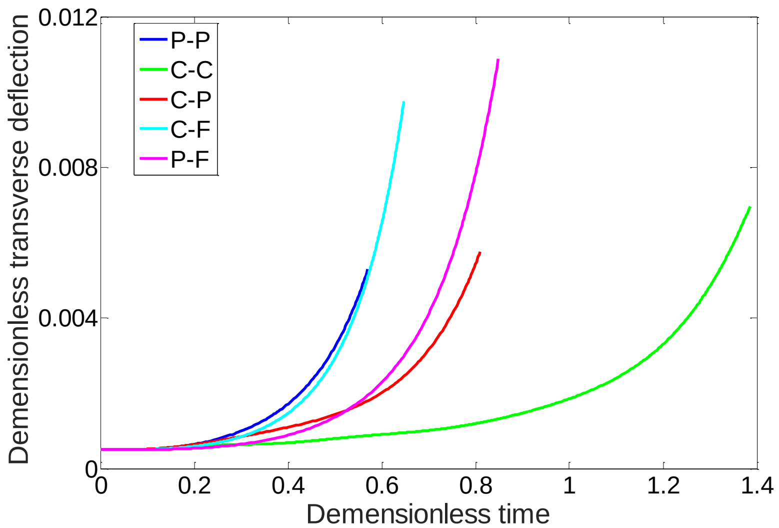

Figure 3.18 The time-deflection curve for different boundary conditions

In this section, five typical boundary conditions, such as P-P, C-C, C-P, C-F, P-F, are discussed, where P, C and F denote pinned, clamped and free, respectively. Figure 3.17 depicts the variation of the dimensionless axial load with the dimensionless time for five different boundary conditions. If one sort the critical buckling load in descending order, the following conclusion be made: C-C>P-F>C-P>C-F>P-P. The time-deflection curve is also shown in Figure 3.18. Similarly, the buckle time in descending order is that, C-C>P-F>C-P>C-F>P-P. However, the dimensionless transverse deflections in descending order is C-P>C-F>C-C>C-P>P-P. These conclusions are much more important for engineers during the design of beam or column structure subjected to dynamic loading. They can compare the results from critical buckling load, buckle time and transverse deflections.

3.4.6 *The relationship of velocity, damping effects and thermal effects*

In addition to the parametric analysis, the critical loads of different damping coefficients for different velocities are discussed. Ten dimensionless velocities v^* from 0.1 to 1.5 and ten different dimensionless damping coefficients c_d^* from 0 to 0.09 are explicitly investigated. Figure 3.19 shows the relationship between the load, velocity and damping coefficient. The increase of velocities will result in an increase of dynamic critical load, which is also shown in Figure 3.10. In order to further explore the relationship between damping coefficient and critical load, the projection of Figure 3.19 is also established and shown in Figure 3.20. It can be observed that dynamic critical load increases slightly with an increase of the damping coefficients.

Figure 3.21 shows the relationship of load, velocity and temperature change. Similarly, ten dimensionless temperature changes ΔT^* from -0.15 to 0.15 and ten different dimensionless velocities v^* from 0.1 to 1.5 are studied. With the increase of temperature change, the critical load increase from 0.8328 to 1.165, while the critical load has a significant increase due to the increase of velocities. When both velocity and temperature change reach to the maximum value, one can see that the maximum dynamic buckling load and the beams need to sustain a much larger load than static one in some special situations, which tells us that ignoring these effects can be very dangerous for structures.

Figure 3.22 shows the relationship between the critical buckling load, damping coefficient and temperature change. Similarly, ten dimensionless temperature changes ΔT^* from -0.15 to 0.15 and ten different dimensionless damping coefficients c_d^* from 0 to 0.09 are explicitly analysed. With the increase of damping coefficients, the critical load increase from 1.309 to 1.351, while the critical load has a significant increase due to the increase of temperature change. When both velocity and temperature change equal the maximum value, one can see the maximum critical load, which is lower than the combined temperature changes and velocities. Therefore, for a beam-column subjected to a compression rate in the presence of damping effects under thermal environment, velocities of load are the most important parameter for structures, then temperature change. And the last one is damping effects.

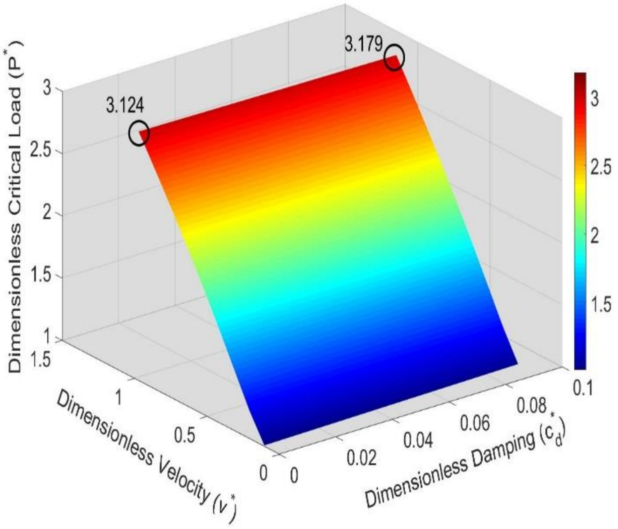

Figure 3.19 The relationship of load, velocity and damping coefficient

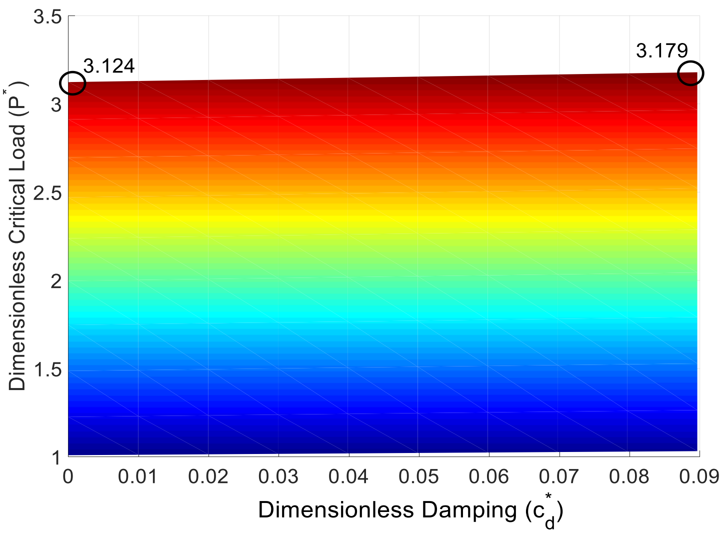

Figure 3.20 The critical load under different damping coefficient

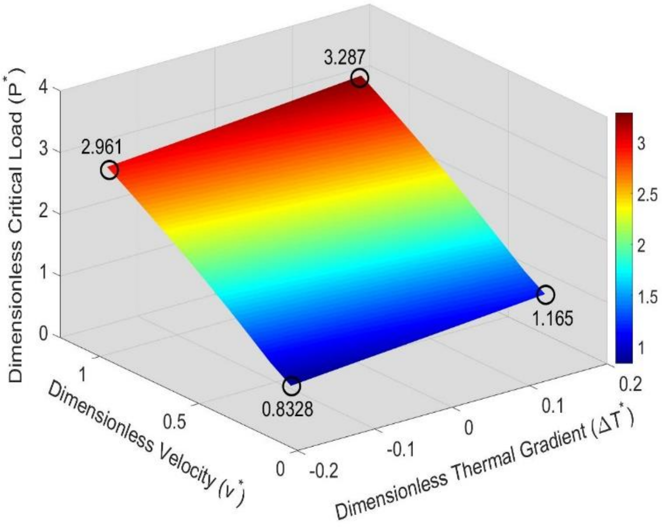

Figure 3.21 The relationship of load, velocity and temperature change

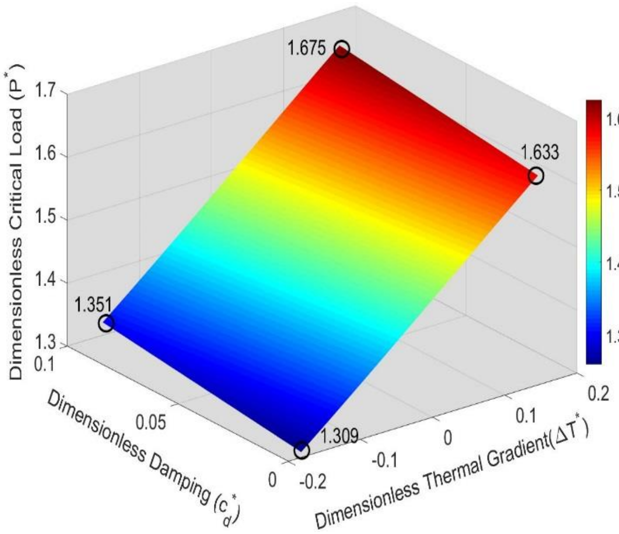

Figure 3.22 The relationship of load, damping coefficient and temperature change

3.5 Conclusion

This chapter presents two analytical-numerical methods (EM and GFM) for dynamic stability assessment of Euler-Bernoulli beam. The proposed analytical-numerical methods are able to incorporate multiple types of parameters of the dynamic response of structures within a unified nonlinear ordinary differential equation, such as beam geometry, material properties, loading rate, and different boundary conditions, especially damping and thermal effects. Consequently, the structure stability assessment against dynamic loading can be examined. By further comparing with FEM, the accuracy of the proposed method has been rigorously justified. All computational results have shown that the proposed method is in good agreement with FEM with/without damping effects or/and with/without thermal effects and the following remarks can be concluded:

1) The presence of the damping effects can strengthen structure ability against buckling by increasing the dynamic buckling load. However, the buckling time of structure will be delayed for a damped system.

2) The critical buckling is deceased for the temperature change from temperature fall to temperature rise. Moreover, temperature rise would defer the time of buckling while temperature fall would accelerate the time of buckling.

3) For a beam-column subjected to a compression rate in the presence of damping effects under thermal environment, velocities of load are the most important parameter for structures, then temperature change. However, in this case, the damping effect has the least effects.

4) Compared with the traditional FEM, the proposed method is time-saving and more accurate. Because one does not need to deal with problems such as mesh refinement, element types, modelling, analysis types, boundary conditions, etc. Moreover, the developed method can help optimum design of beam-columns structures under dynamic loadings.

Therefore, the developed method presented herein provides a comprehensive analytical analysis framework for dynamic stability assessment of beam-columns, as well as a vivid modelling on the damping effects under thermal environment for structures under dynamic loadings.

Chapter 4 Nonlinear dynamic characteristics and stability of composite orthotropic plate on elastic foundation under thermal environment

4.1 Introduction

For dynamic analysis of orthotropic plates, many researchers paid attention to natural frequency, linear and nonlinear vibration responses, and frequency-amplitude curves. From authors' knowledge and above reviewed literature, there are no researches about nonlinear dynamic characteristics and stability of orthotropic plate subjected to constant velocities on the elastic foundation under thermal environment, even considering damping effects.

Therefore, the dynamic behaviours and stability of the eccentrically composite rectangular orthotropic plates subjected to different loading rates is investigated in this chapter. The dynamic longitudinal loading on the plate is accomplished by a constant displacement rate of one end with respect to the other. The nonlinear compatibility equation is derived by using the classical plate theory with the consideration of von-Kármán strain-displacement relation. Then the nonlinear dynamic buckling equation considering thermal effects and damping effects on Winkler-Pasternak elastic foundation is obtained by Airy's stress function and Galerkin method. Finally, the nonlinear compatibility equation is solved by fourth-order Runge-Kutta method and the nonlinear dynamic stability of the composite rectangular orthotropic plates are presented based on Budiansky-Roth criterion[2, 6, 202]. Various effects of constant velocity, damping ratio, temperature change, buckling mode, initial imperfection, foundation parameter on nonlinear dynamic buckling of the plate are discussed.

4.2 Theory and formulation

Consider a simply-supported composite orthotropic plate resting on a Winkler-Pasternak elastic foundation with length *a*, width *b* and thickness *h* under uniform thermal environment ΔT, as shown in Figure 4.1. The Cartesian coordinate system (x,y,z) is established, in which the (x,y) plane is on the middle surface of the plate and *z* is the thickness direction. Also, the plate is subjected to a constant compression rate *v* along the *x* direction.

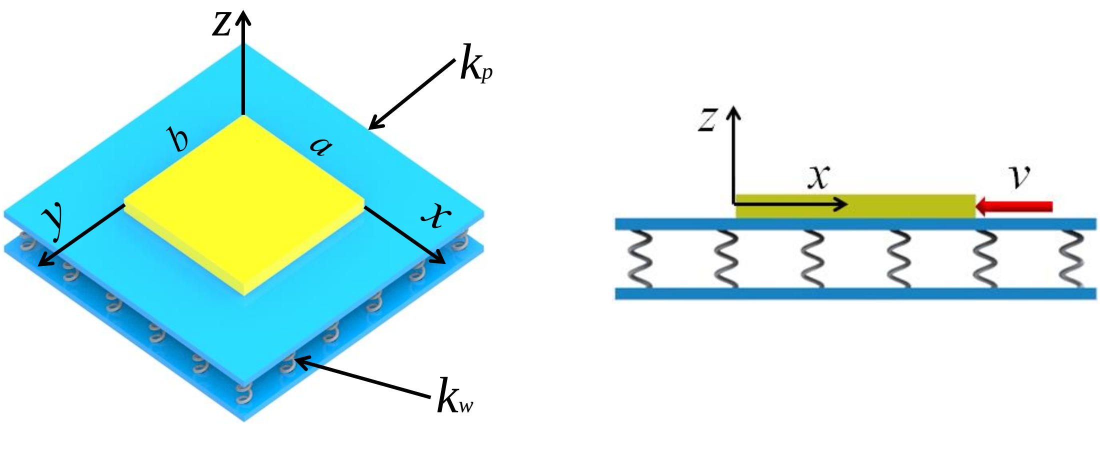

(a) (b)

Figure 4.1 Geometry and dimensions of composite orthotropic plate resting on a Winkler-Pasternak elastic foundation under uniform thermal environment subjected to constant axial velocity

According to Hooker's stress-strain relation, the constitutive equations of an orthotropic plate under uniform environment *ΔT* have the form.

$$\begin{Bmatrix} \sigma_x \\ \sigma_y \\ \tau_{xy} \end{Bmatrix} = \begin{bmatrix} C_{11} & C_{12} & 0 \\ C_{21} & C_{22} & 0 \\ 0 & 0 & C_{66} \end{bmatrix} \begin{Bmatrix} \varepsilon_x - \varepsilon_x^T \\ \varepsilon_y - \varepsilon_y^T \\ \gamma_{xy} \end{Bmatrix} \tag{4.1}$$

and

$$\begin{Bmatrix} \varepsilon_x \\ \varepsilon_y \\ \gamma_{xy} \end{Bmatrix} = \begin{bmatrix} 1/E_1 & -v_{21}/E_2 & 0 \\ -v_{12}/E_1 & 1/E_2 & 0 \\ 0 & 0 & 1/G_{12} \end{bmatrix} \begin{Bmatrix} \sigma_x \\ \sigma_y \\ \tau_{xy} \end{Bmatrix} + \begin{Bmatrix} \varepsilon_x^T \\ \varepsilon_y^T \\ 0 \end{Bmatrix} \tag{4.2}$$

where thermal strains have the following form

$$\begin{cases} \varepsilon_x^T = \alpha_x \Delta T(x,y,z,t) \\ \varepsilon_y^T = \alpha_y \Delta T(x,y,z,t) \end{cases} \tag{4.3}$$

with α_x, α_y the coefficients of linear thermal expansion along the x and y axes, respectively.

in which the elastic constants for orthotropic materials are given following:

$$\begin{cases} C_{11} = \dfrac{E_1}{(1 - v_{12}v_{21})} \\ C_{12} = \dfrac{E_2 v_{12}}{(1 - v_{12}v_{21})} \\ C_{21} = \dfrac{E_1 v_{21}}{(1 - v_{12}v_{21})} \\ C_{22} = \dfrac{E_2}{(1 - v_{12}v_{21})} \\ C_{66} = G_{12} \end{cases} \tag{4.4}$$

where E_1, E_2, v_{12} and v_{21} are the moduli of elasticity and Poisson ratio in x and y directions, respectively. G_{12} is the shear modulus.

The expansion of Eq.(4.1) can be written as

$$\begin{cases} \sigma_x = C_{11}(\varepsilon_x - \varepsilon_x^T) + C_{12}(\varepsilon_y - \varepsilon_y^T) \\ \sigma_y = C_{21}(\varepsilon_x - \varepsilon_x^T) + C_{22}(\varepsilon_y - \varepsilon_y^T) \\ \tau_{xy} = C_{66}\gamma_{xy} \end{cases} \tag{4.5}$$

Considering the initial imperfection, the von-Kármán nonlinear strain-displacement relations can be written

$$\begin{aligned} \varepsilon_x &= \frac{\partial u}{\partial x} + \frac{1}{2}\left(\frac{\partial w}{\partial x}\right)^2 - \frac{1}{2}\left(\frac{\partial w_0}{\partial x}\right)^2 - z\frac{\partial^2 (w-w_0)}{\partial x^2} \\ \varepsilon_y &= \frac{\partial v}{\partial y} + \frac{1}{2}\left(\frac{\partial w}{\partial y}\right)^2 - \frac{1}{2}\left(\frac{\partial w_0}{\partial y}\right)^2 - z\frac{\partial^2 (w-w_0)}{\partial y^2} \\ \gamma_{xy} &= \frac{\partial u}{\partial y} + \frac{\partial v}{\partial x} + \frac{\partial w}{\partial x}\frac{\partial w}{\partial y} - \frac{\partial w_0}{\partial x}\frac{\partial w_0}{\partial y} - 2z\frac{\partial^2 (w-w_0)}{\partial x \partial y} \end{aligned} \tag{4.6}$$

where u, v, w are the displacement components of middle surface of the plate in x,y,z direction, respectively.

Following the classical (Kirchhoff) plate theory and substituting Eqs.(4.6) into Eqs.(4.5), the moment resultants of an orthotropic plate are given following:

$$\begin{aligned} M_x &= \int_{-h/2}^{h/2} \sigma_x z dz = -\frac{h^3}{12}\left[C_{11}(w-w_0)_{,xx} + C_{12}(w-w_0)_{,yy}\right] - \left(M_{11}^T + M_{12}^T\right) \\ M_y &= \int_{-h/2}^{h/2} \sigma_y z dz = -\frac{h^3}{12}\left[C_{21}(w-w_0)_{,xx} + C_{22}(w-w_0)_{,yy}\right] - \left(M_{21}^T + M_{22}^T\right) \\ M_{xy} &= \int_{-h/2}^{h/2} \tau_{xy} z dz = -\frac{h^3}{6} C_{66}(w-w_0)_{,xy} \end{aligned} \tag{4.7}$$

where the bending moment due to the thermal effects can be obtained

$$
\begin{aligned}
M_{11}^{T} &= C_{11}\int_{-h/2}^{h/2}\varepsilon_x^T zdz \\
M_{12}^{T} &= C_{12}\int_{-h/2}^{h/2}\varepsilon_y^T zdz \\
M_{21}^{T} &= C_{21}\int_{-h/2}^{h/2}\varepsilon_x^T zdz \\
M_{22}^{T} &= C_{22}\int_{-h/2}^{h/2}\varepsilon_y^T zdz
\end{aligned} \tag{4.8}
$$

By differentiating ε_x , ε_y , γ_{xy} from Eqs.(4.6) twice with respect to *y*,*x* and *x*,*y* ,respectively, one can obtain the nonlinear kinematic compatibility equilibrium

$$
\frac{\partial^2\varepsilon_x}{\partial y^2}+\frac{\partial^2\varepsilon_y}{\partial x^2}-\frac{\partial^2\gamma_{xy}}{\partial x\partial y}=\left(\frac{\partial^2 w}{\partial x\partial y}\right)^2-\frac{\partial^2 w}{\partial^2 y}\frac{\partial^2 w}{\partial^2 x}-\left(\frac{\partial^2 w_0}{\partial x\partial y}\right)^2+\frac{\partial^2 w_0}{\partial^2 y}\frac{\partial^2 w_0}{\partial^2 x} \tag{4.9}
$$

Airy's stress function *F*(*x*,*y*), is defined as follows

$$
\sigma_x=\frac{\partial^2 F(x,y)}{\partial y^2},\sigma_y=\frac{\partial^2 F(x,y)}{\partial x^2},\tau_{xy}=-\frac{\partial^2 F(x,y)}{\partial x\partial y} \tag{4.10}
$$

Substituting Eqs.(4.2) and (4.10) into Eq.(4.9), the nonlinear compatibility equation for buckling of imperfect rectangular plates can be written

$$
\begin{aligned}
&\frac{1}{E_2}\frac{\partial^4 F}{\partial x^4}+2\left(-\frac{\nu_{21}}{E_2}+\frac{1}{2G_{12}}\right)\frac{\partial^4 F}{\partial^2 x\partial^2 y}+\frac{1}{E_1}\frac{\partial^4 F}{\partial y^4}+\frac{\partial^2\varepsilon_x^T}{\partial y^2}+\frac{\partial^2\varepsilon_y^T}{\partial x^2} \\
&=\left(\frac{\partial^2 w}{\partial x\partial y}\right)^2-\frac{\partial^2 w}{\partial^2 y}\frac{\partial^2 w}{\partial^2 x}-\left(\frac{\partial^2 w_0}{\partial x\partial y}\right)^2+\frac{\partial^2 w_0}{\partial^2 y}\frac{\partial^2 w_0}{\partial^2 x}
\end{aligned} \tag{4.11}
$$

The nonlinear dynamic equilibrium equations for an eccentrically orthotropic plate resting on the Winkler-Pasternak elastic foundation under uniform temperature change and uniformly out-plate distributed load q_0 including damping effects based on classical plate theory are

$$\frac{\partial N_x}{\partial x}+\frac{\partial N_{yx}}{\partial y}=\rho h\frac{\partial^2 u}{\partial t^2}+c_d\rho h\frac{\partial u}{\partial t} \tag{4.12}$$

$$\frac{\partial N_{xy}}{\partial x}+\frac{\partial N_y}{\partial y}=\rho h\frac{\partial^2 v}{\partial t^2}+c_d\rho h\frac{\partial v}{\partial t} \tag{4.13}$$

$$\begin{aligned}&N_x\frac{\partial^2 w}{\partial x^2}+N_y\frac{\partial^2 w}{\partial y^2}+2N_{xy}\frac{\partial^2 w}{\partial x\partial y}+\frac{\partial^2 M_x}{\partial x^2}+\frac{\partial^2 M_y}{\partial y^2}+2\frac{\partial^2 M_{xy}}{\partial x\partial y}\\&-k_w(w-w_0)+k_{px}\frac{\partial^2(w-w_0)}{\partial x^2}+k_{py}\frac{\partial^2(w-w_0)}{\partial y^2}+q_0\\&=\rho h\frac{\partial^2 w}{\partial t^2}+c_d\rho h\frac{\partial w}{\partial t}\end{aligned} \tag{4.14}$$

where c_d denotes the damping coefficient of the structure; k_w is Winkler foundation modulus, k_{px} and k_{py} is the shear layer foundation stiffness of Pasternak model along x and y direction. If the foundation is isotropic, it is obvious that $k_{px}=k_{py}=k_p$.

and where

$$N_x=\int_{-h/2}^{h/2}\sigma_x dz,\quad N_{xy}=\int_{-h/2}^{h/2}\tau_{xy} dz,\quad N_y=\int_{-h/2}^{h/2}\sigma_y dz \tag{4.15}$$

Substituting Eqs.(4.7) and Eqs.(4.8) into Eq.(4.14), the dynamic equation of the plate can be obtained

$$D_{11}\frac{\partial^4(w-w_0)}{\partial x^4}+2(D_{12}+2D_{66})\frac{\partial^4(w-w_0)}{\partial x^2\partial y^2}+D_{22}\frac{\partial^4(w-w_0)}{\partial y^4}+\frac{\partial^2\left(M_{11}^T+M_{12}^T\right)}{\partial x^2}$$
$$+\frac{\partial^2\left(M_{21}^T+M_{22}^T\right)}{\partial y^2}=h\left[\frac{\partial^2 w}{\partial x^2}\frac{\partial^2 F}{\partial y^2}+\frac{\partial^2 w}{\partial y^2}\frac{\partial^2 F}{\partial^2 x}-2\frac{\partial^2 w}{\partial x\partial y}\frac{\partial^2 F}{\partial x\partial y}-\rho\frac{\partial^2 w}{\partial t^2}-c_d\rho\frac{\partial w}{\partial t}\right]$$
$$-k_w(w-w_0)+k_{px}\frac{\partial^2(w-w_0)}{\partial x^2}+k_{py}\frac{\partial^2(w-w_0)}{\partial y^2}+q_0$$

(4.16)

From $E_1v_{21}=E_2v_{12}$, so that $C_{12}=C_{21}$. The flexural rigidities are given by $D_{ij}=C_{ij}h^3/12$

$$\begin{cases} D_{11}=\dfrac{E_1h^3}{12(1-v_{12}v_{21})} \\ D_{22}=\dfrac{E_2h^3}{12(1-v_{12}v_{21})} \\ D_{12}=\dfrac{E_1v_{21}h^3}{12(1-v_{12}v_{21})}=\dfrac{E_2v_{12}h^3}{12(1-v_{12}v_{21})} \\ D_{66}=\dfrac{G_{12}h^3}{12} \end{cases} \tag{4.17}$$

When considering uniform temperature changes in the environment, the nonlinear compatibility equation for buckling of imperfect rectangular plates Eq.(4.11) can be reduced to

$$\begin{aligned}&\frac{1}{E_2}\frac{\partial^4 F}{\partial x^4}+2\left(-\frac{v_{21}}{E_2}+\frac{1}{2G_{12}}\right)\frac{\partial^4 F}{\partial^2 x\partial^2 y}+\frac{1}{E_1}\frac{\partial^4 F}{\partial y^4}\\ &=\left(\frac{\partial^2 w}{\partial x\partial y}\right)^2-\frac{\partial^2 w}{\partial^2 y}\frac{\partial^2 w}{\partial^2 x}-\left(\frac{\partial^2 w_0}{\partial x\partial y}\right)^2+\frac{\partial^2 w_0}{\partial^2 y}\frac{\partial^2 w_0}{\partial^2 x}\end{aligned} \tag{4.18}$$

And the dynamic equation for orthotropic plate Eq.(4.16) can be reduced to

$$D_{11}\frac{\partial^4(w-w_0)}{\partial x^4}+2(D_{12}+2D_{66})\frac{\partial^4(w-w_0)}{\partial x^2\partial y^2}+D_{22}\frac{\partial^4(w-w_0)}{\partial y^4}$$
$$=h\left[\frac{\partial^2 w}{\partial x^2}\frac{\partial^2 F}{\partial y^2}+\frac{\partial^2 w}{\partial y^2}\frac{\partial^2 F}{\partial^2 x}-2\frac{\partial^2 w}{\partial x\partial y}\frac{\partial^2 F}{\partial x\partial y}-\rho\frac{\partial^2 w}{\partial t^2}-c_d\rho\frac{\partial w}{\partial t}\right] \tag{4.19}$$
$$-k_w(w-w_0)+k_{px}\frac{\partial^2(w-w_0)}{\partial x^2}+k_{py}\frac{\partial^2(w-w_0)}{\partial y^2}+q_0$$

4.3 Nonlinear dynamic analysis of an orthotropic plate

4.3.1 *Solution of the problem*

The boundary conditions for w and w_0 of a supported plate where the edges remain straight after buckling are

$$\left.\begin{array}{r} w=w_0=0 \\ \dfrac{\partial^2 w}{\partial x^2}=\dfrac{\partial^2 w_0}{\partial x^2}=0 \end{array}\right\} x=0 \text{ and } x=a \tag{4.20}$$

and

$$\left.\begin{array}{r} w=w_0=0 \\ \dfrac{\partial^2 w}{\partial y^2}=\dfrac{\partial^2 w_0}{\partial y^2}=0 \end{array}\right\} y=0 \text{ and } y=b \tag{4.21}$$

From the above figure, the average stress in each direction becomes

$$\left.\begin{array}{l} \dfrac{1}{b}\displaystyle\int_0^b \sigma_x dy=\dfrac{1}{b}\int_0^b \dfrac{\partial^2 F(x,y)}{\partial^2 y}dy=-p(t) \\ \dfrac{1}{b}\displaystyle\int_0^b \tau_{xy} dy=-\dfrac{1}{b}\int_0^b \dfrac{\partial^2 F(x,y)}{\partial x\partial y}dy=N_{xy} \end{array}\right\} for\ \ x=0,a \tag{4.22}$$

where $p(t)$ is the average compressive stress due to the constant compression rates.

$$\left.\begin{aligned}\frac{1}{a}\int_0^a \sigma_y dx = \frac{1}{a}\int_0^a \frac{\partial^2 F(x,y)}{\partial^2 x} dx = 0 \\ \frac{1}{a}\int_0^a \tau_{yx} dx = -\frac{1}{a}\int_0^a \frac{\partial^2 F(x,y)}{\partial x \partial y} dx = N_{yx}\end{aligned}\right\} for \;\; y = 0, b \tag{4.23}$$

The deflection function for the SSSS boundary condition plate will be assumed to be the single mode[74]

$$w(x,y,t) = W_{mn}(t)\sin(\frac{m\pi x}{a})\sin(\frac{n\pi y}{b}) \tag{4.24}$$

where $W_{mn}(t)$ is the time-varying amplitude of w, and m and n are the number of half waves in the x and y directions, respectively. Moreover, other boundary conditions can be considered if one selects the proper trigonometric admissible functions[75].

Also, the initial shape function can be taken as

$$w_0(x,y) = W_0 \sin(\frac{m\pi x}{a})\sin(\frac{n\pi y}{b}) \tag{4.25}$$

where W_0 represents the initial eccentricity value of the plate.

Substituting Eq.(4.24) and Eq.(4.25) into the nonlinear compatibility Eq.(4.18) and solving the obtained equation for unknown F lead to

$$\begin{aligned}F(x,y,t) = &\frac{a^2 n^2 E_2}{32 b^2 m^2}(W_{mn}^2 - W_0^2)\cos\frac{2m\pi x}{a} + \frac{b^2 m^2 E_1}{32 a^2 n^2}(W_{mn}^2 - W_0^2)\cos\frac{2n\pi y}{b} \\ &-\frac{1}{2}p(t)y^2\end{aligned} \tag{4.26}$$

Then, using Eqs.(4.24), (4.25) and (4.26), Eq.(4.19) can be rewritten as

$$
\left[D_{11}\frac{m^4}{a^4} + 2(D_{12}+2D_{66})\frac{m^2n^2}{a^2b^2} + D_{22}\frac{n^4}{b^4} + k_w\frac{1}{\pi^4} + k_{px}\frac{m^2}{a^2\pi^2} + k_{py}\frac{n^2}{b^2\pi^2} \right](W_{mn}-W_0)
$$
$$
-\frac{q_0h}{\pi^4} = \frac{m^2hp(t)}{a^2\pi^2}W_{mn} - \frac{\rho h}{\pi^4}\left(\frac{\partial^2 W_{mn}}{\partial t^2} + c_d\frac{\partial W_{mn}}{\partial t}\right)
$$
$$
+\frac{h}{8}\left[\frac{m^4}{a^4}E_1\cos\frac{2n\pi y}{b} + \frac{n^4}{b^4}E_2\cos\frac{2m\pi x}{a} \right](W_{mn}^2 - W_0^2)W_{mn}
$$

(4.27)

Applying the Galerkin method to Eq.(4.27) and multiplying each term with sin*(mπx/a)*sin*(nπy/b)dxdy*, then integrating over the middle surface of the plate, the equation becomes

$$
\begin{aligned}
&\frac{\partial^2 W_{mn}}{\partial t^2} + c_d\frac{\partial W_{mn}}{\partial t} - \frac{q_0}{\rho} \\
&+\frac{\pi^4}{\rho h}\left[D_{11}\frac{m^4}{a^4} + 2(D_{12}+2D_{66})\frac{m^2n^2}{a^2b^2} + D_{22}\frac{n^4}{b^4} + k_w\frac{1}{\pi^4} + k_{px}\frac{m^2}{a^2\pi^2} + k_{py}\frac{n^2}{b^2\pi^2} \right] \\
&\bullet(W_{mn}-W_0) - \frac{m^2\pi^2p(t)}{a^2\rho}W_{mn} + \frac{\pi^4}{24\rho}\left(\frac{m^4}{a^4}E_1 + \frac{n^4}{b^4}E_2 \right)(W_{mn}^2 - W_0^2)W_{mn} = 0
\end{aligned}
\tag{4.28}
$$

4.3.2 *In-plane compressive force*

Substitute Eq.(4.26) into Eq.(4.22), the membrane stresses can be obtained

$$
\begin{aligned}
\sigma_x &= -\frac{m^2\pi^2E_1}{8a^2}(W_{mn}^2 - W_0^2)\cos\frac{2n\pi y}{b} - p(t) \\
\sigma_y &= -\frac{n^2\pi^2E_2}{8b^2}(W_{mn}^2 - W_0^2)\cos\frac{2m\pi x}{a} \\
\tau_{xy} &= 0
\end{aligned}
\tag{4.29}
$$

Getting together Eq.(4.6) with Eq.(4.2), we can have the following equations

$$
\begin{aligned}
\varepsilon_x &= \frac{\partial u}{\partial x} + \frac{1}{2}\left(\frac{\partial w}{\partial x}\right)^2 - \frac{1}{2}\left(\frac{\partial w_0}{\partial x}\right)^2 - z\frac{\partial^2 (w-w_0)}{\partial x^2} \\
\varepsilon_x &= \frac{\sigma_x}{E_1} - v_{21}\frac{\sigma_y}{E_2} + \varepsilon_x^T
\end{aligned}
\tag{4.30}
$$

Substitute Eq.(4.29) into Eqs.(4.30) and eliminating ε_x, then $\partial u / \partial x$ can be expressed

$$
\begin{aligned}
&\frac{\partial u}{\partial x} = -\pi^2\left[\frac{m^2}{8a^2}\left(1+\cos\frac{2m\pi x}{a} - \cos\frac{2m\pi x}{a}\cos\frac{2n\pi y}{b}\right) - v_{21}\frac{n^2}{8b^2}\cos\frac{2m\pi x}{a}\right] \\
&\bullet(W_{mn}^2 - W_0^2) - z\frac{m^2\pi^2}{a^2}\sin\frac{m\pi x}{a}\sin\frac{n\pi y}{b}(W_{mn} - W_0) - \frac{p(t)}{E_1} + \varepsilon_x^T \\
&+z(W_{mn} - W_0)\frac{m^2\pi^2}{a^2}\sin(\frac{m\pi x}{a})\sin(\frac{n\pi y}{b})
\end{aligned}
\tag{4.31}
$$

where $\partial u/\partial x$ strain at any point through the plate thickness in x-direction; when z=0, $\partial u/\partial x$ represents the strain at points on the plate middle plane. Therefore, for simplification, in this chapter we just consider the strain at points on the plate middle plane.

The dynamic longitudinal loading on the plate is accomplished by a constant displacement rate v along x-axis of one end with respect to the other; therefore, the displacement along x-axis due to the loading rate can be solved by

$$
\begin{aligned}
U &= \int_0^a \frac{\partial u}{\partial x}dx = -\frac{m^2\pi^2}{8a}(W_{mn}^2 - W_0^2) - \frac{p(t)a}{E_1} + a\varepsilon_x^T \\
U &= -vt
\end{aligned}
\tag{4.32}
$$

where negative in the displacement means the plate edge is shorten.

Also, the average value of compressive stress $p(t)$ can be expressed

$$p(t) = \frac{E_1}{a} vt - \frac{m^2 E_1 \pi^2}{8a^2} (W_{mn}^2 - W_0^2) + E_1 \varepsilon_x^T \tag{4.33}$$

The coefficient of thermal expansion in plate is positive (α_x=12×10^{-6} K^{-1}) for the fall of temperature and is negative (α_x=-12×10^{-6} K^{-1}) for the rise of temperature based on the room temperature (T=300K). This is because the plate will expand due to the rise of temperature, which may result in tension force along the edge of the plate.

4.3.3 *Vibration analysis*

For an imperfect orthotropic plate on Winkler-Pasternak elastic foundation in thermal environment subjected to out-plane uniformly distributed load (UDL) $q_0 = Q\sin(wt)$ and in-plane compressive force $p(t)$, respectively. Then Eq.(4.28) can be written as

$$\begin{aligned}
&\frac{\partial^2 W_{mn}}{\partial t^2} + c_d \frac{\partial W_{mn}}{\partial t} - \frac{Q\sin(wt)}{\rho} \\
&+ \frac{\pi^4}{\rho h} \begin{bmatrix} D_{11} \dfrac{m^4}{a^4} + 2(D_{12} + 2D_{66}) \dfrac{m^2 n^2}{a^2 b^2} + D_{22} \dfrac{n^4}{b^4} \\ + k_w \dfrac{1}{\pi^4} + k_{px} \dfrac{m^2}{a^2 \pi^2} + k_{py} \dfrac{n^2}{b^2 \pi^2} \end{bmatrix} (W_{mn} - W_0) \\
&- \frac{m^2 \pi^2 p(t)}{a^2 \rho} W_{mn} + \frac{\pi^4}{24\rho} \left(\frac{m^4}{a^4} E_1 + \frac{n^4}{b^4} E_2 \right) (W_{mn}^2 - W_0^2) W_{mn} = 0
\end{aligned} \tag{4.34}$$

where Q is the amplitude of the UDL and w is the frequency of the excitation force.

By solving Eq.(4.34), the natural frequencies of the orthotropic plate, and the frequency-amplitude relation of nonlinear vibration with or without damping, the nonlinear behaviour of the orthotropic plate on Winkler-Pasternak elastic foundation can be obtained.

For the free and linear vibration without damping effect, considering only initially perfect plates, $W_0=0$, the Eq.(4.34) becomes

$$\frac{\partial^2 W_{mn}}{\partial t^2}+\frac{\pi^4}{\rho h}\left[\begin{array}{l} D_{11}\dfrac{m^4}{a^4}+2(D_{12}+2D_{66})\dfrac{m^2n^2}{a^2b^2}+D_{22}\dfrac{n^4}{b^4} \\ +k_w\dfrac{1}{\pi^4}+k_{px}\dfrac{m^2}{a^2\pi^2}+k_{py}\dfrac{n^2}{b^2\pi^2} \end{array}\right]W_{mn}=0 \tag{4.35}$$

For harmonic motion, $W_{mn}(t)$ may be taken in the form

$$W_{mn}(t)=A\sin(\omega t) \tag{4.36}$$

where A is the amplitude of the vibration.

Substituting Eq.(4.36) into Eq.(4.35), the fundamental frequency of natural vibration of orthotropic plate on Winkler-Pasternak elastic foundation can be determined by

$$\omega_{mn}=\sqrt{\frac{\pi^4}{\rho h}\left[\begin{array}{l} D_{11}\dfrac{m^4}{a^4}+2(D_{12}+2D_{66})\dfrac{m^2n^2}{a^2b^2}+D_{22}\dfrac{n^4}{b^4} \\ +k_w\dfrac{1}{\pi^4}+k_{px}\dfrac{m^2}{a^2\pi^2}+k_{py}\dfrac{n^2}{b^2\pi^2} \end{array}\right]} \tag{4.37}$$

When the compressive loading rate $v=0$ and considering an initially perfect plate, the nonlinear vibration of an orthotropic plate with the consideration of damping effect on Winkler-Pasternak elastic foundation can be obtain from Eqs.(4.33) and (4.34)

$$\frac{\partial^2 W_{mn}}{\partial t^2}+c_d\frac{\partial W_{mn}}{\partial t}-\frac{Q\sin\left(wt\right)}{\rho}$$
$$+\frac{\pi^4}{\rho h}\left[\begin{array}{l}D_{11}\frac{m^4}{a^4}+2(D_{12}+2D_{66})\frac{m^2n^2}{a^2b^2}+D_{22}\frac{n^4}{b^4}\\+k_w\frac{1}{\pi^4}+k_{px}\frac{m^2}{a^2\pi^2}+k_{py}\frac{n^2}{b^2\pi^2}\end{array}\right]W_{mn} \tag{4.38}$$
$$-\frac{E_1m^2\pi^2\varepsilon_x^T}{\rho a^2}W_{mn}+\frac{\pi^4}{24\rho}\left(\frac{4m^4}{a^4}E_1+\frac{n^4}{b^4}E_2\right)W_{mn}^3=0$$

Substituting Eq.(4.36) into nonlinear vibration equation (4.38) and applying Galerkin method, one can obtain that

$$\omega^2-\frac{2}{\pi}c_d\omega=c_1-c_2+\frac{3}{4}c_3A^2-\frac{Q}{\rho A} \tag{4.39}$$

where

$$c_1=\omega_{mn}^2=\frac{\pi^4}{\rho h}\left[\begin{array}{l}D_{11}\frac{m^4}{a^4}+2(D_{12}+2D_{66})\frac{m^2n^2}{a^2b^2}+D_{22}\frac{n^4}{b^4}\\+k_w\frac{1}{\pi^4}+k_{px}\frac{m^2}{a^2\pi^2}+k_{py}\frac{n^2}{b^2\pi^2}\end{array}\right]$$
$$c_2=\frac{E_1m^2\pi^2\varepsilon_x^T}{\rho a^2} \tag{4.40}$$
$$c_3=\frac{\pi^4}{24\rho}\left(\frac{4m^4}{a^4}E_1+\frac{n^4}{b^4}E_2\right)$$

Eq.(4.39) is the nonlinear vibration equation of an orthotropic plate subjected to out-plane uniformly distributed load (UDL) and uniformly temperature changes environment on Winkler-Pasternak elastic foundation with damping effects.

1) When Q=0, the nonlinear free vibration of an orthotropic plate under uniformly temperature changes environment on Winkler-Pasternak elastic foundation is obtained

$$\omega^2 - \frac{2}{\pi} c_d \omega = c_1 - c_2 + \frac{3}{4} c_3 A^2 \tag{4.41}$$

2) When ε_x^T =0, the nonlinear free vibration of an orthotropic plate under out-plane uniformly distributed load on Winkler-Pasternak elastic foundation is obtained

$$\omega^2 - \frac{2}{\pi} c_d \omega = c_1 + \frac{3}{4} c_3 A^2 - \frac{Q}{\rho A} \tag{4.42}$$

3) When Q=0 and ε_x^T =0, the nonlinear free vibration of an orthotropic plate on Winkler-Pasternak elastic foundation can be determined by

$$\omega^2 - \frac{2}{\pi} c_d \omega = c_1 + \frac{3}{4} c_3 A^2 \tag{4.43}$$

4.3.4 *Buckling analysis*

4.3.4.1 *Static buckling analysis*

For an initially perfect plate, by omitting the out-plane UDL, velocity, acceleration and high-order terms, Eq.(4.28) can be reduced into

$$\begin{aligned}&\frac{\pi^2}{h}\left[D_{11}\frac{m^4}{a^4} + 2(D_{12}+2D_{66})\frac{m^2n^2}{a^2b^2} + D_{22}\frac{n^4}{b^4} + k_w\frac{1}{\pi^4} + k_{px}\frac{m^2}{a^2\pi^2} + k_{py}\frac{n^2}{b^2\pi^2}\right]\\&-\frac{m^2 p(t)}{a^2} = 0\end{aligned} \tag{4.44}$$

Eq.(4.44) is the linear static equation of the orthotropic plate on an elastic foundation, which can also obtain from the corresponding static case using the linear theory. Then the critical buckling load is

$$p_{st} = \frac{a^2\pi^2}{m^2 h}\left[\begin{array}{l} D_{11}\dfrac{m^4}{a^4} + 2(D_{12}+2D_{66})\dfrac{m^2n^2}{a^2b^2} + D_{22}\dfrac{n^4}{b^4} \\ +k_w\dfrac{1}{\pi^4} + k_{px}\dfrac{m^2}{a^2\pi^2} + k_{py}\dfrac{n^2}{b^2\pi^2} \end{array}\right] \tag{4.45}$$

Therefore, the dimensionless in-plane static buckling load is defined as follows:

$$\begin{aligned} \bar{p}_{st} &= p_{st}\frac{a^2h}{D_{11}\pi^2} \\ &= m^2 + \frac{2(D_{12}+2D_{66})}{D_{11}}\frac{a^2n^2}{b^2} + \frac{D_{22}}{D_{11}}\frac{a^2n^2}{b^4} \\ &+k_w\frac{1}{D_{11}m^2\pi^4} + k_{px}\frac{a^2}{D_{11}m^2\pi^2} + k_{py}\frac{a^4n^2}{D_{11}b^2m^2\pi^2} \end{aligned} \tag{4.46}$$

4.3.4.2 *Dynamic buckling analysis*

Then substituting Eq.(4.33) into Eq.(4.28), the governing equation of nonlinear dynamic buckling of an orthotropic rectangular plate subjected to a constant loading rate *v* with thermal effect and damping effect can be derived

$$
\begin{aligned}
&\frac{\partial^2 W_{mn}}{\partial t^2}+c_d\frac{\partial W_{mn}}{\partial t}\\
&+\frac{\pi^4}{\rho h}\begin{bmatrix} D_{11}\frac{m^4}{a^4}+2(D_{12}+2D_{66})\frac{m^2n^2}{a^2b^2}+D_{22}\frac{n^4}{b^4}\\ +k_w\frac{1}{\pi^4}+k_{px}\frac{m^2}{a^2\pi^2}+k_{py}\frac{n^2}{b^2\pi^2}\end{bmatrix}(W_{mn}-W_0)\\
&-\frac{m^2\pi^2W_{mn}}{a^2\rho}\left\{\frac{E_1}{a}vt-\frac{m^2E_1\pi^2}{8a^2}(W_{mn}^2-W_0^2)+E_1\varepsilon_x^T\right\}\\
&+\frac{\pi^4}{24\rho}\left(\frac{m^4}{a^4}E_1+\frac{n^4}{b^4}E_2\right)(W_{mn}^2-W_0^2)W_{mn}
\end{aligned}
\tag{4.47}
$$

Introduce the following non-dimensional parameters and constants

$$
\begin{gathered}
W_{mn}^*=\frac{W_{mn}}{h},W_0^*=\frac{W_0}{h},\tau=\frac{t}{\sqrt{\frac{\rho ha}{E_1}}},v^*=\frac{v}{a\sqrt{\frac{E_1}{\rho ha}}},\\
d_1=\frac{D_{11}\pi^4}{E_1a^3},d_2=\frac{2(D_{12}+2D_{66})}{D_{11}},d_3=\frac{a}{b}\\
d_4=\frac{D_{22}}{D_{11}},d_5=\frac{h}{a},d_6=\frac{E_2}{E_1},\\
K_w=\frac{k_wa^4}{D_{11}\pi^4},K_{px}=\frac{k_{px}a^2}{D_{11}\pi^2},K_{py}=\frac{k_{py}a^4}{D_{11}b^2\pi^2}
\end{gathered}
\tag{4.48}
$$

By considering the viscous damping as internal damping effects, one can obtain that:

$$
\begin{aligned}
c_d&=2\omega_{mn}\zeta\\
c_d^*&=c_d\sqrt{\frac{\rho ha}{E_1}}
\end{aligned}
\tag{4.49}
$$

where c_d denotes the damping coefficient of the structure; ω_{mn} denotes the circular natural frequency of the plate corresponding to mode (m,n); and ζ denotes the damping ratio of the plate.

Therefore, the differential equations governing the nonlinear behaviour of an orthotropic plate can be written in a non-dimensional form

$$\begin{aligned}
&\frac{\partial^2 W_{mn}^*}{\partial \tau^2} + c_d^* \frac{\partial W_{mn}^*}{\partial \tau} \\
&+ d_1 \left(m^4 + d_2 d_3^2 m^2 n^2 + d_4 d_3^4 n^4 + K_w + K_{px} m^2 + K_{py} n^2 \right) (W_{mn}^* - W_0^*) \\
&- d_5 m^2 \pi^2 W_{mn}^* \left[v^* \tau - \frac{m^2 \pi^2 d_5^2}{8} (W_{mn}^{*\,2} - W_0^{*2}) + \varepsilon_x^T \right] \\
&+ \frac{\pi^4 d_5^3}{24} \left(m^4 + d_6 d_3^4 \right) (W_{mn}^{*\,2} - W_0^{*2}) W_{mn}^*
\end{aligned} \tag{4.50}$$

According to the dimensionless quantities of Eq.(4.48), the normalised buckling load from Eq.(4.33) can be represented as:

$$p_{cr}^* = \frac{p(t)}{p_{st}} = d_7 \left[v^* \tau - \frac{m^2 \pi^2 d_5^2}{8} (W_{mn}^{*\,2} - W_0^{*2}) + \varepsilon_x^T \right] \tag{4.51}$$

where

$$d_7 = \frac{E_1 a^2 h m^2}{D_{11} \pi^2 (m^4 + d_2 d_3^2 m^2 n^2 + d_4 d_3^4 n^4 + K_w + K_{px} m^2 + K_{py} n^2)} \tag{4.52}$$

4.4 Numerical results and discussion

4.4.1 *Verification of proposed method*

In this section, the accuracy of the proposed method is verified with published papers and the following dimensionless parameters are defined.

Natural frequency of orthotropic plate without Winkler-Pasternak elastic foundation

$$\overline{\omega}_{mn} = a \cdot \sqrt[4]{\frac{\rho h \omega_{mn}^2}{D_{22}(1-\nu_{12}\nu_{21})}} \tag{4.53}$$

Natural frequency of orthotropic plate with Winkler-Pasternak elastic foundation

$$\overline{\omega}_{mn} = a \cdot \sqrt[4]{\frac{\rho h \omega_{mn}^2}{D_{11}}} \tag{4.54}$$

The dimensionless elastic constants of foundations may also be defined as follows[203],[204]

$$\overline{K}_w = \frac{k_w a^4}{D_{11}}, \overline{K}_p = \frac{k_{px} a^2}{D_{11}} = \frac{k_{py} a^2}{D_{11}} \tag{4.55}$$

Table 4.1 Comparison on the frequency parameter of SSSS orthotropic plate without Winkler-Pasternak elastic foundation

Mode sequence number	Present method	Ref.[204]	Ref.[205]	Ref.[206]	Average Error(%) with Ref. [204-206]
1st	4.90236 (1,1)*	4.88896	4.902	4.9002	0.27%
2nd	7.25736 (1,2)	7.23752	7.253	7.2562	0.27%
3rd	8.38189 (2,1)	8.35899	8.34	8.3823	0.27%
4th	9.80473 (2,2)	9.77791	9.795	9.7997	0.27%
5th	10.10273 (1,3)	10.07513	10.079	10.1161	0.27%
6th	11.95108 (2,3)	11.91839	11.924	11.9501	0.27%

*Numbers in parentheses refer to mode type (*m*,*n*).

At first, the natural frequencies of perfect SSSS orthotropic plate without Winkler-Pasternak elastic foundation is calculated by present analysis and compared with Huang et al.[205] using the discrete method, Bahmyari et al.[206] based on element free Galerkin method, and Rahbar-Ranji et al.[204] based on Rayleigh-Ritz method, as shown in Table 4.1. For Table 4.1, the dimensions of plate are a=b=1m, h=0.01a, the material properties are taken as E_1=60.7GPa, E_2=24.8GPa, G_{12}=12GPa, v_{12}=0.23, v_{21}=0.094, ρ=1600kg/m^3. As can be seen, in this comparison study outstanding agreements are achieved and the average errors in different modes have 0.27%.

Then the comparison on the frequency parameter of SSSS orthotropic plate with Winkler-Pasternak elastic foundation solved by presented method with the results of Rahbar-Ranji et al. [204] based on Rayleigh-Ritz method is investigated, as shown in Table 4.2. In this part, dimensions of plate are a=b=1.2m, h=0.02a, the material properties are taken as E_1=185GPa, E_2=10.5GPa, G_{12}=7.3GPa, v_{12}=0.28, v_{21}=0.01589, ρ=1600kg/m^3. Again it can be concluded that the proposed method has good accuracy for different modes with or without elastic foundation. Additionally, the proposed analytical solution is quite simpler and faster than the cited references.

Table 4.2 Comparison on the frequency parameter of SSSS orthotropic plate with Winkler-Pasternak elastic foundation

Method	$\overline{K}_w$	$\overline{K}_p$	Frequency parameter					
			1st	2nd	3rd	4th	5th	6th
Present	0	100	6.76565 (1,1)*	8.4894 (1,2)	9.00394 (2,1)	9.95903 (2,2)	10.14206 (1,3)	11.15779 (2,3)
Ref.[204]			6.76565	8.48948	9.00394	9.95903	10.14210	11.15780
Present	100	0	3.85714 (1,1)	4.35429 (1,2)	5.33623 (1,3)	6.45643 (2,1)	6.60842 (1,4)	6.72178 (2,2)
Ref.[204]			3.85714	4.35429	5.33624	6.45643	6.60842	6.72178

Present	100	100	6.84497 (1,1)	8.53005 (1,2)	9.03799 (2,1)	9.98424 (2,2)	10.16594 (1,3)	11.17574 (2,3)
Ref.[204]			6.84497	8.53005	9.03799	9.98424	10.16590	11.17570

*Numbers in parentheses refer to mode type (*m*,*n*).

Figure 4.2 and Figure 4.3 show the 3D plot of simultaneous effects of $\overline{K}_w$ and $\overline{K}_p$ on dimensionless parameter of natural frequency $\overline{\omega}_{mn}$ and static buckling load $\overline{p}_{st}$, respectively. As can be seen, with the increase of $\overline{K}_w$ and $\overline{K}_p$, the natural frequencies and static buckling load become larger. While the influence of $\overline{K}_p$ is more pronounced than $\overline{K}_w$, especially for the static buckling load.

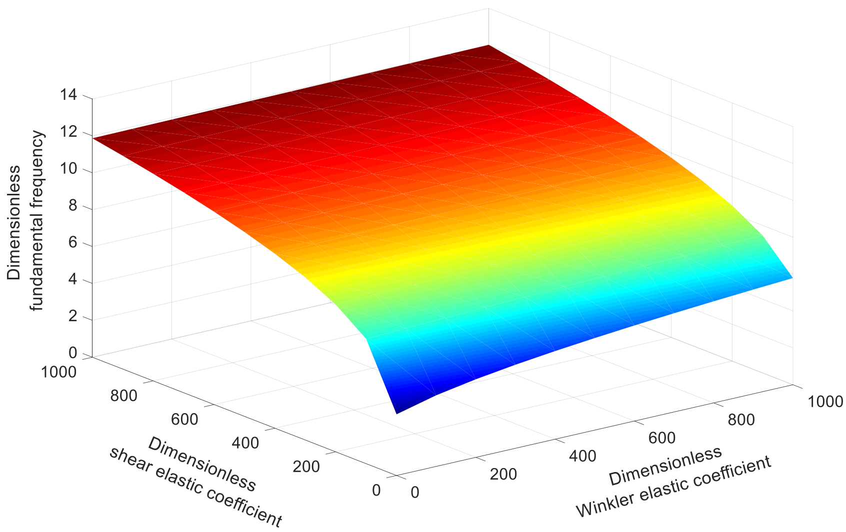

Figure 4.2 Dimensionless parameter of natural frequency $\overline{\omega}_{mn}$ of an orthotropic rectangular plate on Winkler-Pasternak elastic foundation with variable foundation parameters

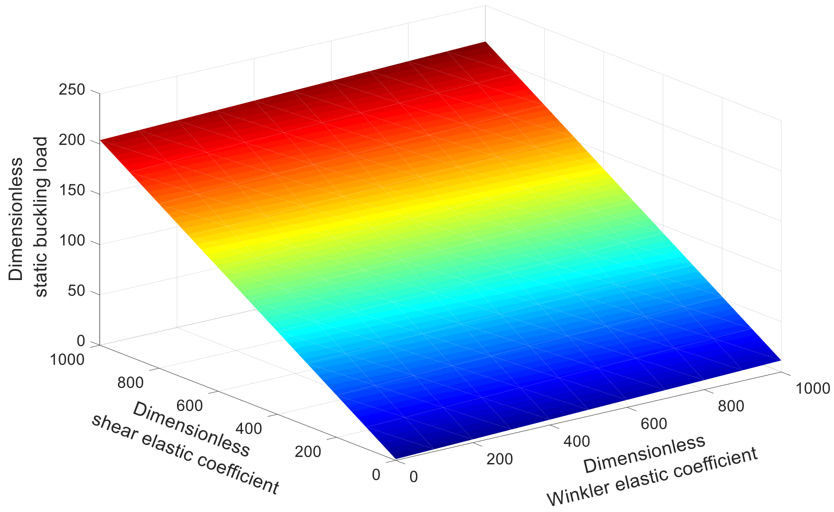

Figure 4.3 Dimensionless parameter of static buckling load $\bar{p}_{st}$ of an orthotropic rectangular plate on Winkler-Pasternak elastic foundation with variable foundation parameters

4.4.2 *Dynamic characteristics of orthotropic plate on Winkler-Pasternak elastic foundation*

4.4.2.1 *Natural frequency and linear vibration*

The results from Table 4.1 and Table 4.2 have verified the proposed methods. Additional the effects of different aspect ratios, foundation parameters and mode numbers on natural frequencies and static buckling, respectively, are shown in Table 4.3. Obviously, the increasing of *a/b* leads to the increase of natural frequencies and static buckling for the same foundation parameters, while the influence of $\bar{K}_p$ is more pronounced than $\bar{K}_w$, especially for the static buckling load. Same results are shown before. One interesting finding is that the influence of modes (*m*,*n*) does not have specific laws. The increase of m will not cause the increase of static buckling. For example, the static buckling of *m*=2,3 is smaller than *m*=1 when *a*=1,2.

Table 4.3 Dimensionless parameter of natural frequency $\overline{\omega}_{mn}$ and static buckling $\overline{p}_{st}$ load of SSSS orthotropic plate on Winkler-Pasternak elastic foundation for different aspect ratios and foundation parameters (m=1-3, n=1, h=0.02a)

a/b	$\overline{K}_w$	$\overline{K}_p$	$\overline{\omega}_{mn}$			$\overline{p}_{st}$		
			m=1	m=2	m=3	m=1	m=2	m=3
0.5	0	0	3.1807	6.3020	9.4372	1.0508	4.0481	9.0476
	100	0	3.7716	6.3996	9.4668	2.0774	4.3048	9.1617
	0	100	6.0458	8.7162	11.4289	13.7159	14.8135	19.4612
	100	100	6.1559	8.7538	11.4456	14.7425	15.0701	19.5753
1	0	0	3.3190	6.3615	9.4755	1.2457	4.2031	9.1952
	100	0	3.8571	6.4564	9.5047	2.2723	4.4598	9.3093
	0	100	6.7656	9.0039	11.5718	21.5099	16.8683	20.4531
	100	100	6.8450	9.0380	11.5879	22.5365	17.1249	20.5672
2	0	0	4.0135	6.6379	9.6414	2.6638	4.9827	9.8566
	100	0	4.3543	6.7218	9.6692	3.6904	5.2393	9.9706
	0	100	8.4895	9.9590	12.1050	53.3244	25.2469	24.4918
	100	100	8.5301	9.9842	12.1191	54.3510	25.5036	24.6059

4.4.2.2 ***Frequency-amplitude curve***

In a damped nonlinear forced or nonlinear free vibration system, the Frequency-Amplitude (F-A) curve is of important impacts to study the oscillation laws of the system. Normally, the graph of A versus F called a 'backbone curve' because of its shape. In this subsection, the FA curve of an SSSS orthotropic plate resting on the elastic foundation subjected to out-plane UDL including damping effects is investigated. The dimensions of plate are a=b=25.4cm, h=0.005a, the material properties are taken as E_1=275.79GPa,

E_2=27.579GPa, G_{12}=10.756GPa, v_{12}=0.25, v_{21}=0.025, ρ=1619kg/m^3. The coefficients of Winkler-Pasternak elastic foundation are k_w =5×10^{5}N/m^2, k_{px} = k_{py}=2.5×10^{4}N/m.

Substituting Eq.(4.49) into Eq.(4.39), the nonlinear free vibration frequency can be obtained

$$\omega^2 - \frac{4}{\pi}\omega_{mn}\zeta \cdot \omega = c_1 - c_2 + \frac{3}{4}c_3 A^2 - \frac{Q}{\rho A} \tag{4.56}$$

where ζ denotes the damping ratio of the plate.

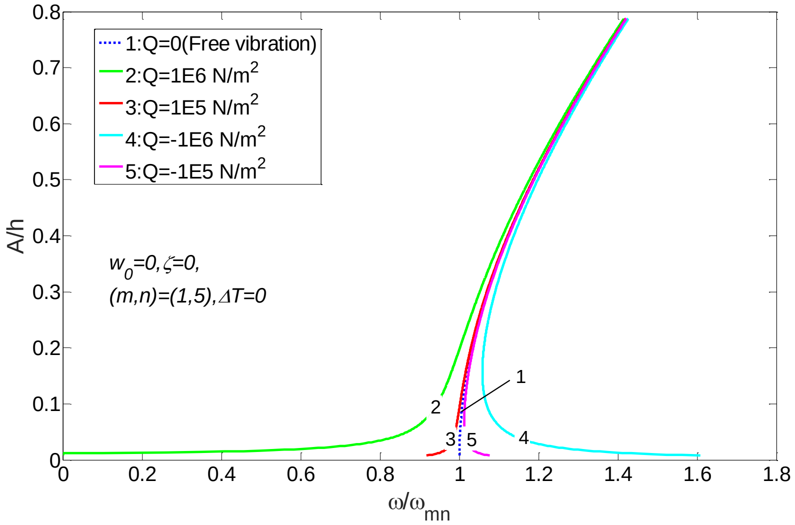

Figure 4.4 The frequency-amplitude curve of the nonlinear vibration of a SSSS orthotropic plate resting on the elastic foundation subjected to different external UDL

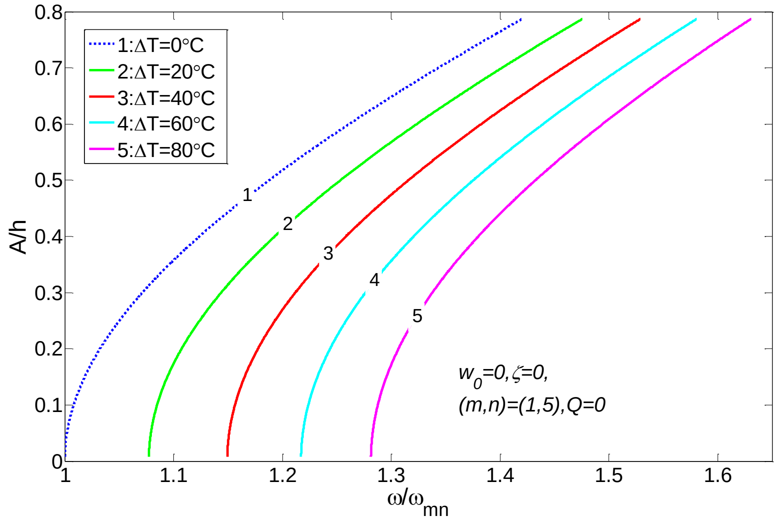

Figure 4.5 The frequency-amplitude curve of the nonlinear vibration of a SSSS orthotropic plate resting on the elastic foundation subjected to different temperature changes

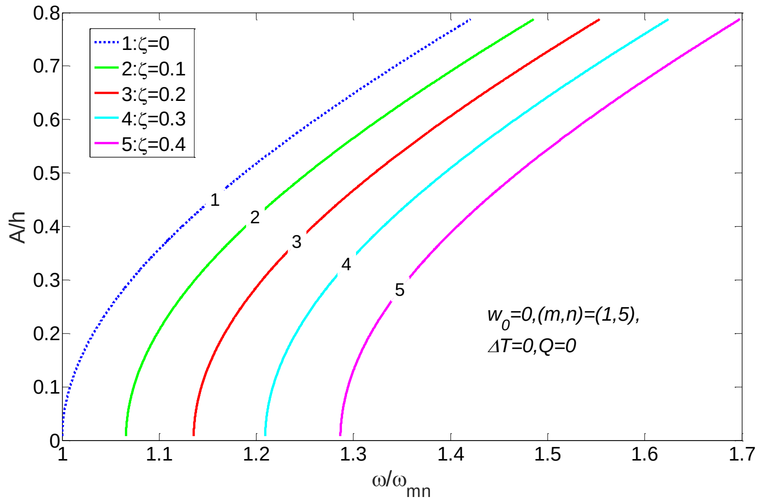

Figure 4.6 The frequency-amplitude curve of the nonlinear vibration of an SSSS orthotropic plate resting on the elastic foundation subjected to different damping ratios

Figure 4.4 shows the effects of different external UDL *Q* on the FA curves of an SSSS orthotropic plate resting on the elastic foundation while holding other parameters constant. *Q*=0 is the nonlinear free vibration of the plate. As can be seen, for the relatively small magnitude of Q, the FA curve follows the one of nonlinear free vibration. Positive means the force is upward, and vice versa. The FA curves of the nonlinear free vibration of an SSSS orthotropic plate resting on the elastic foundation subjected to different temperature changes are illustrated in

Figure 4.5. Five thermal changes are considered, which are 0°C, 20°C, 40°C, 60°C, 80°C. For the same amplitude, the frequencies ratios increase with an increase of temperature changes. And for each single FA curve, the amplitudes increase monotonically with an increase of frequencies ratios for all five cases.

Figure 4.6 investigates the effect of varying damping ratios f a SSSS orthotropic plate resting on the elastic foundation while holding other parameters constant. As can be seen, for the same amplitude, the increase of damping ratios leads to the increase of frequency ratios; for the same frequency, damping ratios increase, while the amplitude decreases. Also for each single FA curve, the amplitudes increase monotonically with an increase of frequencies ratios for all five cases. The effects of the two parameters of Winkler-Pasternak elastic foundation on FA curves are presented in

Figure 4.7. For the same amplitude, the increase of both k_w and k_p will cause the decrease of frequency ratios; while the influence of k_p is more pronounced than k_w.

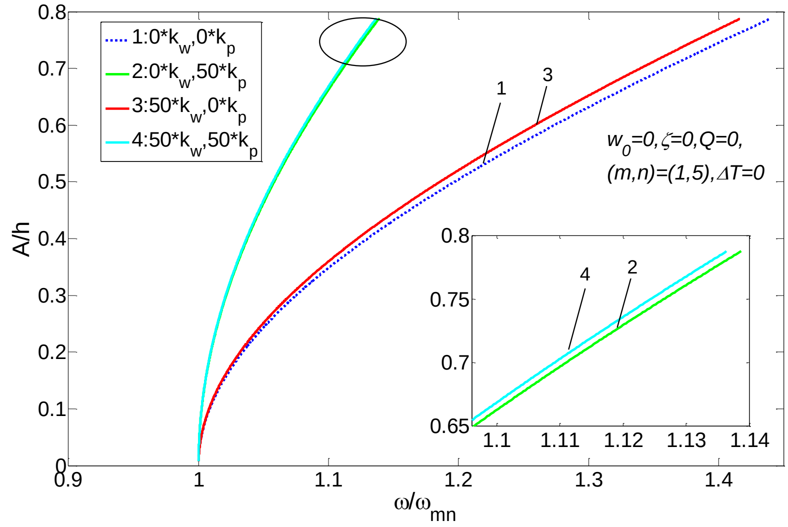

Figure 4.7 The frequency-amplitude curve of the nonlinear vibration of a SSSS orthotropic plate resting on the elastic foundation subjected to different foundation parameters

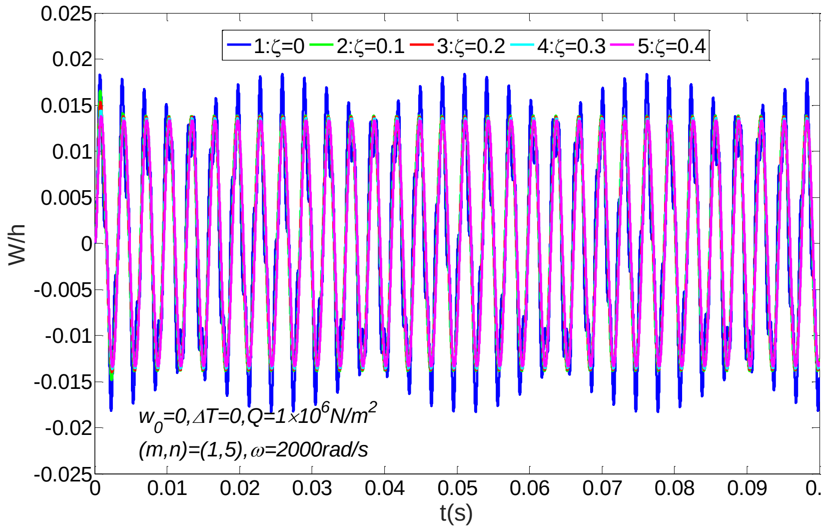

Figure 4.8 The nonlinear dynamic responses of a SSSS orthotropic plate resting on the elastic foundation subjected to different damping ratios

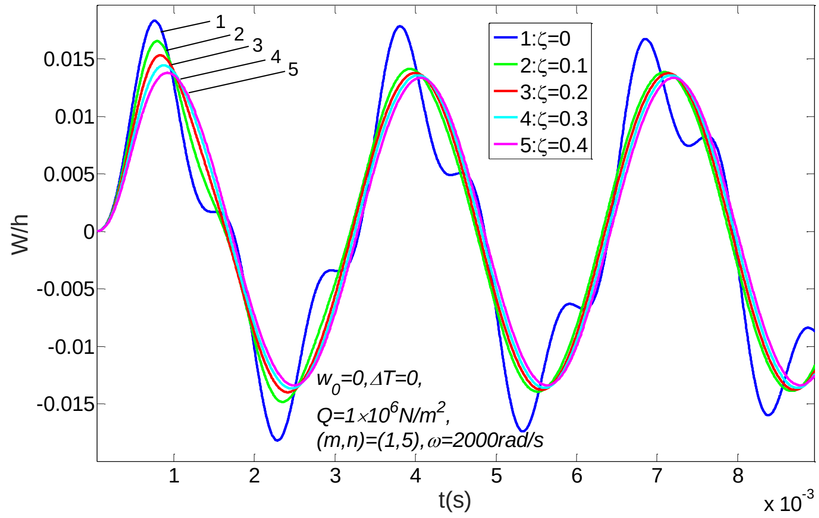

Figure 4.9 The zoom in of the first period of Figure 4.8

4.4.2.3 *Nonlinear dynamic responses*

In order to study the nonlinear dynamic responses of an orthotropic plate on Winkler-Pasternak elastic foundation in a thermal environment subjected to out-plane UDL, Eq.(38) is solved based on fourth-order Runge-Kutta method. The dimensions of the plate and the material properties are the same as last subsection, while the coefficients of Winkler-Pasternak elastic foundation are k_w =1×10^{5}N/m^2, k_{px} = k_{py}=1×10^{3}N/m and the initial imperfection is 0.

Figure 4.8 and Figure 4.9 show the nonlinear dynamic responses of a SSSS orthotropic plate resting on the elastic foundation subjected to different damping ratios. The excited frequency ω=2000rad/s and the amplitude Q=1×10^{6}N/m^2. As can be seen from Figure 4.8, the damping effects have a significant influence on the structure, especially in the first vibration period, while after that the amplitude of plate keeps nearly the same for different damping ratios. Figure 4.9 is the zoom in of the first period of Figure 4.8.

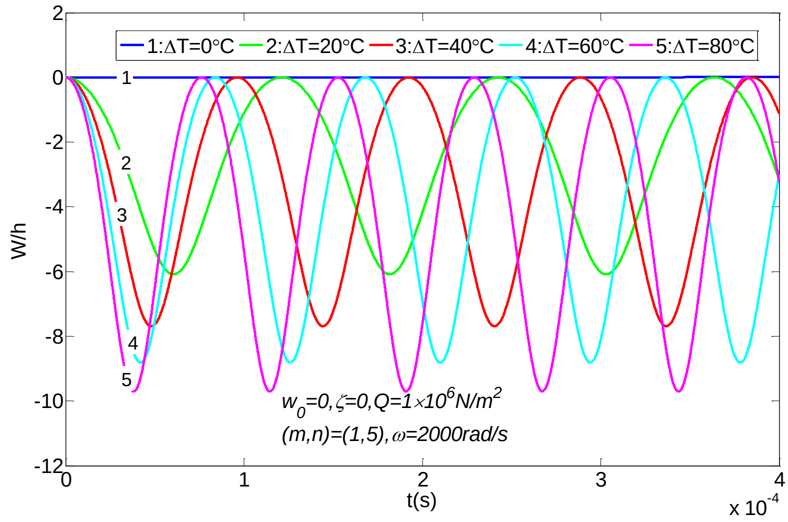

Figure 4.10 The nonlinear dynamic responses of a SSSS orthotropic plate resting on the elastic foundation subjected to different temperature changes

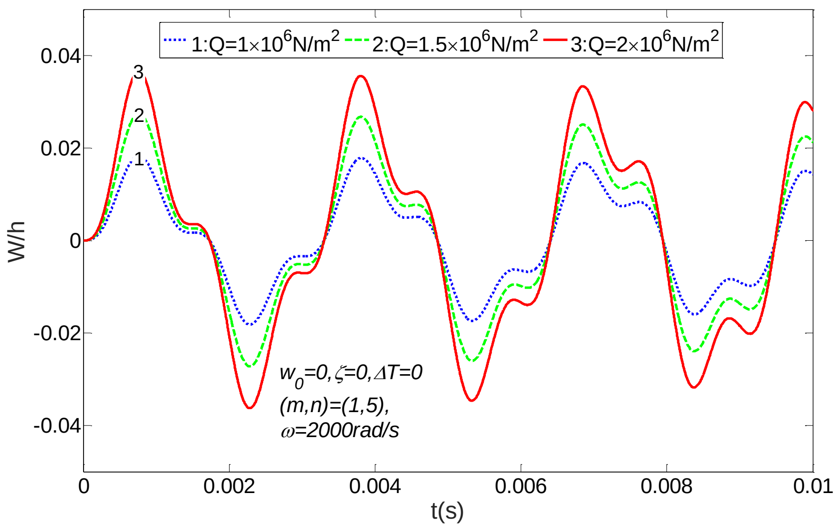

Figure 4.11 The influence of different magnitudes of the excited forces on the nonlinear dynamic responses of a SSSS orthotropic plate

The effects of different temperature changes on the nonlinear dynamic responses of a SSSS orthotropic plate resting on the elastic foundation are shown in Figure 4.10. It shows that the increase of temperature changes leads to the increase of amplitudes. This is because the temperature rise will cause the increase of axial compression stresses and further reduce the transverse stiffness of plate. Additionally, the uniform temperature changes look like the prestressing force on the plate edge, which will influence the plate vibration frequencies, amplitudes, and undermine the critical buckling load. The same results have been witnessed by Li et al. [207] and Bich et al.[208, 209]. When ΔT=0, the amplitudes of the plate is almost the same and keep a line near 0; then when temperature rise, the plate bend to the downward direction. Before applying the UDL, the plate is in a uniform temperature field, which means the plate will bend under such environment and the amplitudes is negative.

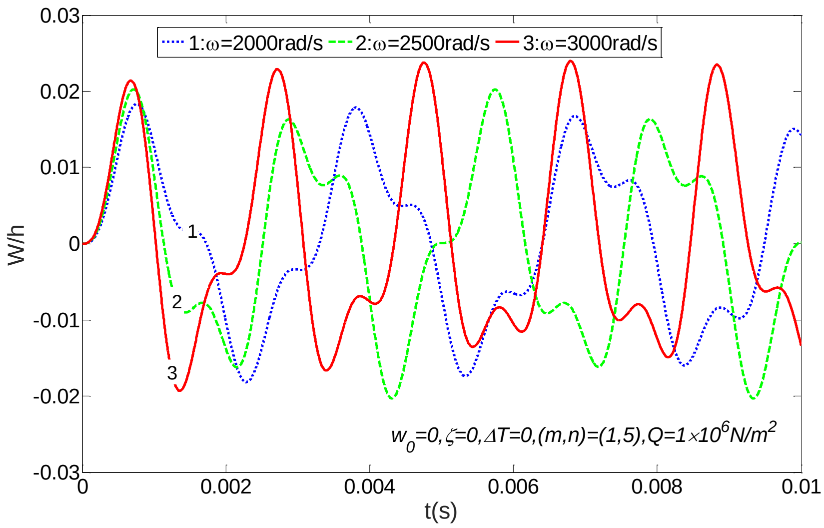

Figure 4.12 The influence of different frequencies of the excited forces on the nonlinear dynamic responses of a SSSS orthotropic plate

Figure 4.11 and Figure 4.12 illustrate the influence of different magnitudes and frequencies of the excited forces, respectively. As can be observed, the increase of the magnitudes of excited force will increase the amplitude of the plate, which the oscillation period remains unchanged. While when the forcing frequencies increase, both the oscillation frequencies and amplitudes increase.

Figure 4.13 depicts the nonlinear responses of the orthotropic plate resting on the elastic foundation subjected to different foundation parameters. Considering the elastic foundation, the deflection of the plate will decrease; while k_p is more sensitive than k_w for the structures. This is because the elastic foundation restricts the transverse vibration.

Figure 4.14 shows the deflection-velocity relation of a SSSS orthotropic plate resting on the elastic foundation. As can be seen that the deflection-velocity curve is closed and symmetrical with respect to amplitudes equals to 0.

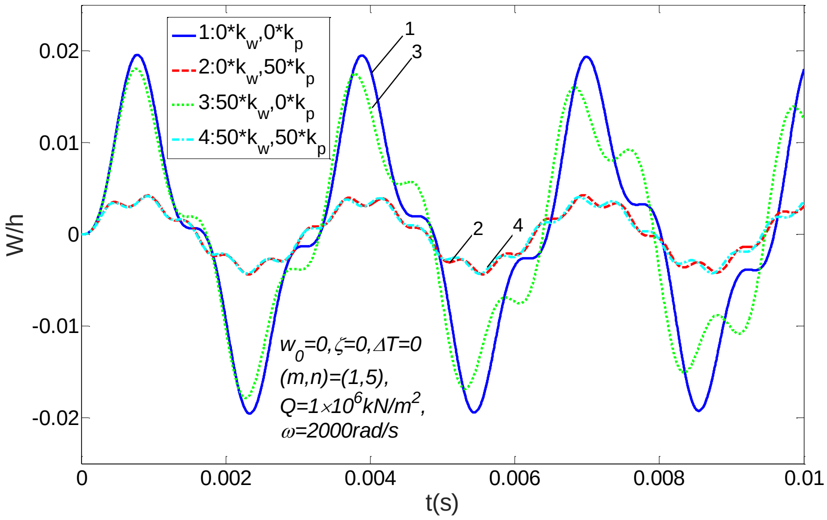

Figure 4.13 The nonlinear dynamic responses of a SSSS orthotropic plate resting on the elastic foundation subjected to different foundation parameters

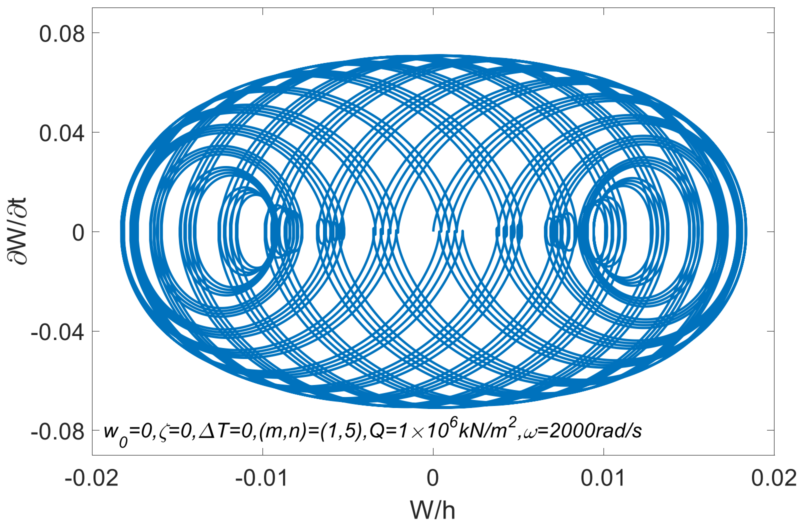

Figure 4.14 Deflection-velocity relation of a SSSS orthotropic plate resting on the elastic foundation

4.4.3 *Dynamic stability of orthotropic plate on Winkler-Pasternak elastic foundation*

To investigate the nonlinear dynamic stability of an orthotropic plate on Winkler-Pasternak elastic foundation in a thermal environment subjected to a constant compression rate, Eq.(4.50) was solved numerically based on fourth-order Runge-Kutta method. The dimensions of the plate and the material properties are the same as last subsection, while the coefficients of Winkler-Pasternak elastic foundation are k_w $=1\times10^5$N/m^2, $k_{px} = k_{py}=1\times10^3$N/m and the initial imperfection is $W_0=0.01\times h$. Three value of velocity *v:* 0.001m/s, 0.002m/s, 0.003m/s.

Figure 4.15 and Figure 4.16 show the dimensionless time-deflection curve, the dimensionless time-load curve of a SSSS orthotropic plate resting on the elastic foundation subjected to different velocities, respectively. When time multiplies velocity, the longitudinal end-shortening can be obtained. Static post-buckling solution is solved from the reduced form of Eq.(4.50), which ignore the transverse velocity and acceleration terms. As can be seen from Figure 4.15 that all the static buckling curves have two phases, which is a sudden increase of deflection from initial position and then nearly a linear increase of deflection with respect to time. Moreover, all the dynamic buckling curves have three phases, which are slow increase, rapid increase and then plate vibration. Figure 4.17 is the enlarged view of Figure 4.16. From Figure 4.16 and Figure 4.17, we can observe that all the static buckling curves have two phases, which are linear pre-buckling curves and linear post-buckling curves. Moreover, all the dynamic buckling curves have two phases, which are linear pre-buckling and then plate vibration.

From Figure 4.15, it is interesting to note that as velocity is small, the deflection of static buckling is larger than the dynamic one, while after the first inflexion the dynamic curves are oscillated about static ones when the velocity is increased. Therefore, as we mentioned before, constant velocity schemes can help us find the threshold velocity values between static and dynamic in experiments and theoretical analysis. Moreover, from Figure 4.17, critical static buckling loads are the same for different velocity and equals to 0.33. This is just we expected, and the velocity has no influence on the critical buckling load. Because the eccentricity is $0.01\times h$ in this section, p_{mn}* is not equal to 1.

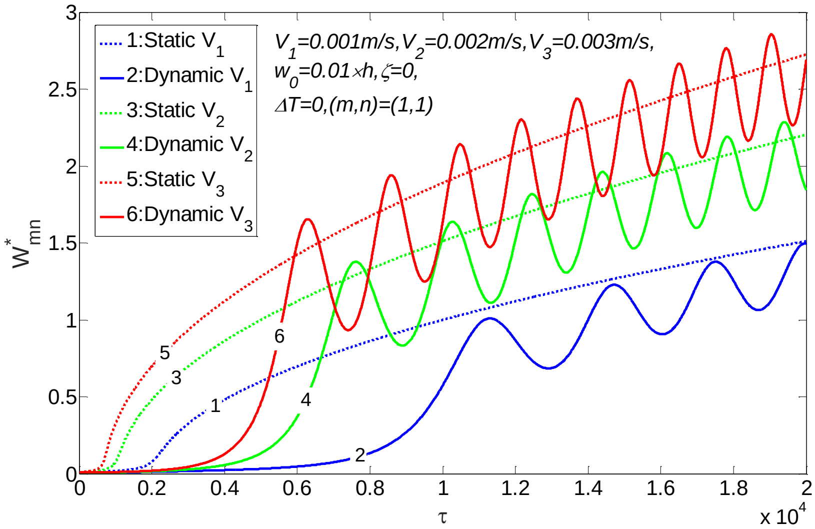

Figure 4.15 Dimensionless time-deflection curve of a SSSS orthotropic plate resting on the elastic foundation subjected to different velocities

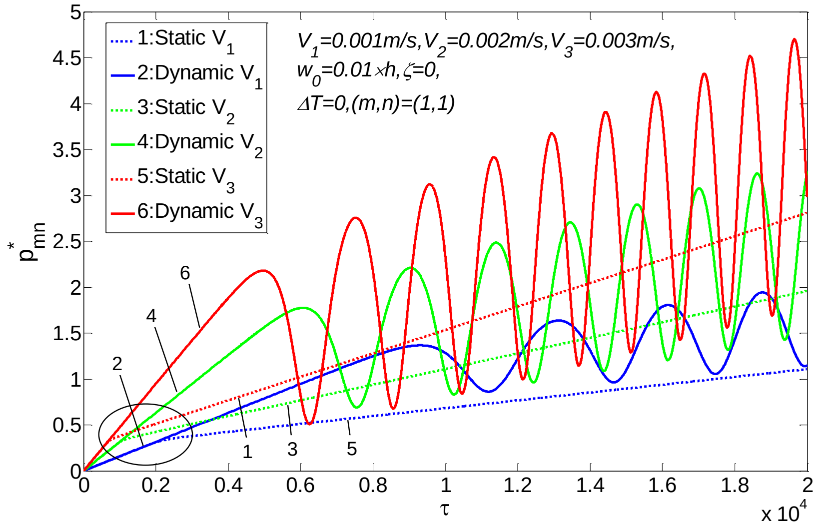

Figure 4.16 Dimensionless time-load curve of a SSSS orthotropic plate resting on the elastic foundation subjected to different velocities

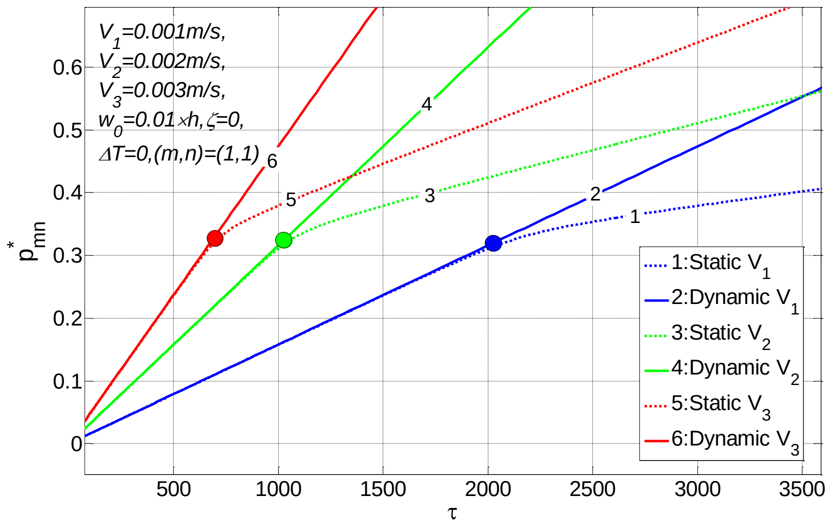

Figure 4.17 The zoom in of Figure 4.16(b)

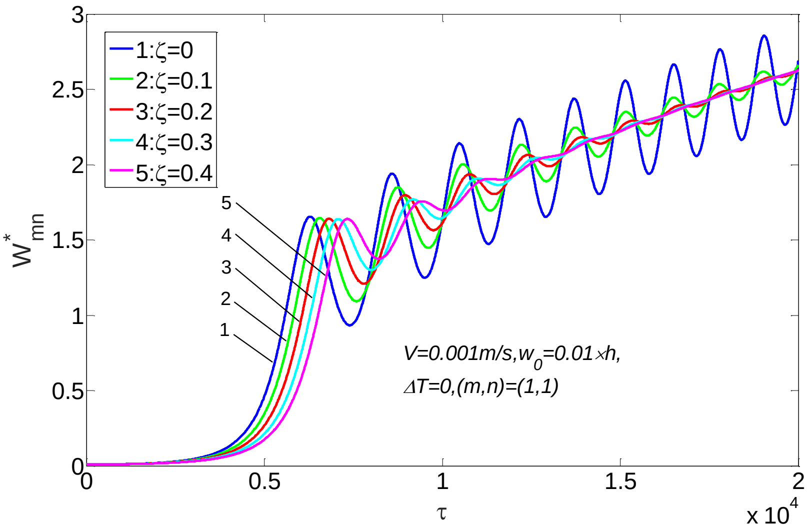

Figure 4.18 Dimensionless time-deflection curve of a SSSS orthotropic plate resting on the elastic foundation subjected to damping ratios

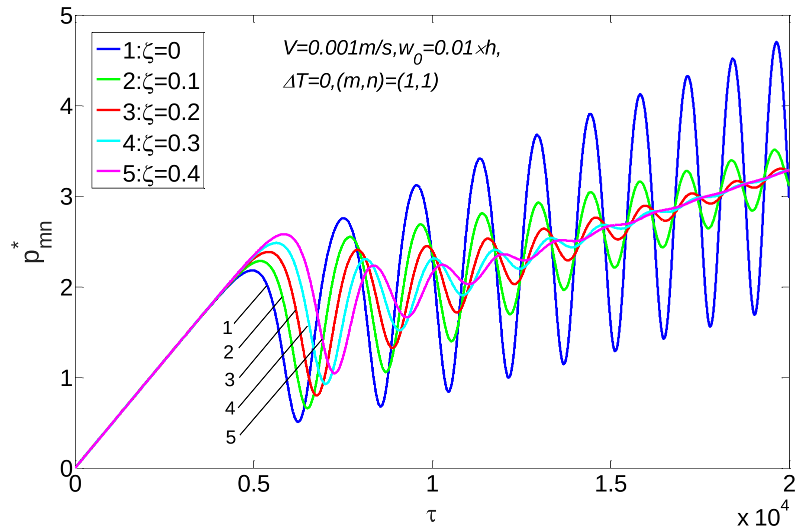

Figure 4.19 Dimensionless time-load curve of a SSSS orthotropic plate resting on the elastic foundation subjected to different damping ratios

The effect of damping ratios on nonlinear dynamic buckling of orthotropic plate is shown in Figure 4.18 and Figure 4.19. Clearly, the influence of increasing of damping ratios is not very pronounced for deflections when compared with dynamic buckling load. While the increasing damping ratios increases the dynamic buckling load and eliminates the oscillations in the third phases. This is because damping depletes the strain energy which stored in the first two phases. The larger that damping ratios are, the more the depletion.

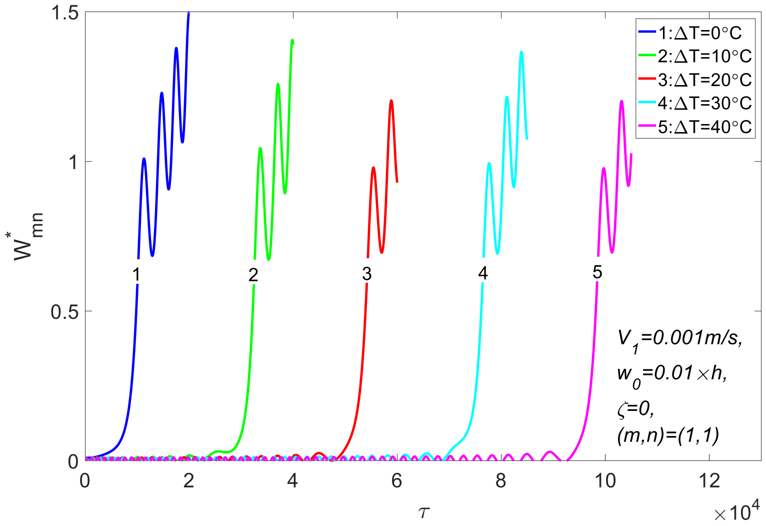

Figure 4.20 Dimensionless time-deflection curve of a SSSS orthotropic plate resting on the elastic foundation subjected to different temperature changes

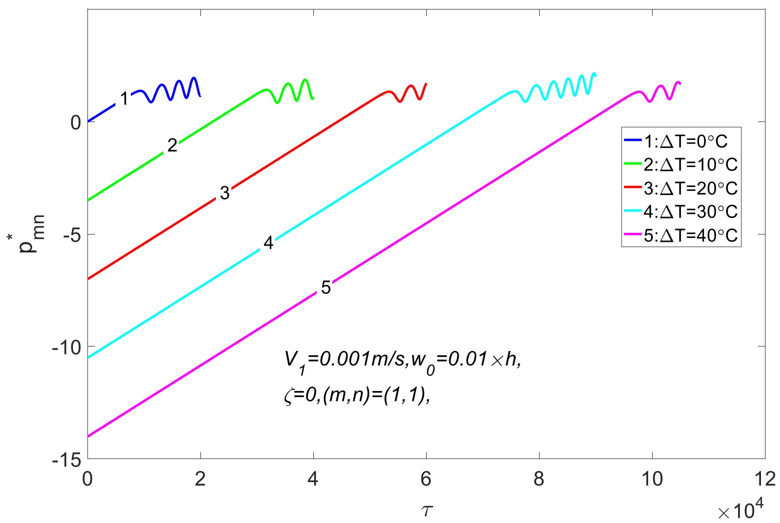

Figure 4.21 Dimensionless time-load curve of a SSSS orthotropic plate resting on the elastic foundation subjected to different temperature changes

Figure 4.20 and Figure 4.21 show the influence of temperature changes on nonlinear dynamic buckling of orthotropic plate resting on the elastic foundation. It shows that the increase of temperature changes will delay the buckling time. If observing the two figures carefully, one can find that the increase of temperature changes also decreases the buckling load and increase the deflection of the plate. The same results also concluded in the last subsection.

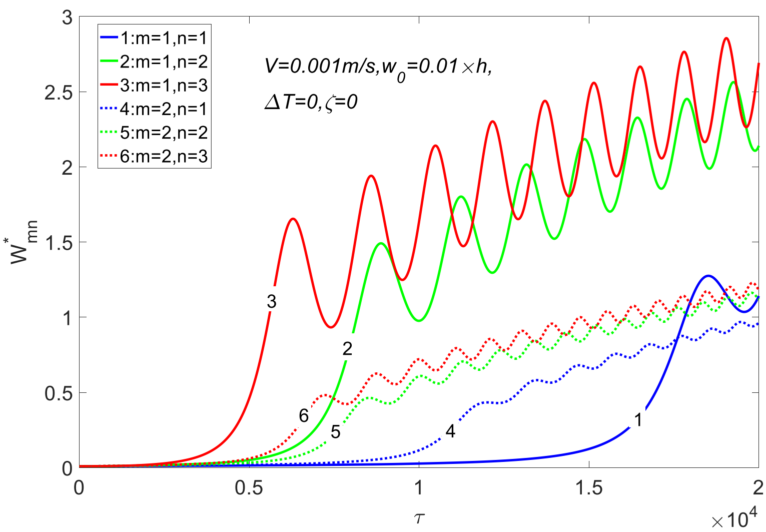

Figure 4.22 Dimensionless time-deflection curve of a SSSS orthotropic plate resting on the elastic foundation for different buckling modes

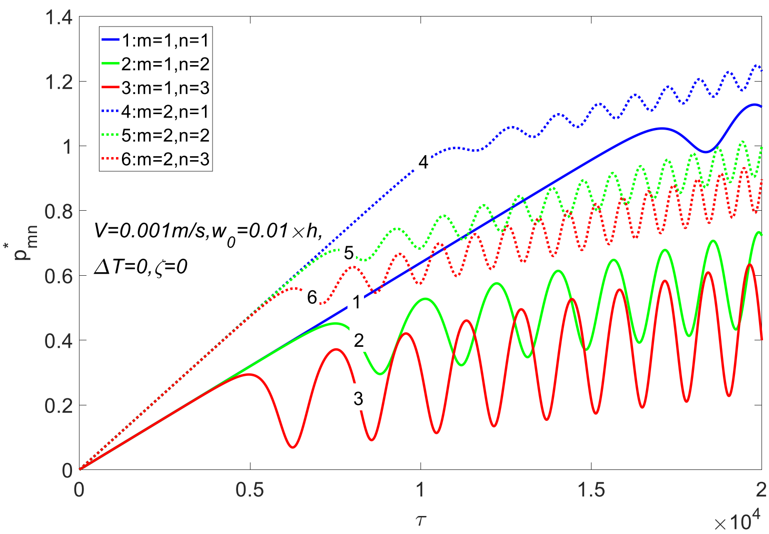

Figure 4.23 Dimensionless time-load curve of a SSSS orthotropic plate resting on the elastic foundation for different buckling modes

Figure 4.22 and Figure 4.23 show the buckling modes on nonlinear dynamic buckling of orthotropic plate resting on the elastic foundation. It is found that the increase of *n* (the half-wave along *y*-axis) will decrease the critical buckling load and enlarge the oscillation; while m (the half-wave along *x*-axis) increase, the critical load maybe increases or decrease. However, the oscillation will be weakened due to the increase of *m*.

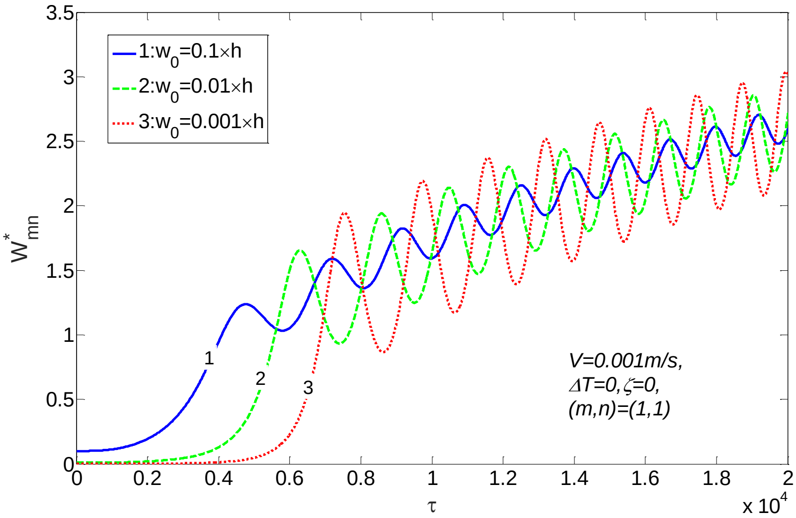

Figure 4.24 Dimensionless time-deflection curve of a SSSS orthotropic plate resting on the elastic foundation for different initial imperfections

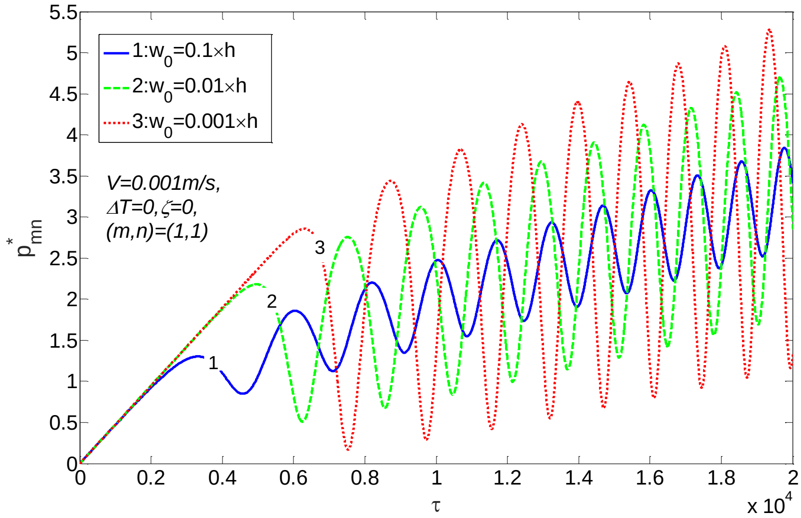

Figure 4.25 Dimensionless time-load curve of a SSSS orthotropic plate resting on the elastic foundation for different initial imperfections

In Figure 4.24 and Figure 4.25, the effects of different initial imperfections on nonlinear dynamic buckling of orthotropic plate resting on the elastic foundation. Three values are chosen, i.e.$W_0 = 0.1\times h,\ 0.01\times h,\ 0.001\times h$. As shown, initial imperfections greatly influence the dynamic buckling load and oscillation of third phases. When initial imperfections increase, both the critical buckling load and oscillation of third phases decrease.

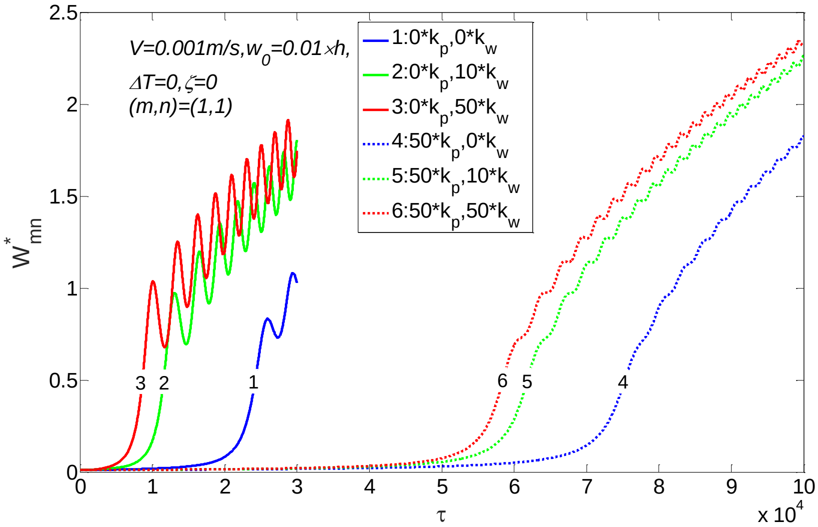

Figure 4.26 Dimensionless time-deflection curve of a SSSS orthotropic plate resting on the elastic foundation for different foundation parameters

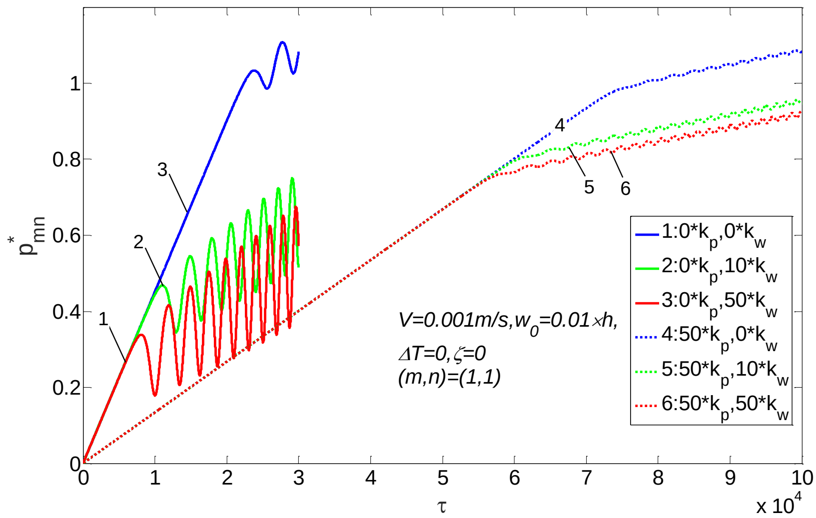

Figure 4.27 Dimensionless time-load curve of a SSSS orthotropic plate resting on the elastic foundation for different foundation parameters

The influence of different elastic foundation parameters on nonlinear dynamic buckling of orthotropic plate is also illustrated in Figure 4.26 and Figure 4.27. It is obvious that the increase of k_w would reduce the onset of buckling amplitudes and decrease dynamic buckling load while holding all other things fixed. An interesting finding is that when k_p reaches 50*k_p, there is an absence of dynamic buckling point or even a clearly inflexion according to Budiansky-Roth criterion[2, 6, 202]. This is due to the increase of k_p restrict the transverse deflection of the plate and further mitigate dynamic buckling load.

From the figures, although there is no clearly buckling point, there is a clear turning between second phase and the third phase for W_{mn}^{*}-τ and between the first phase and second phase for p_{mn}-τ. Some of the researchers give the explanation according to this phenomenon. Bich et al. [210] took the intermediate value of the turning satisfying the condition $\frac{d^2W_{mn}}{d\tau^2} = 0$ when $\tau=\tau_{cr}$ .Huang et al. [102] selected the first inflexion on the response curve which also needs to satisfy $\frac{d^2W_{mn}}{d\tau^2} = 0$. Based on authors' knowledge, giving $\frac{d^2W_{mn}}{d\tau^2} = 0$ as the buckling points cannot accurately predicts the exact dynamic buckling of orthotropic plate on the elastic foundation. This is because the slight disturbance or inflexion is just the release of strain energy, and both W_{mn}^{*}, τ and p_{mn} change very small. Actually, as we all known, the load-capability is larger for an orthotropic plate, moreover, the plate on an elastic foundation which restrict its transverse movement. Therefore, the author thinks that the B-R criterion is unsuitable for the plate on elastic foundation when foundation parameters become larger.

4.5 Conclusion

The chapter develops the nonlinear dynamic characteristics and stability of composite orthotropic plate on Winkler-Pasternak elastic foundation subjected to different axial velocities with damping and thermal effects for the first time. The Galerkin method and Airy's stress function were used to obtain the nonlinear differential equations. By using fourth-order Runge-Kutta method and B-R criterion, the characteristics of natural frequency, linear and nonlinear vibration, frequency-amplitude curve and nonlinear dynamic responses were investigated; then various effects of constant velocity, damping ratio, temperature change, buckling mode, initial imperfection, elastic foundation parameter on nonlinear dynamic buckling of the plate were also discussed and the following remarks can be concluded:

1. The formulation for dynamic responses is converted into an ordinary differential equation with consideration of out-plate UDL, in-plate axial velocity, damping effects, thermal effects and elastic foundation. The accuracy of the obtained results of frequency parameters is verified against the published paper by other methods and shows that the proposed method has good accuracy. Moreover, the proposed method can be applied to micro- and nanostructures.
2. For the time-deflection relation, static buckling curves have two phases, which are a sudden increase of deflection from initial position and then nearly a linear increase of deflection with respect to time. The dynamic buckling curves have three phases, which are slow increase, rapid increase of deflection with respect to time and then plate oscillation; while for the time-load relation, static buckling curves have two phases, which are linear pre-buckling curves and

linear post-buckling curves, the dynamic buckling curves have two phases, which are linear pre-buckling and then plate oscillation.

3. When considering dynamic terms, the dynamic buckling loads are larger than the static ones. However, the mid-plane deflections of dynamic are smaller than static ones. The threshold velocity values between static and dynamic can be solved, which are the key concerns in experiments and theoretical analysis.
4. For the out-plate vibration due to UDL, the damping effects have a significant influence on the structure, especially in the first vibration period, while after that the amplitude of plate keeps nearly the same for different damping ratios. And the velocity impulse dynamic stability analysis shows that the increase of damping ratios increases the dynamic buckling load and eliminates the oscillations in the third phases.
5. Temperature rise will cause the increase of axial compression stresses and further reduce the transverse stiffness of plate. Additionally, the uniform temperature changes look like the prestressing force on the plate edge, which will influence the plate vibration frequencies, amplitudes, and undermine the critical buckling load.
6. The two parameters of Winkler-Pasternak elastic foundation have a significant influence on structural dynamic responses. Considering the elastic foundation, the deflection of the plate will decrease; while Pasternak parameter is more sensitive than Winkler one for the structures. Also the increase of foundation parameters would reduce the onset of buckling amplitudes and decrease dynamic buckling load. The author thought that the B-R criterion is unsuitable for the plate on elastic foundation when foundation parameters become larger.

Chapter 5 Nonlinear primary resonance of functionally graded porous cylindrical shells using the method of multiple scales

5.1 Introduction

As one of the most promising materials in lightweight structures, the mechanics and mechanism of FG porous structures have been investigated extensively in recent years. Additionally, the understanding of free vibration and nonlinear vibration analysis is crucial to FG porous cylindrical shells. However, no previous work has been done for FG porous cylindrical shells with external harmonic excitation, especially for the resonant characteristics with different internal porosity distributions. Thus, it is of great importance to analyse the forced vibration behaviour of FG porous cylindrical shell due to the time-dependent external forces and the proper understanding and development of primary resonance of FG porous cylindrical shell can help engineers avoid the peak resonances of the structural system in the design process.

The purpose of this chapter is to study the nonlinear forced vibration characteristics of the cylindrical shell made of functionally graded porous materials subjected to a uniformly distributed harmonic loading. The nonlinear compatibility equation is derived by using the Donnell shell theory with the consideration of von-Kármán strain-displacement relation and damping effect. With an acceptable accuracy, neglecting the inertia and rotary inertia terms, the single-mode approximation of deflection was assumed, which satisfies the boundary conditions[54, 211, 212]. Then the Galerkin method in conjunction with the method of multiple scales is used to obtain a second-order nonlinear ordinary equation with the cubic nonlinear term, named Duffing-type equation. Based on this equation, the frequency-response analysis is investigated for three types of FG porous cylindrical shells, that are symmetric porosity distribution, non-symmetric porosity stiff or soft distribution, and uniform porosity distribution. The influences of porosity distribution, porosity coefficient, damping ratio, amplitude and frequency of the external harmonic excitation, aspect ratio and thickness ratio on the nonlinear dynamic behaviour are discussed in detail.

5.2 Material gradient of an FG porous cylindrical shell

In this chapter, three types of FG porous distributions, namely Type 1(symmetric porosity distribution) [142-149], Type 2 (non-symmetric porosity distribution) [76, 152-154, 173] and Type 3 (uniform porosity distribution) are considered in cylindrical shells, as shown in Figure 5.1. The elastic modulus and mass density of porous materials vary through the thickness direction based on the assumption of a typical mechanical feature of the open-cell metal foam. The variation of Young's modulus $E(z)$, shear modulus $G(z)$ and density $\rho(z)$ through the thickness direction of the cylindrical shell is described by Eqs.(5.1)-(5.4).

A novel non-symmetric porosity soft distribution is also proposed and Young's module E, shear modulus G and density ρ of this type of distribution gradually become small from inside diameter to outside diameter, as shown in Figure 5.1(c). Though non-symmetric porosity soft distribution is different from that of stiff type, both of them occupy similar free vibration and forced vibration behaviour due to the same stiffness and mass. Thus, for the convenience, in this chapter, both non-symmetric porosity stiff distribution and soft distribution are called Type 2.

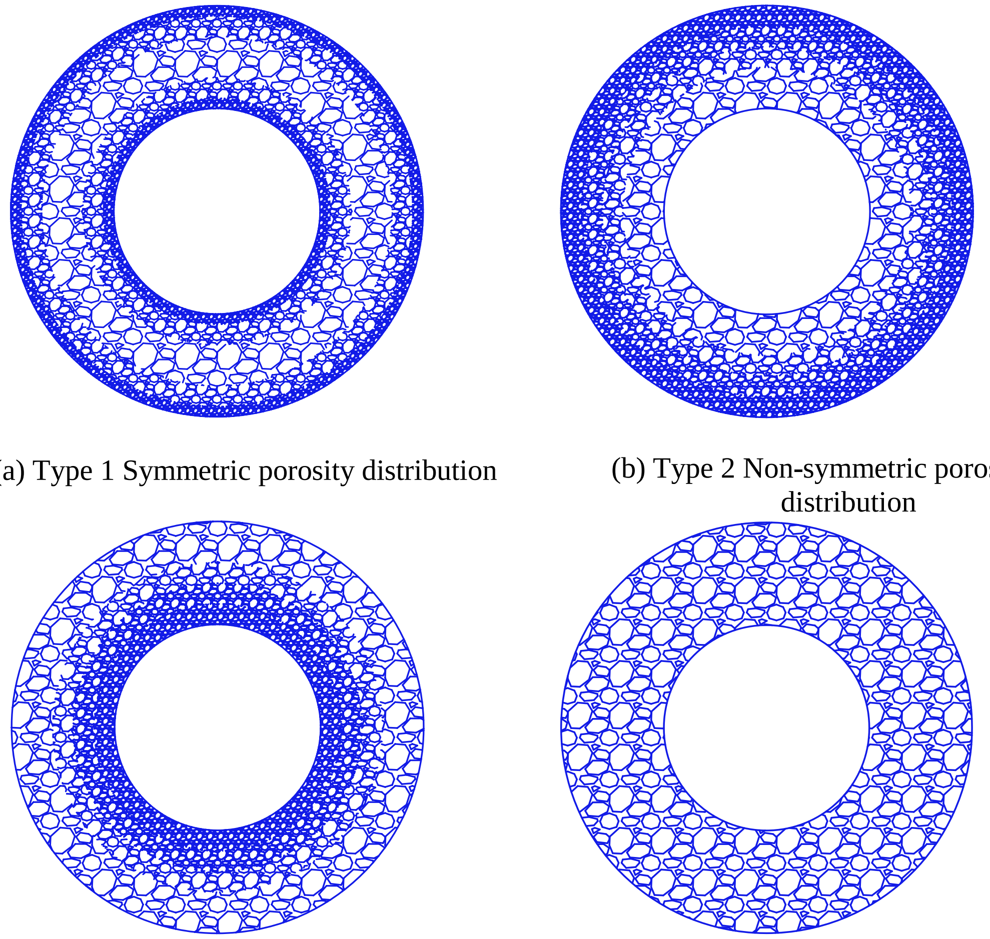

(a) Type 1 Symmetric porosity distribution

(b) Type 2 Non-symmetric porosity stiff distribution

(c) Type 2 Non-symmetric porosity soft distribution

(d) Type 3 Uniform porosity distribution

Figure 5.1 Cross-section of an FG porous cylindrical shell with different porosity distributions

Type1: symmetric porosity distribution

$$
\begin{aligned}
E(z) &= E_{\max}\left[1-N_0\cos\left(\frac{\pi z}{h}\right)\right]\\
G(z) &= G_{\max}\left[1-N_0\cos\left(\frac{\pi z}{h}\right)\right]\\
\rho(z) &= \rho_{\max}\left[1-N_m\cos\left(\frac{\pi z}{h}\right)\right]
\end{aligned} \tag{5.1}
$$

Type2: non-symmetric porosity stiff distribution

$$
\begin{aligned}
E(z) &= E_{\max}\left[1-N_0\cos\left(\frac{\pi z}{2h}+\frac{\pi}{4}\right)\right]\\
G(z) &= G_{\max}\left[1-N_0\cos\left(\frac{\pi z}{2h}+\frac{\pi}{4}\right)\right]\\
\rho(z) &= \rho_{\max}\left[1-N_m\cos\left(\frac{\pi z}{2h}+\frac{\pi}{4}\right)\right]
\end{aligned} \tag{5.2}
$$

Or non-symmetric porosity soft distribution

$$
\begin{aligned}
E(z) &= E_{\max}\left[1-N_0\sin\left(\frac{\pi z}{2h}+\frac{\pi}{4}\right)\right]\\
G(z) &= G_{\max}\left[1-N_0\sin\left(\frac{\pi z}{2h}+\frac{\pi}{4}\right)\right]\\
\rho(z) &= \rho_{\max}\left[1-N_m\sin\left(\frac{\pi z}{2h}+\frac{\pi}{4}\right)\right]
\end{aligned} \tag{5.3}
$$

Type3: uniform porosity distribution

$$
\begin{aligned}
E(z) &= E_{\max}\left(1-N_0\lambda\right)\\
G(z) &= G_{\max}\left(1-N_0\lambda\right)\\
\rho(z) &= \rho_{\max}\left(1-N_m^*\lambda\right)
\end{aligned} \tag{5.4}
$$

where h is the thickness of the shell and varies from $-h/2$ to $h/2$. z is the coordinate in the thickness direction. N_0 is the coefficient of cylindrical shell porosity $0<N_0<1$ and can be obtained by $N_0=1-E_{min}/E_{max}=1-G_{min}/G_{max}$. The porosity coefficient of mass density is defined as $N_m=1-\rho_{min}/\rho_{max}$. E_{min}, G_{min} and ρ_{min} are the minimum values of Young's modulus, shear modulus and mass density in the thickness direction of the cylindrical shell, while E_{max}, G_{max} and ρ_{max} are the corresponding maximum values, respectively. Also $G(z)=E(z)/[2(1+v)]$ from the relationship between Young's modulus and shear modulus. In this chapter, we assume that Poisson's ratio v of the shell is considered to be constant because the effect of Poisson's ratio on the deformation is much less than other material properties[213]. The variations of Young's modulus through the dimensionless thickness z/h for different types of porosity distributions are shown in Figure 5.2.

The relation between Young's modulus and mass density of metal foam materials was presented by Gibson and Ashby [214] in the following form

$$\frac{E_{\min}}{E_{\max}}=\left(\frac{\rho_{\min}}{\rho_{\max}}\right)^2 \tag{5.5}$$

Following this equation, one can obtain the expression between N_m and N_0

$$N_m=1-\sqrt{1-N_0} \tag{5.6}$$

Since the total masses M of the cylindrical shell with different porosity distributions are the same, then the porosity coefficient of mass density N_m^* in Eq.(5.4) for uniform porosity distribution can be derived from Eq.(5.6) as follows

$$N_m^* = \frac{1-\sqrt{1-N_0\lambda}}{\lambda}; \lambda = \frac{2N_m}{\pi N_m^*} \tag{5.7}$$

Furthermore, the λ in Eq.(5.4) for uniform porosity can be rewritten as

$$\lambda = \frac{1}{N_0} - \frac{1}{N_0}\left(1-\frac{2N_m}{\pi}\right)^2 \tag{5.8}$$

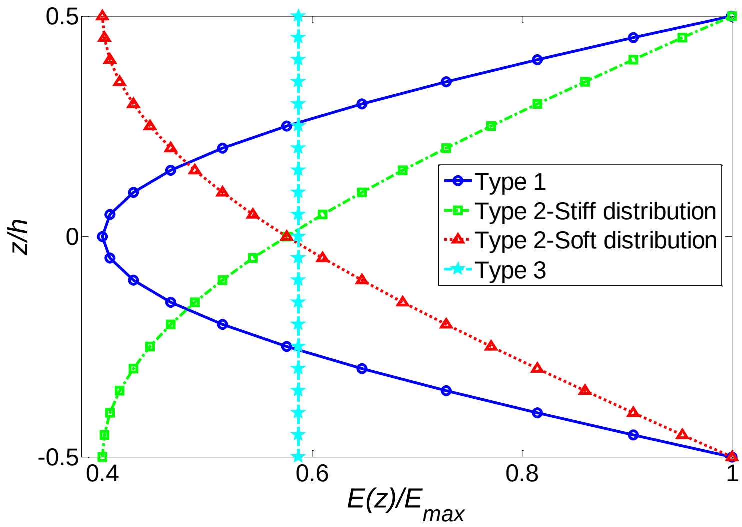

Figure 5.2 Variation of Young's modulus through the dimensionless thickness *z/h* for different types of porosity distributions

5.3 Theory and formulation

Consider a functionally graded porous cylindrical shell with length *L*, mean radius *R* and thickness *h*, as shown in Figure 5.3. The Cartesian coordinate system (*x*,*y*,*z*) is established, in which point *O* is located on the middle plane and at the left side of the cylindrical shell. *z* is the thickness direction. Also, the cylindrical shell is subjected to a uniformly distributed harmonic loading *q*(*t*) at both upper side and bottom side of the cylindrical shell along the *z* direction.

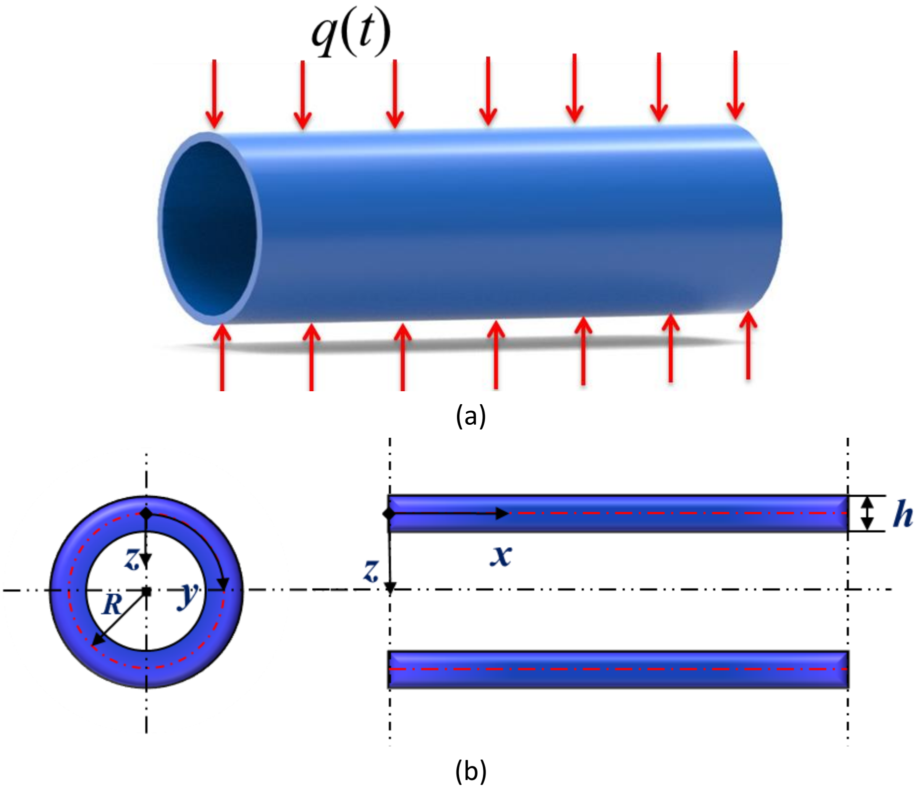

Figure 5.3 Geometry and the coordinate system of the FG porous cylindrical shell subjected to a uniformly distributed harmonic loading $q(t)$

Based on the classical shell theory, the von-Kármán nonlinear strain-displacement relation on the middle plane of FG porous cylindrical shell can be written as

$$
\begin{aligned}
\varepsilon_x^0 &= \frac{\partial u}{\partial x} + \frac{1}{2}\left(\frac{\partial w}{\partial x}\right)^2 \\
\varepsilon_y^0 &= \frac{\partial v}{\partial y} - \frac{w}{R} + \frac{1}{2}\left(\frac{\partial w}{\partial y}\right)^2 \\
\gamma_{xy}^0 &= \frac{\partial u}{\partial y} + \frac{\partial v}{\partial x} + \frac{\partial w}{\partial x}\frac{\partial w}{\partial y}
\end{aligned}
\tag{5.9}
$$

where ε_x^0 and ε_y^0 are normal strains, γ_{xy}^0 is the shear strain at the middle surface of the shell. u, v, and w are the displacement components of middle surface of the cylindrical shell in x, y, and z direction, respectively.

The strain components across the shell thickness are

$$\varepsilon_x = \varepsilon_x^0 + z\kappa_x, \varepsilon_y = \varepsilon_y^0 + z\kappa_y, \gamma_{xy} = \gamma_{xy}^0 + 2z\kappa_{xy} \tag{5.10}$$

where κ_x , κ_y and κ_{xy} are the change of curvatures and twist and can be expressed as $\kappa_x = -\partial^2 w / \partial x^2$, $\kappa_y = -\partial^2 w / \partial y^2$, $\kappa_{xy} = -\partial^2 w / \partial x \partial y$, respectively.

By differentiating ε_x^0 , ε_y^0 γ_{xy}^0 from Eq.(5.9) twice with respect to *y*, *x* and *x*, *y*, respectively, one can obtain the nonlinear kinematic compatibility equilibrium as

$$\frac{\partial^2 \varepsilon_x^0}{\partial y^2} + \frac{\partial^2 \varepsilon_y^0}{\partial x^2} - \frac{\partial^2 \gamma_{xy}^0}{\partial x \partial y} = \left(\frac{\partial^2 w}{\partial x \partial y} \right)^2 - \frac{\partial^2 w}{\partial^2 y} \frac{\partial^2 w}{\partial^2 x} - \frac{1}{R} \frac{\partial^2 w}{\partial x^2} \tag{5.11}$$

According to Hooker's stress-strain relation, the constitutive equations of an FG porous cylindrical shell are as follows

$$\begin{aligned} \sigma_x &= \frac{E(z)}{1-v^2}\left(\varepsilon_x + v\varepsilon_y\right) \\ \sigma_y &= \frac{E(z)}{1-v^2}\left(\varepsilon_y + v\varepsilon_x\right) \\ \tau_{xy} &= \frac{E(z)}{2(1+v)}\gamma_{xy} \end{aligned} \tag{5.12}$$

where E and v are the moduli of elasticity and Poisson ratios.

The internal forces N_x, N_y, N_{xy} and the moment resultants M_x, M_y, M_{xy} of the cylindrical shell can be obtained by integrating the stresses through the thickness of the shell, as follows

$$\left\{\left(N_x, N_y, N_{xy}\right), \left(M_x, M_y, M_{xy}\right)\right\} = \int_{-h/2}^{h/2} \left\{\sigma_x, \sigma_y, \tau_{xy}\right\}(1, z)dz \tag{5.13}$$

Inserting Eqs.(5.9), (5.10) and (5.12) into Eq.(5.13) gives the constitutive relations in matrix form as

$$\begin{gathered}
\begin{Bmatrix} N_x \\ N_y \\ N_{xy} \end{Bmatrix} = \begin{bmatrix} A_{11} & A_{12} & 0 \\ A_{21} & A_{22} & 0 \\ 0 & 0 & A_{66} \end{bmatrix} \begin{Bmatrix} \varepsilon_x^0 \\ \varepsilon_y^0 \\ \gamma_{xy}^0 \end{Bmatrix} + \begin{bmatrix} B_{11} & B_{12} & 0 \\ B_{21} & B_{22} & 0 \\ 0 & 0 & B_{66} \end{bmatrix} \begin{Bmatrix} \kappa_x \\ \kappa_y \\ 2\kappa_{xy} \end{Bmatrix} \\
\begin{Bmatrix} M_x \\ M_y \\ M_{xy} \end{Bmatrix} = \begin{bmatrix} B_{11} & B_{12} & 0 \\ B_{21} & B_{22} & 0 \\ 0 & 0 & B_{66} \end{bmatrix} \begin{Bmatrix} \varepsilon_x^0 \\ \varepsilon_y^0 \\ \gamma_{xy}^0 \end{Bmatrix} + \begin{bmatrix} D_{11} & D_{12} & 0 \\ D_{21} & D_{22} & 0 \\ 0 & 0 & D_{66} \end{bmatrix} \begin{Bmatrix} \kappa_x \\ \kappa_y \\ 2\kappa_{xy} \end{Bmatrix}
\end{gathered} \tag{5.14}$$

Then, Eq.(5.14) can be further simplified as

$$\{N\} = \boldsymbol{A}\{\varepsilon\} + \boldsymbol{B}\{\kappa\}, \{M\} = \boldsymbol{B}\{\varepsilon\} + \boldsymbol{D}\{\kappa\} \tag{5.15}$$

where $\boldsymbol{A}$, $\boldsymbol{B}$ and $\boldsymbol{D}$ are the matrixes about A_{ij}, B_{ij} and D_{ij} (i, j=1,2,6).

Using the matrix calculus, the following equations can be obtained

$$\{\varepsilon\} = \boldsymbol{A}^*\{N\} + \boldsymbol{B}^*\{\kappa\}, \{M\} = \boldsymbol{C}^*\{N\} + \boldsymbol{D}^*\{\kappa\} \tag{5.16}$$

where $\boldsymbol{A}^*=\boldsymbol{A}^{-1}$, $\boldsymbol{B}^*=-\boldsymbol{A}^{-1}\mathbf{B}$, $\boldsymbol{C}^*=\boldsymbol{B}\boldsymbol{A}^{-1}=-(\boldsymbol{B}^*)^T$ and $\boldsymbol{D}^*=\boldsymbol{D}-\boldsymbol{B}\boldsymbol{A}^{-1}\boldsymbol{B}$.

Then by solving Eq.(5.16), one can be obtained

$$
\begin{aligned}
\varepsilon_x^0 &= \frac{A_{22}N_x - A_{12}N_y - A_{22}(B_{11}\kappa_x + B_{12}\kappa_y) + A_{12}(B_{21}\kappa_x + B_{22}\kappa_y)}{A_{11}^2 - A_{21}^2} \\
\varepsilon_y^0 &= -\frac{A_{21}N_x - A_{11}N_y - A_{21}(B_{11}\kappa_x + B_{12}\kappa_y) + A_{11}(B_{21}\kappa_x + B_{22}\kappa_y)}{A_{11}^2 - A_{21}^2} \\
\gamma_{xy}^0 &= \frac{N_{xy} - 2B_{66}\kappa_{xy}}{A_{66}}
\end{aligned}
\tag{5.17}
$$

where

$$
\begin{aligned}
&A_{11} = A_{22} = \int_{-h/2}^{h/2} \frac{E}{1-v^2} dz, A_{12} = A_{21} = \int_{-h/2}^{h/2} \frac{Ev}{1-v^2} dz, A_{66} = \int_{-h/2}^{h/2} G_{xy} dz, \\
&B_{11} = B_{22} = \int_{-h/2}^{h/2} \frac{Ez}{1-v^2} dz, B_{12} = B_{21} = \int_{-h/2}^{h/2} \frac{Evz}{1-v^2} dz, B_{66} = \int_{-h/2}^{h/2} Gzdz, \\
&D_{11} = D_{22} = \int_{-h/2}^{h/2} \frac{Ez^2}{1-v^2} dz, D_{12} = D_{21} = \int_{-h/2}^{h/2} \frac{Evz^2}{1-v^2} dz, D_{66} = \int_{-h/2}^{h/2} Gz^2 dz
\end{aligned}
\tag{5.18}
$$

The nonlinear dynamic equilibrium equations, for an FG porous cylindrical shell subjected to a uniformly distributed harmonic loading $q(t)$ including damping effect based on classical shell theory, are given by

$$
\frac{\partial N_x}{\partial x} + \frac{\partial N_{yx}}{\partial y} = \rho_t \frac{\partial^2 u}{\partial t^2} + c_d \rho_t \frac{\partial u}{\partial t}
\tag{5.19}
$$

$$
\frac{\partial N_{xy}}{\partial x} + \frac{\partial N_y}{\partial y} = \rho_t \frac{\partial^2 v}{\partial t^2} + c_d \rho_t \frac{\partial v}{\partial t}
\tag{5.20}
$$

$$
\begin{aligned}
&N_x \frac{\partial^2 w}{\partial x^2} + N_y \frac{\partial^2 w}{\partial y^2} + 2N_{xy} \frac{\partial^2 w}{\partial x \partial y} + \frac{\partial^2 M_x}{\partial x^2} + \frac{\partial^2 M_y}{\partial y^2} + 2\frac{\partial^2 M_{xy}}{\partial x \partial y} + \frac{N_y}{R} + q(t) \\
&= \rho_t \frac{\partial^2 w}{\partial t^2} + c_d \rho_t \frac{\partial w}{\partial t}
\end{aligned}
\tag{5.21}
$$

where

$$\rho_t = \int_{-h/2}^{h/2} \rho(z) dz, q(t) = Q\cos(\omega t) \tag{5.22}$$

and where c_d denotes the damping coefficient of the structure.

Similarly, from Eq. (5.15) the moment resultants can be obtained

$$\begin{aligned} M_x &= B_{11}\varepsilon_x^0 + B_{12}\varepsilon_y^0 + D_{11}\kappa_x + D_{12}\kappa_y \\ M_y &= B_{21}\varepsilon_x^0 + B_{22}\varepsilon_y^0 + D_{21}\kappa_x + D_{22}\kappa_y \\ M_{xy} &= B_{66}\gamma_{xy}^0 + 2D_{66}\kappa_{xy} \end{aligned} \tag{5.23}$$

With an acceptable accuracy and based on the assumption that the flexural motion is predominant in the present investigation[215], $u \ll w$ and $v \ll w$, $\frac{\partial^2 u}{\partial t^2}$, $\frac{\partial u}{\partial t}$, $\frac{\partial^2 v}{\partial t^2}$ and $\frac{\partial v}{\partial t}$ approach to 0. Thus, considering Eqs.(5.19) and (5.20), the Airy's stress function $F(x,y)$ is defined as follows

$$\sigma_x = \frac{\partial^2 F(x,y)}{\partial y^2}, \sigma_y = \frac{\partial^2 F(x,y)}{\partial x^2}, \tau_{xy} = -\frac{\partial^2 F(x,y)}{\partial x \partial y} \tag{5.24}$$

With Eqs.(5.17) and (5.22), substituting Eq.(5.23) into Eq.(5.11), the nonlinear kinematic compatibility equilibrium equation can be rewritten as

$$\begin{aligned} &h\left[A_{11}^* \frac{\partial^4 F}{\partial x^4} + (A_{66}^* + 2A_{12}^*) \frac{\partial^4 F}{\partial x^2 \partial y^2} + A_{11}^* \frac{\partial^4 F}{\partial y^4} \right] - B_{11}^* \frac{\partial^4 w}{\partial x^4} \\ &-(2B_{12}^* - B_{66}^*) \frac{\partial^4 w}{\partial x^2 \partial y^2} - B_{22}^* \frac{\partial^4 w}{\partial y^4} = \left(\frac{\partial^2 w}{\partial x \partial y} \right)^2 - \frac{\partial^2 w}{\partial^2 y} \frac{\partial^2 w}{\partial^2 x} - \frac{1}{R} \frac{\partial^2 w}{\partial x^2} \end{aligned} \tag{5.25}$$

where

$$\begin{aligned}
&\Delta = A_{11}^2 - A_{21}^2;\\
&A_{11}^* = A_{22}^* = \frac{A_{11}}{\Delta}; A_{12}^* = A_{21}^* = -\frac{A_{12}}{\Delta};\\
&B_{11}^* = B_{22}^* = \frac{B_{11}A_{21} - B_{21}A_{11}}{\Delta}; B_{12}^* = B_{21}^* = \frac{B_{12}A_{21} - B_{22}A_{11}}{\Delta};\\
&A_{66}^* = \frac{1}{A_{66}}; B_{66}^* = -\frac{2B_{66}}{A_{66}}
\end{aligned} \tag{5.26}$$

With Eqs.(5.12) and (5.13), substituting Eq.(5.14) into Eq.(5.21), the dynamic equation of the FG porous cylindrical shell can be obtained as

$$\begin{aligned}
&h\left[C_{12}^* \frac{\partial^4 F}{\partial x^4} + 2\left(C_{11}^* - C_{66}^*\right)\frac{\partial^4 F}{\partial x^2 \partial y^2} + C_{21}^* \frac{\partial^4 F}{\partial y^4}\right]\\
&-D_{11}^* \frac{\partial^4 w}{\partial x^4} - 2(D_{12}^* + D_{66}^*)\frac{\partial^4 w}{\partial x^2 \partial y^2} - D_{11}^* \frac{\partial^4 w}{\partial y^4} + \frac{h}{R}\frac{\partial^2 F}{\partial x^2}\\
&+h\left[\frac{\partial^2 F}{\partial y^2}\frac{\partial^2 w}{\partial x^2} - 2\frac{\partial^2 F}{\partial x \partial y}\frac{\partial^2 w}{\partial x \partial y} + \frac{\partial^2 F}{\partial x^2}\frac{\partial^2 w}{\partial y^2}\right] + Q\cos(\omega t) = \rho_t \frac{\partial^2 w}{\partial t^2} + c_d \rho_t \frac{\partial w}{\partial t}
\end{aligned} \tag{5.27}$$

where

$$\begin{aligned}
&C_{11}^* = C_{22}^* = B_{11}A_{22}^* + B_{12}A_{21}^*; C_{12}^* = C_{21}^* = B_{11}A_{12}^* + B_{12}A_{11}^*;\\
&D_{11}^* = D_{22}^* = B_{11}B_{21}^* + B_{12}B_{11}^* + D_{11}; D_{12}^* = D_{21}^* = B_{11}B_{22}^* + B_{12}B_{12}^* + D_{12};\\
&C_{66}^* = B_{66}A_{66}^*; D_{66}^* = B_{66}B_{66}^* + 2D_{66}
\end{aligned} \tag{5.28}$$

5.4 Nonlinear dynamic analysis of an FG orthotropic cylindrical shell

5.4.1 *Solution of the problem*

To solve the dynamic equation of FG porous cylindrical shell, the assumed deflection shape plays a vital role in the analysis. Actually, there are several assumed deflection shapes based on different assumptions and methods subjected to various specified problems. While this is not principal objective in this chapter, more details can be found in [216-219]. Generally, the first mode assumption permitted to obtain analytical solutions for the amplitude frequency dependence and the nonlinear forced frequency response function. Though some researchers reported that excessive simplification of the assumed deflection shape would lead to large errors and even inaccurate results[220, 221] due to the ignore of companion mode, the single mode approach is still prevalent among literature because it is good enough to estimate the nonlinear frequency and total regularity of structures.

Therefore, in this chapter, the simply-supported boundary conditions are considered, and the approximate solution of Eq.(5.27) can be written as assumed to be the single mode [74]

$$w(x,y,t) = W_{mn}(t)\sin(\alpha x)\sin(\beta y) \tag{5.29}$$

where $W_{mn}(t)$ is the time-varying amplitude of w, and $\alpha = m\pi/L$ and $\beta = n/R$ are the number of half waves in the x and y directions, respectively. Moreover, other boundary conditions can be considered if one selects the proper trigonometric admissible functions[75].

Substituting Eq.(5.29 into the nonlinear compatibility Eq.(5.25), a particular solution of Eq.(5.25) is given

$$F(x,y,t) = F_1\cos(2\alpha x) + F_2\cos(2\beta y) + F_3\sin(\alpha x)\sin\left(\beta y\right) \tag{5.30}$$

where

$$F_1 = \frac{\beta^2}{32\alpha^2 A_{11}^* h} W_{mn}^2;$$
$$F_2 = \frac{\alpha^2}{32\beta^2 A_{11}^* h} W_{mn}^2 \tag{5.31}$$
$$F_3 = \frac{B_{11}^*\alpha^4 + (2B_{12}^* - B_{66}^*)\alpha^2\beta^2 + B_{11}^*\beta^4 + \frac{\alpha^2}{R}}{A_{11}^*\alpha^4 + (2A_{12}^* + A_{66}^*)\alpha^2\beta^2 + A_{11}^*\beta^4} \frac{W_{mn}}{h}$$

Substituting Eqs.(5.29 and (5.30) into Eq.(5.27) and then applying the Galerkin method[222, 223]. Each term in Eq.(5.27) is multiplying with sin*(mπx/L)*sin*(ny/R)dxdy*, then integrating over the middle surface of the cylindrical shell, the equation of motion becomes

$$\rho_t \frac{\partial^2 W_{mn}}{\partial t^2} + \rho_t c_d \frac{\partial W_{mn}}{\partial t} - \left(MK - N\right) W_{mn} + H W_{mn}^3 - \frac{4Q\cos(\omega t)}{mn\pi^2} r_1 r_2 = 0 \tag{5.32}$$

where

$$M = C_{12}^*\alpha^4 + 2(C_{11}^* - C_{66}^*)\alpha^2\beta^2 + C_{21}^*\beta^4 - \frac{\alpha^2}{R}$$
$$N = D_{11}^*\alpha^4 + 2(D_{12}^* + D_{66}^*)\alpha^2\beta^2 + D_{11}^*\beta^4$$
$$K = \frac{B_{11}^*\alpha^4 + (2B_{12}^* - B_{66}^*)\alpha^2\beta^2 + B_{11}^*\beta^4 + \frac{\alpha^2}{R}}{A_{11}^*\alpha^4 + (2A_{12}^* + A_{66}^*)\alpha^2\beta^2 + A_{11}^*\beta^4} \tag{5.33}$$
$$H = \frac{\alpha^4 + \beta^4}{16A_{11}^*}$$

and where

$$r_1 = (-1)^m - 1;$$
$$r_2 = (-1)^n - 1 \tag{5.34}$$

By considering the viscous damping as internal damping effect, one can obtain that

$$c_d = 2\omega_{mn}\zeta \tag{5.35}$$

where c_d denotes the damping coefficient of the structure; ω_{mn} denotes the circular natural frequency of the cylindrical shell corresponding to mode (m, n); and ζ denotes the damping ratio of the cylindrical shell.

Substituting Eq.(5.35) into Eq.(5.32), one can obtain

$$\frac{\partial^2 W_{mn}}{\partial t^2} + 2\omega_{mn}\zeta\frac{\partial W_{mn}}{\partial t} + \omega_{mn}^2 W_{mn} + c_1 W_{mn}^3 = c_2\cos(\omega t) \tag{5.36}$$

where

$$\omega_{mn}^2 = \frac{N - MK}{\rho_t}, c_1 = \frac{H}{\rho_t}, c_2 = \frac{4r_1 r_2 Q}{mn\pi^2\rho_t} \tag{5.37}$$

5.4.2 *Primary resonance of FG porous cylindrical shells*

In this section, the primary resonance of different types of FG porous cylindrical shells is investigated. Based on the method of multiple scales, Eq.(5.36) can be further simplified by using the following transformation

$$\omega_{mn}\zeta = \varepsilon\mu, c_1 = \varepsilon c_3, c_2 = \varepsilon c_4 \tag{5.38}$$

where ε is the small parameter in the order of the amplitude of the response. Then, substituting the above equation into Eq.(5.36), one can obtain

$$\ddot{W}_{mn}(t) + 2\varepsilon\mu\dot{W}_{mn}(t) + \omega_{mn}^2 W_{mn}(t) + \varepsilon c_3 W_{mn}^3(t) = \varepsilon c_4\cos(\omega t) \tag{5.39}$$

To determine an approximate solution to Eq.(5.39), the new scaled times T_r according to method of multiple scales[224] are introduced

$$T_r = \varepsilon^r t \,, r = 0,1,2,... \tag{5.40}$$

Then the derivatives with respect to t can be expressed in terms of the new scaled times T_r using chain rule as

$$\begin{aligned}
\frac{d}{dt} &= \frac{\partial}{\partial T_0} + \varepsilon \frac{\partial}{\partial T_1} + \varepsilon^2 \frac{\partial}{\partial T_2} + ... = D_0 + \varepsilon D_1 + \varepsilon^2 D_2 + ... \\
\frac{d^2}{dt^2} &= \frac{d}{dt}\left(\frac{\partial}{\partial T_0} + \varepsilon \frac{\partial}{\partial T_1} + \varepsilon^2 \frac{\partial}{\partial T_2} + ... \right) = \left(D_0 + \varepsilon D_1 + \varepsilon^2 D_2 + ... \right)^2 \\
&= D_0^2 + 2\varepsilon D_0 D_1 + \varepsilon^2 (D_1^2 + 2 D_0 D_2) + ...
\end{aligned} \tag{5.41}$$

where D_r (r=0,1,2,…) is the partial differential operator and can be defined as follows

$$D_r \equiv \frac{\partial}{\partial T_r} \,, r = 0,1,2,... \tag{5.42}$$

According to the perturbation method, the response W can be expanded with respect to ε as follows

$$W(t;\varepsilon) = W_0(T_0, T_1, ...) + \varepsilon W_1(T_0, T_1, ...) + \varepsilon^2 W_2(T_0, T_1, ...) + ... \tag{5.43}$$

In primary resonance, it is assumed that the frequency of the excitation ω and the natural frequency of the corresponding system ω_{mn} are close to each other, then

$$\omega = \omega_{mn} + \varepsilon\sigma \tag{5.44}$$

where σ indicates the detuning parameter quantitatively describing the nearness of frequency of the excitation ω to the natural frequency of the corresponding system ω_{mn}. Therefore, $\cos(\omega t)$ can be rewritten as

$$\cos(\omega t)=\cos(\omega_{mn}t+\varepsilon\sigma t)=\cos(\omega_{mn}T_0+\sigma T_1) \tag{5.45}$$

Substituting Eqs.(5.41)-(5.45) into Eq.(5.39), then equating the coefficients of ε^0 and ε to zero, one can obtain a first-order approximation of the Duffing equation

$$D_0^2W_0+\omega_{mn}^2W_0=0 \tag{5.46}$$

$$D_0^2W_1+\omega_{mn}^2W_1=-2(D_0D_1+\mu D_0)W_0-c_3W_0^3+c_4\cos(\omega_{mn}T_0+\sigma T_1) \tag{5.47}$$

The solution of Eq.(5.46) can be defined as

$$W_0(T_0,T_1)=a(T_1)\cos\left[\omega_{mn}T_0+\varphi(T_1)\right]=A(T_1)e^{i\omega_{mn}T_0}+cc \tag{5.48}$$

where $A(T_1)$ is an unknown complex function; cc stands for the complex conjugate of the preceding terms and $i=\sqrt{-1}$; $a(T_1)$ and $\varphi(T_1)$ are both real functions of T_1. And $A(T_1)$ can be written as

$$A(T_1)=\frac{1}{2}a(T_1)e^{i\varphi(T_1)} \tag{5.49}$$

To simplify the calculation, the above equation can be rewritten in the plural form as follows

$$W_0=\frac{a(T_1)}{2}(e^{i(\omega_{mn}T_0+\varphi(T_1))}+e^{-i(\omega_{mn}T_0+\varphi(T_1))}) \tag{5.50}$$

Substituting Eq.(5.50) into Eq.(5.47), one can obtain

$$\begin{aligned} & D_0^2 W_1 + \omega_{mn}^2 W_1 \\ & = -\left[2i\omega_{mn}(D_1 A + \mu A) + 3c_3 A^2 \bar{A}\right] e^{i\omega_{mn}T_0} - c_3 A^3 e^{3i\omega_{mn}T_0} + \frac{1}{2} c_4 e^{i(\omega_{mn}T_0 + \sigma T_1)} + cc \end{aligned} \tag{5.51}$$

In order to avoid secular behaviour in the system, the following equation must be satisfied

$$2i\omega_{mn}(D_1 A + \mu A) + 3c_3 A^2 \bar{A} - \frac{1}{2} c_4 e^{i\sigma T_1} = 0 \tag{5.52}$$

Substituting Eq.(5.49) into Eq.(5.52), then separating the real and imaginary parts, one can obtain

$$\begin{cases} D_1 a = -\mu a + \dfrac{c_4}{2\omega_{mn}} \sin(\sigma T_1 - \varphi) \\ a D_1 \varphi = \dfrac{3c_3\omega_{mn}}{8} a^3 - \dfrac{c_4}{2\omega_{mn}} \cos(\sigma T_1 - \varphi) \end{cases} \tag{5.53}$$

where the new phase angle define as $\gamma=\sigma T_1\text{-}\varphi(T_1)$. Then the above equation can be rewritten as

$$\begin{cases} D_1 a = -\mu a + \dfrac{c_4}{2\omega_{mn}} \sin\gamma \\ a D_1 \varphi = \sigma a - \dfrac{3c_3\omega_{mn}}{8} a^3 + \dfrac{c_4}{2\omega_{mn}} \cos\gamma \end{cases} \tag{5.54}$$

The first approximation to the steady state solution can be written as

$$W = a(T_1)\cos\left[\omega_{mn}T_0 + \sigma T_1 - \varphi(T_1)\right] = a(\varepsilon t)\left[\cos\omega_{mn} t - \varphi(\varepsilon t)\right] \tag{5.55}$$

For the steady-state response, both D_1a and $D_1\varphi$ in Eq.(5.53) equal to 0. Hence, the amplitude a and the phase γ of the steady-state response satisfy

$$\begin{cases} \mu a = \dfrac{c_4}{2\omega_{mn}} \sin\gamma \\ \sigma a - \dfrac{3c_3\omega_{mn}}{8} a^3 = -\dfrac{c_4}{2\omega_{mn}} \cos\gamma \end{cases} \tag{5.56}$$

By eliminating γ, squaring and adding these two equations, one obtains

$$\left[\mu^2 + \left(\sigma - \frac{3c_3\omega_{mn}}{8} a^2\right)^2\right] a^2 = \left(\frac{c_4}{2\omega_{mn}}\right)^2 \tag{5.57}$$

Eq.(5.57) is an implicit equation for the amplitude of response a as a function of the detuning parameter σ, also called the frequency-response equation. Similarly, by dividing the two equations in Eq.(5.56), the phase-frequency equation can be obtained as follows

$$\varphi = \tan^{-1}\left(\frac{-\mu}{\sigma - 3c_3\omega_{mn} a^2 / 8}\right) \tag{5.58}$$

By multiplying ε^2 to both sides of Eq.(5.57), then replacing all the parameters by the original ones according to Eq.(5.38), the above equations can be rewritten as

$$\left[(\zeta\omega_{mn})^2 + \left(\omega - \omega_{mn} - \frac{3c_1\omega_{mn}}{8} a^2\right)^2\right] a^2 = \left(\frac{c_2}{2\omega_{mn}}\right)^2 \tag{5.59}$$

$$\varphi = \tan^{-1}\left(\frac{-\zeta\omega_{mn}}{\omega - \omega_{mn} - 3c_1\omega_{mn} a^2 / 8}\right) \tag{5.60}$$

As Eq.(5.59) is a quadratic equation in terms of ω. For 0<a< $\frac{c_2}{2\zeta\omega_{mn}^2}$, by solving the equation, a set of real roots can be obtained

$$\omega = \omega_{mn}\left(1+\frac{3c_1a^2}{8}\right)\pm\sqrt{\left(\frac{c_2}{2\omega_{mn}a}\right)^2-\left(\zeta\omega_{mn}\right)^2} \tag{5.61}$$

The peak amplitude $a_{\max}$ gives

$$a_{\max} = \frac{c_2}{2\zeta\omega_{mn}^2} \tag{5.62}$$

As can be seen, the nonlinearity has no impact on the peak amplitude $a_{\max}$, while the excitation frequency ω of the corresponding peak amplitude $a_{\max}$ affected by the nonlinearity.

$$\omega = \omega_{mn}\left(1+\frac{3c_1a_{\max}^2}{8}\right) \tag{5.63}$$

5.5 Results and discussions

5.5.1 *Validation of present study*

In this section, the accuracy of the proposed method is verified with the numerical results in the open literature. Due to the lack of results in the nonlinear primary resonance of the FG porous cylindrical shells, the present theories and formulations are examined by comparing the results of natural frequencies of the FG porous cylindrical shell reported by Wang and Wu[173] based on the Rayleigh-Ritz method.

For Table 5.1 and Table 5.2, the dimensions of circular orthotropic cylindrical shell are E=200GPa, v=0.3, ρ=7850kg/m^3, R/h=100, L/R=0.2 from [173]. The natural frequency ω_{mn} can be calculated by Eq.(5.37). For simplicity, the non-dimensional natural frequency is introduced as

$$\omega_{mn}^{*} = \omega_{mn} R \sqrt{\rho_{\max} / E_{\max}} \tag{5.64}$$

According to the comparisons from Table 5.1 and Table 5.2 for symmetric porosity distribution and non-symmetric porosity distribution, respectively, it is clear that the proposed method matches very well with the published journals and the differences for various porosity coefficients N_0 are around 0.3%-0.5%.

Table 5.1 Comparison of the non-dimensional natural frequencies of a simply supported FG cylindrical shell with symmetric porosity distribution with results reported by Wang and Wu[173] (m=1)

	Ref [173]	Present	Ref [173]	Present	Ref [173]	Present	Ref [173]	Present
N_0	n=1		n=2		n=3		n=4	
0	1.2429	1.2466	1.2387	1.2426	1.2325	1.2368	1.2256	1.2305
0.2	1.2155	1.2194	1.2118	1.2159	1.2064	1.2110	1.2006	1.2057
0.4	1.1893	1.1935	1.1862	1.1906	1.1818	1.1867	1.1772	1.1827
0.6	1.1677	1.1725	1.1653	1.1704	1.162	1.1676	1.1590	1.1652
0.8	1.1633	1.1693	1.1617	1.1681	1.1599	1.1668	1.1591	1.1666

Table 5.2 Comparison of the non-dimensional natural frequencies of a simply supported FG cylindrical shell with non-symmetric porosity distribution with results reported by Wang and Wu[173] (m=1)

	Ref [173]	Present	Ref [173]	Present	Ref [173]	Present	Ref [173]	Present
N_0	n=1		n=2		n=3		n=4	
0	1.2429	1.2466	1.2387	1.2426	1.2325	1.2368	1.2256	1.2305
0.2	1.2037	1.2075	1.1997	1.2037	1.1938	1.1982	1.1872	1.1922
0.4	1.1598	1.1637	1.1559	1.1600	1.1501	1.1546	1.1438	1.1488
0.6	1.1093	1.1133	1.1054	1.1096	1.0995	1.1041	1.0930	1.0980
0.8	1.0507	1.0548	1.0463	1.0505	1.0396	1.0440	1.0317	1.0365

To further verify the method developed in present study, the adaptive step-size fourth-order Runge-Kutta method is employed to analyse Eq.(5.36) numerically. The initial conditions of the ordinary differential equation are $W_{mn}(0) = \dot{W}_{mn}(0) = 0$ and then each of the maximum response amplitudes corresponding to various excitation frequencies can be extracted from the time-domain responses. Figure 5.4 shows the comparison of the dimensionless amplitude-frequency curves of FG porous cylindrical shell obtained by proposed method with that by Runge-Kutta method for Type 1. In Figure 5.4, the hollow circle dot denotes the results obtained from Runge-Kutta method, while solid curve represents the response from proposed method. As can be seen, the present method is in agreement with that from the numerical simulation, and then the validity of the present study is examined.

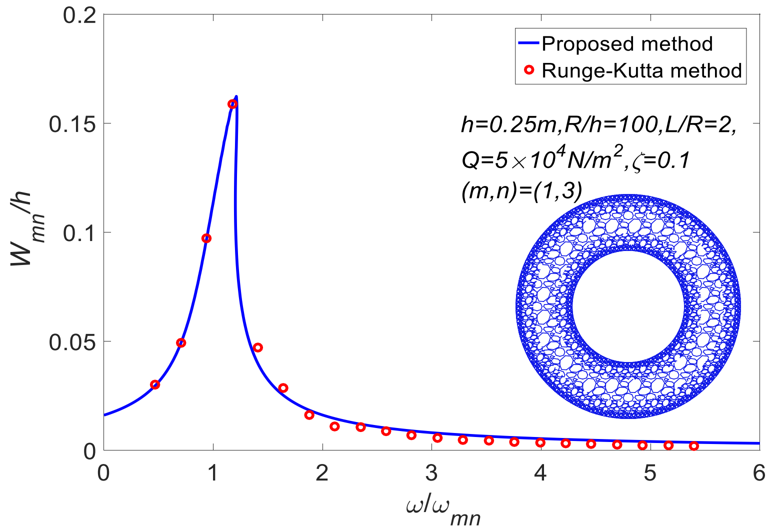

Figure 5.4 Comparison of the dimensionless amplitude-frequency curve of FG porous cylindrical shell calculated by proposed method with that by Runge-Kutta method for Type 1

5.5.2 *Results of natural frequencies of free vibration*

The results from the last subsection have verified the proposed methods. Additional effects of different modes (m, n), different types porosity distributions, different L/R ratios and R/h ratios on natural frequencies ω^*_{mn} (calculated from Eq. (64)) a simply supported FG porous cylindrical shell are investigated below. E_{max}=200GPa, v=0.3, ρ_{max}=7850kg/m^3, which were taken from Wang and Wu[173]. The geometrical parameters are h=0.25m, R=100×h, L=10×R. Figure 5.5 shows the dimensionless natural frequencies of FG porous cylindrical shell for different porosity distributions when m=1.

To further investigate the natural frequencies of FG porous cylindrical shell, the effect of L/R ratio and R/h ratio are presented. The material properties are same as before, except that L/R=10, 20 and 40, L=10×R for Table 5.3 and R/h=100, 150 and 200, L=50*R for Table 5.4, respectively. Clearly, for different cases, the dimensionless natural frequency of Type 1 is the largest among all the porosity distributions. By increasing the porosity coefficient, the dimensionless natural frequencies decrease, as well as the increase of *L/R* ratio and *R/h* ratio. Moreover, the fundamental natural frequency is affected by *L/R* ratio and *R/h* ratio; this is also consistent with the results reported by Wang and Wu[173].

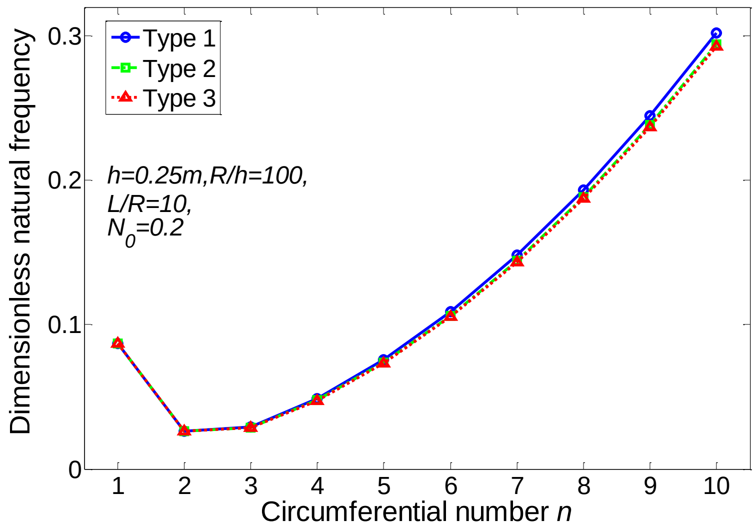

Figure 5.5 Dimensionless natural frequencies of FG porous cylindrical shell for different porosity distributions (m=1)

Table 5.3 Dimensionless natural frequencies for different *L/R* ratios, porosity coefficients and porosity distributions (m=1, $\omega^*_{mn}\times10^{-2}$)

L/R	N_0	Type 1	Type 2	Type 3
10 (n=2)	0.2	2.637	2.622	2.616
	0.4	2.566	2.528	2.507
	0.6	2.5	2.425	2.371
	0.8	2.465	2.319	2.181
20 (n=2)	0.2	1.352	1.323	1.317
	0.4	1.345	1.274	1.262
	0.6	1.349	1.209	1.193
	0.8	1.382	1.113	1.098

40 (n=1)	0.2	0.666	0.663	0.661
	0.4	0.648	0.639	0.634
	0.6	0.631	0.613	0.599
	0.8	0.621	0.587	0.551

Table 5.4 Dimensionless natural frequencies for different *R/h* ratios, porosity coefficients and porosity distributions (m=1, $\omega_{mn}^{*}\times10^{-2}$)

R/h	N_0	Type 1	Type 2	Type 3
100 (n=1)	0.2	0.486	0.481	0.480
	0.4	0.476	0.464	0.460
	0.6	0.468	0.444	0.435
	0.8	0.467	0.420	0.400
150 (n=1)	0.2	0.431	0.428	0.427
	0.4	0.419	0.413	0.409
	0.6	0.408	0.396	0.387
	0.8	0.403	0.379	0.356
200 (n=1)	0.2	0.409	0.408	0.407
	0.4	0.397	0.393	0.390
	0.6	0.385	0.378	0.369
	0.8	0.377	0.363	0.339

5.5.3 ***Nonlinear primary resonance of FG porous cylindrical shells subjected to a uniformly distributed harmonic loading***

In this subsection, the nonlinear primary resonance of the FG porous cylindrical shell subjected to a uniformly distributed harmonic loading $q(t)$ with the consideration of damping effect is investigated. The influences of porosity distribution, porosity coefficient, damping ratio, amplitude and frequency of the external harmonic excitation, aspect ratio and thickness ratio on the nonlinear dynamic behaviour are discussed in details. The material properties of the open-cell foam are chosen: E_{max}=200GPa, v=1/3, ρ_{max}=7850kg/m^3. The geometrical parameters are h=0.25m, R=100×h, L=2×R. The amplitude of the uniformly distributed harmonic loading $q(t)$ is Q=5×10^{4}N/m^2 and the damping ratio of the cylindrical shell is 0.1. ω_{mn} denotes the circular natural frequency of the cylindrical shell corresponding to mode (1, 7).

5.5.3.1 *The influence of different porosity coefficients N0 for various porosity distributions*

Figure 5.6 illustrates the frequency-response curves of free and nonlinear forced vibrations of FG porous cylindrical shells for different porosity coefficients with symmetric porosity distribution, non-symmetric porosity distribution, and uniform porosity distribution, respectively. Four different of porosity coefficients N_0=0, 0.2, 0.4 and 0.6 are selected. For N_0=0, the structures reduce to the homogeneous case. It is can be seen that by increasing the value of the coefficient of porosity, the maximum amplitude of primary resonance is shifted to the higher detuning parameters σ (calculated by Eq.(5.44)) for all the distribution types. The frequency-response curve of free vibration is a single-valued parabola and shown by the black dash line, also named backbone curve. Furthermore, it is observed that porosity coefficient has a significant effect on the jump height a of the frequency-response curve, which can be obtained by Eq.(5.62). As we can see, all the frequency-response curves bend to the right side. We call this phenomenon hardening nonlinearity. While for the frequency-response curve bending to the opposite direction is called softening nonlinearity. Therefore, Figure 5.6 also indicates that hardening nonlinearity can be weakened by the increase of porosity coefficients.

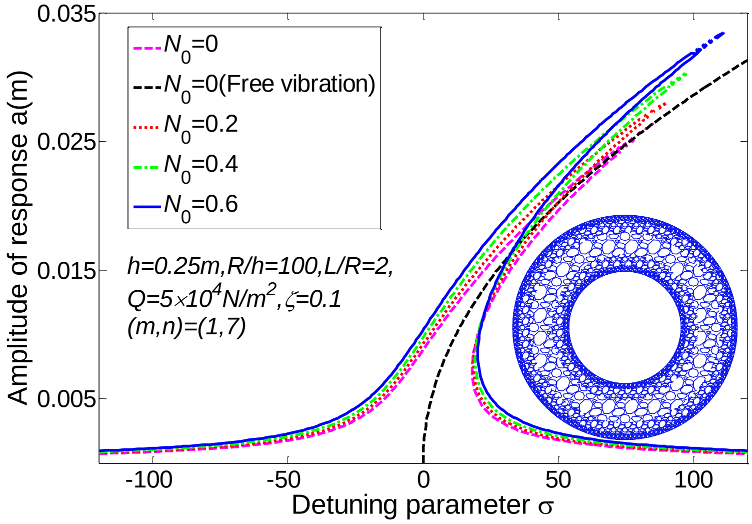

(a) Type 1

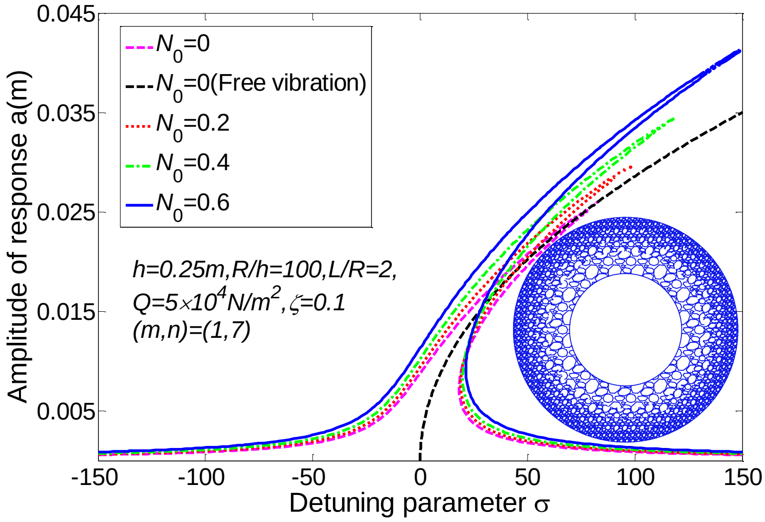

(b) Type 2

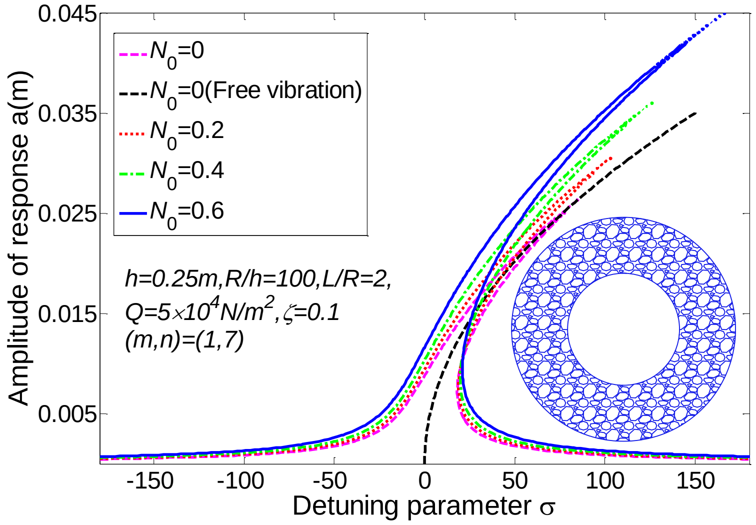

(c) Type 3

Figure 5.6 Effect of porosity coefficient N_0 on the amplitude-frequency response of FG porous cylindrical shells for different porosity distributions

The influence of different porosity distribution types on the amplitude-frequency response of FG porous cylindrical shell with same porosity coefficient is demonstrated in Figure 5.7. The porosity coefficient N_0=0.8 is chosen while holding all other parameters fixed. It is clear that the jump height of Type 1 (symmetric porosity distribution) is much less than the other two types while the height of jump for Type 2 and Type 3 is almost the same. However, Type 1 (symmetric porosity distribution) exhibits more hardening nonlinearity behaviour than the other two types. Another notable feature is primary resonance region, the area covered by the frequency-response curve. From the figure, one can obtain that Type 1< Type 2< Type 3 for primary resonance region. This is due to the symmetric porosity distribution occupies more stiffness than the other two types and consequently, the detuning parameters and amplitude of response are the smallest.

Figure 5.8 presents the effect of porosity distribution on the variation of the amplitude of response with the amplitude of excitation for FG porous cylindrical shells. The porosity coefficient N0=0.6 is chosen while holding all other parameters fixed. As it can be predicted, Type 1 occupies more stiffness feature when compared with other two types. Thus the jump height of Type 1 is smaller than that of Type 2 and Type 3. Similar conclusions are obtained from Figure 5.7.

As the above conclusions, though symmetric porosity distribution exhibits more stiffness behaviour, the jump height and the primary resonance region is smaller than Type 2 and Type 3, especially the jump height, one of the most important governing parameters. Additionally, frequency-response curves are quite similar for all three types of distribution. Thus, in the following sections, our main research object is Type 1.

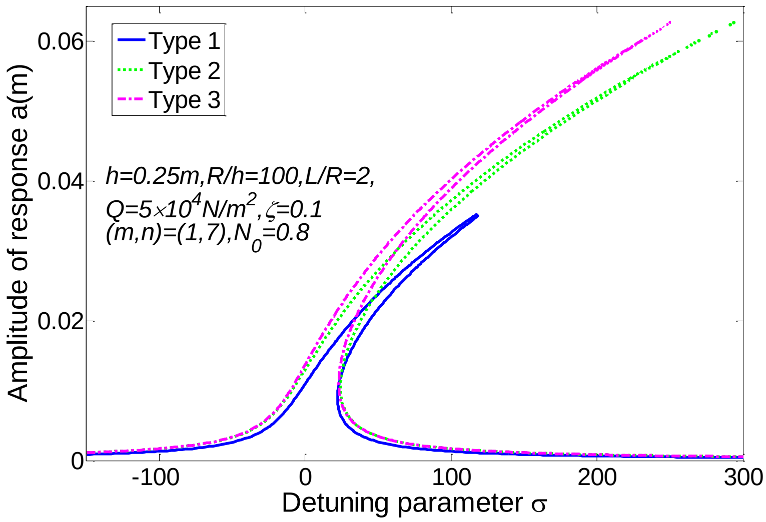

Figure 5.7 Effect of porosity distribution on the amplitude-frequency response of FG porous cylindrical shells with same porosity coefficient

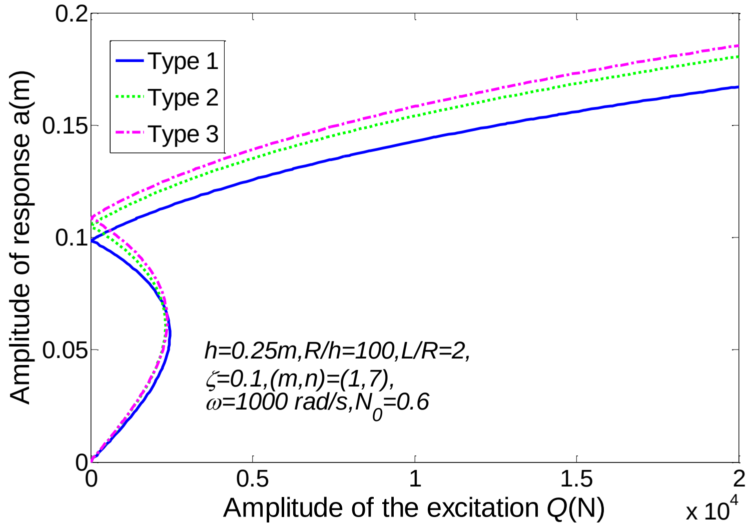

Figure 5.8 Effect of porosity distribution on the amplitude of the response of FG porous cylindrical shells as a function of amplitude of the excitation

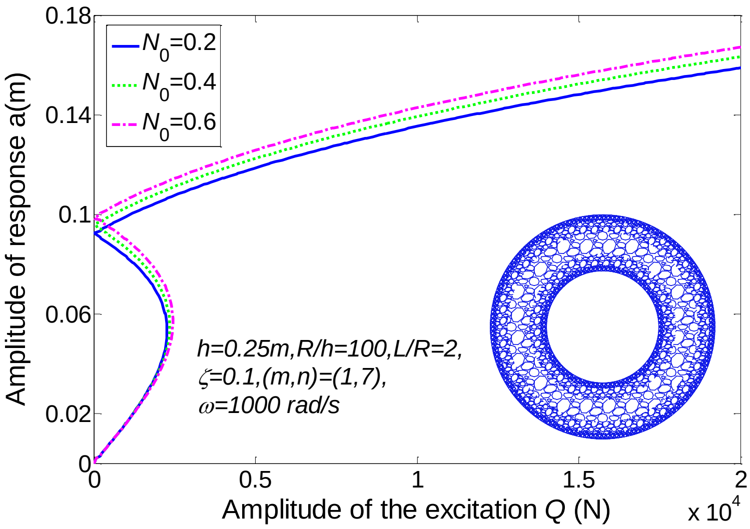

Figure 5.9 Effect of porosity coefficient N_0 on the amplitude of the response of FG porous cylindrical shells as a function of amplitude of the excitation

If the frequency of the excitation ω held fixed while the amplitude of the excitation is varied slowly, a similar jump phenomenon can be observed, as shown in Figure 5.9, the variation of the amplitude of response a with the amplitude of excitation Q corresponding to different porosity coefficients N_0 for Type 1. As can be seen, at first, Q increases slowly from 0, suddenly, there will be an apparent upward jump for the amplitude of response a

and after the jump, an increase almost linearly with the increase of the amplitude of excitation *Q*. According to Nayfeh's explanation[224], the multivaluedness of the response curves (jump phenomena) is due to influence of the nonlinearity. Moreover, by increasing the coefficient of porosity, the jump height of *a*-*Q* curves increases. This is because the increase of the porosity coefficients would lead to the decrease of nonlinearity stiffness.

5.5.3.2 *The influence of amplitude of excitation Q on primary resonance*

Depicted in Figure 5.10 is the influence of amplitude of excitation *Q* on the amplitude-frequency response of FG porous cylindrical shell. Four different amplitude of excitation Q=0, 1×10^4N/m^2, 2.5×10^4N/m^2 and 5×10^4N/m^2 are selected. It can be found that when the amplitude of the excitation *Q* increases, the hardening nonlinearity becomes worse and the maximum amplitude of responses *a* increases. This is because the increase of the amplitude of external excitation will lead to the increase of vibration amplitude. And also the frequency interval for unstable region is prolonged. When the amplitude of the excitation *Q* is small, like Q=0 and 1×10^4 N/m^2, as can be seen in Figure 5.10, there is no unstable region.

5.5.3.3 *The influence of damping ratio ζ on primary resonance*

The effect of damping ratio ζ on the amplitude-frequency response of FG porous cylindrical shell is demonstrated in Figure 5.11. Three different damping ratios are considered, which are ζ =0,0.1 and 0.2. In the absence of damping effect, the peak amplitude is infinite. While in the presence of damping effect, the amplitude-frequency curves are finite. And as the value of damping ratio increases, the peak amplitude decreases.

Figure 5.12 indicates the influence of damping effect on the variation of the amplitude of response with the amplitude of excitation. Three different damping ratios are considered, which are ζ =0, 0.1 and 0.2. The frequency of the excitation ω=1000 *rad*/*s* and other parameters are unchanged. It is clear that damping effect does not have a significant effect on the jump height of the *a*-*Q* curves.

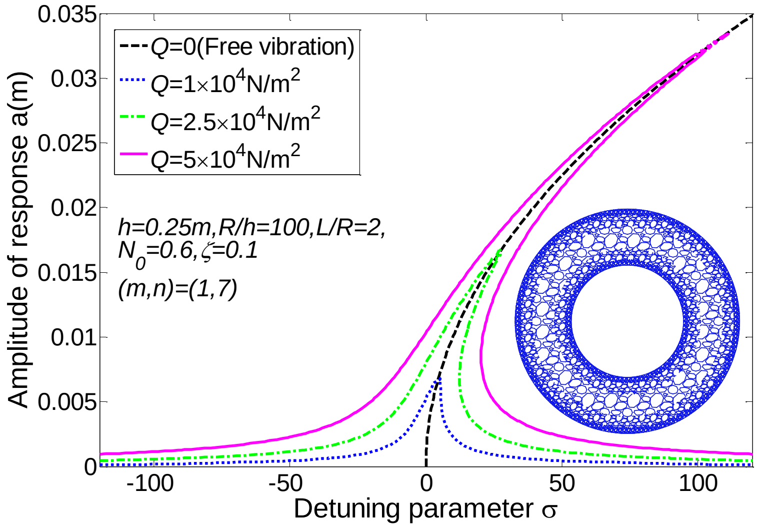

Figure 5.10 Effect of amplitude of excitation Q on the amplitude-frequency response of FG porous cylindrical shells

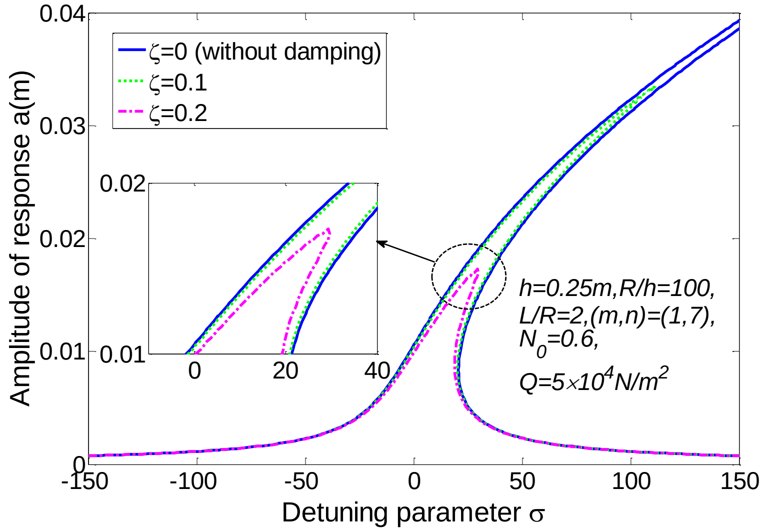

Figure 5.11 Effect of damping ratio ζ on the amplitude-frequency response of FG porous cylindrical shells

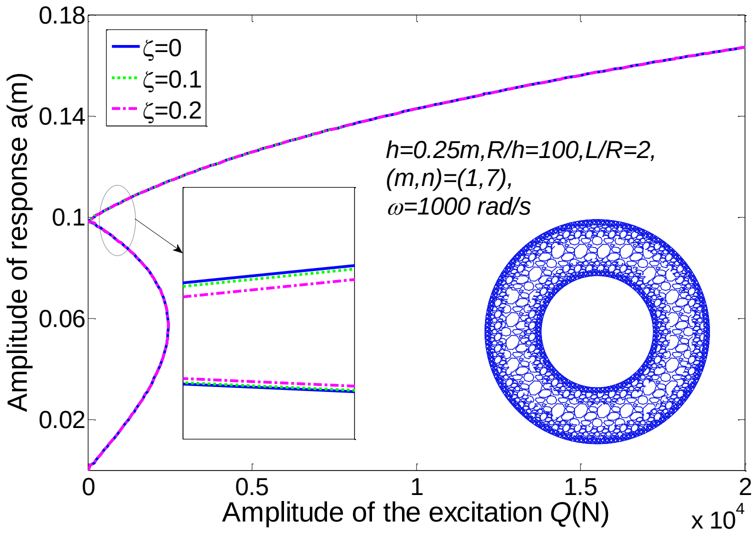

Figure 5.12 Effect of damping effect on the amplitude of the response of FG porous cylindrical shells as a function of amplitude of the excitation

5.5.3.4 *The influence of L/R and R/h ratios on primary resonance*

Figure 5.13 shows the amplitude-frequency curves for various *L/R* ratios. The geometrical parameters are *h*=0.25m, *R*=100×*h*. The results of three different *L*/*R* ratios, i.e. *L*/*R*=2, 4 and 6 are given. It is found that by increasing the *L/R* ratios the jump height becomes larger while the hardening nonlinearity diminishes. One interesting finding is that jump height is not continually increasing due to the increase of *L/R* ratios. The amplitude-frequency curves for *L/R* ratios equal to 4 and 6 are almost the same.

If we examined Table 5.3 carefully, one conclusion can be made is that the lowest frequency is always associated with *m*=1 for different types of distribution; however, the increase of *L/R* ratios will decrease the number of circumferential waves *n* and the frequency of the structure. Therefore, as the *L/R* ratios increase the hardening nonlinearity will decrease. Similar phenomenon can be observed from Figure 5.13. Then for a very long shell, namely *L* is larger than *R*, the number of circumferential waves *n* will approach to 1 slowly and amplitude of the response *a* also grows tardy when the *L/R* ratio reaches a certain level.

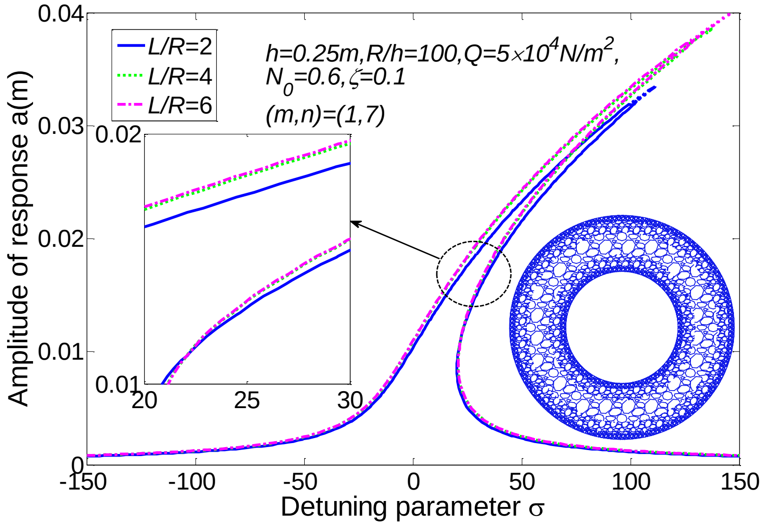

Figure 5.13 Effect of *L/R* ratios on the amplitude-frequency response of FG porous cylindrical shells

The effect of *L/R* ratios on the variation of the amplitude of response with the amplitude of excitation is plotted in Figure 5.14. It is observed that *L/R* ratio does not have a significant effect on the *a*-*Q* curves, though jump height of *L/R* ratio equals to 2 is a little bit smaller than that of the other two cases.

Figure 5.15 demonstrates the amplitude-frequency curves for various *R/h* ratios. The geometrical parameters are *h*=0.25m, *L*=2×*R*. Three different of radius-to-thickness ratios, i.e. *R*/*h*=100, 150 and 200 are chosen. All the other parameters remain the same as before. As can be seen, the ratio of radius-to-thickness plays an important role in the primary resonance. The increase of the *R/h* ratio would weaken the hardening nonlinearity and the resonant region becomes wider.

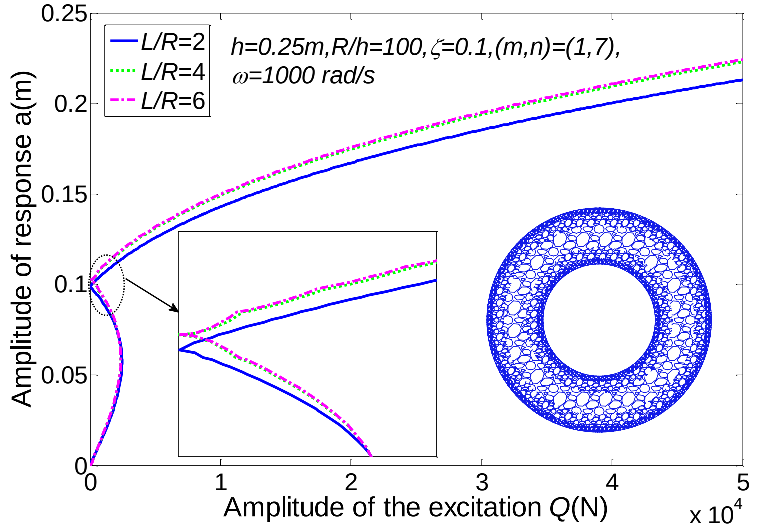

Figure 5.14 Effect of *L/R* ratios on the amplitude of the response of FG porous cylindrical shells as a function of amplitude of the excitation

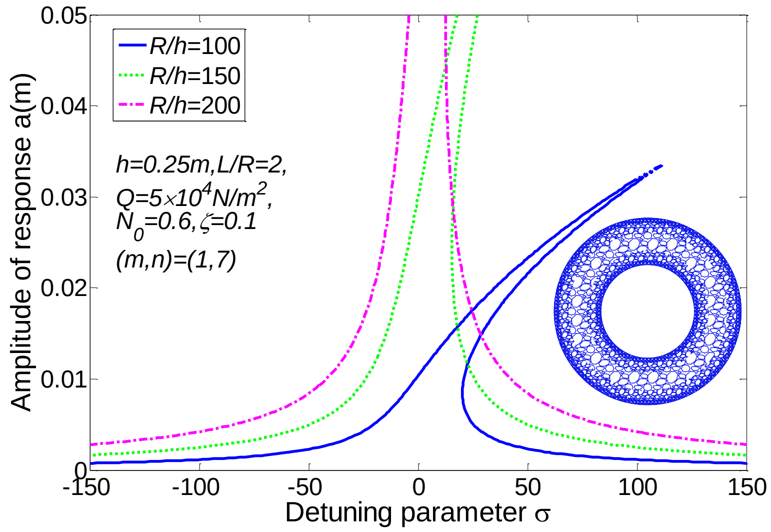

Figure 5.15 Effect of *R/h* ratios on the amplitude-frequency response of FG porous cylindrical shells

The effect of *R/h* ratios on the variation of the amplitude of response with the amplitude of excitation is plotted in Figure 5.16. It is observed that *R/h* ratio has a significant effect on the *a*-*Q* curves and with the increase of radius-to-thickness ratio the jump height becomes larger.

The simultaneous effect of *L/R* ratios and *R/h* ratios on the peak amplitude of response for the primary resonance of FG porous cylindrical shell is highlighted in Figure 5.17 for the case of detuning parameter σ=0 (the frequency of excitation is equal to the natural frequency of the corresponding Duffing-type system). It is seen that as the *R/h* ratios the peak amplitude of response for primary resonance increases for all values of *L/R* ratios, though the growth is uneven for different cases.

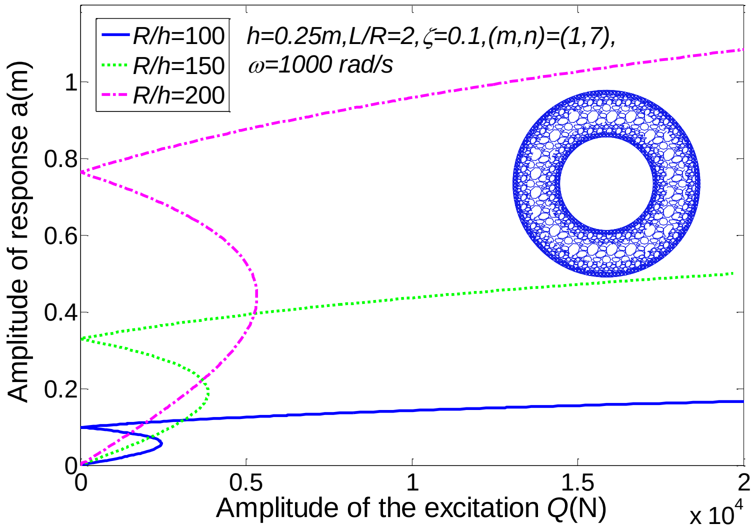

Figure 5.16 Effect of *R/h* ratios on the amplitude of the response of FG porous cylindrical shells as a function of amplitude of the excitation

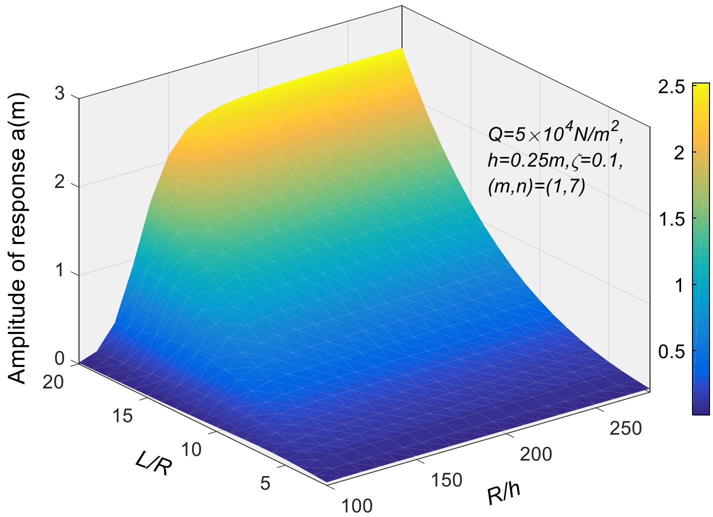

Figure 5.17 The relationship of different *L/R* ratios and *R/h* ratios on the peak amplitude of response for primary resonance of FG porous cylindrical shells

5.5.3.5 ***The influence of detuning parameters σ on primary resonance***

Figure 5.18 presents the variation of the amplitude of response with the amplitude of excitation for different detuning parameters σ. Five different of detuning parameters, i.e. σ=1000, 500, 0, -500 and -1000 are chosen. All the other parameters remain the same as before. When detuning parameters σ=0, it means the frequency of excitation is equal to the natural frequency of the corresponding Duffing-type system; when σ> 0, it corresponds to the frequency of excitation is larger than the natural frequency while σ <0 means the frequency of excitation is smaller than the natural frequency of the system. As can be seen, depending on the detuning parameters σ, some curves are multivalued while others are single-valued.

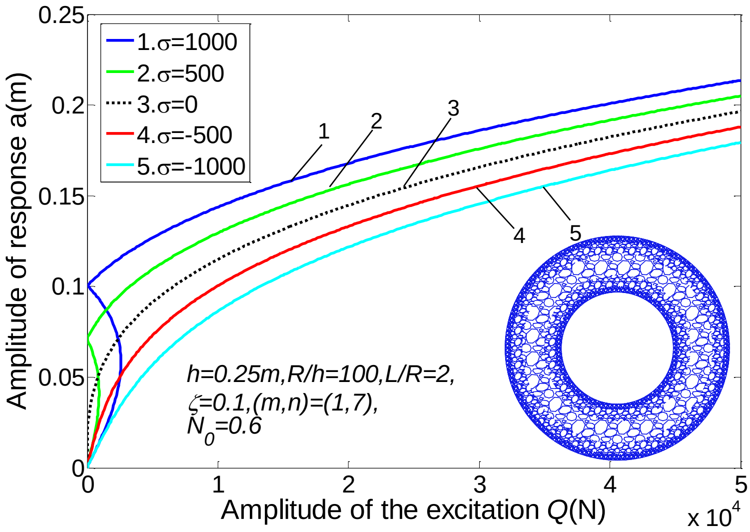

Figure 5.18 Effect of detuning parameters σ on the amplitude of the response of FG porous cylindrical shells as a function of amplitude of the excitation

For the single-valued curves, namely, the frequency of excitation is smaller than or equals to the natural frequency of the system, the increase of the amplitude of the excitation Q will lead to the increase of response amplitude. There is no jump phenomenon. While for the multivalued curves, that is the frequency of excitation is larger than the natural frequency, the discontinuous changes of the curve will result in the instability of the system. For instance, when σ=1000, with the amplitude of the excitation Q increasing from 0, the amplitude of the response a increases continuously from 0. When Q reaches around 0.25×10^4 N/m^2, the response amplitudes suddenly changes from 0.06 m to 0.11m and then increases gradually. Similarly, when the external excitation Q decreases from 5×10^4 N/m^2, the amplitude response a decreases continuously at first and then jumps rapidly from 0.11 m to 0.06 m. This is called the discontinuous changes of the curve or the jump phenomenon.

5.6 Conclusions

This chapter investigates the nonlinear primary resonance behaviour of cylindrical shells made of functionally graded (FG) porous materials subjected to a uniformly distributed harmonic load including the damping effect. To develop this model, the Donnell shell theory (DST) and accounting for von-Kármán strain-displacement relation and damping effect was employed. The Galerkin method in conjunction with the method of multiple scales (MMS) was utilised to obtain a second-order nonlinear ordinary equation with the cubic nonlinear term, named Duffing-type equation. Three types of FG porous distributions, namely symmetric porosity distribution, non-symmetric porosity stiff or soft distribution and uniform porosity distribution were considered in this chapter. Then, the influence of porosity distribution, porosity coefficient, damping ratio, amplitude and frequency of the external harmonic excitation, aspect ratio and thickness ratio were discussed in details and the following conclusions can be made:

1. By increasing the value of the coefficient of porosity, hardening nonlinearity is weakened for all the distributions.

2. Although Type 1 (symmetric porosity distribution) exhibits more stiffness behaviour, the jump height and the primary resonance region are smaller than Type 2 and Type 3, especially the jump height. This is because the symmetric porosity distribution occupies more stiffness than the other two types and consequently the detuning parameters and amplitude of response are the smallest.
3. The amplitude of the excitation increases, the hardening nonlinearity becomes worse and the maximum amplitude of responses increases.
4. In the absence of damping effect, the peak amplitude is infinite. While in the presence of damping effect, the amplitude-frequency curves are finite. And as the value of damping ratio increases, the peak amplitude decreases as the value of damping ratio increases.
5. L/R ratio does not have a significant effect on the primary resonance behaviour while R/h ratio does.
6. Depending on the detuning parameters σ, some curves are multivalued while others are single-valued.

Therefore, the proposed method presented herein provides a comprehensive analytical analysis framework for nonlinear primary resonance behaviour assessment of FG porous cylindrical shells, as well as a useful help for design and analysis of nano/micro-sized devices and systems.

Chapter 6 Nonlinear dynamic stability of the orthotropic functionally graded cylindrical shell surrounded by Winkler-Pasternak elastic foundation subjected to a linearly increasing load

6.1 Introduction

The thin-walled cylindrical shell structure has been widely used in aerospace engineering and other engineering disciplines for many decades, such as propellant tank of space shuttle, the skin of ballistic missile, air receiver tanks, distillation columns, heat exchangers/condensers, due to its outstanding stiffness, large space cover, lower cost and high strength-weight ratio.

Despite mentioned studies, up to date, dynamic buckling of FG orthotropic cylindrical shells is a novel topic that cannot be found in the literature. Furthermore, with the application of FG orthotropic cylindrical shells, these structures rest on or embed in elastic foundation/medium have attracted much attention. Damping property (i.e., a non-conservative energy contribution), as one of the most important aspects of engineering dynamics, is also considered in this chapter.

Therefore, to the best of authors' knowledge, the dynamic stability of an FG orthotropic circular cylindrical shell surrounded by a two-parameter (Winkler-Pasternak) elastic foundation subjected to linearly increasing load with the consideration of damping effect is first investigated in this chapter. Equations of motion are derived from Hamilton's principle and the nonlinear compatibility equation is considered by means of modified Donnell shell theory including large deflection. Then the nonlinear dynamic buckling equation is solved by a hybrid analytical-numerical method (combined Galerkin method and fourth-order Runge-Kutta method). Effects of different parameters such as various inhomogeneous parameters, loading speeds, damping ratios and aspect ratios and thickness ratios of the structure on dynamic buckling are discussed in detail. Finally, the proposed method was validated with other publications.

6.2 Orthotropic FGMs cylindrical shell surrounded by Winkler-Pasternak elastic foundation subjected to a linearly increasing load

6.2.1 *FG orthotropic cylindrical shell*

The orthotropic FGMs cylindrical shell surrounded by a two-parameter (Winkler-Pasternak) elastic foundation subjected to a linearly increasing load is shown in Figure 6.1. The geometrical dimensions are as follows: length L, mean radius R and thickness h. The Cartesian coordinate system (x,y,z) is established, in which point O is located on the middle plane and at the left side of the cylindrical shell. z is in the thickness direction. And the linearly increasing load $P(t)$ is at the end of right side along the x direction.

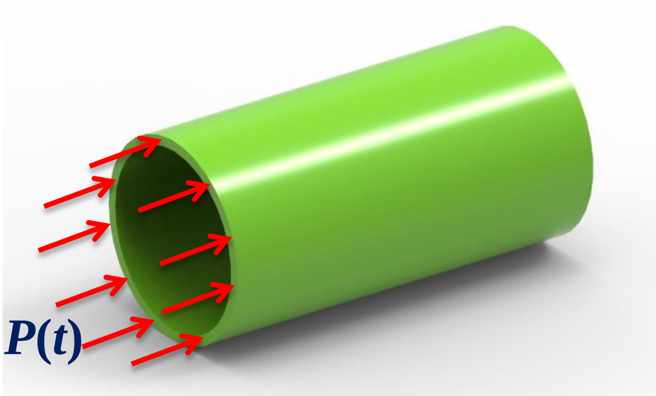

(1)

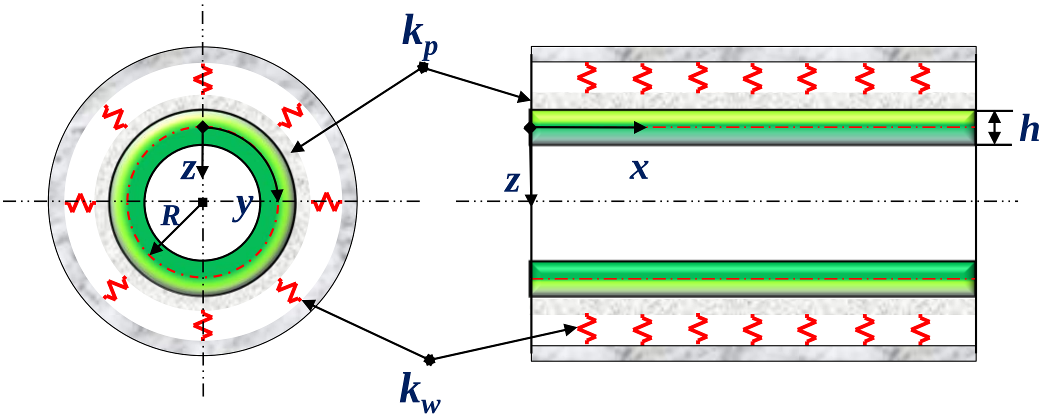

(2)

Figure 6.1 Geometry and the coordinate system of the orthotropic FGMs cylindrical shell surrounded by Winkler-Pasternak elastic foundation subjected to a linearly increasing load

FGMs in this chapter is assumed to be made from a mixture of ceramic and metal with exponentially varying material properties that have been reported by many scholars [127-133, 225]. The Young's moduli *E*, shear modulus *G* and density can be given in the following form

$$\begin{aligned}&E_x = E_{01}\psi_1(z); E_y = E_{02}\psi_1(z); G_{xy} = G_0\psi_1(z);\\&\rho(z) = \rho_0\psi_2(z);\end{aligned} \tag{6.1}$$

where

$$\psi_i(z) = e^{\kappa_i(\frac{z}{h}+0.5)} \tag{6.2}$$

and where $\psi(z)$ is the material's exponential function. κ_i is the exponential factor, and also denotes the non-homogenous parameter because it characters the degree of the material gradient in the z-direction. In this chapter, we assume that Poisson's ratio of the shell is considered to be constant due to the effect of Poisson's ratio on the deformation is much less than other material properties[213]. E_{01} and E_{02} represent Young's moduli of the homogeneous orthotropic material along x, y directions, respectively. Similarly, G_0 and ρ_0 are the shear modulus and density of the homogeneous orthotropic material, respectively. As can be seen, when κ_i =0, Eq.(6.1) reduces to the homogeneous case; when κ_i > 0, it corresponds to the graded stiff material while κ_i <0 means graded soft material[226].

6.2.2 *Constitutive relations*

Considering the initial imperfection w_0, the von-Kármán nonlinear strain-displacement relation on the middle plane of the circular cylindrical shell can be written as

$$\begin{aligned}
\varepsilon_x^0 &= \frac{\partial u}{\partial x} + \frac{1}{2}\left(\frac{\partial w}{\partial x}\right)^2 - \frac{1}{2}\left(\frac{\partial w_0}{\partial x}\right)^2 \\
\varepsilon_y^0 &= \frac{\partial v}{\partial y} - \frac{w-w_0}{R} + \frac{1}{2}\left(\frac{\partial w}{\partial y}\right)^2 - \frac{1}{2}\left(\frac{\partial w_0}{\partial y}\right)^2 \\
\gamma_{xy}^0 &= \frac{\partial u}{\partial y} + \frac{\partial v}{\partial x} + \frac{\partial w}{\partial x}\frac{\partial w}{\partial y} - \frac{\partial w_0}{\partial x}\frac{\partial w_0}{\partial y}
\end{aligned} \tag{6.3}$$

where ε_x^0, ε_y^0 and γ_{xy}^0 are normal strains, shear strain at the middle surface with the consideration of initial imperfection of the FG orthotropic circular cylindrical shell, respectively. u, v and w are the displacement components of middle surface of the cylindrical shell in x, y, and z direction, respectively.

The strain components across the shell thickness at a distance z from the middle surface are

$$\begin{aligned}
\varepsilon_x &= \varepsilon_x^0 + z\kappa_x \\
\varepsilon_y &= \varepsilon_y^0 + z\kappa_y \\
\gamma_{xy} &= \gamma_{xy}^0 + 2z\kappa_{xy}
\end{aligned} \tag{6.4}$$

$$\kappa_x = -\frac{\partial^2 (w-w_0)}{\partial x^2}; \kappa_y = -\frac{\partial^2 (w-w_0)}{\partial y^2}; \kappa_{xy} = -\frac{\partial^2 (w-w_0)}{\partial x \partial y} \tag{6.5}$$

where κ_x, κ_y and κ_{xy} are the change of curvatures and twist.

According to Hooker's stress-strain relation, the constitutive equations of an FG orthotropic cylindrical shell are as follows

$$\begin{Bmatrix} \sigma_x \\ \sigma_y \\ \tau_{xy} \end{Bmatrix} = \begin{bmatrix} C_{11} & C_{12} & 0 \\ C_{21} & C_{22} & 0 \\ 0 & 0 & C_{66} \end{bmatrix} \begin{Bmatrix} \varepsilon_x \\ \varepsilon_y \\ \gamma_{xy} \end{Bmatrix} \tag{6.6}$$

and

$$\begin{Bmatrix} \varepsilon_x \\ \varepsilon_y \\ \gamma_{xy} \end{Bmatrix} = \begin{bmatrix} 1/E_x & -v_{yx}/E_y & 0 \\ -v_{xy}/E_x & 1/E_y & 0 \\ 0 & 0 & 1/G_{xy} \end{bmatrix} \begin{Bmatrix} \sigma_x \\ \sigma_y \\ \tau_{xy} \end{Bmatrix} \tag{6.7}$$

where the elastic constants for orthotropic materials C_{ij} (i,j=1,2,6) are given in the following

$$\begin{cases} C_{11} = \dfrac{E_x}{1 - v_{xy} v_{yx}} \\ C_{12} = \dfrac{E_y v_{xy}}{1 - v_{xy} v_{yx}} \\ C_{21} = \dfrac{E_x v_{yx}}{1 - v_{xy} v_{yx}} \\ C_{22} = \dfrac{E_y}{1 - v_{xy} v_{yx}} \\ C_{66} = G_{xy} \end{cases} \tag{6.8}$$

where E_x, E_y, v_{xy}, and v_{yx} are the moduli of elasticity and Poisson ratios in x and y directions, respectively. For an FG orthotropic cylindrical shell, it has $E_x v_{yx} = E_y v_{xy}$. G_{xy} is the shear modulus. E_x, E_y and G_{xy} are in an exponential function form, as shown in Eq.(6.1).

Therefore, Eq.(6.6) can be further formulated as

$$\begin{cases} \sigma_x = C_{11} \varepsilon_x + C_{12} \varepsilon_y \\ \sigma_y = C_{21} \varepsilon_x + C_{22} \varepsilon_y \\ \tau_{xy} = C_{66} \gamma_{xy} \end{cases} \tag{6.9}$$

The internal forces N_x, N_y, N_{xy} and the moment resultants M_x, M_y, M_{xy} of the FG orthotropic cylindrical shell can be defined in terms of the stress components in Eq.(6.9) across the thickness direction as

$$\left\{ \left(N_x, N_y, N_{xy} \right), \left(M_x, M_y, M_{xy} \right) \right\} = \int_{-h/2}^{h/2} \left\{ \sigma_x, \sigma_y, \tau_{xy} \right\} (1, z) dz \tag{6.10}$$

Inserting Eqs.(6.3)-(6.7) into Eq.(6.10) gives the constitutive relations in matrix form as

$$
\begin{Bmatrix} N_x \\ N_y \\ N_{xy} \end{Bmatrix} = \begin{bmatrix} A_{11} & A_{12} & 0 \\ A_{21} & A_{22} & 0 \\ 0 & 0 & A_{66} \end{bmatrix} \begin{Bmatrix} \varepsilon_x^0 \\ \varepsilon_y^0 \\ \gamma_{xy}^0 \end{Bmatrix} + \begin{bmatrix} B_{11} & B_{12} & 0 \\ B_{21} & B_{22} & 0 \\ 0 & 0 & B_{66} \end{bmatrix} \begin{Bmatrix} \kappa_x \\ \kappa_y \\ 2\kappa_{xy} \end{Bmatrix}
$$

$$
\begin{Bmatrix} M_x \\ M_y \\ M_{xy} \end{Bmatrix} = \begin{bmatrix} B_{11} & B_{12} & 0 \\ B_{21} & B_{22} & 0 \\ 0 & 0 & B_{66} \end{bmatrix} \begin{Bmatrix} \varepsilon_x^0 \\ \varepsilon_y^0 \\ \gamma_{xy}^0 \end{Bmatrix} + \begin{bmatrix} D_{11} & D_{12} & 0 \\ D_{21} & D_{22} & 0 \\ 0 & 0 & D_{66} \end{bmatrix} \begin{Bmatrix} \kappa_x \\ \kappa_y \\ 2\kappa_{xy} \end{Bmatrix} \tag{6.11}
$$

Then, Eq.(6.11) can be further simplified as

$$
\{N\} = \boldsymbol{A}\{\varepsilon\} + \boldsymbol{B}\{\kappa\}, \{M\} = \boldsymbol{B}\{\varepsilon\} + \boldsymbol{D}\{\kappa\} \tag{6.12}
$$

where ***A***, ***B*** and ***D*** are the matrixes about A_{ij}, B_{ij} and D_{ij} (i, j=1,2,6). Using the matrix calculus, the following equations can be obtained

$$
\{\varepsilon\} = \boldsymbol{A}^*\{N\} + \boldsymbol{B}^*\{\kappa\}, \{M\} = \boldsymbol{C}^*\{N\} + \boldsymbol{D}^*\{\kappa\} \tag{6.13}
$$

where $\boldsymbol{A}^*=\boldsymbol{A}^{-1}$, $\boldsymbol{B}^*=-\boldsymbol{A}^{-1}\mathbf{B}$, $\boldsymbol{C}^*=\boldsymbol{B}\boldsymbol{A}^{-1}=-(\boldsymbol{B}^*)^{\mathrm{T}}$ and $\boldsymbol{D}^*=\boldsymbol{D}-\boldsymbol{B}\boldsymbol{A}^{-1}\boldsymbol{B}$.

By solving Eq.(6.13), the normal strains, shear strain at the middle surface can be obtained

$$
\begin{aligned}
\varepsilon_x^0 &= \frac{A_{22}N_x - A_{12}N_y - A_{22}(B_{11}\kappa_x + B_{12}\kappa_y) + A_{12}(B_{21}\kappa_x + B_{22}\kappa_y)}{A_{11}A_{22} - A_{21}A_{12}} \\
\varepsilon_y^0 &= -\frac{A_{21}N_x - A_{11}N_y - A_{21}(B_{11}\kappa_x + B_{12}\kappa_y) + A_{11}(B_{21}\kappa_x + B_{22}\kappa_y)}{A_{11}A_{22} - A_{21}A_{12}} \\
\gamma_{xy}^0 &= \frac{N_{xy} - 2B_{66}\kappa_{xy}}{A_{66}}
\end{aligned} \tag{6.14}
$$

where A_{ij} and B_{ij} (i,j=1,2,6) are given in the following.

$$A_{11}=\int_{-h/2}^{h/2}\frac{E_x}{1-\nu_{xy}\nu_{yx}}dz,\ A_{12}=\int_{-h/2}^{h/2}\frac{E_y\nu_{xy}}{1-\nu_{xy}\nu_{yx}}dz,\ A_{21}=\int_{-h/2}^{h/2}\frac{E_x\nu_{yx}}{1-\nu_{xy}\nu_{yx}}dz,$$
$$A_{22}=\int_{-h/2}^{h/2}\frac{E_y}{1-\nu_{xy}\nu_{yx}}dz,\ A_{66}=\int_{-h/2}^{h/2}G_{xy}dz,\ B_{11}=\int_{-h/2}^{h/2}\frac{E_x z}{1-\nu_{xy}\nu_{yx}}dz,$$
$$B_{12}=\int_{-h/2}^{h/2}\frac{E_y\nu_{xy}z}{1-\nu_{xy}\nu_{yx}}dz,\ B_{21}=\int_{-h/2}^{h/2}\frac{E_x\nu_{yx}z}{1-\nu_{xy}\nu_{yx}}dz,\ B_{22}=\int_{-h/2}^{h/2}\frac{E_y z}{1-\nu_{xy}\nu_{yx}}dz, \tag{6.15}$$
$$B_{66}=\int_{-h/2}^{h/2}G_{xy}zdz,\ D_{11}=\int_{-h/2}^{h/2}\frac{E_x z^2}{1-\nu_{xy}\nu_{yx}}dz,\ D_{12}=\int_{-h/2}^{h/2}\frac{E_y\nu_{xy}z^2}{1-\nu_{xy}\nu_{yx}}dz,$$
$$D_{21}=\int_{-h/2}^{h/2}\frac{E_x\nu_{yx}z^2}{1-\nu_{xy}\nu_{yx}}dz,\ D_{22}=\int_{-h/2}^{h/2}\frac{E_y z^2}{1-\nu_{xy}\nu_{yx}}dz,\ D_{66}=\int_{-h/2}^{h/2}G_{xy}z^2dz$$

Similarly, from Eq.(6.13) the moment resultants can be obtained

$$\begin{aligned} M_x &= B_{11}\varepsilon_x^0 + B_{12}\varepsilon_y^0 + D_{11}\kappa_x + D_{12}\kappa_y \\ M_y &= B_{21}\varepsilon_x^0 + B_{22}\varepsilon_y^0 + D_{21}\kappa_x + D_{22}\kappa_y \\ M_{xy} &= B_{66}\gamma_{xy}^0 + 2D_{66}\kappa_{xy} \end{aligned} \tag{6.16}$$

6.2.3 *Equations of motion and the nonlinear compatibility equation for orthotropic FG cylindrical shell*

The equations of motion for an eccentricity orthotropic FGMs cylindrical shell surrounded by Winkler-Pasternak elastic foundation subjected to a linearly increasing load are derived based on Hamilton's principle. According to this theory, the following equation is given

$$\int_0^T(\delta U_s+\delta U_e+\delta V_e+\delta V_d-\delta K)dt=0 \tag{6.17}$$

where δU_s, δU_e, δV_e, δV_d and δK are the virtual variation of the strain energy of the orthotropic FG cylindrical shell, the virtual variation of potential energy stored in the deformed elastic foundation, the variation of work done by the external load (linearly increasing load), the virtual variation of potential energy of non-conservative forces (i.e. damping effect in this chapter) and the virtual variation of the kinetic energy, respectively. Firstly, the expression of the virtual strain energy is given by

$$\delta U_s = \int_0^{2\pi R}\int_0^L\int_{-h/2}^{h/2}\left(\sigma_x\delta\varepsilon_x + \sigma_y\delta\varepsilon_y + \tau_{xy}\delta\gamma_{xy}\right)dxdydz \tag{6.18}$$

The virtual variation of potential energy stored in the deformed softening nonlinear elastic foundation can be expressed by

$$\delta U_e = \int_0^{2\pi R}\int_0^L\left[\begin{array}{l} k_w\left(w-w_0\right)\delta(w-w_0) + \\ \frac{1}{2}k_p(w-w_0)_{,x}\delta(w-w_0)_{,x} + \frac{1}{2}k_p(w-w_0)_{,y}\delta(w-w_0)_{,y}\end{array}\right]dxdy \tag{6.19}$$

where k_w is Winkler foundation modulus and k_p is the shear layer foundation stiffness of Pasternak model, respectively. The variation of work done by the external load (linearly increasing load) can be described by the following equation

$$\delta V_e = -ph\int_0^{2\pi R}\int_0^L u_{,x}\delta u_{,x}dxdy \tag{6.20}$$

By substituting the displacement component from Eq.(6.3) into δV_e, the following equation can obtain

$$\begin{aligned}\delta V_e &= -ph\int_0^{2\pi R}\int_0^L u_{,x}\delta u_{,x}dxdy \\ &= -ph\int_0^{2\pi R}\int_0^L \begin{array}{c}\left[\varepsilon_x^0 - \frac{1}{2}\left(\frac{\partial w}{\partial x}\right)^2 + \frac{1}{2}\left(\frac{\partial w_0}{\partial x}\right)^2\right] \\ \delta\left[\varepsilon_x^0 - \frac{1}{2}\left(\frac{\partial w}{\partial x}\right)^2 + \frac{1}{2}\left(\frac{\partial w_0}{\partial x}\right)^2\right]\end{array} dxdy\end{aligned} \tag{6.21}$$

where p is the average axial stress of the applied external force. The virtual variation of potential energy of non-conservative forces due to damping effect can be expressed as follows

$$\delta V_d = \rho_t \int_0^{2\pi R} \int_0^L c_d (\dot{u}\delta u + \dot{v}\delta v + \dot{w}\delta w) dxdy \tag{6.22}$$

where c_d denotes the damping coefficient of the structure. The virtual variation of the kinetic energy is given by

$$\delta K = \rho_t \int_0^{2\pi R} \int_0^L (\ddot{u}\delta u + \ddot{v}\delta v + \ddot{w}\delta w) dxdy \tag{6.23}$$

Recalling Eq.(6.10) and substituting Eqs.(6.18)-(6.23) into Eq.(6.17), then integrating the equation by parts and rearranging the coefficients of δu, δv and δw leads to the nonlinear dynamic equilibrium equations for an eccentrically FG orthotropic cylindrical shell surrounded by a Winkler-Pasternak elastic foundation with the consideration of damping effect based on classical shell theory

$$\delta u: \frac{\partial N_x}{\partial x} + \frac{\partial N_{yx}}{\partial y} = \rho_t \frac{\partial^2 u}{\partial t^2} + c_d \rho_t \frac{\partial u}{\partial t} \tag{6.24}$$

$$\delta v: \frac{\partial N_{xy}}{\partial x} + \frac{\partial N_y}{\partial y} = \rho_t \frac{\partial^2 v}{\partial t^2} + c_d \rho_t \frac{\partial v}{\partial t} \tag{6.25}$$

$$\begin{aligned} \delta w: N_x \frac{\partial^2 w}{\partial x^2} + N_y \frac{\partial^2 w}{\partial y^2} + 2N_{xy} \frac{\partial^2 w}{\partial x \partial y} + \frac{\partial^2 M_x}{\partial x^2} + \frac{\partial^2 M_y}{\partial y^2} + 2\frac{\partial^2 M_{xy}}{\partial x \partial y} + \frac{N_y}{R} \\ -k_w (w - w_0) + k_p \frac{\partial^2 (w - w_0)}{\partial x^2} + k_p \frac{\partial^2 (w - w_0)}{\partial y^2} = \rho_t \frac{\partial^2 w}{\partial t^2} + c_d \rho_t \frac{\partial w}{\partial t} \end{aligned} \tag{6.26}$$

where

$$\rho_t = \int_{-h/2}^{h/2} \rho(z)dz = \int_{-h/2}^{h/2} \rho_0 \psi_2(z)dz \tag{6.27}$$

Based on the assumption[227], $u \ll w$ and $v \ll w$, $\frac{\partial^2 u}{\partial t^2}$, $\frac{\partial u}{\partial t}$, $\frac{\partial^2 v}{\partial t^2}$ and $\frac{\partial v}{\partial t}$ approach to 0. Thus, considering Eqs.(6.24) and (6.25), the Airy's stress function $F(x,y)$ is defined as follows

$$\sigma_x = \frac{\partial^2 F(x,y)}{\partial y^2}, \sigma_y = \frac{\partial^2 F(x,y)}{\partial x^2}, \tau_{xy} = -\frac{\partial^2 F(x,y)}{\partial x \partial y} \tag{6.28}$$

By differentiating ε_x^0, ε_y^0, γ_{xy}^0 from Eq.(6.3) twice with respect to y, x and x, y ,respectively, one can obtain the nonlinear kinematic compatibility equilibrium as

$$\begin{aligned} &\frac{\partial^2 \varepsilon_x^0}{\partial y^2} + \frac{\partial^2 \varepsilon_y^0}{\partial x^2} - \frac{\partial^2 \gamma_{xy}^0}{\partial x \partial y} = \left(\frac{\partial^2 w}{\partial x \partial y}\right)^2 - \frac{\partial^2 w}{\partial^2 y}\frac{\partial^2 w}{\partial^2 x} - \left(\frac{\partial^2 w_0}{\partial x \partial y}\right)^2 + \frac{\partial^2 w_0}{\partial^2 y}\frac{\partial^2 w_0}{\partial^2 x} \\ &-\frac{1}{R}\frac{\partial^2 (w - w_0)}{\partial x^2} \end{aligned} \tag{6.29}$$

With Eq.(6.28), substituting Eq.(6.14) into Eq.(6.29), the nonlinear kinematic compatibility equilibrium equation can be rewritten as

$$\begin{aligned} &h\left[A_{11}^* \frac{\partial^4 F}{\partial x^4} + (A_{12}^* + A_{21}^* + A_{66}^*)\frac{\partial^4 F}{\partial x^2 \partial y^2} + A_{22}^* \frac{\partial^4 F}{\partial y^4}\right] - B_{11}^* \frac{\partial^4 (w - w_0)}{\partial x^4} \\ &-(B_{12}^* + B_{21}^* - B_{66}^*)\frac{\partial^4 (w - w_0)}{\partial x^2 \partial y^2} - B_{22}^* \frac{\partial^4 (w - w_0)}{\partial y^4} \\ &= \left(\frac{\partial^2 w}{\partial x \partial y}\right)^2 - \frac{\partial^2 w}{\partial^2 y}\frac{\partial^2 w}{\partial^2 x} - \left(\frac{\partial^2 w_0}{\partial x \partial y}\right)^2 + \frac{\partial^2 w_0}{\partial^2 y}\frac{\partial^2 w_0}{\partial^2 x} - \frac{1}{R}\frac{\partial^2 (w - w_0)}{\partial x^2} \end{aligned} \tag{6.30}$$

where A_{ij}^* and B_{ij}^* (i,j=1,2,6) are given in the following.

$$
\begin{aligned}
&\Delta = A_{11}A_{22} - A_{12}A_{21};\\
&A_{11}^* = \frac{A_{11}}{\Delta}; A_{12}^* = -\frac{A_{12}}{\Delta}; A_{21}^* = -\frac{A_{21}}{\Delta}; A_{22}^* = \frac{A_{22}}{\Delta}\\
&B_{11}^* = \frac{B_{11}A_{21} - B_{21}A_{11}}{\Delta}; B_{12}^* = \frac{B_{12}A_{21} - B_{22}A_{11}}{\Delta};\\
&B_{21}^* = \frac{B_{21}A_{12} - B_{11}A_{22}}{\Delta}; B_{22}^* = \frac{B_{22}A_{12} - B_{12}A_{22}}{\Delta};\\
&A_{66}^* = \frac{1}{A_{66}}; B_{66}^* = -\frac{2B_{66}}{A_{66}}
\end{aligned}
\tag{6.31}
$$

With Eqs.(6.11), (6.16), substituting Eq.(6.28) into Eq.(6.26), nonlinear dynamic buckling equation for an eccentrically FG orthotropic cylindrical shell surrounded by a Winkler-Pasternak elastic foundation with the consideration of damping effect can be obtained as

$$
\begin{aligned}
&h\left[C_{12}^* \frac{\partial^4 F}{\partial x^4} + \left(C_{11}^* - 2C_{66}^* + C_{22}^*\right)\frac{\partial^4 F}{\partial x^2 \partial y^2} + C_{21}^* \frac{\partial^4 F}{\partial y^4}\right]\\
&-D_{11}^* \frac{\partial^4 \left(w - w_0\right)}{\partial x^4} - (D_{12}^* + 2D_{66}^* + D_{21}^*)\frac{\partial^4 (w - w_0)}{\partial x^2 \partial y^2} - D_{22}^* \frac{\partial^4 (w - w_0)}{\partial y^4}\\
&+\frac{h}{R}\frac{\partial^2 F}{\partial x^2} + h\left[\frac{\partial^2 F}{\partial y^2}\frac{\partial^2 w}{\partial x^2} - 2\frac{\partial^2 F}{\partial x \partial y}\frac{\partial^2 w}{\partial x \partial y} + \frac{\partial^2 F}{\partial x^2}\frac{\partial^2 w}{\partial y^2}\right]\\
&-k_w(w - w_0) + k_p \frac{\partial^2 (w - w_0)}{\partial x^2} + k_p \frac{\partial^2 (w - w_0)}{\partial y^2}\\
&= \rho_t \frac{\partial^2 w}{\partial t^2} + c_d \rho_t \frac{\partial w}{\partial t}
\end{aligned}
\tag{6.32}
$$

where C_{ij}^* and D_{ij}^* (i,j=1,2,6) are given in the following.

$$
\begin{aligned}
&C_{11}^{*}=B_{11}A_{22}^{*}+B_{12}A_{21}^{*};C_{12}^{*}=B_{11}A_{12}^{*}+B_{12}A_{11}^{*};\\
&C_{21}^{*}=B_{21}A_{22}^{*}+B_{22}A_{21}^{*};C_{22}^{*}=B_{21}A_{12}^{*}+B_{22}A_{11}^{*};\\
&D_{11}^{*}=B_{11}B_{21}^{*}+B_{12}B_{11}^{*}+D_{11};D_{12}^{*}=B_{11}B_{22}^{*}+B_{12}B_{12}^{*}+D_{12};\\
&D_{21}^{*}=B_{21}B_{21}^{*}+B_{22}B_{11}^{*}+D_{21};D_{22}^{*}=B_{21}B_{22}^{*}+B_{22}B_{12}^{*}+D_{22};\\
&C_{66}^{*}=B_{66}A_{66}^{*};D_{66}^{*}=B_{66}B_{66}^{*}+2D_{66}
\end{aligned}
\tag{6.33}
$$

6.3 Static buckling and dynamic buckling analysis of an FG orthotropic cylindrical shell surrounded by Winkler-Pasternak elastic foundation

6.3.1 *Solution of the governing equations*

The deflection function for a simply supported boundary condition cylindrical shell is assumed to be the single mode [74], which means w equals to 0 at x=0, L and at y=0,2πR.

$$
w(x,y,t)=W_{mn}(t)\sin(\alpha x)\sin(\beta y) \tag{6.34}
$$

where $W_{mn}(t)$ is the time-varying amplitude of w , and $\alpha=m\pi/L$ and $\beta=n/R$ are the number of half waves in the x and y directions, respectively. Moreover, other boundary conditions can be considered if one selects the proper trigonometric admissible functions[75].

Also, the initial shape function can be taken as

$$
w_0(x,y)=W_0\sin(\alpha x)\sin(\beta y) \tag{6.35}
$$

where W_0 represents the initial eccentricity value of the cylindrical shell.

Substituting Eq.(6.34) and Eq.(6.35) into the nonlinear compatibility Eq.(6.30), a solution is given

$$
\begin{aligned}
F(x,y,t) &= \frac{\beta^2}{32\alpha^2 A_{11}^* h}(W_{mn}^2 - W_0^2)\cos(2\alpha x) \\
&+ \frac{\alpha^2}{32\beta^2 A_{22}^* h}(W_{mn}^2 - W_0^2)\cos(2\beta y) \\
&+ \frac{B_{11}^*\alpha^4 + (B_{12}^* + B_{21}^* - B_{66}^*)\alpha^2\beta^2 + B_{22}^*\beta^4 + \dfrac{\alpha^2}{R}}{A_{11}^*\alpha^4 + (A_{12}^* + A_{21}^* + A_{66}^*)\alpha^2\beta^2 + A_{22}^*\beta^4}\frac{(W_{mn} - W_0)}{h}\sin(\alpha x)\sin(\beta y) \\
&- \frac{1}{2}p(t)y^2
\end{aligned}
\tag{6.36}
$$

Substituting Eqs.(6.34)-(6.36) into Eq.(6.32) and then applying the Galerkin method. Each term in Eq.(6.32) is multiplying with sin*(mπx/L)*sin*(ny/R)dxdy*, then integrating over the middle surface of the cylindrical shell, the equation of motion becomes

$$
\begin{aligned}
&\rho_t \frac{\partial^2 W_{mn}}{\partial t^2} + \rho_t c_d \frac{\partial W_{mn}}{\partial t} - \left[K_1 K_2 - K_3 - \left(k_w + k_p(\alpha^2 + \beta^2)\right)\right](W_{mn} - W_0) \\
&+ K_4 W_{mn}(W_{mn}^2 - W_0^2) - \alpha^2 h p(t) W_{mn} = 0
\end{aligned}
\tag{6.37}
$$

where K_1, K_2, K_3 and K_4 are given in the following.

$$
\begin{aligned}
K_1 &= C_{12}^*\alpha^4 + (C_{11}^* - 2C_{66}^* + C_{22}^*)\alpha^2\beta^2 + C_{21}^*\beta^4 - \frac{\alpha^2}{R} \\
K_2 &= \frac{B_{11}^*\alpha^4 + (B_{12}^* + B_{21}^* - B_{66}^*)\alpha^2\beta^2 + B_{22}^*\beta^4 + \dfrac{\alpha^2}{R}}{A_{11}^*\alpha^4 + (A_{12}^* + A_{21}^* + A_{66}^*)\alpha^2\beta^2 + A_{22}^*\beta^4} \\
K_3 &= D_{11}^*\alpha^4 + (D_{12}^* + 2D_{66}^* + D_{21}^*)\alpha^2\beta^2 + D_{22}^*\beta^4 \\
K_4 &= \frac{1}{16}\left(\frac{\alpha^4}{A_{22}^*} + \frac{\beta^4}{A_{11}^*}\right)
\end{aligned}
\tag{6.38}
$$

6.4 Buckling analysis of FG orthotropic cylindrical shell

6.4.1 *Static buckling analysis*

For an initially perfect FG orthotropic cylindrical shells, by omitting the velocity, acceleration and high-order terms, Eq.(6.37) can be reduced into

$$-\alpha^2 hpW_{mn} - \left(K_1K_2 - K_3\right)W_{mn} + \left(k_w + k_p(\alpha^2 + \beta^2)\right)W_{mn} = 0 \tag{6.39}$$

Eq.(6.39) is the linear static equation of the FG orthotropic cylindrical shell on an elastic foundation, which can also obtain from the corresponding static case using the linear theory. Then the static buckling load is

$$p_{st} = \frac{1}{\alpha^2 h}\left[K_3 - K_1K_2 + \left(k_w + k_p(\alpha^2 + \beta^2)\right)\right] \tag{6.40}$$

where the least static buckling load p_{cr}^{st} can also be obtained with respect to various modes (m, n), which can be further reduced into classical buckling load of the isotropic circular cylindrical shell by giving κ_i, k_w and k_p equal to 0, respectively. And the equation is given as follows

$$\sigma_{cr} = \frac{Eh}{R\sqrt{3(1-v^2)}} \tag{6.41}$$

6.4.2 *Nonlinear dynamic buckling analysis*

In this chapter, an eccentrically FG orthotropic simply supported cylindrical shell surrounded by a Winkler-Pasternak elastic foundation with the consideration of damping effect is subjected to a linearly increasing load p(t)=ct at the end of the boundary condition along the longitudinal direction, as shown in Figure 6.1. Here, introducing the following non-dimensional parameters and constants

$$W_{mn}^{*}=\frac{W_{mn}}{h},W_{0}^{*}=\frac{W_{0}}{h},\tau=\frac{p(t)}{p_{cr}^{st}}=\frac{ct}{p_{cr}^{st}},$$
$$J_{1}=\frac{\alpha^{2}h}{c^{2}\rho_{t}}(p_{cr}^{st})^{3}, \tag{6.42}$$
$$J_{2}=\frac{h^{2}(p_{cr}^{st})^{2}}{c^{2}\rho_{t}}K_{4},$$

where p_{cr}^{st} is depend on different modes (m, n). Normally, most of the structures buckling locate in low-order modes. Thus, in this chapter, we choose the top 30 modes, which means m=n=(1,2,3…30).

For the harmonic motion of FG orthotropic cylindrical shell, $W_{mn}(t)$ may be taken in the form

$$W_{mn}(t)=\sum_{m=1}^{\infty}\sum_{n=1}^{\infty}A\sin(\alpha x)\sin(\beta y)e^{i\omega_{mn}t} \tag{6.43}$$

where $W_{mn}(t)$ is the time-varying amplitude of w, A is the amplitude of the vibration, $i=\sqrt{-1}$, and $\alpha=m\pi/L$ and $\beta=n/R$ are the number of half waves in the x and y directions, respectively. Then substituting Eq.(6.43) into Eq.(6.37), the closed form expression for natural frequencies is obtained as follows

$$\omega_{mn}=\sqrt{\frac{1}{\rho_{t}}\left[K_{3}-K_{1}K_{2}+\left(k_{w}+k_{p}(\alpha^{2}+\beta^{2})\right)\right]},m,n=1,2,3,... \tag{6.44}$$

By considering the viscous damping as internal damping effects, one can obtain that

$$c_d = 2\omega_{mn}\zeta$$
$$c_d^* = c_d \frac{p_{cr}^{st}}{c} \tag{6.45}$$

where c_d denotes the damping coefficient of the structure; ω_{mn} denotes the circular natural frequency of the cylindrical shell corresponding to buckling mode (m, n); and ζ denotes the damping ratio of the cylindrical shell.

Therefore, the differential equations governing the nonlinear behaviour of an FG orthotropic cylindrical shell can be written in a non-dimensional form

$$\frac{\partial^2 W_{mn}^*}{\partial \tau^2} + c_d^* \frac{\partial W_{mn}^*}{\partial \tau} + J_1(W_{mn}^* - W_0^*) + J_2 W_{mn}^*(W_{mn}^{*\,2} - W_0^{*2}) - J_1 W_{mn}^* \tau = 0 \tag{6.46}$$

Eq.(6.46) can be solved by fourth-order Runge-Kutta method based on mathematical computing software MATLAB. m and n equal to (1,2,3…30) are considered in this equation, which means 900 ordinary differential equations are solved. Utilizing Budiansky-Roth criterion to search the buckling point at $\left.\frac{\partial^2 W_{mn}^*}{\partial \tau^2}\right|_{\tau=\tau_{cr}} = 0$, namely ($\tau_{cr}$, W_{mn}^*), then the least dynamic buckling load $p(t)=c\tau_{cr}$ is determined corresponding to mode (m, n). The initial conditions for the problem are $W_{mn}^*=W_0^*$ and $\partial W_{mn}^*/\partial \tau=0$ at $\tau=0$.

6.5 Numerical results and discussions

6.5.1 *Validation of proposed formulation*

In this section, the accuracy of proposed method is verified with published papers and the following dimensionless parameters are defined.

1. Dimensionless critical static buckling load of FG orthotropic cylindrical shell

$$p_{cr}^{st*} = \frac{p_{cr}^{st} L^2}{E_{02} h^3} \tag{6.47}$$

2. Dimensionless natural frequency of orthotropic plate

$$\omega_{mn}^{*} = L \cdot \sqrt[4]{\frac{\rho_t \omega_{mn}^2}{D_{11}^{*}}} \tag{6.48}$$

3. Dimensionless elastic constants of foundations may also be defined as follows [228]

$$k_w^{*} = \frac{k_w L^4}{D_{11}^{*}}, k_p^{*} = \frac{k_p L^2}{D_{11}^{*}} \tag{6.49}$$

Example 1. For Table 6.1, the dimensions of circular orthotropic cylindrical shell are E_{01}=275.8×10^9 Pa, E_{02}= 27.58×10^9 Pa, ν_{12}=0.25, ν_{21}=0.025, G_0=10.34×10^9 Pa, h =0.00254 m, R/h =100, L/R =2, ρ=1619.27 kg/m^3 from [229]. As can be seen, in this comparison study very good agreements are achieved and the average errors in different modes are just 0.008%-0.449%.

Table 6.1 Comparison of dimensionless axial static buckling load $p_{cr}^{st} L^2 / (E_{02} h^3)$ of S-S orthotropic cylindrical shell without Winkler-Pasternak elastic foundation with the results of Eq.(6.47) from Lee [229]

(m,n)	Lee [229]	Present method	Difference
(1,1)	78139.72	78145.73	0.008%
(1,2)	29556.79	29580.83	0.081%
(1,3)	13850.67	13904.75	0.390%

(2,1)	32341.27	32347.28	0.019%
(2,2)	19852.90	19876.93	0.121%
(2,3)	12046.73	12100.82	0.449%

To further validate the proposed method, the dynamic response of isotropic cylindrical shell of an S-S cylindrical shell without Winkler-Pasternak elastic foundation subjected to axial load is analysed by reducing damping effects and material's exponential function in Eq.(6.46). Figure 6.2 and Figure 6.3 show the time-deflection curve of an eccentricity simply supported orthotropic cylindrical shell subjected to linearly increasing load c_0 $=2.068\times10^9$ Pa/s, c_0 $=4.136\times10^9$ Pa/s with the results of Eq.(33) from Lee [229], respectively. The material properties are E_{01}=275.8×10^9 Pa, E_{02}= 27.58×10^9 Pa, v_{12}=0.25, v_{21}=0.025, G_0=10.34×10^9 Pa, h =0.00254 m, R/h =100, L/R =2, ρ=1619.27 kg/m^3 from [229]. As can be seen from Figure 6.2 and Figure 6.3, a very good agreement is obtained.

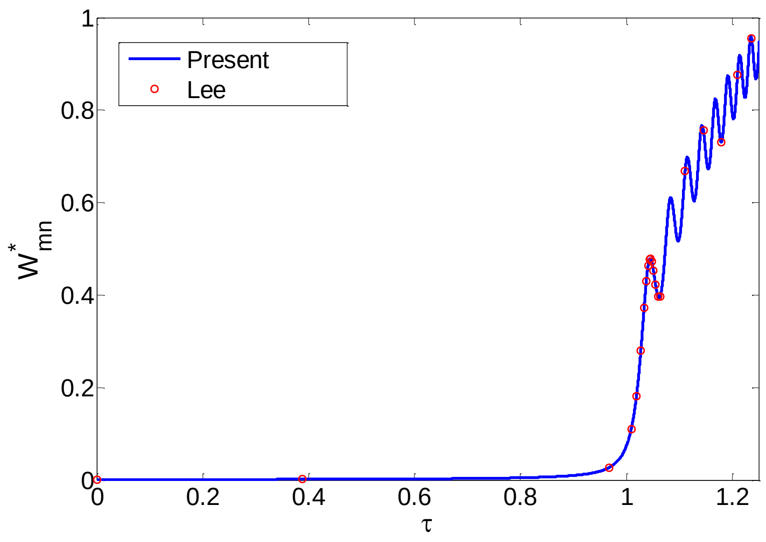

Figure 6.2 Comparison of the time-deflection curve of an eccentricity simply supported orthotropic cylindrical shell subjected to linearly increasing load c_0 $=2.068\times10^9$ Pa/s with Lee [229]

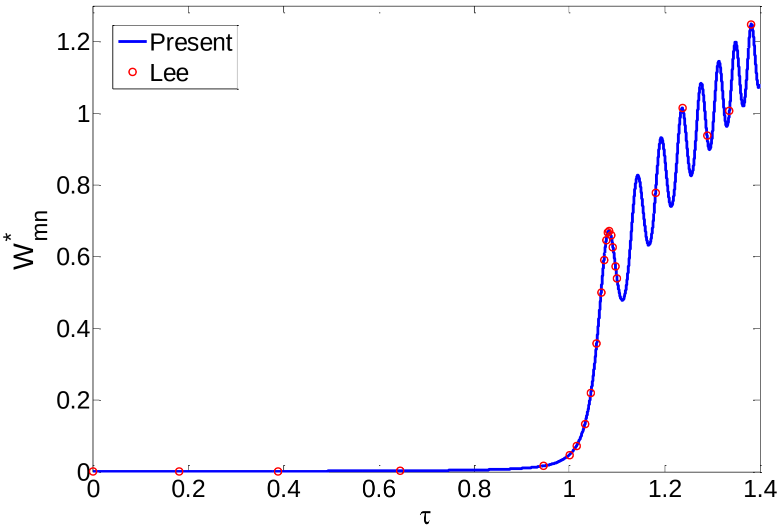

Figure 6.3 Comparison of the time-deflection curve of an eccentricity simply supported isotropic cylindrical shell subjected to linearly increasing load c_0 =4.136×10^9 Pa/s with Lee [229]

Table 6.2 Comparison of the natural frequencies (Hz) with experimental results by Sewall and Naumann [230] and other theoretical methods by Naeem and Sharma [231] of an S-S cylindrical shell without Winkler-Pasternak elastic foundation (*m*=1)

n	Present Method	Experimental results of Swall and Naumann[230]	Results of Trigonometric function by Naeem and Sharma [231]	Results of Ritz polynomial function by Naeem and Sharma [231]
6	168.01	175.0	166.59	166.59
7	167.56	163.0 and 169.0	166.22	166.22
8	190.33	188.0	189.26	189.29
9	227.39	224.0	226.88	226.88
10	273.88	268.0	274.07	274.09
11	327.59	326.0	328.62	328.64
12	387.51	382.0 and 385.0	389.49	389.49
13	453.20	440	456.21	456.21

Example 2. For Table 6.2, the comparison of the natural frequencies given by proposed method with the results of Swall and Naumann[230] based on experimental results,

Naeem and Sharma [231] based on trigonometric function and Ritz polynomial function of an S-S cylindrical shell without Winkler-Pasternak elastic foundation is suggested. The dimensions of circular isotropic cylindrical shell are $E_{01}=E_{02}=E_0$, $v_{12}=v_{21}=v_0$, the material properties are taken as E_0=68.95GPa, v_0=0.315, ρ=2714.5kg/m^3, h=0.648mm, R=242.3mm, L=609.6mm from Ref.[230, 231]. $G_0=E_0/2(1+v)$=26.22GPa. The results show that the proposed results are falling somewhere between Swall and Naumann[230] , Naeem and Sharma [231]. According to the comparisons from example 1 and 2, it is clear that the proposed method matches very well with the published journals and the reliability and accuracy of our method are validated.

6.5.2 *Results of natural frequencies and static buckling*

The results from Table 6.1 and Table 6.2 have verified the proposed methods. Additional effects of different (k_w^*, k_p^*) and E_{01}/E_{02} on natural frequencies ω_{mn}^* (calculated from Eq.(6.48)) and static buckling load $p_{cr}^{st^*}$ (calculated from Eq. (6.47)) of a simply supported orthotropic cylindrical shell are shown in Table 6.3. E_{02}=20.69GPa, v_{12}=0.3, v_{21}=0.03, ρ=1950kg/m^3, which were taken from Reddy's book[232]. The geometrical parameters are h=0.01m, L=5m, R=1.0m. E_{02} remain unchanged and E_{01} is variable with respect to the ratios. Clearly, for a fixed (k_w^*, k_p^*), the increasing of E_{01}/E_{02} causes the increase of the buckling load; while leading to the decrease of natural frequencies. One interesting finding is that the influence of modes (1,n) does not have specific laws. Moreover, with the increase of k_w^* and k_p^*, the natural frequencies and static buckling load become larger. While the influence of k_p^* is more pronounced than k_w^*, especially for the static buckling load.

Table 6.3 Comparison of natural frequencies ω_{mn}^{*} and static buckling load $p_{cr}^{st^{*}}$ of a simply supported orthotropic cylindrical shell surrounded by Winkler-Pasternak elastic foundations for different (k_w^*, k_p^*) and E_{01}/E_{02} (E_{02}=20.69GPa, m=1)

(k_w^*, k_p^*)	E_{01}/E_{02}	ω_{mn}^{*}			$p_{cr}^{st^{*}}$ (×10^6)		
		n =1	n =2	n =3	n=1	n =2	n =3
(0,0)	10	43.13	27.38	19.27	29.48	4.79	1.17
	20	39.44	27.03	19.15	41.23	9.09	2.29
	30	36.93	26.69	19.09	47.55	12.99	3.40
	40	35.06	26.40	19.06	51.50	16.53	4.50
(0,100)	10	43.14	27.51	20.04	29.51	4.88	1.37
	20	39.45	27.16	19.94	41.29	9.28	2.69
	30	36.95	26.84	19.89	47.64	13.27	4.00
	40	35.08	26.54	19.86	51.62	16.91	5.30
(100,0)	10	43.13	27.38	19.27	29.48	4.79	1.18
	20	39.44	27.03	19.16	41.23	9.09	2.30
	30	36.93	26.70	19.10	47.55	12.99	3.40
	40	35.06	26.39	19.06	51.50	16.54	4.50
(100,100)	10	43.14	27.51	20.04	29.51	4.88	1.38
	20	39.46	27.17	19.94	41.29	9.28	2.70
	30	36.95	26.84	19.89	47.64	13.27	4.00
	40	35.08	26.54	19.86	51.62	16.91	5.30

6.5.3 *Dynamic buckling of FG orthotropic cylindrical shell surrounded by Winkler-Pasternak elastic foundations subjected to a linearly increasing load*

In this section, the dynamic stability of an FG orthotropic circular cylindrical shell surrounded by a Winkler-Pasternak elastic foundation subjected to linearly increasing load with the consideration of damping effect is investigated. The nonlinear dynamic buckling Eq.(6.46) is solved by a hybrid analytical-numerical method (combined Galerkin method and fourth-order Runge-Kutta method). Then the nonlinear dynamic stability of the FG orthotropic cylindrical shell is assessed based on Budiansky-Roth criterion. Effects of different parameters such as various inhomogeneous parameters, loading speeds, damping ratios and aspect ratios and thickness ratios of the structure on dynamic buckling are discussed in detail. The material properties are E_{01}=275.8 GPa, E_{02}=27.58 GPa, v_{12}=0.25, v_{21}=0.025, ρ=1619.27kg/m^3. The geometrical parameters are h=0.00254m, R=100×h, L=2×R, G_0=10.34 GPa.

6.5.3.1 *The influence of different non-homogenous parameters κ_1*

According to Eq.(6.1), Young's moduli $E(z)$ and shear modulus $G(z)$ is governed by the exponential factor κ_1, while density $\rho(z)$ is governed by κ_2. All these material coefficients may influence the dynamic response of the FG orthotropic cylindrical shell. In this subsection, we focused on the effects of κ_1 (or Young's module and shear modulus) while κ_2 (or density) keeps invariable. Five different inhomogeneous parameters κ_i =-1, -0.5, 0, 0.5, 1 are selected. For κ_1 =0, Eq. (6.1) reduces to the homogeneous case; when κ_1 > 0, it corresponds to the graded stiff material while κ_1 <0 means graded soft material. The initial imperfection is W_0=0.001×h. And the loading speed c=4.137e9 Pa/s.

The initial conditions for the problem are $W_{mn}^* = W_0^* = 0.001$ and $\partial W_{mn}^* / \partial \tau = 0$ at $\tau = 0$. The dynamic buckling point at $\partial^2 W_{mn}^* / \partial \tau^2 \big|_{\tau=\tau_{cr}} = 0$ based on Budiansky-Roth criterion by considering m and n equal to (1, 2, 3…30). Then the least dynamic buckling load $p(t)=c\tau_{cr}$ is determined corresponding to different modes (m, n). Figure 6.4 shows the effects of different κ_1 on the dimensionless time-deflection curve of a simply supported FG orthotropic cylindrical shell subjected to linearly increasing load c=4.137GPa/s. It is clear that for all the cases, critical buckling time $\tau_{cr}>1$, which means dynamic critical buckling loads is larger than the static ones. With the increase of inhomogeneous parameters κ_1, critical buckling time τ_{cr} decreases but dynamic buckling loads and the vibration of the structure increase. This is due to the increase of κ_1 would lead to the increasing of shell stiffness. Similar results also obtained from Table 6.4. Furthermore, one interesting finding is that when the shell becomes stiffer, the dynamic buckling mode (m, n) jumps from (1, 23) to (1, 11), as shown in Table 6.4.

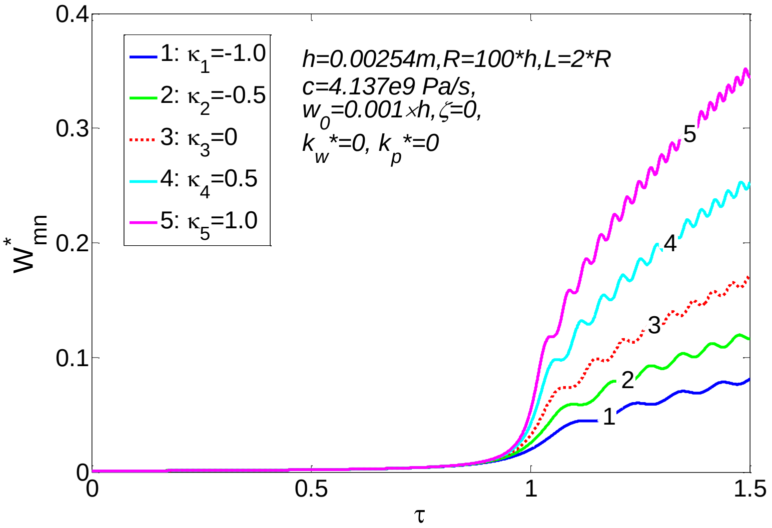

Figure 6.4 The dimensionless time-deflection curve of a simply supported FG orthotropic cylindrical shell subjected to linearly increasing load c=4.137 GPa/s for different κ_1

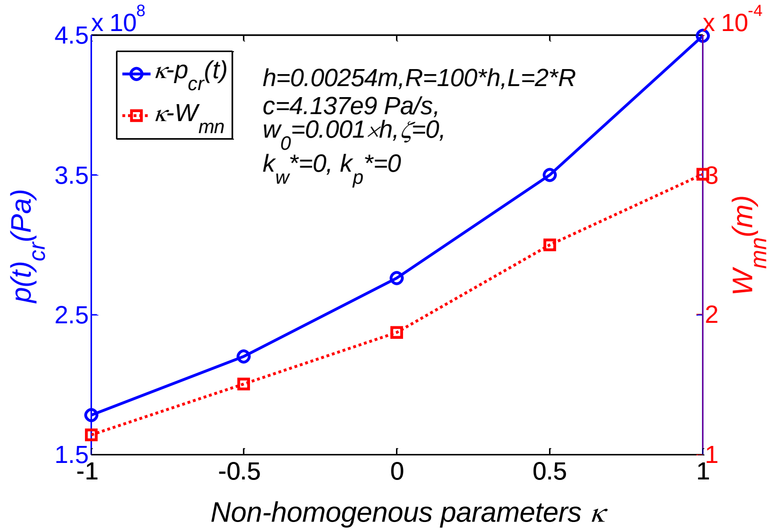

Figure 6.5 The effects of different κ_1 on $p(t)_{cr}$ and W_{mn} of a simply supported FG orthotropic cylindrical shell subjected to linearly increasing load c =4.137 GPa/s

The effects of different κ_1 on $p(t)_{cr}$ and W_{mn} is shown in Figure 6.5. The blue circular represents κ-$p(t)_{cr}$ curve while the red rectangular refers to κ-W_{mn} curve. Both of them increase significantly when the materials become stiffer.

6.5.3.2 *The influence of different non-homogenous parameters κ_2*

Effects of inhomogeneous parameters κ_2 are investigated in this subsection. As shown before, five different κ_2=-1, -0.5, 0, 0.5, 1 are selected. κ_1 (or Young's module and shear modulus) keeps invariable while holding all other parameters fixed.

Figure 6.6 depicts the dimensionless time-deflection curve of a simply supported FG orthotropic cylindrical shell subjected to linearly increasing load c=4.137e9 Pa/s for different κ_2. The increase in κ_2 would increase the dynamic buckling load but the growth rate is prolonged. For example, κ_2 change from -1.0 to 1.0, the dynamic buckling loads increase by 1.025 times, as shown in Table 6.4. The dynamic buckling mode (m, n) also changes from (1, 14) to (1, 18) while the critical static buckling load keeps constant.

The effects of different κ_2 on $p(t)_{cr}$ and W_{mn} also illustrated in Figure 6.7. A similar phenomenon can also be witnessed that dynamic buckling load increases slowly with the increase of κ_2. However, the deflection of W_{mn} decreases by 1.4 times with the increase of κ_2, as shown in Table 6.4.

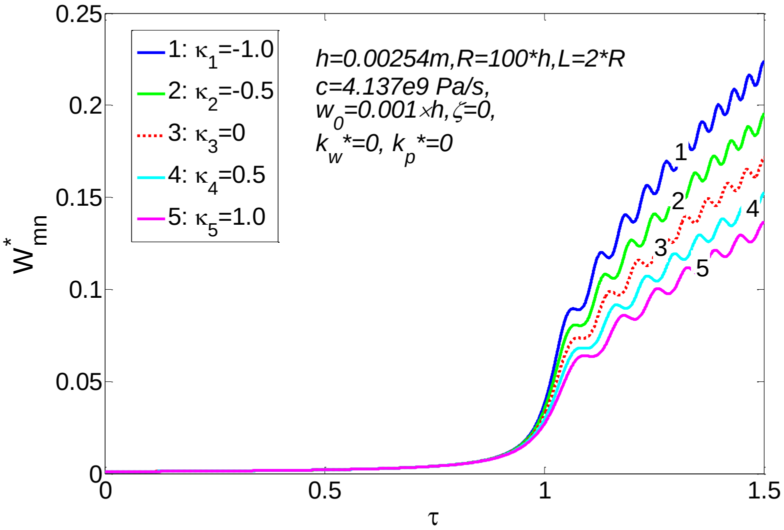

Figure 6.6 The dimensionless time-deflection curve of a simply supported FG orthotropic cylindrical shell subjected to linearly increasing load c=4.137 GPa/s for different κ_2

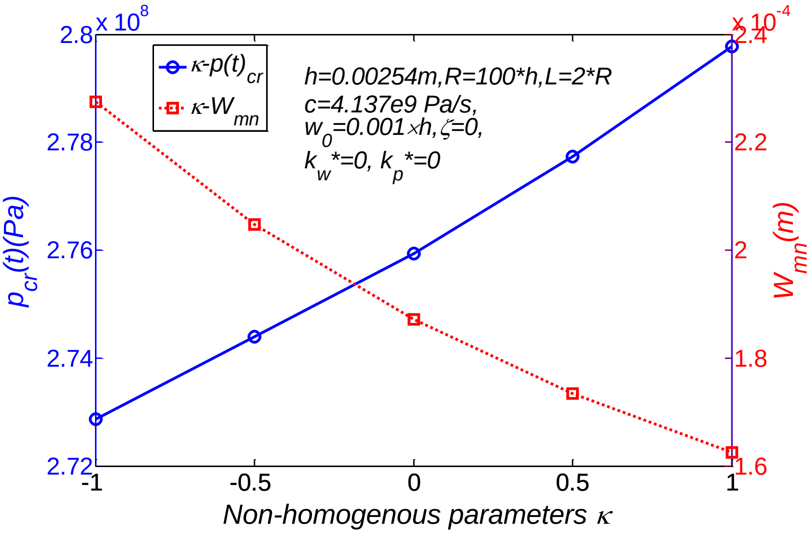

Figure 6.7 The effects of different κ_2 on $p(t)_{cr}$ and W_{mn} of a simply supported FG orthotropic cylindrical shell subjected to linearly increasing load c =4.137GPa/s

6.5.3.3 *The combined effects of κ_1 and κ_2 on dynamic buckling responses*

In the subsections 6.5.3.1 and 6.5.3.2, the effects of κ_1, κ_2 on the dynamic buckling of an FG orthotropic cylindrical shell has been presented, respectively. As can be seen, both of them have a significant influence on dynamic buckling responses. Therefore, it is obvious for us to investigate the combined effects of these two parameters.

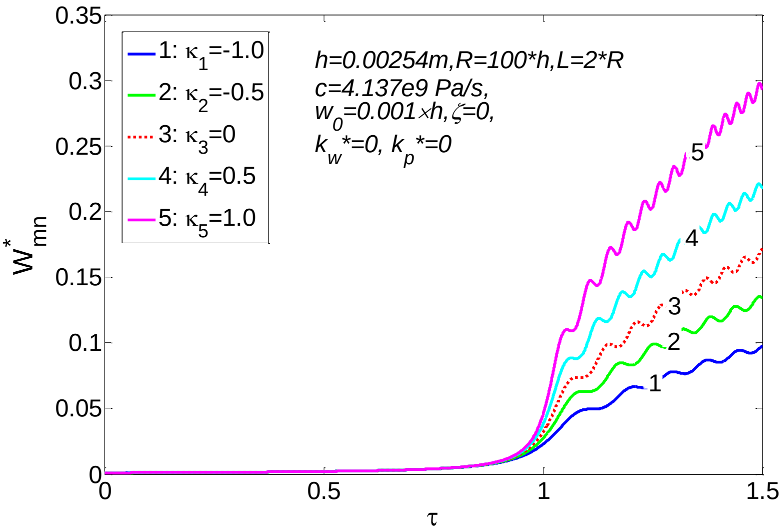

Figure 6.8 The dimensionless time-deflection curve of a simply supported FG orthotropic cylindrical shell subjected to linearly increasing load c=4.137GPa/s for different κ_1 and κ_2

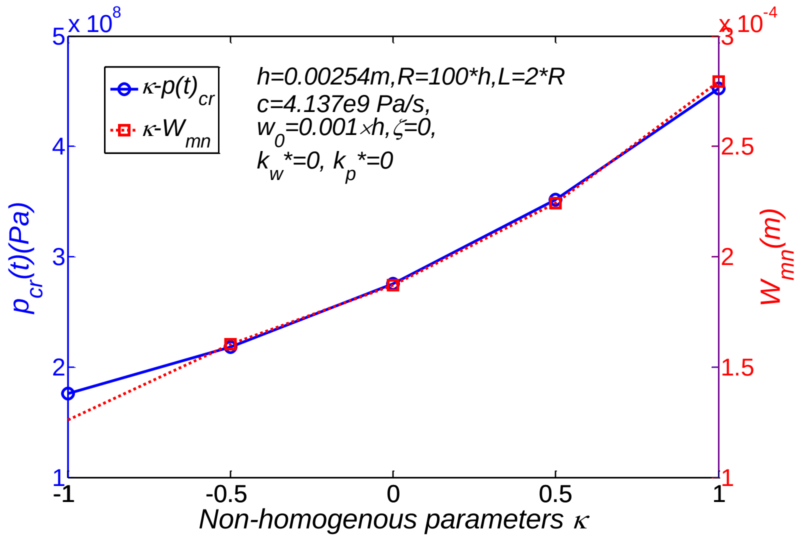

Figure 6.9 The effects of different κ_1 and κ_2 on $p(t)_{cr}$ and W_{mn} of a simply supported FG orthotropic cylindrical shell subjected to linearly increasing load c=4.137GPa/s

Table 6.4 Comparison of critical buckling time τ_{cr}, static critical buckling load p_{cr}^{st}, dynamic critical buckling load p_{cr}^{dy} and deflection W_{mn} for various material exponential factor κ_i

Material gradient	κ_i	τ_{cr}	p_{cr}^{st} (Pa)	p_{cr}^{dy} (Pa)	W_{mn} (m)
κ_1 (or Young's module and shear modulus) change, κ_2 (or density) keeps constant	-1	1.127	1.58E+08(3,8)	1.78E+08(1,23)	1.14E-04
	-0.5	1.099	2.00E+08(3,8)	2.2E+08(1,19)	1.50E-04
	0	1.078	2.56E+08(3,8)	2.76E+08(1,16)	1.87E-04
	0.5	1.06	3.30E+08(3,8)	3.5E+08(1,13)	2.50E-04
	1	1.046	4.30E+08(3,8)	4.49E+08(1,11)	3.00E-04
κ_1 keeps constant, κ_2 change	-1	1.066	2.56E+08(3,8)	2.73E+08(1,14)	2.27E-04
	-0.5	1.072	2.56E+08(3,8)	2.74E+08(1,15)	2.05E-04
	0	1.078	2.56E+08(3,8)	2.76E+08(1,16)	1.87E-04
	0.5	1.085	2.56E+08(3,8)	2.78E+08(1,17)	1.73E-04
	1	1.093	2.56E+08(3,8)	2.8E+08(1,18)	1.63E-04
Both κ_1 and κ_2 change	-1	1.111	1.58E+08(3,8)	1.76E+08(1,21)	1.26E-04
	-0.5	1.09	2.00E+08(3,8)	2.18E+08(1,18)	1.60E-04
	0	1.077	2.56E+08(3,8)	2.76E+08(1,16)	1.87E-04
	0.5	1.065	3.30E+08(3,8)	3.52E+08(1,14)	2.24E-04
	1	1.053	4.30E+08(3,8)	4.52E+08(1,12)	2.79E-04

Figure 6.8 gives the comparison of different κ_1 and κ_2 on the dimensionless time-deflection curve of an FG orthotropic cylindrical shell. Both κ_1 and κ_2 increase simultaneously while keeps other parameters unchanged. With the increase of non-homogenous parameters κ, the critical buckling time τ_{cr} decreases but dynamic buckling loads and the vibration of the structure increase. And the dynamic buckling mode (m, n)

jumps significantly from (1, 21) to (1, 12), as shown in Table 6.4. The effects of different κ_1 and κ_2 on $p(t)_{cr}$ and W_{mn} also shown in Figure 6.9. Both κ-$p(t)_{cr}$ curve and κ-W_{mn} curve increase simultaneously with the increase of non-homogenous parameters κ. From subsection 6.5.3.1 to 6.5.3.3, it is clear that both κ_1 and κ_2 have an impact on dynamic buckling responses; while the influence of κ_1 is more prominent than that of κ_2.

6.5.3.4 ***The influence of various linearly increasing loads***

As one of the major coefficients in governing Eqs. (6.37), (6.46), the linearly increasing load has a significant effect on dynamic buckling load[102, 112]. Therefore, it is essential to study the impact of different loading speeds acting on an FG orthotropic cylindrical shell. The exponential factor or material gradient in this subsection chooses κ_i =1.0. Three different loading speeds c equals to 4.137GPa/s, 8.274GPa/s and 16.55GPa/s are discussed.

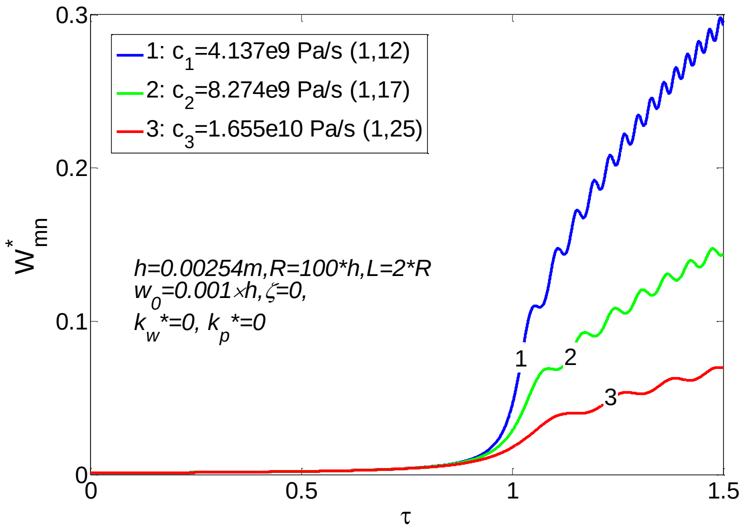

Figure 6.10 The dimensionless time-deflection curve of a simply supported FG orthotropic cylindrical shell subjected to different linearly increasing loads c

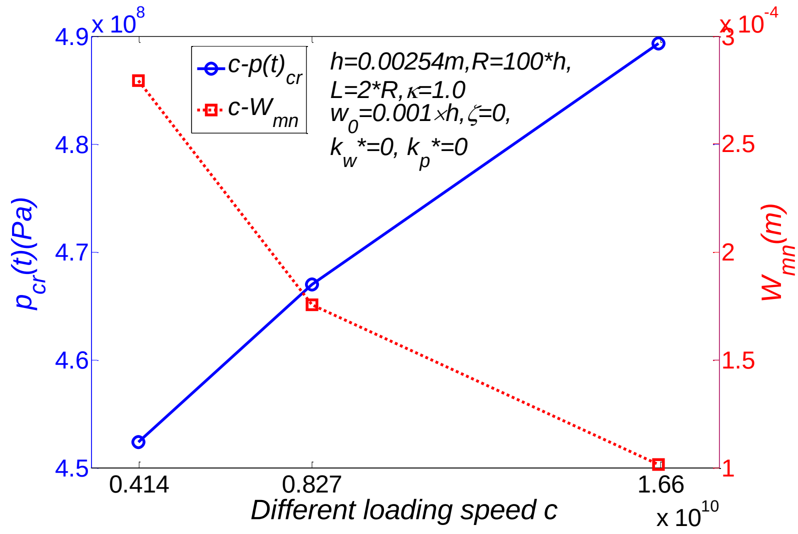

Figure 6.11 The effects of different linearly increasing loads c on $p(t)_{cr}$ and W_{mn} of a simply supported FG orthotropic cylindrical shell

Figure 6.10 shows the dimensionless time-deflection curve of a simply supported FG orthotropic cylindrical shell subjected to different linearly increasing loads c. The numbers in the parenthesis denote the dynamic buckling modes (m, n) in the figure. Obviously, with the increase of loading speed, the critical buckling time τ_{cr}, dynamic buckling loads $p(t)_{cr}$ and the vibration of the structure increase. And the buckling modes jumps from (1, 12) to (1, 25).

The effects of different linearly increasing loads c on $p(t)_{cr}$ and W_{mn} of a simply supported FG orthotropic cylindrical shell is shown in Figure 6.11. The deflection W_{mn} would decrease due to the increase of loading speeds. This is because the increase of the loading speeds makes the onset of buckling in advance of the release of strain in the cylindrical shell.

6.5.3.5 *The influence of different damping ratios*

To explore the influence of different damping ratios, five damping ratios ζ from 0 (undamped system) to 0.05 are explicitly investigated. The exponential factor or material gradient in this subsection chooses κ_i =1.0. And the loading speed is c=4.137G Pa/s.

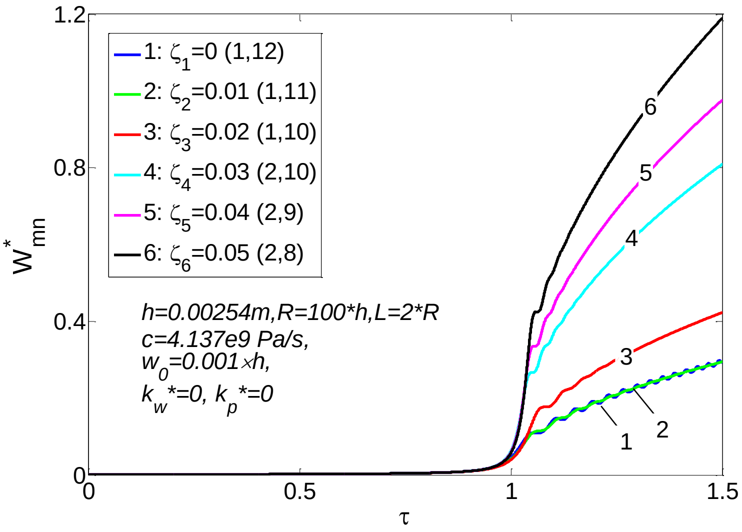

Figure 6.12 The dimensionless time-deflection curve of a simply supported FG orthotropic cylindrical shell for various damping ratios

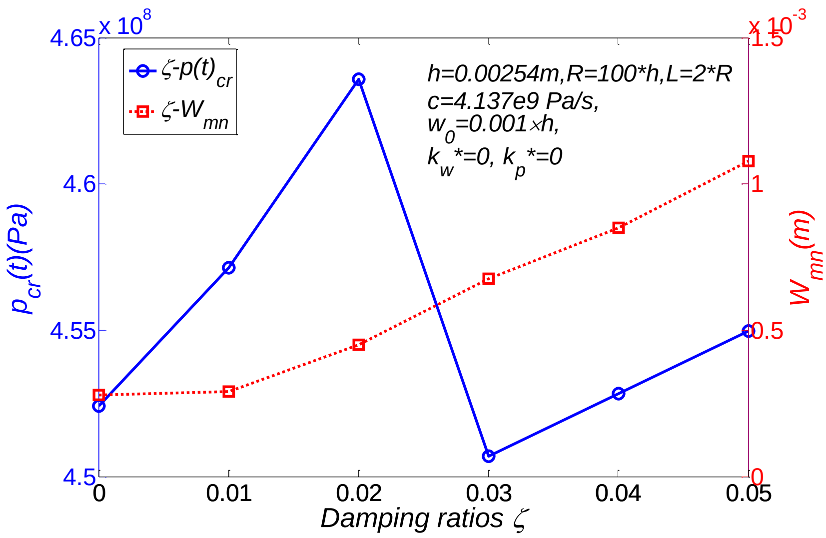

Figure 6.13 The effects of various damping ratios ζ on $p(t)_{cr}$ and W_{mn} of a simply supported FG orthotropic cylindrical shell

In Figure 6.12 the effects of various damping ratios on the dimensionless time-deflection curve are illustrated. It is noted that the oscillations after buckling are greatly eliminated with the consideration of damping effects. One interesting finding is that the half wave number in the axial direction *m* jumps from 1 to 2 when the damping ratio reaches at 0.03. The numbers of wave in the circumferential direction *n* is decrease with an increasing of damping ratios. Normally, some researchers[73, 211] believed in that the increasing of damping ratios increases the dynamic buckling load. In this study, however, the increasing of damping ratios not always results in the rise of buckling load, as the ζ-$p(t)_{cr}$ curve shown in Figure 6.13. This is due to the buckling modes jumps from (1,10) to (2,10) when the damping ratios reach at 0.03. As to the ζ-W_{mn} curve, the deflection increases with the increase of damping ratios.

6.5.3.6 *The influence of R/h ratios*

The effects of R/h ratios of a simply supported FG orthotropic cylindrical shell subjected to a linearly increasing load are discussed in this subsection. The geometrical parameters are h=0.00254m, L=0.508m. Three different of radius-to-thickness ratios, i.e. R/h=60, 80 and 100 are chosen. All the other parameters remain the same as before. As shown in Figure 6.14, with the increase of R/h ratios, both the critical buckling time τ_{cr} and dynamic buckling loads $p(t)_{cr}$ apparently changed. When R/h ratios increase from 60 to 100, $p(t)_{cr}$ decreases by 1.64 times and the buckling modes jumps from (1,6) to (1,12). As can be seen from Figure 6.15, the increase of R/h ratios would reduce the largest deflection W_{mn} of the cylindrical shell.

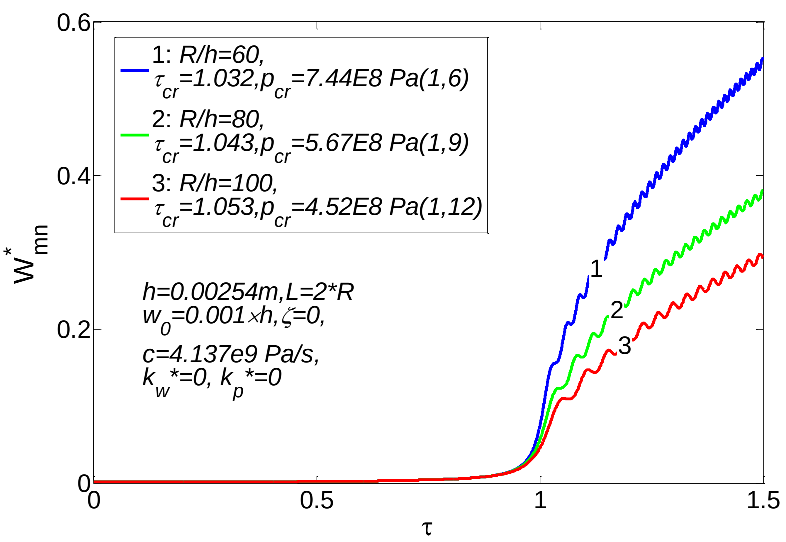

Figure 6.14 The dimensionless time-deflection curve of a simply supported FG orthotropic cylindrical shell for various *R*/*h* ratios

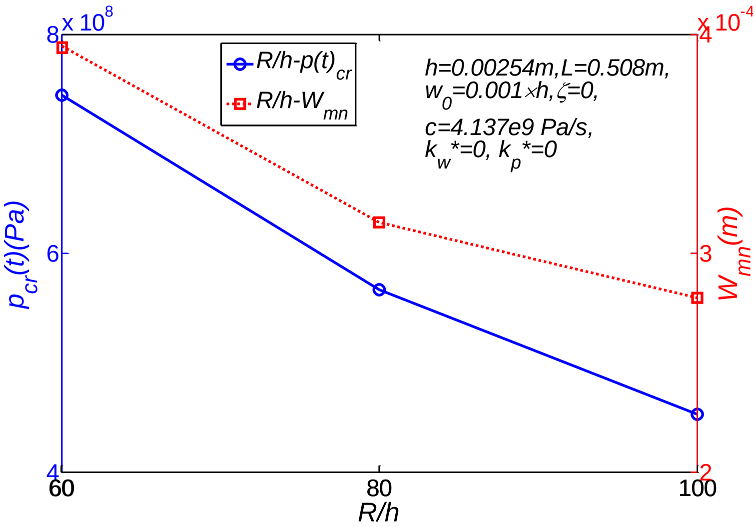

Figure 6.15 The effects of various *R*/*h* ratios on $p(t)_{cr}$ and W_{mn} of a simply supported FG orthotropic cylindrical shell

6.5.3.7 *The influence of L/R ratios*

Figure 6.16 depicts the dimensionless time-deflection curve for various *L*/*R* ratios. The geometrical parameters are h=0.00254m, R=100×h. The results of three different *L*/*R* ratios, i.e. *L*/*R*=2, 4 and 6 are given. The dynamic buckling load $p(t)_{cr}$ increases slowly with the increase of different *L*/*R* ratios, which are 452 MPa, 467 MPa and 478 MPa for *L*/*R*=2,4 and 6, respectively. The dynamic buckling modes (m, n) remain the same for different L/R ratios. According to Figure 6.17, the increase of R/h ratios would reduce the deflection W_{mn} of the structure.

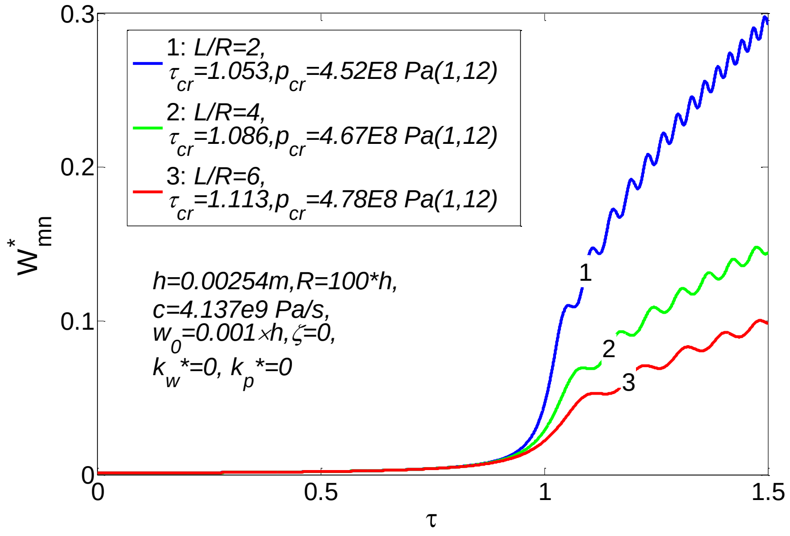

Figure 6.16 The dimensionless time-deflection curve of a simply supported FG orthotropic cylindrical shell for various L/R ratios

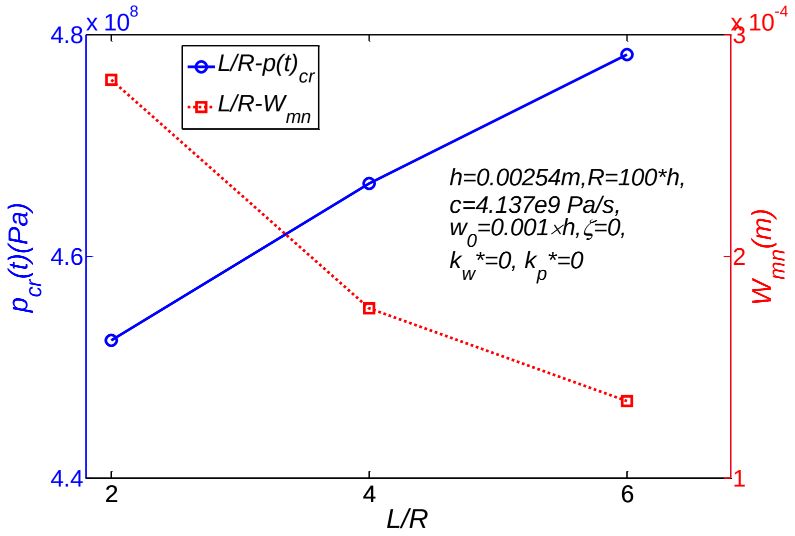

Figure 6.17 The effects of various R/h ratios on $p(t)_{cr}$ and W_{mn} of a simply supported FG orthotropic cylindrical shell

6.5.3.8 *The influence of the Winkler-Pasternak elastic foundation*

In this subsection, the effects of the Winkler-Pasternak elastic foundation on FG orthotropic cylindrical shell are investigated. Four sets of different (k_w^*, k_p^*) were used, such as (k_w^*, k_p^*) equals to (0, 0), (0, 100), (100, 0) and (100, 0). The other parameters keep unchanged. Clearly, from Figure 6.18, when (k_w^*, k_p^*) equals to (0, 0), (100, 0), the dimensionless time-deflection curves are almost the same, similar rules can be obtained when (k_w^*, k_p^*) equals to (0, 100) and (100, 100); while the influence of k_p^* is more pronounced than k_w^*.

The effects of different (k_w^*, k_p^*) on $p(t)_{cr}$ and W_{mn} of a simply supported FG orthotropic cylindrical shell are shown in Figure 6.19, for both (k_w^*, k_p^*)-$p(t)_{cr}$ and (k_w^*, k_p^*)-W_{mn} curves, the influence of k_p^* is more prominent than k_w^*. By considering the Winkler-Pasternak elastic foundation, the dynamic buckling load will increase, and Pasternak parameter is more sensitive than Winkler one. As for the deflection of the cylindrical shell, the increase of k_w^* would reduce the deflection, while the increase of k_p^* would increase the deflection. Because k_w^* (Winkler foundation modulus) restricts the circumferential deflection of the cylindrical shell and k_p^* strengthens shear layer foundation stiffness and then eliminates the axial movement. Also, the influence of k_p^* is more pronounced than k_w^* on the deflection of the cylindrical shell.

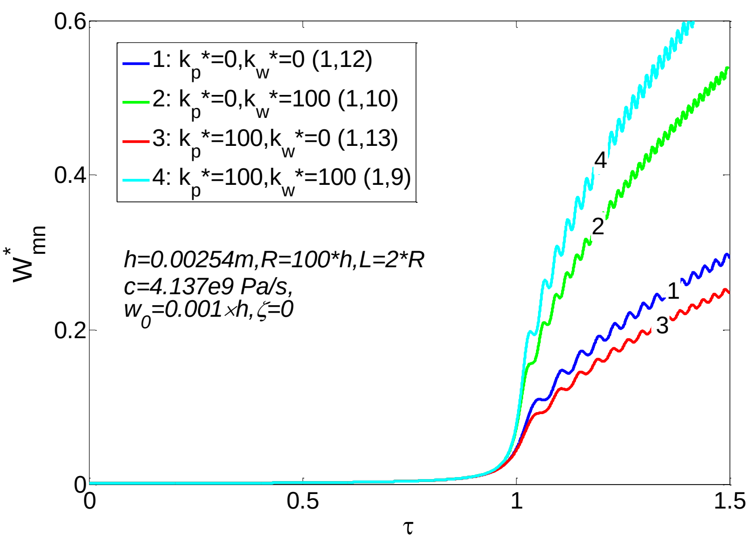

Figure 6.18 The dimensionless time-deflection curve of a simply supported FG orthotropic cylindrical shell for different (k_w^*, k_p^*)

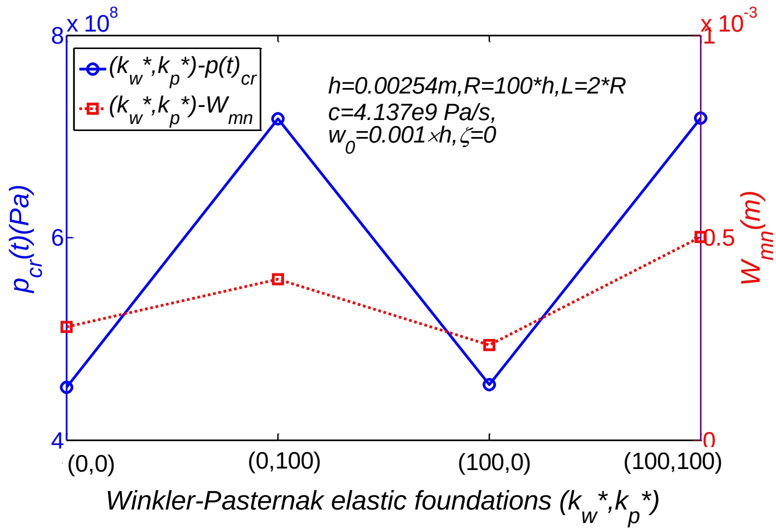

Figure 6.19 The effects of different (k_w^*, k_p^*) on $p(t)_{cr}$ and W_{mn} of a simply supported FG orthotropic cylindrical shell

6.6 Conclusions

This chapter presents the dynamic stability analysis of an FG orthotropic circular cylindrical shell surrounded by a Winkler-Pasternak elastic foundation subjected to linearly increasing load with the consideration of damping effect. Utilizing Hamilton's principle, the equations of motions are derived. And the nonlinear compatibility equation is considered by means of modified Donnell shell theory including large deflection. Based on a hybrid analytical-numerical method (Galerkin method and fourth-order Runge-Kutta method), the dynamic governing equation can be solved. Effects of different parameters such as various inhomogeneous parameters, loading speeds, damping ratios and aspect ratios and thickness ratios of the structure on dynamic buckling were studied systematically and the following conclusions can be made:

1. The non-homogenous parameters κ_i have a great effect on dynamic buckling behaviours (critical load, buckling modes, deflection, etc.). Additionally, the

effect of κ_1 (governed Young's module and shear modulus) is more distinct than κ_2 (governed density) for dynamic stability behaviours. Therefore, a rational design of κ_1 and κ_2 is necessary for buckling analysis of an FG orthotropic cylindrical shell.

2. The dynamic critical buckling loads are larger than the static ones when considering the dynamic terms for all the cases. With the increase of loading speed, the critical buckling time, dynamic buckling loads and the vibration of the structure increase; while deflection decrease.
3. The increasing of damping ratios not always results in the rise of buckling load, which may affect by buckling modes or other uncertainty factors. The deflection increases with the increase of damping ratios.
4. The increase of *R/h* ratios leads to the decrease of dynamic buckling load dramatically; while the increase of *L*/*R* ratios results in slowly increase of dynamic buckling. Moreover, dynamic buckling modes changed greatly for different *R/h* ratios while seems invariable for different *L*/*R* ratios.
5. Dynamic buckling load would increase due to the effect of the Winkler-Pasternak elastic foundation and Pasternak parameter is more sensitive than Winkler one. The influence of Pasternak parameter is more pronounced than Winkler foundation modulus on the deflection of the cylindrical shell. The increase of Winkler foundation modulus would reduce the deflection; while the increase of Pasternak parameter would increase the deflection.

Chapter 7 Nonlinear dynamic buckling of the imperfect orthotropic E-FGM circular cylindrical shells subjected to the longitudinal constant velocity

7.1 Introduction

The dynamic buckling of isotropic FG cylindrical shells subjected to the longitudinal constant velocity has not been reported yet, and even the dynamic buckling of orthotropic FG cylindrical shells. Therefore, in this chapter, the dynamic stability of the imperfect orthotropic Exponential Law Functionally Graded Material (E-FGM) circular cylindrical shell subjected to the constant longitudinal velocity is investigated. The dynamic longitudinal loading on the shell is accomplished by applying a constant displacement rate at one end with respect to the other. The nonlinear compatibility equation is derived by using the improved Donnell shell theory with the consideration of von-Kármán strain-displacement relation and damping effect. Then the nonlinear dynamic buckling equation considering initial imperfections and damping effect is obtained by Airy's stress function and Galerkin method based on Volmir's approach[233]. Finally, the nonlinear compatibility equation is solved by fourth-order Runge-Kutta method and the nonlinear dynamic stability of the orthotropic FG cylindrical shell are assessed based on Budiansky-Roth criterion[2, 6, 202].

7.2 Theory and formulation

7.2.1 *Material gradient of orthotropic FG cylindrical shells*

Orthotropic functionally graded cylindrical shell in this chapter is assumed to be made from a mixture of ceramic and metallic with exponentially varying material properties $P(z)$ and can be given as follows

$$P(z) = P \cdot \psi_i(z) \tag{7.1}$$

where

$$\psi_i(z) = e^{\kappa_i(\frac{z}{h}+0.5)} \tag{7.2}$$

where $\psi(z)$ is the material's exponential function. κ_i is the exponential factor, and also denotes the non-homogenous parameter because it characters the degree of the material gradient in the z-direction. h is the thickness of the shell and varies from $-h/2$ to $h/2$. z is the coordinate in the thickness direction. Figure 7.1 illustrates the material's exponential function for five different non-homogenous parameters (-1.5, -0.5, 0, 0.5, 1.5) along the z-direction. As can be seen, when κ_i =0, Eq.(1) reduces to the homogenous case; when $\kappa_i >$ 0, it corresponds to the graded stiff material while κ_i <0 means the graded soft material, as shown in Figure 7.2.

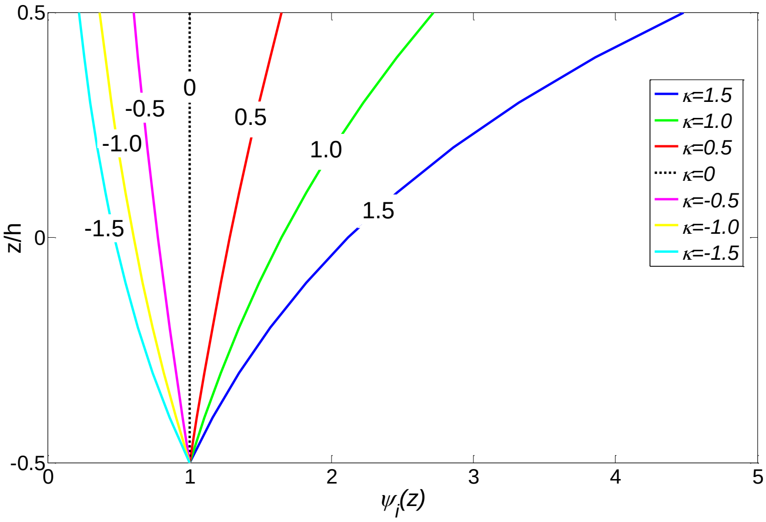

Figure 7.1 Material's exponential function $\psi_i(z)$ over z/h for five different non-homogenous parameters (-1.5, -0.5, 0, 0.5, 1.5)

For an orthotropic functionally graded cylindrical shell, Young's module $E(z)$, shear modulus $G(z)$, and density $\rho(z)$ can be given in the similar form as Eq.(7.1).

$$\begin{aligned} &E_x = E_{01}\psi_1(z); E_y = E_{02}\psi_1(z); G_{xy} = G_0\psi_1(z); \\ &\rho(z) = \rho_0\psi_2(z); \end{aligned} \tag{7.3}$$

where E_{01} , E_{02} represent Young's moduli of homogeneous orthotropic material along x, y directions, respectively. Similarly, G_0 and ρ_0 are the shear modulus and density of the homogenous orthotropic material, respectively. Poisson's ratio in this chapter is assumed to be invariable because Poisson's ratio has less effect on structures than other material properties[213].

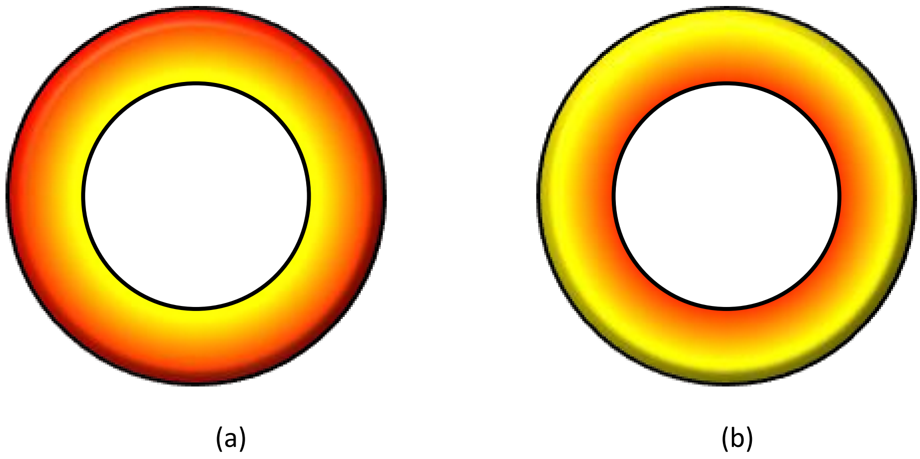

Figure 7.2 Cross-section of (a) FG stiff circular cylindrical shell; (b) FG soft circular cylindrical shell

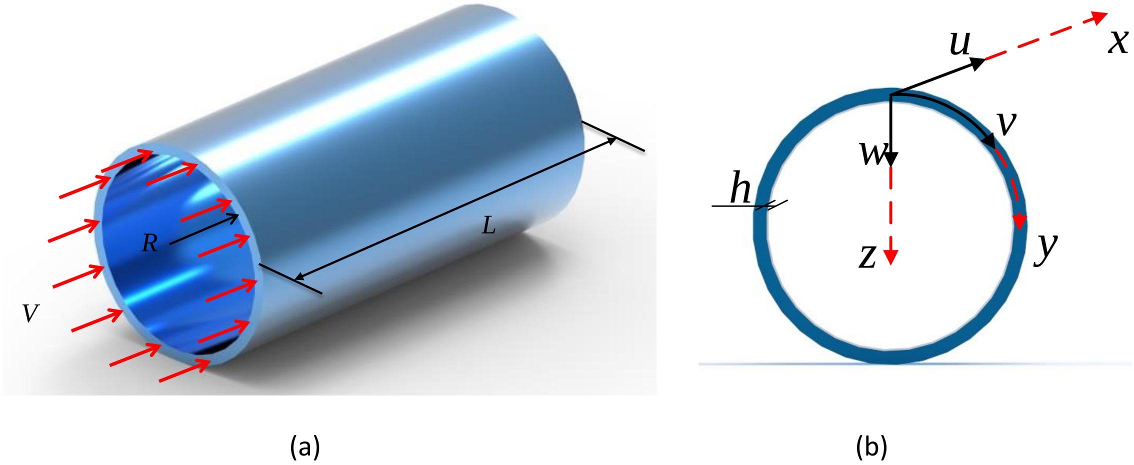

Figure 7.3 Geometry and Cartesian coordinate system of an orthotropic FG cylindrical shell subjected to a constant axial velocity

7.2.2 *Governing equations*

Consider an orthotropic functionally graded cylindrical shell with length L, mean radius R and thickness h, as shown in Figure 7.3. The Cartesian coordinate system (x,y,z) is established, in which point O is located on the middle plane and at the left side of the cylindrical shell. z is the thickness direction. Also, the cylindrical shell is subjected to a constant compression rate v at the end of right side along the x direction.

The governing equation same as Section 6.2.2 and Section 6.2.3 when the elastic foundation parameters equals to 0.

$$\begin{aligned}
&h\left[C_{12}^{*}\frac{\partial^4 F}{\partial x^4}+\left(C_{11}^{*}-2C_{66}^{*}+C_{22}^{*}\right)\frac{\partial^4 F}{\partial x^2\partial y^2}+C_{21}^{*}\frac{\partial^4 F}{\partial y^4}\right] \\
&-D_{11}^{*}\frac{\partial^4\left(w-w_0\right)}{\partial x^4}-(D_{12}^{*}+2D_{66}^{*}+D_{21}^{*})\frac{\partial^4(w-w_0)}{\partial x^2\partial y^2}-D_{22}^{*}\frac{\partial^4(w-w_0)}{\partial y^4}+\frac{h}{R}\frac{\partial^2 F}{\partial x^2} \\
&+h\left[\frac{\partial^2 F}{\partial y^2}\frac{\partial^2 w}{\partial x^2}-2\frac{\partial^2 F}{\partial x\partial y}\frac{\partial^2 w}{\partial x\partial y}+\frac{\partial^2 F}{\partial x^2}\frac{\partial^2 w}{\partial y^2}\right]=\rho_t\frac{\partial^2 w}{\partial t^2}+c_d\rho_t\frac{\partial w}{\partial t}
\end{aligned} \tag{7.4}$$

7.3 Nonlinear dynamic analysis of an orthotropic FG cylindrical shell

7.3.1 *Solution of the problem*

The boundary conditions for w and w_0 of a supported cylindrical shell where the edges remain straight after buckling are

$$\left.\begin{aligned} w=w_0&=0 \\ \frac{\partial^2 w}{\partial x^2}=\frac{\partial^2 w_0}{\partial x^2}&=0 \end{aligned}\right\} x=0 \text{ and } x=L \tag{7.5}$$

And

$$\left.\begin{aligned} w=w_0&=0 \\ \frac{\partial^2 w}{\partial y^2}=\frac{\partial^2 w_0}{\partial y^2}&=0 \end{aligned}\right\} y=0 \text{ and } y=2\pi R \tag{7.6}$$

From the above figure, the average stress in each direction becomes

$$\left.\begin{aligned}\frac{1}{2\pi R}\int_0^{2\pi R}\sigma_x dy = \frac{1}{2\pi R}\int_0^{2\pi R}\frac{\partial^2 F(x,y)}{\partial y^2}dy = -p(t)\\ \frac{1}{2\pi R}\int_0^{2\pi R}\tau_{xy}dy = = -\frac{1}{2\pi R}\int_0^{2\pi R}\frac{\partial^2 F(x,y)}{\partial x\partial y}dy = 0\end{aligned}\right\} for \quad x = 0, L \tag{7.7}$$

where $p(t)$ is the average compressive stress due to the constant compression rates and

$$\left.\begin{aligned}\frac{1}{L}\int_0^{L}\sigma_y dx = \frac{1}{L}\int_0^{L}\frac{\partial^2 F(x,y)}{\partial x^2}dx = 0\\ \frac{1}{L}\int_0^{L}\tau_{yx}dx = -\frac{1}{L}\int_0^{L}\frac{\partial^2 F(x,y)}{\partial x\partial y}dx = 0\end{aligned}\right\} for \quad y = 0, 2\pi R \tag{7.8}$$

The deflection function for the SSSS boundary condition cylindrical shell is assumed to be the single mode [74]

$$w(x,y,t) = W_{mn}(t)\sin(\alpha x)\sin(\beta y) \tag{7.9}$$

where $W_{mn}(t)$ is the time-varying amplitude of w, and $\alpha = m\pi/L$ and $\beta = n/R$ are the number of half waves in the x and y directions, respectively. Moreover, other boundary conditions can be considered if one selects the proper trigonometric admissible functions[75].

Also, the initial shape function can be taken as

$$w_0(x,y) = W_0 \sin(\alpha x)\sin(\beta y) \tag{7.10}$$

where W_0 represents the initial eccentricity value of the cylindrical shell.

Substituting Eq.(7.9) and Eq.(7.10) into the nonlinear compatibility Eq.(6.30) and combined with the boundary conditions Eqs.(7.5)-(7.8), a solution is given

$$F(x,y,t) = F_1\cos(2\alpha x) + F_2\cos(2\beta y) + F_3\sin(\alpha x)\sin(\beta y) - \frac{1}{2}p(t)y^2 \qquad (7.11)$$

Where

$$\begin{aligned} F_1 &= \frac{\beta^2}{32\alpha^2 A_{11}^* h}(W_{mn}^2 - W_0^2); \\ F_2 &= \frac{\alpha^2}{32\beta^2 A_{22}^* h}(W_{mn}^2 - W_0^2) \\ F_3 &= \frac{B_{11}^*\alpha^4 + (B_{12}^* + B_{21}^* - B_{66}^*)\alpha^2\beta^2 + B_{22}^*\beta^4 + \frac{\alpha^2}{R}}{A_{11}^*\alpha^4 + (A_{12}^* + A_{21}^* + A_{66}^*)\alpha^2\beta^2 + A_{22}^*\beta^4}\frac{(W_{mn} - W_0)}{h} \end{aligned} \qquad (7.12)$$

Substituting Eqs.(7.9)-(7.11) into Eq.(7.4) and then applying the Galerkin method. Each term in Eq.(7.4) is multiplying with sin*(mπx/L)*sin*(ny/R)dxdy*, then integrating over the middle surface of cylindrical shell, the equation of motion becomes

$$\begin{aligned} &\int_0^{2\pi R}\int_0^L eq(6.4)\sin(\alpha x)\sin(\beta y)dxdy \\ &= \rho_t\frac{\partial^2 W_{mn}}{\partial t^2} + \rho_t c_d\frac{\partial W_{mn}}{\partial t} - \left(M_1K_1 - N_1\right)\left(W_{mn} - W_0\right) \\ &+ H_1 W_{mn}(W_{mn}^2 - W_0^2) - \alpha^2 h p(t) W_{mn} = 0 \end{aligned} \qquad (7.13)$$

Where

$$\begin{aligned} M_1 &= C_{12}^*\alpha^4 + (C_{11}^* - 2C_{66}^* + C_{22}^*)\alpha^2\beta^2 + C_{21}^*\beta^4 - \frac{\alpha^2}{R} \\ N_1 &= D_{11}^*\alpha^4 + (D_{12}^* + 2D_{66}^* + D_{21}^*)\alpha^2\beta^2 + D_{22}^*\beta^4 \\ K_1 &= \frac{B_{11}^*\alpha^4 + (B_{12}^* + B_{21}^* - B_{66}^*)\alpha^2\beta^2 + B_{22}^*\beta^4 + \frac{\alpha^2}{R}}{A_{11}^*\alpha^4 + (A_{12}^* + A_{21}^* + A_{66}^*)\alpha^2\beta^2 + A_{22}^*\beta^4} \\ H_1 &= \frac{1}{16}\left(\frac{\alpha^4}{A_{22}^*} + \frac{\beta^4}{A_{11}^*}\right) \end{aligned} \qquad (7.14)$$

7.3.2 *In-plane compressive force*

Substituting Eq. (7.11) into Eq. (6.28), the membrane stresses can be obtained

$$
\begin{aligned}
\sigma_x &= -\frac{\alpha^2\cos(2\beta y)}{8A_{22}^*h}(W_{mn}^2 - W_0^2) - \frac{\beta^2 K_1 \sin(\alpha x)\sin(\beta y)}{h}(W_{mn} - W_0) - p(t) \\
\sigma_y &= -\frac{\beta^2\cos(2\alpha x)}{8A_{11}^*h}(W_{mn}^2 - W_0^2) - \frac{\alpha^2 K_1 \sin(\alpha x)\sin(\beta y)}{h}(W_{mn} - W_0)
\end{aligned}
\tag{7.15}
$$

Getting together Eq.(6.3) with Eq.(6.14), we can have the following equations

$$
\begin{aligned}
\varepsilon_x^0 &= \frac{\partial u}{\partial x} + \frac{1}{2}\left(\frac{\partial w}{\partial x}\right)^2 - \frac{1}{2}\left(\frac{\partial w_0}{\partial x}\right)^2 \\
\varepsilon_x^0 &= \frac{A_{22}N_x - A_{12}N_y - A_{22}(B_{11}\kappa_x + B_{12}\kappa_y) + A_{12}(B_{21}\kappa_x + B_{22}\kappa_y)}{A_{11}A_{22} - A_{21}A_{12}}
\end{aligned}
\tag{7.16}
$$

Substitute Eqs.(7.9), (7.10) into Eqs.(7.16) and eliminating ε_x^0, then $\partial u/\partial x$ can be expressed

$$
\begin{aligned}
&\frac{\partial u}{\partial x} = h(A_{22}^*\sigma_x + A_{12}^*\sigma_y) + B_{21}^*\kappa_x + B_{22}^*\kappa_y \\
&-\frac{1}{2}\alpha^2\cos^2(\alpha x)\sin^2(\beta y)(W_{mn}^2 - W_0^2)
\end{aligned}
\tag{7.17}
$$

where $\partial u/\partial x$ denotes the strain at any point through the cylindrical shell thickness in the *z*-direction.

The dynamic longitudinal loading on the cylindrical shell is accomplished by a constant displacement rate *v* along *x*-axis of one end with respect to the other; therefore the displacement along *x*-axis due to the loading rate can be solved by

$$U=\frac{1}{2\pi R}\int_0^{2\pi R}\int_0^L\frac{\partial u}{\partial x}dxdy=-\frac{\alpha^2 L}{8}(W_{mn}^2-W_0^2)-A_{22}^*hLp(t)+$$
$$L(A_{22}^*N_x^T+A_{12}^*N_y^T)+\frac{r_1r_2}{\pi R}\left[\frac{\beta}{\alpha}(B_{22}^*-A_{22}^*K_1)+\frac{\alpha}{\beta}(B_{21}^*-A_{12}^*K_1)\right](W_{mn}-W_0) \quad (7.18)$$

$$U=-vt \quad (7.19)$$

where negative displacement means the cylindrical shell edge is shortened.

From Eqs.(7.18) and (7.19), the average value of compressive stress *p(t)* can be expressed

$$p(t)=\frac{1}{A_{22}^*hL}vt-\frac{\alpha^2}{8A_{22}^*h}(W_{mn}^2-W_0^2)$$
$$+\frac{r_1r_2}{A_{22}^*hL\pi R}\left[\frac{\beta}{\alpha}(B_{22}^*-A_{22}^*K_1)+\frac{\alpha}{\beta}(B_{21}^*-A_{12}^*K_1)\right](W_{mn}-W_0) \quad (7.20)$$

Where

$$r_1=(-1)^m-1;$$
$$r_2=(-1)^n-1 \quad (7.21)$$

7.3.3 *Buckling analysis*

7.3.3.1 *Static buckling analysis*

For an initially perfect orthotropic FG cylindrical shell, by omitting the velocity, acceleration and high-order terms, Eq. (7.13) can be reduced into

$$-\alpha^2 hpW_{mn}-\left(M_1K_1-N_1\right)W_{mn}=0 \quad (7.22)$$

Eq. (7.22) is the linear static equation of the orthotropic FG cylindrical shell, which can also obtain from the corresponding static case using the linear theory. Then the static buckling load is

$$p_{st} = \frac{1}{\alpha^2 h}\left(N_1 - M_1 K_1\right) \tag{7.23}$$

where the least static buckling load p_{cr}^{st} can also obtain with respect to various modes (*m*, *n*), which can be further reduced into classical buckling load of an isotropic circular cylindrical shell by giving κ_i equals to 0, respectively. And the equation is given as follows

$$\sigma_{cr} = \frac{Eh}{R\sqrt{3(1-v^2)}} \tag{7.24}$$

7.3.3.2 *Dynamic buckling analysis*

Substituting Eq. (7.20) into Eq. (7.13), the government equation of nonlinear dynamic buckling of orthotropic FG cylindrical shell subjected to a constant loading rate *v* with damping effect can be derived

$$\begin{aligned}
&\rho_t \frac{\partial^2 W_{mn}}{\partial t^2} + \rho_t c_d \frac{\partial W_{mn}}{\partial t} \\
&-\left(M_1 K_1 - N_1\right)\left(W_{mn} - W_0\right) + H_1 W_{mn}(W_{mn}^2 - W_0^2) \\
&-\alpha^2 h W_{mn} \left\{ \begin{aligned} &\frac{1}{A_{22}^* h L} vt - \frac{\alpha^2}{8A_{22}^* h}(W_{mn}^2 - W_0^2) \\ &+ \frac{r_1 r_2}{A_{22}^* h L \pi R}\left[\frac{\beta}{\alpha}(B_{22}^* - A_{22}^* K_1) + \frac{\alpha}{\beta}(B_{21}^* - A_{12}^* K_1)\right](W_{mn} - W_0) \end{aligned} \right\} = 0
\end{aligned} \tag{7.25}$$

Here, introduce the following non-dimensional parameters and constants

$$W_{mn}^* = \frac{W_{mn}}{h}, W_0^* = \frac{W_0}{h}, \tau = \frac{t}{\sqrt{\rho_t L A_{22}^* h}}, v^* = \frac{v}{\sqrt{\frac{L}{A_{22}^* h \rho_t}}},$$

$$L_1 = \left(N_1 - M_1 K_1\right) A_{22}^* h L \tag{7.26}$$

$$L_2 = h^3 L H_1 A_{22}^*$$

$$L_3 = \frac{h}{\pi R L} r_1 r_2 \left[\frac{\beta}{\alpha}(B_{22}^* - A_{22}^* K_1) + \frac{\alpha}{\beta}(B_{21}^* - A_{12}^* K_1)\right]$$

By considering the viscous damping as internal damping effects, one can obtain that

$$c_d = 2\omega_{mn}\zeta$$
$$c_d^* = c_d \sqrt{\rho_t L A_{22}^* h} \tag{7.27}$$

where c_d denotes the damping coefficient of the structure; ω_{mn} denotes the circular natural frequency of the cylindrical shell corresponding to mode (m, n); and ζ denotes the damping ratio of the cylindrical shell.

For harmonic motion, $W_{mn}(t)$ may be taken in the form

$$W_{mn}(t) = A\sin(\omega t) \tag{7.28}$$

where A is the amplitude of the vibration.

Substituting Eq. (7.28) into Eq. (7.25), the fundamental frequency of natural vibration of the orthotropic FG cylindrical shell can be determined by

$$\omega_{mn} = \sqrt{\frac{1}{\rho_t}\left(N_1 - M_1 \cdot K_1\right)} \tag{7.29}$$

Therefore, the differential equations governing the nonlinear behaviour of an orthotropic FG cylindrical shell can be written in a non-dimensional form

$$\begin{aligned}&\frac{\partial^2 W_{mn}^*}{\partial \tau^2}+c_d^*\frac{\partial W_{mn}^*}{\partial \tau}+L_1(W_{mn}^*-W_0^*)+L_2W_{mn}^*(W_{mn}^{*\,2}-W_0^{*2})\\&-\alpha^2 hLW_{mn}^*\left[v^*\tau-\frac{\alpha^2h^2}{8}(W_{mn}^{*\,2}-W_0^{*2})+L_3(W_{mn}^*-W_0^*)\right]=0\end{aligned}\tag{7.30}$$

According to the dimensionless quantities of Eq. (7.28), the normalized buckling load from Eq. (7.20) can be represented as

$$p_{cr}^*=\frac{p(t)}{p_{cr}^{st}}=\frac{1}{A_{22}^*hp_{cr}^{st}}\left[v^*\tau-\frac{\alpha^2h^2}{8}(W_{mn}^{*\,2}-W_0^{*2})+L_3(W_{mn}^*-W_0^*)\right]\tag{7.31}$$

7.4 Results and discussions

7.4.1 *Validation of present study*

In this section, the accuracy of proposed method is verified with published papers. First of all, the comparison on the static buckling of simply supported isotropic cylindrical shell p_{st} (calculated from Eq.(7.23)) given by the proposed analysis with the results Huang and Han [102] based on the Euler-Lagrange equation, as shown in Table 7.1. The dimensions of the circular cylindrical shell are $E_{01}=E_{02}=E_0$, $v_{12}=v_{21}=v_0$. The material properties are taken as E_0=200GPa, G_0=77.3GPa, ρ=1200kg/m^3, $h=4\times10^{-3}$m, R/h=125, L/R=1. The Poisson's ratio is chosen to be 0.3. As can be seen, in this comparison study outstanding agreements are achieved and the average errors in different modes just have around 0.11%-0.32%.

Table 7.1 Comparison of the static buckling load of a simply supported isotropic cylindrical shell with the results reported by Huang and Han[102]

(m,n)	Huang and Han[102](GPa)	Present method (GPa)	Difference (%)
(1,1)	16.721	16.739	0.11
(1,2)	10.284	10.311	0.26
(1,3)	5.586	5.604	0.32
(1,4)	3.029	3.038	0.30
(2,4)	2.657	2.664	0.26
(3,4)	1.762	1.765	0.16

Furthermore, the natural frequencies (in Eq.(7.29)) of the simply supported anisotropic circular cylindrical shell is calculated by present analysis and compared with Greenberg and Stavsky [234] based on the Love-type theory solved by finite Fourier transform, Sofiyev et al.[118] based on Donnell's nonlinear shell theory and solved by homotopy perturbation method, Liu et al.[235] based upon the Donell-Mushtari shell theory solved by closed-form vibration solution. The comparisons are carried out for the following circular cylindrical shell material properties: E_{01}=120GPa, E_{02}=10GPa, G_0=5.5GPa, v_{12}=0.27, v_{21}=0.0225, ρ=1700kg/m^3, h=0.01m, L=5m, R=1.0m, which were taken from the study of Liu et al.[235]. As shown in Table 7.2, a good agreement can be witnessed.

Table 7.2 Comparison of the natural frequencies of a simply supported orthotropic cylindrical shell with results reported by Greenberg and Stavsky [234], Sofiyev et al.[118] and Liu et al.[235]

n	Present Method	Ref. [234]	Ref. [118]	Ref. [235]	Average Error (%) with Ref. [118, 234, 235]
3	272.0	266	273	258	2.33%
4	203.99	202	204	198	1.30%

5	213.05	211	210	209	1.43%
6	269.81	270	265	266	1.04%
7	353.57	358	347	350	0.54%
8	455.93	464	448	452	0.28%

7.4.2 *Results of natural frequencies and static buckling loads*

The results from Table 7.1 and Table 7.2 have verified the proposed methods. Additional effects of different L/R and E_{01}/E_{02} on natural frequencies ω_{mn} (calculated from Eq.(7.29)) and static buckling load of p_{st} (calculated from Eq.(7.23)) of a simply supported orthotropic cylindrical shell are shown in Table 7.3. The material properties are same as Table 7.2, expect that E_{02} and R remain unchanged and E_{01} and L are variable with respect to the ratios in Table 7.3, respectively. Obviously, for a fixed E_{01}/E_{02}, the increasing of L/R leads to the decrease of natural frequencies; while static buckling does not have this phenomenon. Similarly, for a fixed L/R, the increasing of E_{01}/E_{02} causes the increase of the buckling load; while natural frequencies do not have this phenomenon. One interesting finding is that the influence of modes (m,1) does not have specific laws.

Table 7.3 Comparison of natural frequencies ω_{mn} and static buckling loads p_{st} of a simply supported orthotropic cylindrical shell for different L/R and E_{01}/E_{02} (E_{02}=10GPa, R=1m,n=1)

L/R	E_{01}/E_{02}	ω_{mn} (Hz)			p_{st} (MPa)		
		m=1	m=2	m=3	m=1	m=2	m=3
2	10	1843.2	2243.5	2386.1	2340.6	867.0	435.9
	20	1845.4	2253.4	2436.1	2346.4	874.7	454.3
	30	1846.7	2263.8	2485.4	2349.7	882.8	472.9

	40	1847.8	2274.3	2533.8	2352.5	890.9	491.5
10	10	449.0	980.3	1373.8	3472.7	4138.5	3611.8
	20	493.2	1004.2	1384.6	4189.8	4342.1	3669.2
	30	511.1	1012.5	1388.4	4499.6	4414.7	3689.3
	40	520.8	1016.8	1390.4	4672.3	4452.1	3699.7
20	10	157.7	449.0	731.6	1714.2	3472.7	4097.4
	20	194.7	493.2	765.5	2612.4	4189.8	4486.5
	30	214.4	511.1	778.0	3166.0	4499.6	4633.3
	40	226.7	520.8	784.4	3541.3	4672.3	4710.4

7.4.3 *Dynamic buckling of the orthotropic FG cylindrical shells subjected to constant velocities*

In this subsection, the nonlinear dynamic stability of an imperfect orthotropic FG cylindrical shell subjected to a constant compression rate is investigated. Eq.(51) was solved numerically based on fourth-order Runge-Kutta method and the nonlinear dynamic stability of the orthotropic FG cylindrical shell are assessed based on Budiansky-Roth criterion[2, 6, 202]. The following material properties are chosen: E_{01}=206.9GPa, E_{02}=20.69GPa, G_0=6.9GPa, v_{12}=0.3, v_{21}=0.03, ρ=1950kg/m^3, which were taken from Reddy's book[232]. The geometrical parameters are h=0.01m, L=5m, R=1.0m. And the initial imperfection is W_0=0.001×h.

7.4.3.1 *The influence of various compression rates*

The constant velocity or displacement loading scheme of dynamic buckling, which was first studied by Hoff [53] in 1951, and shown that the critical force strongly depends on compression rate and initial imperfection of a beam-column structure. Moreover, velocity is one of the key parameters in the governing Eqs.(7.30) and (7.31). Therefore, it is essential to study the impact of different velocities acting on an imperfect orthotropic FG cylindrical shell. The exponential factor or material gradient in this subsection chooses κ_i =1.0. Three different compression rates v equal to 0.1m/s, 0.2 m/s and 0.3m/s are discussed.

Figure 7.4 and Figure 7.5 show the dimensionless time-deflection curve, the dimensionless time-load curve of an eccentricity simply supported orthotropic FG cylindrical shell subjected to different velocities, respectively. Obviously, with the increase of axial compression rates, the critical buckling load and vibration of the cylindrical shell increases; while the time of the onset of buckling decrease and the deflection at the buckling point (which is shown as coloured dots in Figure 7.5) decreases as well. As can be seen from Figure 7.4 that all dynamic buckling curves have three phases, which are a very slow increase, rapid increase and reach the inflexions and then cylindrical shell begins to vibration. Moreover, the dynamic critical buckling mode (m, n) changes from (8, 8) to (10, 9) with the increase of loading rates. The oscillation amplitude (the third phase) also becomes larger when the velocity reaches 0.3 m/s.

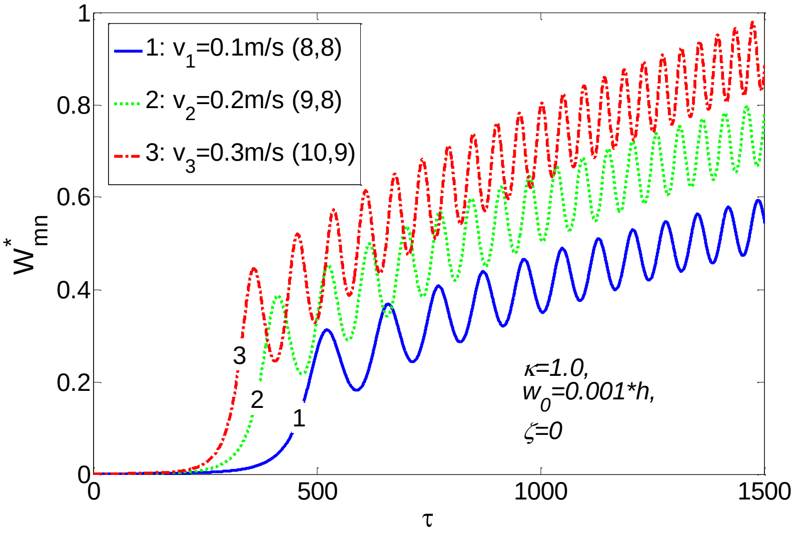

Figure 7.4 Dimensionless time-deflection curve of an eccentricity simply supported orthotropic FG cylindrical shell subjected to different velocities

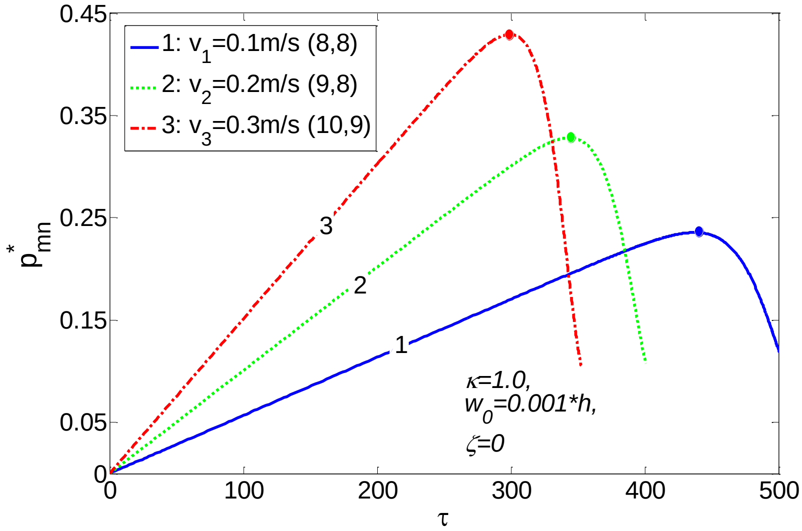

Figure 7.5 Dimensionless time-load curve of an eccentricity simply supported orthotropic FG cylindrical shell subjected to different velocities

7.4.3.2 *The influence of various initial imperfections*

As it has been reported, initial imperfection is one of the most important parameters in dynamic buckling analysis. To investigate effects of the initial imperfection in dynamic buckling analysis, three different initial eccentricities W_0 equal to $0.02\times h$, $0.01\times h$ and

0.001×h are discussed. In Figure 7.6, it is clearly demonstrated that a slight change of initial deflection would result in an apparent change in τ-W_{mn}^* curve and the amplitude of the vibration of the structures increases for smaller imperfections. From Figure 7.7, when the initial imperfection decreases from 0.02×h to 0.001×h, the dynamic buckling load increases.

One interesting finding is that when initial imperfection increases to 0.1×h, there is an absence of dynamic buckling point according to Budiansky-Roth criterion[2, 6, 202]. Similar phenomena also are reported by Papazoglou et al.[73] and Huang et al. [102]. This is because B-R criterion is unsuitable for predicting dynamic buckling load of the cylindrical shell when the imperfection amplitude is large.

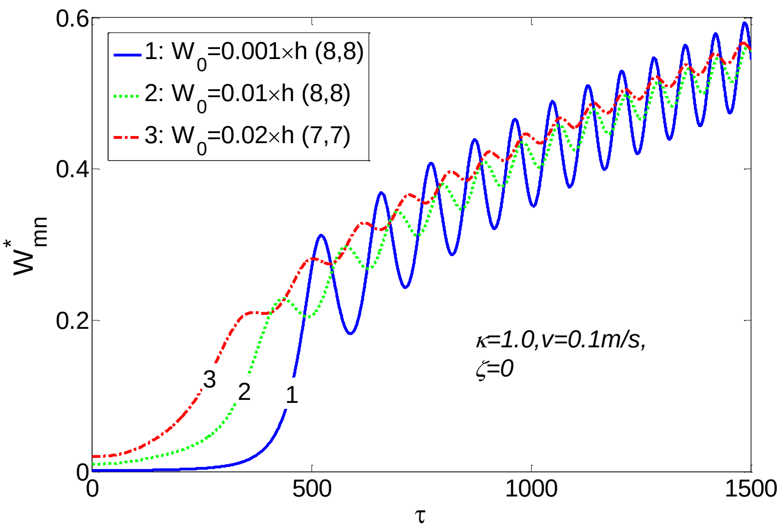

Figure 7.6 Dimensionless time-deflection curve of an eccentricity simply supported orthotropic FG cylindrical shell for various initial eccentricities

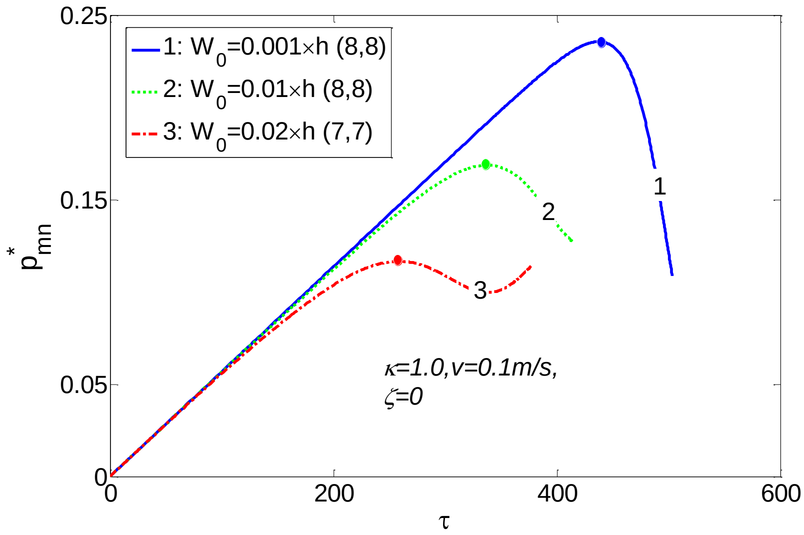

Figure 7.7 Dimensionless time-load curve of an eccentricity simply supported orthotropic FG cylindrical shell for various initial eccentricities

7.4.3.3 *The influence of different damping ratios*

Figure 7.8 and Figure 7.9 show the influence of damping ratios on dynamic buckling of an eccentricity simply supported orthotropic FG cylindrical shell. Three damping ratios ζ from 0 (undamped system) to 0.02 are explicitly investigated. The exponential factor in this subsection chooses κ_{i} =1.0, axial compression velocity is v=0.1m/s, and initial imperfection is 0.001×h. Clearly, the influence of increasing of damping ratios is not very pronounced for deflections when compared with dynamic buckling load. While the increase of damping ratios increases the dynamic buckling load and eliminates the oscillations in the third phases of Figure 7.8. This is because damping depletes the strain energy which stored in the first two phases. The larger the damping ratio increases, the greater the depletion becomes. Besides, the dynamic critical buckling mode (m, n) seems insensitive with the increase of damping ratios. For all three different damping ratios ζ from 0 (undamped system) to 0.02, the dynamic buckling modes are (8, 8).

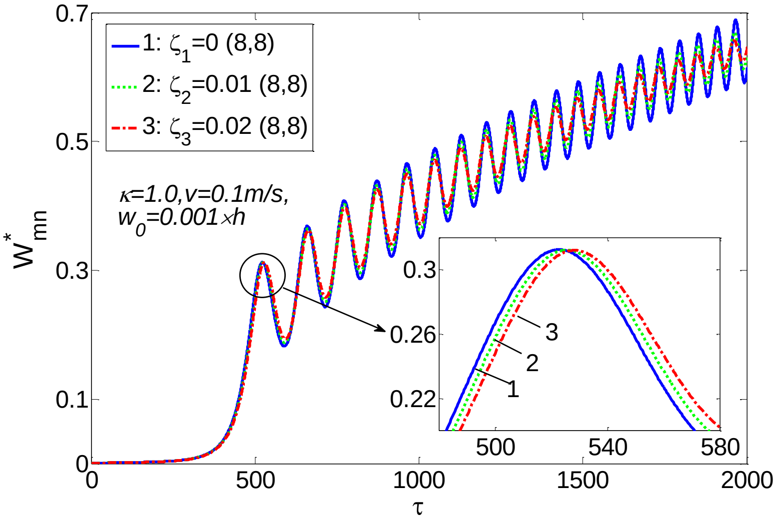

Figure 7.8 Dimensionless time-deflection curve of an eccentricity simply supported orthotropic FG cylindrical shell for various damping ratios

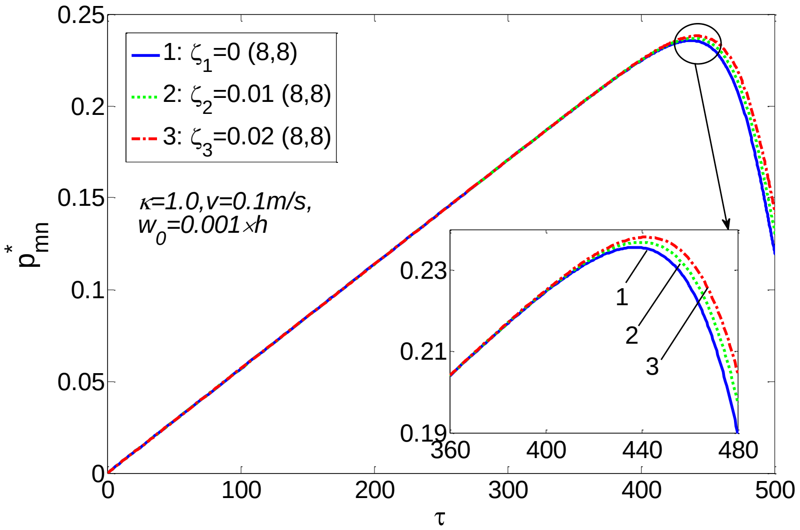

Figure 7.9 Dimensionless time-load curve of an eccentricity simply supported orthotropic FG cylindrical shell for various damping ratios

7.4.3.4 *The influence of different non-homogenous parameters κ_1*

From Figure 7.1, as can be seen, material exponential factor κ_i characters the degree of the material gradient in the *z*-direction and may also influence the dynamic buckling of the structures. For an orthotropic functionally graded cylindrical shell, Young's module $E(z)$, shear modulus $G(z)$ and density $\rho(z)$ are given by Eq.(7.3). In this section, the effects of κ_1 (or Young's module and shear modulus) are focused on. And κ_2 (or density) keeps invariable. Five different inhomogeneous parameters κ_i =-1, -0.5, 0, 0.5, 1 are selected. It is clear that when κ_1 =0, Eq.(7.1) reduces to the homogeneous case; when $\kappa_1 > 0$, it corresponds to the graded stiff material while $\kappa_1 <0$ means graded soft material.

The influence of different $\kappa_1$on dynamic buckling of orthotropic FG cylindrical shells is illustrated in Figure 7.10 and Figure 7.11. It is obvious that with the increase of inhomogeneous parameters or say that the materials become stiffer would reduce the onset of buckling amplitudes and decrease the dynamic buckling loads. When κ_1 increases from -1.0 to 1.0, the dynamic buckling loads increase by 2.56 times and times of onset buckling decrease 1.06 times, as shown in Table 7.4. And the buckling mode remains constant with the change of different inhomogeneous parameters κ_i.

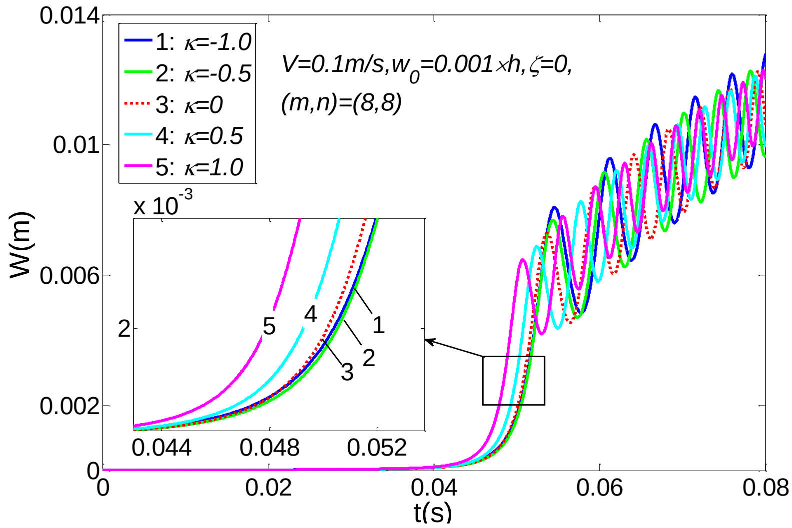

Figure 7.10 The time-deflection curve of an eccentricity simply supported orthotropic FG cylindrical shell for different κ_1

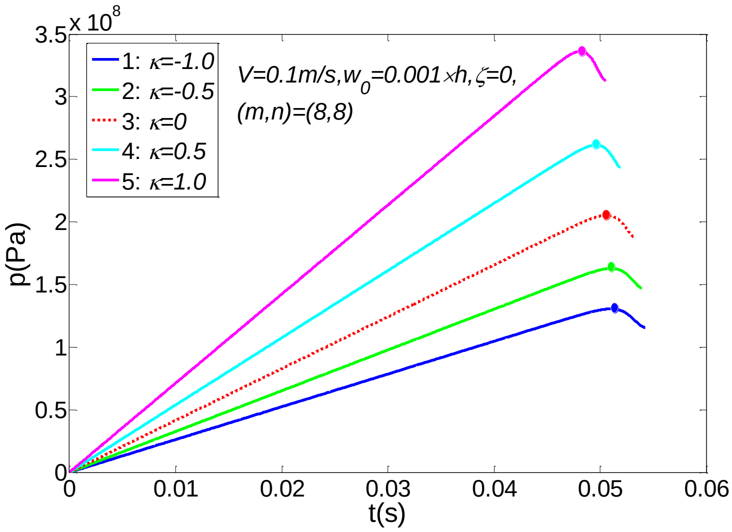

Figure 7.11 The time-load curve of an eccentricity simply supported orthotropic FG cylindrical shell for different κ_1

7.4.3.5 *The influence of different non-homogenous parameters κ_2*

In this subsection, the effects of inhomogeneous parameters κ_2 are investigated. Similarly, five different κ_2=-1, -0.5, 0, 0.5, 1 are selected. κ_1 (or Young's module and shear modulus) keeps invariable while holding all other parameters fixed.

Figure 7.12 and Figure 7.13 depict the time-deflection curve and time-load curve of an eccentricity simply supported orthotropic FG cylindrical shell for different κ_2 subjected to a constant axial velocity v=0.1m/s, respectively. An interesting finding is that the first phases (or say slopes) of the time-load curve of different inhomogeneous parameters κ_2 are almost similar. This is due to the κ_1 (or Young's module and shear modulus) keeps invariable. The increase of κ_2 from -1.0 to 1.0 would increase the dynamic buckling and also extend the time of onset of buckling, which means the larger the density becomes, the bigger the dynamic buckling load is when inhomogeneous parameters κ_2 increases and κ_1 (or Young's module and shear modulus) keeps invariable.

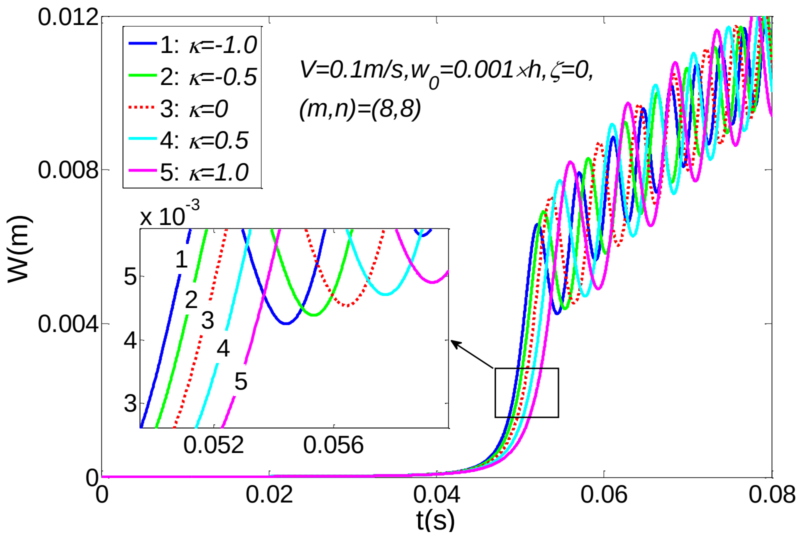

Figure 7.12 The time-deflection curve of an eccentricity simply supported FG orthotropic cylindrical shell for different κ_2

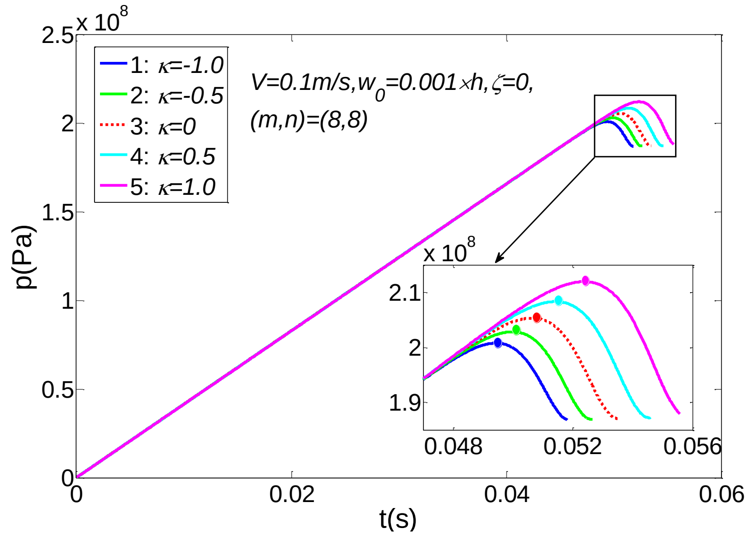

Figure 7.13 The time-load curve of an eccentricity simply supported FG orthotropic cylindrical shell for different κ_2

7.4.3.6 *The combined effects of κ_1 and κ_2 on dynamic buckling of orthotropic FG cylindrical shells*

From the last two subsections, we can see that both κ_1 and κ_2 have a significant influence on the dynamic buckling of an eccentricity simply supported orthotropic FG cylindrical shell. Therefore, it is evident for us to investigate the combined effects of these two parameters. Figure 7.14 and Figure 7.15 give the comparison of different κ_1 and κ_2 on the time-deflection curves and time-load curves, respectively. Both κ_1 and κ_2 increase simultaneously while keeps other parameters unchanged. As can be seen from Figure 7.14, the time-deflection curve of inhomogeneous parameters equal to -1.0 coincides with that of 1.0. Similarly, the curves of -0.5 and 0.5 are almost the same. As shown in Figure 7.15, the dynamic buckling loads increase with the increase of inhomogeneous parameters from -1.0 to 1.0 while the time of onset buckling has no significant rules.

To further explore the relationship between κ_1 and κ_2 on dynamic buckling of orthotropic FG cylindrical shells, eleven different κ_1 from -1.0 to 1.0 and eleven different κ_2 from -1.0 to 1.0 are explicitly investigated. Figure 7.16 shows the relationship of different κ_1 and κ_2 on the peak deflections at the time of onset buckling for an eccentricity simply supported orthotropic FG cylindrical shell. As can be seen, the influence of κ_1 is almost the same as κ_2. Both κ_1 and κ_2 change from (1.0, -1.0) to (-1.0,-1.0) (the softest) and (1.0, 1.0) (the stiffest) area, the peak deflections increase. When κ_1 equals to -1.0 and κ_2 equals to 1.0, the deflection reaches the largest. Similar results also obtained from Table 7.4.

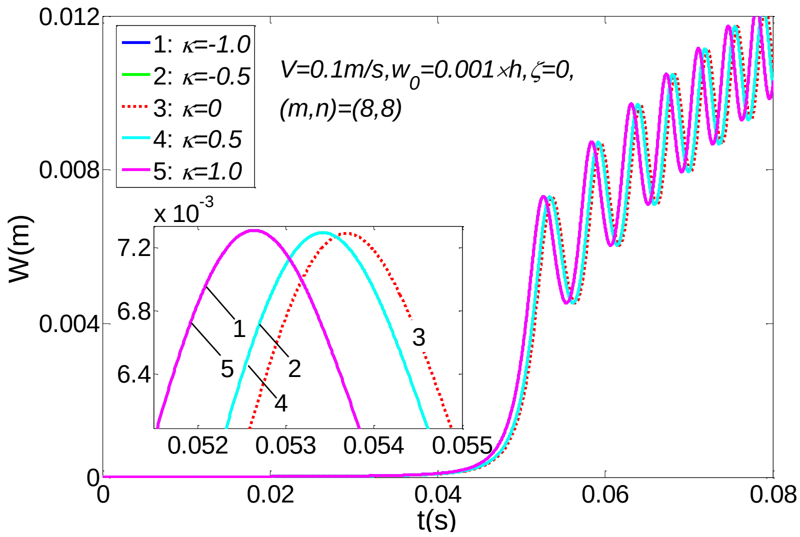

Figure 7.14 The time-deflection curve of an eccentricity simply supported orthotropic FG cylindrical shell for different κ_1 and κ_2

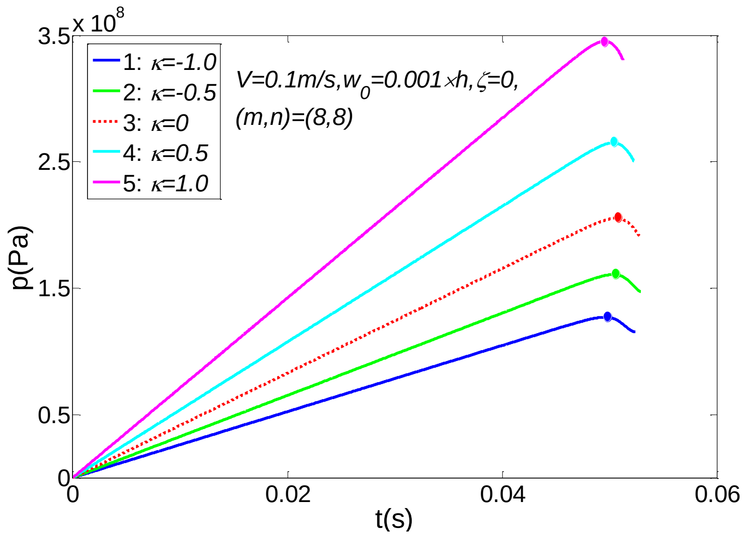

Figure 7.15 The time-deflection curve of an eccentricity simply supported orthotropic FG cylindrical shell for different κ_1 and κ_2

Table 7.4 Comparison of static critical buckling load p_{cr}^{st} , dynamic critical buckling load p_{cr}^{dy} and deflection W_{mn} for various material exponential factors κ_i

Material gradient	κ_i	p_{cr}^{st} (Pa)	p_{cr}^{dy} (Pa)	W_{mn} $\times 10^{-3}$(m)
κ_1 (or Young's module and shear modulus) changes, κ_2 (or density) keeps constant	-1	1.13E+08(7,8)	1.31E+08(8,8)	2.675
	-0.5	1.43E+08(7,8)	1.63E+08(8,8)	2.593

	0	1.82E+08(7,8)	2.05E+08(8,8)	2.524
	0.5	2.35E+08(7,8)	2.61E+08(8,8)	2.446
	1	3.06E+08(7,8)	3.36E+08(8,8)	2.372
	-1	1.82E+08(7,8)	2.01E+08(8,8)	2.385
	-0.5	1.82E+08(7,8)	2.03E+08(8,8)	2.449
κ_1 keeps constant, κ_2 changes	0	1.82E+08(7,8)	2.05E+08(8,8)	2.524
	0.5	1.82E+08(7,8)	2.08E+08(8,8)	2.605
	1	1.82E+08(7,8)	2.12E+08(8,8)	2.7
	-1	1.13E+08(7,8)	1.27E+08(8,8)	2.523
	-0.5	1.43E+08(7,8)	1.61E+08(8,8)	2.52
Both κ_1 and κ_2 change	0	1.82E+08(7,8)	2.05E+08(8,8)	2.524
	0.5	2.35E+08(7,8)	2.65E+08(8,8)	2.52
	1	3.06E+08(7,8)	3.45E+08(8,8)	2.523

The influence of different κ_1 and κ_2 on critical dynamic buckling load at the time of onset buckling for an eccentricity simply supported orthotropic FG cylindrical shell is also illustrated in Figure 7.17. It shows that the increase of both κ_1 and κ_2 will increase the buckling load; while the effect of κ_1 is more distinct than κ_2 for dynamic buckling load, which means Young's module and shear modulus have a more pronounced than density on the buckling load. Therefore, for an eccentricity simply supported orthotropic FG cylindrical shell, a rational design of κ_1 and κ_2 can maximise the material property and optimise the structures.

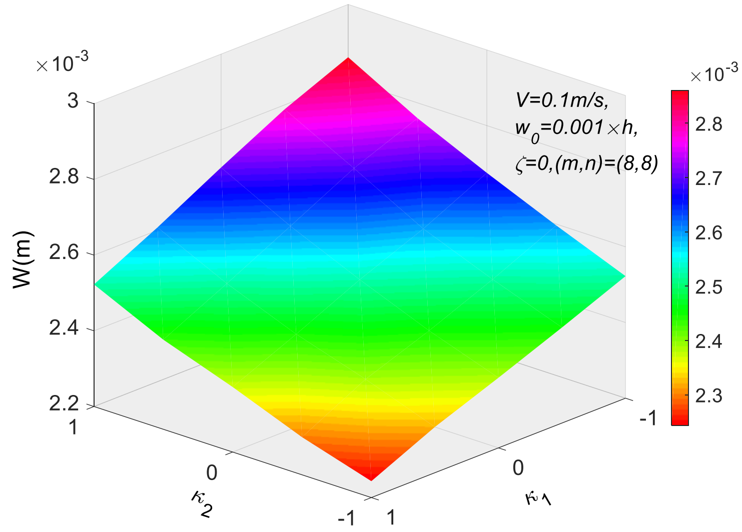

Figure 7.16 The relationship of different κ_1 and κ_2 on the peak deflections at the time of onset buckling for an eccentricity simply supported orthotropic FG cylindrical shell

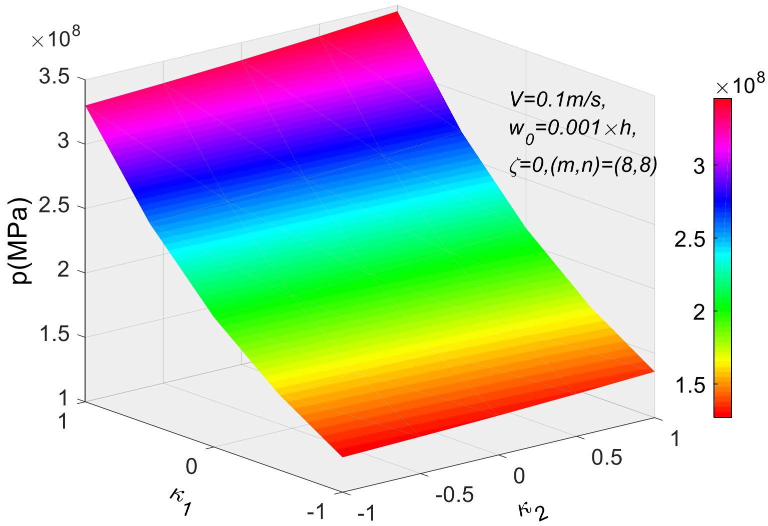

Figure 7.17 The relationship of different κ_1 and κ_2 on critical dynamic buckling load at the time of onset buckling for an eccentricity simply supported orthotropic FG cylindrical shell

7.5 Conclusions

Dynamic stability behaviours of an imperfect orthotropic E-FGM circular cylindrical shell subjected to constant longitudinal velocities were investigated. The dynamic longitudinal loading on the shell is accomplished by applying a constant displacement rate at one end with respect to the other. According to the improved Donnell shell theory, the nonlinear compatibility equation and the equation of motion were derived with the consideration of initial imperfection and damping effects. The governing equation was solved by fourth-order Runge-Kutta method and the nonlinear dynamic stability of the orthotropic FG cylindrical shell is assessed based on Budiansky-Roth criterion. The Effect of various velocities, initial imperfections, damping ratios, inhomogeneous parameters κ_1 and κ_2 on nonlinear dynamic buckling of the orthotropic FG cylindrical shells were studied and the results of this investigation can be summarized as:

1. When considering dynamic terms, the dynamic critical buckling loads are larger than the static ones. Moreover, with the increase of axial compression rates, the critical buckling load and amplitude of the vibration of the cylindrical shell increases; while the time of the onset of buckling decreases and the deflection at the buckling point decreases as well.
2. The presence of initial imperfection considerably reduces the dynamic buckling load and the oscillation of the cylindrical shell after buckling. The large initial imperfection will change the whole appearance of the response curve. At this moment, the B-R criterion is unsuitable for predicting dynamic buckling behaviour of the cylindrical shell.
3. The increasing of the damping ratios results in the rise of dynamic buckling load and eliminates the oscillations in the third phases.
4. Both κ_1 (or Young's module and shear modulus) and κ_2 (density) will increase the buckling load; while the effect of κ_1 is more distinct than κ_2 for dynamic stability behaviours. Therefore, for an eccentricity simply supported orthotropic FG cylindrical shell, a rational design of κ_1 and κ_2 can maximise the material property and optimise the structures.

Chapter 8 Conclusions and further work

8.1 Conclusions

This dissertation provides a comprehensive analytical analysis framework for dynamic behaviour assessment of beam, plate and cylindrical shell made of advanced materials, as well as a vivid modelling on the damping effects, thermal effect and elastic foundation for structures under dynamic loadings. Chapters 3-7 present dynamic characteristics and stability of beams, plates and cylindrical shells under different situations, respectively. A detailed summary is shown below.

Chapter 3 proposes the nonlinear dynamic buckling analysis of Euler-Bernoulli beam-columns under constant loading rates. The critical dynamic buckling load of the damped system is larger than the undamped system. The increasing of the damping ratios results in an increase of dynamic buckling load. However, the buckling time of structure will be delayed for a damped system. The critical buckling is deceased for the temperature change from temperature fall to temperature rise. Moreover, temperature rise would defer the time of buckling while temperature fall would accelerate the time of buckling. For a beam-column subjected to a compression rate in the presence of damping effects under thermal environment, velocities of load are the most crucial parameter for structures, then temperature change. However, in this case, the damping effect has the least effects. The analytical solutions are compared with the FE results and the proposed methods are in a good agreement with the FEM modellings.

Chapter 4 investigates the nonlinear dynamic characteristics and stability of composite orthotropic plate on Winkler-Pasternak elastic foundation subjected to different axial velocities with damping and thermal effects. The accuracy of the obtained results of frequency parameters is verified against the published paper by other methods and shows that the proposed method has a good accuracy. The increase in damping ratios increases the dynamic buckling load and eliminates the oscillations in the third phases. Temperature rise will cause the increase of axial compression stresses and further reduce the transverse stiffness of plate. Considering the elastic foundation, the deflection of the plate will decrease; while Pasternak parameter is more sensitive than Winkler one for the structures. Also the increase of foundation parameters would reduce the onset of buckling amplitudes and decrease dynamic buckling load. The author thought that the B-R criterion is unsuitable for the plate on elastic foundation when foundation parameters become larger.

Chapter 5 implements nonlinear primary resonance behaviour of cylindrical shells made of functionally graded (FG) porous materials subjected to a uniformly distributed harmonic load including the damping effect. Three types of FG porous distributions, namely symmetric porosity distribution, non-symmetric porosity stiff or soft distribution and uniform porosity distribution were considered. By increasing the value of the coefficient of porosity, hardening nonlinearity is weakened for all the distributions. The symmetric porosity distribution occupies more stiffness than the other two types and consequently, the detuning parameters and amplitude of response are the smallest. While in the presence of damping effect, the amplitude-frequency curves are finite. And as the value of damping ratio increases, the peak amplitude decreases as the value of damping ratio increases. The analytical method is further verified by the adaptive step-size fourth-order Runge-Kutta method numerically. The present method is in agreement with that from the numerical simulation, and then the validity of the present study is examined.

Chapter 6 carries out the dynamic stability analysis of an FG orthotropic circular cylindrical shell surrounded by a Winkler-Pasternak elastic foundation subjected to linearly increasing load with the consideration of damping effect. The non-homogenous parameters κ_i have a great effect on dynamic buckling behaviours (critical load, buckling modes, deflection, etc.). Additionally, the effect of κ_1 (governed Young's module and shear modulus) is more distinct than κ_2 (governed density) for dynamic stability behaviours. Therefore, a rational design of κ_1 and κ_2 is necessary for buckling analysis of an FG orthotropic cylindrical shell. The dynamic critical buckling loads are larger than the static ones when considering the dynamic terms for all the cases. With the increase of loading speed, the critical buckling time, dynamic buckling loads and the vibration of the structure increase; while deflection decrease. The increasing of damping ratios not always results in the rise of buckling load, which may affect by buckling modes or other uncertainty factors. The deflection increases with the increase of damping ratios.

Chapter 7 conducts the dynamic stability behaviours of an imperfect orthotropic E-FGM circular cylindrical shell subjected to constant longitudinal velocities. The dynamic longitudinal loading on the shell is accomplished by applying a constant displacement rate at one end with respect to the other. The presence of initial imperfection considerably reduces the dynamic buckling load and the oscillation of the cylindrical shell after buckling. The large initial imperfection will change the whole appearance of the response curve. At this moment, the B-R criterion is unsuitable for predicting dynamic buckling behaviour of the cylindrical shell.

In brief, by comparing with finite element method, the other methods in open literature, the validity, accuracy, applicability of the proposed analytical models and solutions were verified. The analytical analysis framework for dynamic buckling and dynamic assessment of thin-walled structures made of advanced materials with consideration of damping effects, thermal effects and elastic foundations in this dissertation can help to achieve optimum design of such structures under dynamic loadings, as well as a useful benchmark for design and analysis of nano/micro-sized devices and systems.

In engineering practices, there are some examples involving dynamic buckling. 1. Aerospace components or military weapons (i.e. propellant tank of space shuttle, the skin of ballistic missile, aircraft landing struts, etc.) may be exposed to rapid loading caused by sudden gusts, extreme manoeuvres, or ground impacts while landing. 2. The intermediate velocity impact load, or fluid-solid slamming, is a typical example of such dynamic load. For example, when a ship is slammed by sea waves, the beams and plates of its deck are subjected to dynamic load; when an airplane lands on sea water, its landing gear is subjected to dynamic load; when an offshore rigs and wind turbine towers is subjected to sea waves. Underwater vehicles subjected to slamming of the water. 3. Normally, the static loading-bearing capacity of the structure is measured by hydraulic testing machines in the lab, which means the structure is loaded by a constant displacement rate (or displacement control) of the one end with respect to the other. With the increase of the loading rates, the percentage of the dynamic terms will rise. In such situation, it is important to investigate the threshold velocity values between static and dynamic cases.

8.2 Future work

The current research focuses on the analytical analysis of dynamic buckling and dynamic characteristics of thin-walled structures made of advanced materials with consideration of damping effects, thermal effects and elastic foundations. As the application of advanced materials is becoming diversification and more complex, so there are some areas in this work can be extended to fill the insufficient of this study.

The following suggestions are recommended as possible future research:

8.2.1 *Nondeterministic dynamic buckling analysis*

In this dissertation, deterministic dynamic buckling analysis with consideration of damping effects, thermal effects and elastic foundations was conducted. Although deterministic dynamic buckling analysis has been quite prevalent in various engineering fields, the success of this framework was underpinned by the predetermined material and geometric properties as well as acceptable assumptions. However, uncertainty, unpredictability and randomness are the inherent attributes of structural design. Therefore, safety factors or failure factors are applied in most commonly used design standards of structures, such as Chinese design code GB50017-201X (2012) and GB50017-2003 (2003), American code (ANSI/AISC360-10, 2010) and EC3 (2005). In addition, the theoretical predictions do not always match with the results of experimental ones. Under these circumstances, it is not unnatural and essential to consider the influences of uncertainties of system parameters in deterministic dynamic buckling analysis.

8.2.2 *The experimental research*

Though theoretical models of this study can obtain the elaborate and exact results, the experimental studies of dynamic buckling of thin-walled structures made of advanced material are indispensable. Here are two reasons:1. The analytical methods are based on the assumptions or simplified modellings, which could change in different situations. 2. In engineering structures, the phenomenon modelled in analytical way may not correspond to the one in the real world. Thus, the experimental investigations of dynamic characteristics and stability of thin-walled structures made of advanced material under various environmental conditions are needed.

8.2.3 *The gradient thermal effect or thermomechanical loading conditions*

In general engineering applications (i.e. aerospace and mechanical engineering), structures are not only subjected to uniform temperature rise but also exposed to gradient thermal effect or the combination of gradient thermal effect and mechanical load. Temperature changes have a significant influence on dynamic behaviour and further affect the performance and stability of structures, especially for FGMs. i.e., for functionally graded shells, the temperature change is not uniform along the thickness direction due to the various coefficients of elastic moduli, thermal expansion and the coefficient of heat conduction. To the author’s knowledge, although there is much research on buckling of structures, the work of gradient thermal effect and different mechanical loadings on dynamic buckling of thin-walled structures has not been considered simultaneously. Therefore, it is of great significance to study dynamic buckling response of structures in a combined thermo-mechanical loading.

8.2.4 *Extension of the proposed analytical method to other loading conditions*

As demonstrated in Chapter 1, the analytical framework of dynamic buckling was developed based on constant velocity or displacement loading scheme. In Chapter 6, the linearly increasing load was applied in dynamic buckling of the orthotropic functionally graded cylindrical shell. However, in engineering practices, both constant mass impulse loading scheme and force-time impulse loading scheme (i.e., a sinusoidal pulse, an N-wave pulse, and a triangular load, etc.) are also widespread. It is worth to investigate the dynamic buckling of various types of loadings.

8.2.5 *Extension of the proposed analytical method to higher-order shear deformation theory*

The main purpose of this dissertation is to develop an analytical analysis for dynamic buckling and dynamic characteristics of thin-walled structures made of advanced materials and the classical theories for thin elastic structures are utilized. However, the application of such theories to thick and robust structures could lead to more errors even mistakes in deflections, stresses, frequencies and loads. The higher-order shear deformation theories (HSDTs) account for the shear deformation effects, such as the first-order shear deformation theory, the second-order shear deformation theory, third-order shear deformation theory, sinusoidal shear deformation theory or hyperbolic shear deformation theory should be considered in dynamic buckling analysis.

8.2.6 *Optimization/sensitivity analysis of structures under dynamic loadings*

As can be seen, the material, geometrical properties, damping effect, thermal effect, elastic foundation, boundary conditions and different loading types may have a distinct influence on dynamic characteristics of structures. Moreover, in real-life engineering application, more integrated modeling and nonlinear structural dynamics analysis is of interest. The dynamics analysis of built-up structures is also needed due to the complexity of geometry in the future. Therefore, by developing optimisation/sensitivity analysis, one can capture the extent of different effects and the optimised design can be obtained for structures made of advanced materials under dynamic loadings.

References

[1] Karagiozova D, Alves M. Dynamic elastic-plastic buckling of structural elements: a review. Applied Mechanics Reviews. 2008;61:040803.

[2] Budiansky B. Theory of buckling and post-buckling behavior of elastic structures. Advances in applied mechanics. 1974;14:1-65.

[3] Ansari R, Pourashraf T, Gholami R, Shahabodini A. Analytical solution for nonlinear postbuckling of functionally graded carbon nanotube-reinforced composite shells with piezoelectric layers. Composites Part B: Engineering. 2016;90:267-277.

[4] Sevin E. On the elastic bending of columns due to dynamic axial forces including effects of axial inertia. Journal of Applied Mechanics. 1960;27:125-131.

[5] Pi Y-L, Bradford MA. Nonlinear dynamic buckling of pinned–fixed shallow arches under a sudden central concentrated load. Nonlinear Dynamics. 2013;73:1289-1306.

[6] Budiansky B. Buckling of clamped shallow spherical shells. Technical report. Cambridge: Harvard University; 1959.

[7] Azarboni HR, Darvizeh M, Darvizeh A, Ansari R. Nonlinear dynamic buckling of imperfect rectangular plates with different boundary conditions subjected to various pulse functions using the Galerkin method. Thin-Walled Structures. 2015;94:577-584.

[8] Elishakoff I. Probabilistic theory of structures: Courier Corporation, 1999.

[9] Rouhi H, Ansari R. Nonlocal analytical Flugge shell model for axial buckling of double-walled carbon nanotubes with different end conditions. Nano. 2012;7:1250018.

[10] Rahman T, Jansen E, Gürdal Z. Dynamic buckling analysis of composite cylindrical shells using a finite element based perturbation method. Nonlinear Dynamics. 2011;66:389-401.

[11] Lindberg HE, Florence AL. Dynamic pulse buckling: theory and experiment: Springer Science & Business Media, 2012.

[12] Gladden J, Handzy N, Belmonte A, Villermaux E. Dynamic buckling and fragmentation in brittle rods. Physical review letters. 2005;94:035503.

[13] Hutchinson JW, Budiansky B. Dynamic buckling estimates. AIAA Journal. 1966;4:525-530.

[14] Fu Y, Gao Z, Zhu F. Analysis of nonlinear dynamic response and dynamic buckling for laminated shallow spherical thick shells with damage. Nonlinear Dynamics. 2008;54:333-343.

[15] Hoff NJ, Bruce VG. Dynamic analysis of the buckling of laterally loaded flat arches. Studies in Applied Mathematics. 1953;32:276-288.

[16] Bisagni C. Dynamic buckling of fiber composite shells under impulsive axial compression. Thin-Walled Structures. 2005;43:499-514.

[17] Simitses GJ. Simple Mechanical Models. Dynamic Stability of Suddenly Loaded Structures: Springer; 1990. p. 24-53.

[18] Budiansky B, Roth RS. Axisymmetric dynamic buckling of clamped shallow spherical shells. NASA TND-15101962. p. 597-606.

[19] Huyan X, Simitses GJ. Dynamic buckling of imperfect cylindrical shells under axial compression and bending moment. AIAA Journal. 1997;35:1404-1412.

[20] Petry D, Fahlbusch G. Dynamic buckling of thin isotropic plates subjected to in-plane impact. Thin-Walled Structures. 2000;38:267-283.

[21] Tornabene F. Free vibration analysis of functionally graded conical, cylindrical shell and annular plate structures with a four-parameter power-law distribution. Computer Methods in Applied Mechanics and Engineering. 2009;198:2911-2935.

[22] Pradhan S, Loy C, Lam K, Reddy J. Vibration characteristics of functionally graded cylindrical shells under various boundary conditions. Applied Acoustics. 2000;61:111-129.

[23] Loy C, Lam K, Reddy J. Vibration of functionally graded cylindrical shells. International Journal of Mechanical Sciences. 1999;41:309-324.

[24] Chung Y, Chi S. The residual stress of functionally graded materials. J Chin Inst Civil Hydraulic Eng. 2001;13:1-9.

[25] Chi S, Chung Y. Cracking in sigmoid functionally graded coating. J Mech. 2002;18:41-53.

[26] Hamed M, Eltaher M, Sadoun A, Almitani K. Free vibration of symmetric and sigmoid functionally graded nanobeams. Applied Physics A. 2016;122:829.

[27] Jung W-Y, Han S-C, Park W-T. Four-variable refined plate theory for forced-vibration analysis of sigmoid functionally graded plates on elastic foundation. International Journal of Mechanical Sciences. 2016;111:73-87.

[28] Duc ND, Cong PH. Nonlinear dynamic response of imperfect symmetric thin sigmoid-functionally graded material plate with metal-ceramic-metal layers on elastic foundation. Journal of Vibration and Control. 2015;21:637-646.

[29] Ravichandran K. Thermal residual stresses in a functionally graded material system. Materials Science and Engineering: A. 1995;201:269-276.

[30] Atmane HA, Tounsi A, Meftah SA, Belhadj HA. Free vibration behavior of exponential functionally graded beams with varying cross-section. Journal of Vibration and Control. 2010:311–318.

[31] Chakraborty A, Gopalakrishnan S, Reddy J. A new beam finite element for the analysis of functionally graded materials. International Journal of Mechanical Sciences. 2003;45:519-539.

[32] Shen H-S. Postbuckling analysis of axially-loaded functionally graded cylindrical shells in thermal environments. Composites Science and Technology. 2002;62:977-987.

[33] Shen H-S. Postbuckling analysis of pressure-loaded functionally graded cylindrical shells in thermal environments. Engineering Structures. 2003;25:487-497.

[34] Sofiyev A, Kuruoglu N. Torsional vibration and buckling of the cylindrical shell with functionally graded coatings surrounded by an elastic medium. Composites Part B: Engineering. 2013;45:1133-1142.

[35] Shahsiah R, Eslami M. Thermal buckling of functionally graded cylindrical shell. Journal of thermal stresses. 2003;26:277-294.

[36] Shen H-S, Noda N. Postbuckling of FGM cylindrical shells under combined axial and radial mechanical loads in thermal environments. International Journal of Solids and Structures. 2005;42:4641-4662.

[37] Yang J, Liew K, Wu Y, Kitipornchai S. Thermo-mechanical post-buckling of FGM cylindrical panels with temperature-dependent properties. International Journal of Solids and Structures. 2006;43:307-324.

[38] Gary G. Dynamic buckling of an elastoplastic column. International Journal of Impact Engineering. 1983;1:357-375.

[39] Hoff NJ. The dynamics of the buckling of elastic columns. Journal of Applied Mechanics. 1951;18:68-74.

[40] Schmitt A. A method of stepwise integration in problems of impact buckling. J Appl Mech. 1956;23.

[41] Erickson B, Nardo S, Patel S, Hoff N. An experimental investigation of the maximum loads supported by elastic columns in rapid compression tests. Proceedings of the Society for Experimental Stress Analysis. 1956;14:13-20.

[42] Elishakoff I. Hoff's problem in a probabilistic setting. Journal of Applied Mechanics. 1980;47:403-408.

[43] Motamarri P, Suryanarayan S. Unified analytical solution for dynamic elastic buckling of beams for various boundary conditions and loading rates. International Journal of Mechanical Sciences. 2012;56:60-69.

[44] Kuzkin VA, Dannert MM. Buckling of a column under a constant speed compression: a dynamic correction to the Euler formula. Acta Mechanica. 2016:1-8.

[45] Pian T, Siddall JN. Dynamic buckling of slender struts: MIT Press, 1950.

[46] Davidson JF. Buckling of Struts under Dynamic Loading. Journal of the Mechanics and Physics of Solids. 1953;2:54-66.

[47] Hayashi T, Sano Y. Dynamic Buckling of Elastic Bars: 1st Report, The Case of Low Velocity Impact. Bulletin of JSME. 1972;15:1167-1175.

[48] Hayashi T, Sano Y. Dynamic buckling of elastic bars: 2nd Report, The case of high velocity impact. Bulletin of JSME. 1972;15:1176-1184.

[49] Ari-Gur J, Weller T, Singer J. Experimental studies of columns under axial impact. TAE Report (Technion Israel Institute of Technology, Department of Aeronautical Engineering). 1978.

[50] Taub J. Impact buckling of thin bars in the elastic range for any end condition. 1934.

[51] Koning C, Taub J. Impact buckling of thin bars in the elastic range hinged at both ends. 1934.

[52] Huffington NJ. Response of Elastic Columns to Axial Pulse Loading. AIAA Journal. 1963;1:2099-2104.

[53] Hoff NJ. The dynamics of the buckling of elastic columns: Polytechnic Institute of Brooklyn, Department of Aeronautical Engineering and Applied Mechanics, 1951.

[54] Gao K, Gao W, Wu D, Song C. Nonlinear dynamic stability analysis of Euler–Bernoulli beam–columns with damping effects under thermal environment. Nonlinear Dynamics. 2017;90:2423–2444.

[55] Kazemzadeh Azad S, Topkaya C, Bybordiani M. Dynamic buckling of braces in concentrically braced frames. Earthquake Engineering & Structural Dynamics. 2018;47:613-633.

[56] Ghiasian S, Kiani Y, Eslami M. Dynamic buckling of suddenly heated or compressed FGM beams resting on nonlinear elastic foundation. Composite Structures. 2013;106:225-234.

[57] Ren M, Liu Y, Zhe Liu J, Wang L, Zheng Q. Anomalous elastic buckling of layered crystalline materials in the absence of structure slenderness. Journal of the Mechanics and Physics of Solids. 2016;88:83-99.

[58] Wu H, Yang J, Kitipornchai S. Dynamic instability of functionally graded multilayer graphene nanocomposite beams in thermal environment. Composite Structures. 2017;162:244-254.

[59] Smyczynski M, Magnucka-Blandzi E. Static and dynamic stability of an axially compressed five-layer sandwich beam. Thin-Walled Structures. 2015;90:23-30.

[60] Lim J-Y, Bart-Smith H. High velocity compressive response of metallic corrugated core sandwich columns. International Journal of Mechanical Sciences. 2016;106:78-94.

[61] Lim J-Y, Bart-Smith H. Theoretical approach on the dynamic global buckling response of metallic corrugated core sandwich columns. International Journal of Non-Linear Mechanics. 2014;65:14-31.

[62] Adjiman J, Doaré O, Moussou P. Buckling of a Flat Plate in a Confined Axial Flow. ASME 2015 Pressure Vessels and Piping Conference: American Society of Mechanical Engineers; 2015. p. V005T009A009-V005T009A009.

[63] Xiong CA, Jiang WG. Dynamic buckling of single-walled carbon nanotubes under axial impact loading. Applied Mechanics and Materials: Trans Tech Publ; 2014. p. 178-182.

[64] Sun C, Liu K. Dynamic torsional buckling of a double-walled carbon nanotube embedded in an elastic medium. European Journal of Mechanics-A/Solids. 2008;27:40-49.

[65] Sun C, Liu K, Hong Y. Dynamic shell buckling behavior of multi-walled carbon nanotubes embedded in an elastic medium. Science China Physics, Mechanics and Astronomy. 2013;56:483-490.

[66] Hu W, Song M, Deng Z, Yin T, Wei B. Axial dynamic buckling analysis of embedded single-walled carbon nanotube by complex structure-preserving method. Applied Mathematical Modelling. 2017;52:15-27.

[67] Ari-Gur J, Elishakoff I. Dynamic instability of a transversely isotropic column subjected to a compression pulse. Computers & Structures. 1997;62:811-815.

[68] Ari-Gur J, Elishakoff I. Effects of shear deformation and rotary inertia on the dynamic pulse buckling of a structure. Publ by ASME1990.

[69] Ari-Gur J, Weller T, Singer J. Experimental and theoretical studies of columns under axial impact. International Journal of Solids and Structures. 1982;18:619-641.

[70] Ari-Gur J, Singer J. Theoretical studies of columns under axial impact and experimental verification. TAE Report (Technion Israel Institute of Technology, Department of Aeronautical Engineering). 1979.

[71] Ari-Gur J, Singer J, Weller T. Dynamic buckling of plates under longitudinal impact. TAE Report (Technion Israel Institute of Technology, Department of Aeronautical Engineering). 1981.

[72] Ari-Gur J, Simonetta SR. Dynamic pulse buckling of rectangular composite plates. Composites Part B: Engineering. 1997;28:301-308.

[73] Papazoglou V, Tsouvalis N. Large deflection dynamic response of composite laminated plates under in-plane loads. Composite Structures. 1995;33:237-252.

[74] Ekstrom R. Dynamic buckling of a rectangular orthotropic plate. AIAA Journal. 1973;11:1655-1659.

[75] Ramezannezhad Azarboni H, Darvizeh M, Darvizeh A, Ansari R. Nonlinear dynamic buckling of imperfect rectangular plates with different boundary conditions subjected to various pulse functions using the Galerkin method. Thin-Walled Structures. 2015;94:577-584.

[76] Mojahedin A, Jabbari M, Khorshidvand A, Eslami M. Buckling analysis of functionally graded circular plates made of saturated porous materials based on higher order shear deformation theory. Thin-Walled Structures. 2016;99:83-90.

[77] Jabbari M, Hashemitaheri M, Mojahedin A, Eslami M. Thermal buckling analysis of functionally graded thin circular plate made of saturated porous materials. Journal of thermal stresses. 2014;37:202-220.

[78] Eslami H, Kandil OA. Nonlinear forced vibration of orthotropic rectangular plates using the method of multiple scales. AIAA Journal. 1989;27:955-960.

[79] Yeh F, Liu W. Nonlinear analysis of rectangular orthotropic plates. International Journal of Mechanical Sciences. 1991;33:563-578.

[80] Eshmatov BK. Nonlinear vibrations and dynamic stability of viscoelastic orthotropic rectangular plates. Journal of Sound and Vibration. 2007;300:709-726.

[81] Ma'en SS, Al-Kouz WG. Vibration analysis of non-uniform orthotropic Kirchhoff plates resting on elastic foundation based on nonlocal elasticity theory. International Journal of Mechanical Sciences. 2016;114:1-11.

[82] Wang Q, Shi D, Shi X. A modified solution for the free vibration analysis of moderately thick orthotropic rectangular plates with general boundary conditions, internal line supports and resting on elastic foundation. Meccanica. 2016;51:1985-2017.

[83] Ferreira PS, Virtuoso FB. Semi-analytical models for the post-buckling analysis and ultimate strength prediction of isotropic and orthotropic plates under uniaxial compression with the unloaded edges free from stresses. Thin-Walled Structures. 2014;82:82-94.

[84] Golmakani M, Rezatalab J. Nonuniform biaxial buckling of orthotropic nanoplates embedded in an elastic medium based on nonlocal Mindlin plate theory. Composite Structures. 2015;119:238-250.

[85] Patel B, Ganapathi M, Prasad K, Balamurugan V. Dynamic instability of layered anisotropic composite plates on elastic foundations. Engineering Structures. 1999;21:988-995.

[86] Chattopadhyay A, Radu AG. Dynamic instability of composite laminates using a higher order theory. Computers & Structures. 2000;77:453-460.

[87] Kubiak T. Dynamic buckling of thin-walled composite plates with varying widthwise material properties. International Journal of Solids and Structures. 2005;42:5555-5567.

[88] Gao K, Gao W, Wu D, Song C. Nonlinear dynamic characteristics and stability of composite orthotropic plate on elastic foundation under thermal environment. Composite Structures. 2017;168:619–632.

[89] Shen H-S. Postbuckling of nanotube-reinforced composite cylindrical shells in thermal environments, Part II: Pressure-loaded shells. Composite Structures. 2011;93:2496-2503.

[90] Shen H-S. Postbuckling of nanotube-reinforced composite cylindrical shells in thermal environments, Part I: Axially-loaded shells. Composite Structures. 2011;93:2096-2108.

[91] Shen H-S. Thermal buckling and postbuckling behavior of functionally graded carbon nanotube-reinforced composite cylindrical shells. Composites Part B: Engineering. 2012;43:1030-1038.

[92] Shen H-S, Zhang C-L. Thermal buckling and postbuckling behavior of functionally graded carbon nanotube-reinforced composite plates. Materials & Design. 2010;31:3403-3411.

[93] Shen H-S, Xiang Y. Postbuckling of nanotube-reinforced composite cylindrical shells under combined axial and radial mechanical loads in thermal environment. Composites Part B: Engineering. 2013;52:311-322.

[94] Shen H-S, Zhang C-L. Postbuckling of double-walled carbon nanotubes with temperature dependent properties and initial defects under combined axial and radial mechanical loads. International Journal of Solids and Structures. 2007;44:1461-1487.

[95] Shen H-S, Zhang C-L. Torsional buckling and postbuckling of double-walled carbon nanotubes by nonlocal shear deformable shell model. Composite Structures. 2010;92:1073-1084.

[96] Shen H-S. Nonlocal shear deformable shell model for torsional buckling and postbuckling of microtubules in thermal environments. Mechanics Research Communications. 2013;54:83-95.

[97] Shen H-S. Torsional buckling and postbuckling of FGM cylindrical shells in thermal environments. International Journal of Non-Linear Mechanics. 2009;44:644-657.

[98] Wattanasakulpong N, Prusty BG, Kelly DW, Hoffman M. Free vibration analysis of layered functionally graded beams with experimental validation. Materials & Design (1980-2015). 2012;36:182-190.

[99] Sofiyev A. Dynamic buckling of functionally graded cylindrical thin shells under non-periodic impulsive loading. Acta Mechanica. 2003;165:151-163.

[100] Sofiyev A. On the dynamic buckling of truncated conical shells with functionally graded coatings subject to a time dependent axial load in the large deformation. Composites Part B: Engineering. 2014;58:524-533.

[101] Sofiyev A. The buckling of functionally graded truncated conical shells under dynamic axial loading. Journal of Sound and Vibration. 2007;305:808-826.

[102] Huang H, Han Q. Nonlinear dynamic buckling of functionally graded cylindrical shells subjected to time-dependent axial load. Composite Structures. 2010;92:593-598.

[103] Van Dung D. Semi-analytical approach for analyzing the nonlinear dynamic torsional buckling of stiffened functionally graded material circular cylindrical shells surrounded by an elastic medium. Applied Mathematical Modelling. 2015;39:6951-6967.

[104] Bich DH, Van Dung D. Nonlinear static and dynamic buckling analysis of functionally graded shallow spherical shells including temperature effects. Composite Structures. 2012;94:2952-2960.

[105] Shaw D, Shen Y, Tsai P. Dynamic buckling of an imperfect composite circular cylindrical shell. Computers & Structures. 1993;48:467-472.

[106] Liao C-L, Cheng C-R. Dynamic stability of stiffened laminated composite plates and shells subjected to in-plane pulsating forces. Journal of Sound and Vibration. 1994;174:335-351.

[107] Gu W, W. Tang, T. Liu. Dynamic pulse buckling of cylindrical shells subjected to external impulsive loading. Journal of pressure vessel technology. 1996;118:33-37.

[108] Ng T, Lam K, Liew K, Reddy J. Dynamic stability analysis of functionally graded cylindrical shells under periodic axial loading. International Journal of Solids and Structures. 2001;38:1295-1309.

[109] Darabi M, Darvizeh M, Darvizeh A. Non-linear analysis of dynamic stability for functionally graded cylindrical shells under periodic axial loading. Composite Structures. 2008;83:201-211.

[110] Shariyat M. Dynamic thermal buckling of suddenly heated temperature-dependent FGM cylindrical shells, under combined axial compression and external pressure. International Journal of Solids and Structures. 2008;45:2598-2612.

[111] Shariyat M. Dynamic buckling of suddenly loaded imperfect hybrid FGM cylindrical shells with temperature-dependent material properties under thermo-electro-mechanical loads. International Journal of Mechanical Sciences. 2008;50:1561-1571.

[112] Bich DH, Van Dung D, Nam VH, Phuong NT. Nonlinear static and dynamic buckling analysis of imperfect eccentrically stiffened functionally graded circular cylindrical thin shells under axial compression. International Journal of Mechanical Sciences. 2013;74:190-200.

[113] Lei Z, Zhang L, Liew K, Yu J. Dynamic stability analysis of carbon nanotube-reinforced functionally graded cylindrical panels using the element-free kp-Ritz method. Composite Structures. 2014;113:328-338.

[114] Ozturk M, Erdogan F. The mixed mode crack problem in an inhomogeneous orthotropic medium. International Journal of Fracture. 1999;98:243-261.

[115] Ozturk M, Erdogan F. Mode I crack problem in an inhomogeneous orthotropic medium. International Journal of Engineering Science. 1997;35:869-883.

[116] Kaysser WA, Ilschner B. FGM Research Activities in Europe. Mrs Bulletin. 1995;20:22-26.

[117] Sampath S, Herman H, Shimoda N, Saito T. Thermal Spray Processing of FGMs. Mrs Bulletin. 1995;20:27-31.

[118] Sofiyev AH, Karaca Z, Zerin Z. Non-linear vibration of composite orthotropic cylindrical shells on the non-linear elastic foundations within the shear deformation theory. Composite Structures. 2017;159:53-62.

[119] Vel SS. Exact elasticity solution for the vibration of functionally graded anisotropic cylindrical shells. Composite Structures. 2010;92:2712-2727.

[120] Pelletier JL, Vel SS. An exact solution for the steady-state thermoelastic response of functionally graded orthotropic cylindrical shells. International Journal of Solids and Structures. 2006;43:1131-1158.

[121] Wang X, Sudak L. Three-dimensional analysis of multi-layered functionally graded anisotropic cylindrical panel under thermomechanical loading. Mechanics of materials. 2008;40:235-254.

[122] Chen W, Bian Z, Ding H. Three-dimensional vibration analysis of fluid-filled orthotropic FGM cylindrical shells. International Journal of Mechanical Sciences. 2004;46:159-171.

[123] Sofiyev A, Kuruoglu N. Buckling and vibration of shear deformable functionally graded orthotropic cylindrical shells under external pressures. Thin-Walled Structures. 2014;78:121-130.

[124] Najafov A, Sofiyev A, Kuruoglu N. Torsional vibration and stability of functionally graded orthotropic cylindrical shells on elastic foundations. Meccanica. 2013;48:829-840.

[125] Sofiyev A, Deniz A, Mecitoglu Z, Ozyigit P, Pinarlik M. Buckling of Shear Deformable Functionally Graded Orthotropic Cylindrical Shells under a Lateral Pressure. Acta Physica Polonica A. 2015;127:907-909.

[126] Sofiyev A. Large amplitude vibration of FGM orthotropic cylindrical shells interacting with the nonlinear Winkler elastic foundation. Composites Part B: Engineering. 2016;98:141-150.

[127] Sofiyev A. Nonlinear free vibration of shear deformable orthotropic functionally graded cylindrical shells. Composite Structures. 2016;142:35-44.

[128] Rao B, Rahman S. A continuum shape sensitivity method for fracture analysis of orthotropic functionally graded materials. Mechanics of materials. 2005;37:1007-1025.

[129] Xu H, Yao X, Feng X, Hisen YY. Dynamic stress intensity factors of a semi-infinite crack in an orthotropic functionally graded material. Mechanics of materials. 2008;40:37-47.

[130] Chalivendra VB. Mixed-mode crack-tip stress fields for orthotropic functionally graded materials. Acta Mechanica. 2009;204:51-60.

[131] Dag S, Yildirim B, Sarikaya D. Mixed-mode fracture analysis of orthotropic functionally graded materials under mechanical and thermal loads. International Journal of Solids and Structures. 2007;44:7816-7840.

[132] Kim J-H, Paulino GH. Mixed-mode fracture of orthotropic functionally graded materials using finite elements and the modified crack closure method. Engineering fracture mechanics. 2002;69:1557-1586.

[133] Dag S. Thermal fracture analysis of orthotropic functionally graded materials using an equivalent domain integral approach. Engineering fracture mechanics. 2006;73:2802-2828.

[134] Kieback B, Neubrand A, Riedel H. Processing techniques for functionally graded materials. Materials Science and Engineering: A. 2003;362:81-106.

[135] Kannan A, Cindrella L, Munukutla L. Functionally graded nano-porous gas diffusion layer for proton exchange membrane fuel cells under low relative humidity conditions. Electrochimica Acta. 2008;53:2416-2422.

[136] Zhou C, Wang P, Li W. Fabrication of functionally graded porous polymer via supercritical CO 2 foaming. Composites Part B: Engineering. 2011;42:318-325.

[137] Miyamoto Y, Kaysser W, Rabin B, Kawasaki A, Ford RG. Functionally graded materials: design, processing and applications. USA: Springer Science & Business Media, 2013.

[138] García-Moreno F. Commercial applications of metal foams: Their properties and production. Materials. 2016;9:85.

[139] Banhart J. Manufacture, characterisation and application of cellular metals and metal foams. Progress in materials science. 2001;46:559-632.

[140] Han X-H, Wang Q, Park Y-G, T'Joen C, Sommers A, Jacobi A. A review of metal foam and metal matrix composites for heat exchangers and heat sinks. Heat Transfer Engineering. 2012;33:991-1009.

[141] Smith B, Szyniszewski S, Hajjar J, Schafer B, Arwade S. Steel foam for structures: A review of applications, manufacturing and material properties. Journal of Constructional Steel Research. 2012;71:1-10.

[142] Magnucki K, Stasiewicz P. Elastic buckling of a porous beam. Journal of Theoretical and Applied Mechanics. 2004;42:859-868.

[143] Magnucka-Blandzi E, Magnucki K. Effective design of a sandwich beam with a metal foam core. Thin-Walled Structures. 2007;45:432-438.

[144] Magnucka-Blandzi E. Dynamic stability of a metal foam circular plate. Journal of Theoretical and Applied Mechanics. 2009;47:421-433.

[145] Magnucka-Blandzi E. Axi-symmetrical deflection and buckling of circular porous-cellular plate. Thin-Walled Structures. 2008;46:333-337.

[146] Magnucka-Blandzi E. Mathematical modelling of a rectangular sandwich plate with a metal foam core. Journal of Theoretical and Applied Mechanics. 2011;49:439-455.

[147] Belica T, Magnucki K. Dynamic stability of a porous cylindrical shell. PAMM. 2006;6:207-208.

[148] Belica T, Magnucki K. Dynamic stability of a porous cylindrical shell subjected to impulse of forces combined. Journal of KONES. 2007;14:39-48.

[149] Belica T, Malinowski M, Magnucki K. Dynamic stability of an isotropic metal foam cylindrical shell subjected to external pressure and axial compression. Journal of Applied Mechanics. 2011;78:041003.

[150] Belica T, Magnucki K. Stability of a porous-cellular cylindrical shell subjected to combined loads. Journal of Theoretical and Applied Mechanics. 2013;51:927-936.

[151] Jabbari M, Mojahedin A, Khorshidvand A, Eslami M. Buckling analysis of a functionally graded thin circular plate made of saturated porous materials. Journal of Engineering Mechanics. 2013;140:287-295.

[152] Jabbari M, Mojahedin A, Haghi M. Buckling analysis of thin circular FG plates made of saturated porous-soft ferromagnetic materials in transverse magnetic field. Thin-Walled Structures. 2014;85:50-56.

[153] Jabbari M, Mojahedin A, Joubaneh EF. Thermal Buckling Analysis of Circular Plates Made of Piezoelectric and Saturated Porous Functionally Graded Material Layers. Journal of Engineering Mechanics. 2014;141:04014148.

[154] Mojahedin A, Joubaneh EF, Jabbari M. Thermal and mechanical stability of a circular porous plate with piezoelectric actuators. Acta Mechanica. 2014;225:3437-3452.

[155] Biot M. Theory of buckling of a porous slab and its thermoelastic analogy. Journal of Applied Mechanics. 1964;31:194-198.

[156] Feyzi M, Khorshidvand A. Axisymmetric post-buckling behavior of saturated porous circular plates. Thin-Walled Structures. 2017;112:149-158.

[157] Mareishi S, Kalhori H, Rafiee M, Hosseini SM. Nonlinear forced vibration response of smart two-phase nano-composite beams to external harmonic excitations. Curved and Layered Structures. 2015;2.

[158] Rafiee M, Mohammadi M, Aragh BS, Yaghoobi H. Nonlinear free and forced thermo-electro-aero-elastic vibration and dynamic response of piezoelectric functionally graded laminated composite shells, Part I: Theory and analytical solutions. Composite Structures. 2013;103:179-187.

[159] Rafiee M, Mohammadi M, Aragh BS, Yaghoobi H. Nonlinear free and forced thermo-electro-aero-elastic vibration and dynamic response of piezoelectric functionally graded laminated composite shells: Part II: Numerical results. Composite Structures. 2013;103:188-196.

[160] Chen D, Yang J, Kitipornchai S. Free and forced vibrations of shear deformable functionally graded porous beams. International Journal of Mechanical Sciences. 2016;108:14-22.

[161] Chen D, Kitipornchai S, Yang J. Nonlinear free vibration of shear deformable sandwich beam with a functionally graded porous core. Thin-Walled Structures. 2016;107:39-48.

[162] Kitipornchai S, Chen D, Yang J. Free vibration and elastic buckling of functionally graded porous beams reinforced by graphene platelets. Materials & Design. 2017;116:656-665.

[163] Chen D, Yang J, Kitipornchai S. Nonlinear vibration and postbuckling of functionally graded graphene reinforced porous nanocomposite beams. Composites Science and Technology. 2017;142:235-245.

[164] Ghorbanpour Arani A, Khani M, Khoddami Maraghi Z. Dynamic analysis of a rectangular porous plate resting on an elastic foundation using high-order shear deformation theory. Journal of Vibration and Control. 2017.

[165] Ebrahimi F, Habibi S. Deflection and vibration analysis of higher-order shear deformable compositionally graded porous plate. Steel and Composite Structures. 2016;20:205-225.

[166] Wattanasakulpong N, Ungbhakorn V. Linear and nonlinear vibration analysis of elastically restrained ends FGM beams with porosities. Aerospace Science and Technology. 2014;32:111-120.

[167] Ebrahimi F, Mokhtari M. Transverse vibration analysis of rotating porous beam with functionally graded microstructure using the differential transform method.

Journal of the Brazilian Society of Mechanical Sciences and Engineering. 2015;37:1435-1444.

[168] Ebrahimi F, Hashemi M. On vibration behavior of rotating functionally graded double-tapered beam with the effect of porosities. Proceedings of the Institution of Mechanical Engineers, Part G: Journal of Aerospace Engineering. 2016;230:1903-1916.

[169] Duc ND, Quan TQ, Luat VD. Nonlinear dynamic analysis and vibration of shear deformable piezoelectric FGM double curved shallow shells under damping-thermo-electro-mechanical loads. Composite Structures. 2015;125:29-40.

[170] Quan TQ, Duc ND. Nonlinear vibration and dynamic response of shear deformable imperfect functionally graded double-curved shallow shells resting on elastic foundations in thermal environments. Journal of thermal stresses. 2016;39:437-459.

[171] Duc ND, Bich DH, Anh VTT. On the nonlinear stability of eccentrically stiffened functionally graded annular spherical segment shells. Thin-Walled Structures. 2016;106:258-267.

[172] Ghadiri M, SafarPour H. Free vibration analysis of size-dependent functionally graded porous cylindrical microshells in thermal environment. Journal of thermal stresses. 2017;40:55-71.

[173] Wang Y, Wu D. Free vibration of functionally graded porous cylindrical shell using a sinusoidal shear deformation theory. Aerospace Science and Technology. 2017;66:83-91.

[174] Weller T, Abramovich H, Yaffe R. Dynamic buckling of beams and plates subjected to axial impact. Computers & Structures. 1989;32:835-851.

[175] Hughes TJ. The finite element method: linear static and dynamic finite element analysis: Courier Corporation, 2012.

[176] Meier J. On the dynamics of elastic buckling. Journal of the Aeronautical Sciences. 2012.

[177] Jabareen M, Sheinman I. Dynamic buckling of a beam on a nonlinear elastic foundation under step loading. Journal of Mechanics of Materials and Structures. 2009;4:1365-1373.

[178] Lepik U. On dynamic buckling of elastic-plastic beams. International Journal of Non-Linear Mechanics. 2000;35:721-734.

[179] Clough RW, Penzien J. Dynamics of structures. 1975.

[180] Luongo A. Mode localization in dynamics and buckling of linear imperfect continuous structures. Normal Modes and Localization in Nonlinear Systems: Springer; 2001. p. 133-156.

[181] Kounadis AN, Raftoyiannis J. Dynamic Stability-Criteria of Nonlinear Elastic Damped Undamped Systems under Step Loading. AIAA Journal. 1990;28:1217-1223.

[182] Kounadis AN. Nonlinear Dynamic Buckling of Discrete Dissipative or Nondissipative Systems under Step Loading. AIAA Journal. 1991;29:280-289.

[183] Mallon NJ, Fey RHB, Nijmeijer H, Zhang GQ. Dynamic buckling of a shallow arch under shock loading considering the effects of the arch shape. International Journal of Non-Linear Mechanics. 2006;41:1057-1067.

[184] Lee HP. Effects of damping on the dynamic stability of a rod with an intermediate spring support subjected to follower forces. Computers & Structures. 1996;60:31-39.

[185] Ansari R, Mohammadi V, Faghih Shojaei M, Rouhi H. Thermal Post-Buckling Analysis of Nanoscale Films Based on a Non-Classical Finite Element Approach. Journal of thermal stresses. 2015;38:651-664.

[186] Ansari R, Sahmani S, Rouhi H. Axial buckling analysis of single-walled carbon nanotubes in thermal environments via the Rayleigh–Ritz technique. Computational Materials Science. 2011;50:3050-3055.

[187] Ebrahimi F, Barati MR. A unified formulation for dynamic analysis of nonlocal heterogeneous nanobeams in hygro-thermal environment. Applied Physics A. 2016;122:792.

[188] Wu G. The analysis of dynamic instability and vibration motions of a pinned beam with transverse magnetic fields and thermal loads. Journal of Sound and Vibration. 2005;284:343-360.

[189] Ghiasian S, Kiani Y, Eslami M. Nonlinear thermal dynamic buckling of FGM beams. European Journal of Mechanics-A/Solids. 2015;54:232-242.

[190] Li S-R, Zhou Y-H, Song X. Non-linear vibration and thermal buckling of an orthotropic annular plate with a centric rigid mass. Journal of Sound and Vibration. 2002;251:141-152.

[191] Barati MR, Zenkour AM, Shahverdi H. Thermo-mechanical buckling analysis of embedded nanosize FG plates in thermal environments via an inverse cotangential theory. Composite Structures. 2016;141:203-212.

[192] Taczała M, Buczkowski R, Kleiber M. Nonlinear buckling and post-buckling response of stiffened FGM plates in thermal environments. Composites Part B: Engineering. 2017;109:238-247.

[193] Panyatong M, Chinnaboon B, Chucheepsakul S. Free vibration analysis of FG nanoplates embedded in elastic medium based on second-order shear deformation plate theory and nonlocal elasticity. Composite Structures. 2016;153:428-441.

[194] Yang J, Shen H-S. Dynamic response of initially stressed functionally graded rectangular thin plates. Composite Structures. 2001;54:497-508.

[195] Uğurlu B, Kutlu A, Ergin A, Omurtag M. Dynamics of a rectangular plate resting on an elastic foundation and partially in contact with a quiescent fluid. Journal of Sound and Vibration. 2008;317:308-328.

[196] Stanton SC, Mann BP. On the dynamic response of beams with multiple geometric or material discontinuities. Mechanical Systems and Signal Processing. 2010;24:1409-1419.

[197] Shaker FJ. Effect of axial load on mode shapes and frequencies of beams. 1975.

[198] Yang B. Stress, strain, and structural dynamics: an interactive handbook of formulas, solutions, and MATLAB toolboxes: Academic Press, 2005.

[199] Thomsen JJ. Vibrations and stability: advanced theory, analysis, and tools: Springer Science & Business Media, 2013.

[200] Cai C, Zheng H, Khan M, Hung K. Modeling of material damping properties in ANSYS. CADFEM Users' Meeting & ANSYS Conference2002. p. 9-11.

[201] Deniz A, Sofiyev A. The nonlinear dynamic buckling response of functionally graded truncated conical shells. Journal of Sound and Vibration. 2013;332:978-992.

[202] Budiansky B, Roth RS. Axisymmetric dynamic buckling of clamped shallow spherical shells. 1962. 1962:597-606.

[203] Matsunaga H. Vibration and stability of thick plates on elastic foundations. Journal of Engineering Mechanics. 2000;126:27-34.

[204] Rahbar-Ranji A, Shahbaztabar A. Free vibration analysis of non-homogeneous orthotropic plates resting on Pasternak elastic foundation by Rayleigh-Ritz method. Journal of Central South University. 2016;23:413-420.

[205] Huang M, Ma X, Sakiyama T, Matuda H, Morita C. Free vibration analysis of orthotropic rectangular plates with variable thickness and general boundary conditions. Journal of Sound and Vibration. 2005;288:931-955.

[206] Bahmyari E, Rahbar-Ranji A. Free vibration analysis of orthotropic plates with variable thickness resting on non-uniform elastic foundation by element free Galerkin method. Journal of Mechanical Science and Technology. 2012;26:2685-2694.

[207] Li S, Zhou Y. Nonlinear vibration of heated orthotropic annular plates with immovably hinged edges. Journal of thermal stresses. 2003;26:691-700.

[208] Ninh DG, Bich DH. Nonlinear thermal vibration of eccentrically stiffened Ceramic-FGM-Metal layer toroidal shell segments surrounded by elastic foundation. Thin-Walled Structures. 2016;104:198-210.

[209] Bich DH, Ninh DG, Kien BH, Hui D. Nonlinear dynamical analyses of eccentrically stiffened functionally graded toroidal shell segments surrounded by elastic foundation in thermal environment. Composites Part B: Engineering. 2016;95:355-373.

[210] Bich DH, Van Dung D, Nam VH. Nonlinear dynamical analysis of eccentrically stiffened functionally graded cylindrical panels. Composite Structures. 2012;94:2465-2473.

[211] Gao K, Gao W, Wu D, Song C. Nonlinear dynamic characteristics and stability of composite orthotropic plate on elastic foundation under thermal environment. Composite Structures. 2017;168:619-632.

[212] Gao K, Gao W, Wu D, Song C. Nonlinear dynamic stability of the orthotropic functionally graded cylindrical shell surrounded by Winkler-Pasternak elastic foundation subjected to a linearly increasing load. Journal of Sound and Vibration. 2018;415:147-168.

[213] Jin Z-H, Batra R. Stress intensity relaxation at the tip of an edge crack in a functionally graded material subjected to a thermal shock. Journal of thermal stresses. 1996;19:317-339.

[214] Gibson LJ, Ashby MF. The mechanics of three-dimensional cellular materials. Proceedings of the Royal Society of London A: Mathematical, Physical and Engineering Sciences: The Royal Society; 1982. p. 43-59.

[215] Volmir AS. Nonlinear dynamics of plates and shells. Moscow: Science Edition, 1972.

[216] Nowinski J. Nonlinear transverse vibrations of orthotropic cylindrical shells. AIAA Journal. 1963;1:617-620.

[217] Evensen DA. Nonlinear flexural vibrations of thin-walled circular cylinders. Washington, DC: National Aeronautics and Space Administration; 1967.

[218] Dowell E, Ventres C. Modal equations for the nonlinear flexural vibrations of a cylindrical shell. International Journal of Solids and Structures. 1968;4:975-991.

[219] Chu H-N. Influence of large amplitudes on flexural vibrations of a thin circular cylindrical shell. Journal of the Aerospace Sciences. 1961;28:602-609.

[220] Amabili M. Discussion on" Nonlinear vibration of functionally graded circular cylindrical shells based on improved Donnell equations" by DH Bich and N. Xuan Nguyen, Journal of Sound and Vibration 331 (25)(2012) 5488-5501. Journal of Sound Vibration. 2014;333:1851-1852.

[221] Bich DH, Nguyen NX. Reply to: Discussion on" Nonlinear vibration of functionally graded circular cylindrical shells based on improved Donnell equations" by DH Bich and N. Xuan Nguyen, Journal of Sound and Vibration 331 (25)(2012) 5488-5501. Journal of Sound Vibration. 2014;333:1853-1854.

[222] Quan TQ, Tran P, Tuan ND, Duc ND. Nonlinear dynamic analysis and vibration of shear deformable eccentrically stiffened S-FGM cylindrical panels with metal–ceramic–metal layers resting on elastic foundations. Composite Structures. 2015;126:16-33.

[223] Duc ND, Bich DH, Cong PH. Nonlinear thermal dynamic response of shear deformable FGM plates on elastic foundations. Journal of thermal stresses. 2016;39:278-297.

[224] Nayfeh AH, Mook DT. Nonlinear oscillations. New York: John Wiley & Sons, 2008.

[225] Sofiyev AH. Nonlinear free vibration of shear deformable orthotropic functionally graded cylindrical shells. Composite Structures. 2016;142:35-44.

[226] Pan E. Exact solution for functionally graded anisotropic elastic composite laminates. Journal of Composite materials. 2003;37:1903-1920.

[227] Vol'mir AS. Nonlinear Dynamics of Plates and Shells. 1972;Nauka, Moscow:(in Russian).

[228] Shen HS. Postbuckling of shear deformable FGM cylindrical shells surrounded by an elastic medium. International Journal of Mechanical Sciences. 2009;51:372-383.

[229] Lee D-S. Nonlinear dynamic buckling of orthotropic cylindrical shells subjected to rapidly applied loads. Journal of Engineering Mathematics. 2000;38:141-154.

[230] Naumann E, Sewall J. An experimental and analytical vibration study of thin cylindrical shells with and without longitudinal stiffeners. Hampton, VA: Technical Report NASA Langley Research Center; 1968.

[231] Naeem M, Sharma C. Prediction of natural frequencies for thin circular cylindrical shells. Proceedings of the Institution of Mechanical Engineers, Part C: Journal of Mechanical Engineering Science. 2000;214:1313-1328.

[232] Reddy JN. Mechanics of laminated composite plates and shells: theory and analysis: CRC Press, 2004.

[233] Vol′mir AdS. The nonlinear dynamics of plates and shells. DTIC Document; 1974.

[234] Greenberg JB, Stavsky Y. Vibrations of Laminated Filament-Wound Cylindrical-Shells. AIAA Journal. 1981;19:1055-1062.

[235] Liu B, Xing YF, Qatu MS, Ferreira AJM. Exact characteristic equations for free vibrations of thin orthotropic circular cylindrical shells. Composite Structures. 2012;94:484-493.